1-1-2011

Experimental and Theoretical Investigation of Glass Fibre Reinforced Polymer Tension Lap Splices in Ultra High Performance Concrete

Chratien Mak
Ryerson University

EXPERIMENTAL AND THEORETICAL INVESTIGATION OF GLASS FIBRE REINFORCED POLYMER TENSION LAP SPLICES IN ULTRA HIGH PERFORMANCE CONCRETE

By

Chratien Mak

B.Eng. Civil Engineering, Ryerson University, Toronto, 2009

A Thesis

Presented to Ryerson University

in partial fulfillment of the degree of

Master of Applied Science

Civil Engineering

Toronto, Ontario, Canada, 2011

AUTHOR'S DECLARATION PAGE

I hereby declare that I am the sole author of this thesis.

I authorize Ryerson University to lend this thesis to other institutions or individuals for the purpose of scholarly research.

Author's Signature: _____ Date: _____

I further authorize Ryerson University to reproduce this thesis by photocopying or by other means, in total or in part, at the request of other institutions or individuals for the purpose of scholarly research.

Author's Signature: _____ Date: _____

ACKNOWLEDGEMENTS

The author would like to express his utmost appreciation and gratitude towards his supervisor, Dr. K.M. Anwar Hossain, Department of Civil Engineering, Ryerson University, as well as his co-supervisor Dr. Mohamed Lachemi for providing the opportunity to pursue this research. Additional thanks to Dr. K.M. Anwar Hossain for his invaluable guidance, knowledge and experience which have played a significant role in the success of this project while his incredible support and encouragement are greatly appreciated.

The author would also like to thank the research and technical team at Ryerson University for their hard work and assistance throughout this project. The technicians Nidal Jaalouk, Domenic Valle, and Mohammad Aldardari were vital during all phases of planning, construction, and testing and their expertise was extremely helpful. Further appreciation goes to the various research assistants that were involved at different stages of this research. The author would especially like to thank Dave Ametrano for his extraordinary hard work and collaboration as well as Maxime Anstette, a visiting scholar from IMFA, France, that helped bring this project to completion.

Furthermore, the author would like to acknowledge the generosity of various industry organizations for providing the funding and materials to conduct this research. The Ministry of Transportation of Ontario, through their Highway Infrastructure Innovations Program, provided funding for this project. Lafarge North America and King Packaged Materials Ltd provided the main concrete materials. Additional thanks goes to Peter Calcetas from Lafarge North America and Simon Renny from King Packaged Materials Ltd. for providing technical support for their products. Also, thanks to Pultrall Inc. and their representative Gene Latour for providing the GFRP bars.

Most of all, the author would like to thank Desalyn Dizor for her love and patience throughout this project. Her kindness and support are greatly appreciated. The author would also like to give thanks to his family for providing him with this incredible learning opportunity.

DEDICATED TO DESALYN

EXPERIMENTAL AND THEORETICAL INVESTIGATION OF GLASS FIBRE REINFORCED POLYMER TENSION LAP SPLICES IN ULTRA HIGH PERFORMANCE CONCRETE

Chratien Mak

Master of Applied Science, Civil Engineering

Ryerson University, Toronto, Canada, 2011

ABSTRACT

Glass fibre reinforced polymer (GFRP) reinforcements are a viable replacement for corroding steel rebars. GFRP rebar tension lap splices combined with ultra high performance concrete (UHPC) can improve the efficiency of materials and construction in bridge deck construction joints. This thesis investigates the bond performance of high modulus (HM) GFRP rebar splices using UHPC. UHPC slab/beams of 100 -170 MPa concrete having 150 - 300 mm tension splices were tested along with several beams constructed from prefabricated high strength concrete sections with central GFRP spliced UHPC joints. Theoretical analysis was also conducted to evaluate critical splice lengths. Based on comparisons with code design values, recommendations are made on potential failure modes and minimum splice lengths. The serviceability, fatigue, and environmental performance of GFRP in UHPC are also considered. Recommendations from this research will improve the safety and efficiency of GFRP tension lap joints used in bridge decks and other construction.

Table of Contents

List of Tables

List of Figures

Notation

A	a coefficient in the general equation for modulus of displacement analysis
A_b	reinforcing bar area, mm^2
A_c	effective area of concrete in modulus of displacement analysis, mm^2
A_{frp}	total area of main tensile FRP reinforcement, mm^2
A_{HM}	total area of high modulus reinforcement, mm^2
A_{LM}	total area of low modulus reinforcement, mm^2
b	width of flexural member, mm
B	a coefficient in the general equation for modulus of displacement analysis
c	depth of neutral axis, mm
C	resultant compressive force in compression zone of a flexural member, N
C_1	effective cover for ACI 440.1R-06 development length equation, mm
c_e	effective cover, mm
c_y	bottom clear cover, mm
d	effective depth of a flexural member, mm
d_b	bar diameter, mm
d_{cs}	concrete cover contribution to splitting resistance in CSA S6-06 and CSA S806-02 development length equations, mm
d_1	depth to top layer of tensile reinforcement (low modulus reinforcing bars), mm
d_2	depth to bottom layer of tensile reinforcement (high modulus reinforcing bars), mm
e	eccentricity between the centroid of main tensile reinforcement to the centroid of the resultant compressive force in a flexural member, mm
e'	eccentricity between the centroid of secondary tensile reinforcement to the centroid of the resultant compressive force in a flexural member, mm
E_c	modulus of elasticity of concrete, MPa
E_{frp}	modulus of elasticity of FRP reinforcement, MPa
E_{HM}	modulus of elasticity of high modulus glass fibre reinforced polymer reinforcement, MPa
E_{LM}	modulus of elasticity of low modulus glass fibre reinforced polymer reinforcement, MPa
E_s	modulus of elasticity of steel, MPa

F	bar force at location x of an embedment length, N
F_{HM}	bar force in high modulus reinforcing bars, kN
f_c	variable stress in concrete corresponding to ε, MPa
$f'c$	concrete compressive strength, MPa
f_{cr}	cracking strength of concrete, MPa
f_{frp}	stress in FRP reinforcement, MPa
f_{frpu}	ultimate tensile strength or design tensile strength of an FRP reinforcing bar, MPa
frp_1	spliced FRP reinforcing bar with loaded end in negative x direction
frp_2	spliced FRP reinforcing bar with loaded end in positive x direction
k	post peak decay in stress factor for concrete stress distribution
K	modulus of displacement, N/mm^3
k_{tr}	transverse reinforcement index in CSA S6-06 development length equation, mm
k_1	bar location factor
k_2	concrete density factor
k_3	bar size factor
k_4	bar fibre factor or bond dependent coefficient
k_5	bar surface condition factor
l	splice length, mm
$l_{critical}$	critical splice length, mm
l_d	development length, mm
l_e	embedment length, mm
M_r	resisting moment at a section of a flexural member, kNm
n	modular ratio
n_k	curve fitting factor for concrete stress-strain distribution
P	total applied load, kN
r_b	radius of reinforcing bar, mm
T	resultant tensile force in tension zone of a flexural member, N
T_{LM}	total tensile force of low modulus reinforcement, N
T_{HM}	total tensile force of high modulus reinforcement, N
u	perimeter of a reinforcing bar, mm

x distance from mid-splice or distance along an embedment length, mm

α general ratio of average compressive stress in a rectangular stress block to the concrete compressive strength for flexural members

α_1 ratio of average compressive stress in a rectangular stress block to the concrete compressive strength for flexural members with concrete strain at extreme compressive fiber equal to -0.0035

β general ratio of the depth of rectangular stress block to the depth of neutral axis for concrete flexural members

β_1 ratio of the depth of rectangular stress block to the depth of neutral axis for flexural members with concrete strain at extreme compressive fiber equal to -0.0035

γ_1 stiffness degradation factor equal to the ratio of the slope of the load deflection curve at a given cycle to the slope from the first cycle for fatigue loading

γ_2 residual deflection factor equal to the ratio of the x-intercept of the line of best fit passing through the load deflection curve at a given cycle to the x-intercept of the first cycle for fatigue loading

γ_3 crack width factor equal to the ratio between the crack widths at a given cycle to the crack width after the first cycle for fatigue loading

γ_4 load capacity factor equal to the ratio between the ultimate load capacity of a fatigue slab/beam to the load capacity of the non-fatigue slab/beam equivalent

ε variable strain in concrete corresponding to f_c

ε_c maximum strain of concrete at extreme compressive fiber of a flexural member

ε_{cu} ultimate strain of concrete in compression (typically -0.0035)

ε_p peak strain corresponding to peak compressive stress ($f'c$) of concrete

ε_{frpu} ultimate strain of an FRP bar

ε_{HM} strain in high modulus reinforcement

ε_{LM} strain in low modulus reinforcement

κ_1 constant equal to $\sqrt{\frac{uK}{E_{frp}A_b}(1+2n\rho)}$, 1/mm

κ_2 constant equal to $\sqrt{\frac{uK}{E_{frp}A_b}}$, 1/mm

ρ ratio of reinforcing bar area to effective concrete area for modulus of displacement analysis

ρ_{frp} reinforcement ratio

ρ_{frpb} balance reinforcement ratio

σ_b tensile stress in a reinforcing bar at the loaded end of an embedment or splice, MPa

σ_c tensile stress in concrete at extreme compressive fiber, MPa

$\sigma_{cactual}$ concrete tensile stress at the extreme tension fibre of the effective concrete area, MPa

$\sigma_{caverage}$ average tensile stress over the effective concrete area, MPa

σ_{ct} tensile stress in effective concrete area at location x, MPa

σ_{frp0} maximum tensile stress at the loaded end of a spliced FRP reinforcing bar in modulus of displacement calculation, MPa

σ_{frp1} tensile stress at location x of spliced frp_1 reinforcing bar in modulus of displacement calculation, MPa

σ_{frp2} tensile stress at location x of spliced frp_2 reinforcing bar in modulus of displacement calculation, MPa

σ_{HM} tensile stress in high modulus reinforcement, MPa

σ_{LM} tensile stress in low modulus reinforcement, MPa

τ_{avg} average bond stress, MPa

τ_{max} maximum bond stress, MPa

τ_1 bond stress at location x of spliced frp_1 reinforcing bar in modulus of displacement analysis, MPa

τ_2 bond stress at location x of spliced frp_2 reinforcing bar in modulus of displacement analysis, MPa

ϕ_c material resistance factor for concrete

ϕ_{frp} material resistance factor for FRP reinforcing bars

Chapter 1 Introduction

1.1 General Overview

Glass fibre reinforced polymer (GFRP) rebars are increasingly being used as a replacement for conventional steel reinforcement. Steel reinforced structures such as bridges and parking garages pose a long-term issue when exposed to harsh climates and corrosive environments. Corrosion of the steel reinforcement may cause failure of a member, reduce serviceability performance, lead to spalling of the concrete cover and reduce aesthetics (Benmokrane et al. 2007). The use of GFRP reinforcement can help mitigate these effects and thus reduce the future maintenance and repair costs due to GFRP's noncorrosive nature. GFRP also provides other qualities that are superior to steel such as higher strength to weight ratio and greater tensile strength and is expected to provide economic savings in the long run due to the increased durability and service life of the structure (ISIS Canada 2007). This material has already been proven to be a viable replacement for bridge decks and parking garages especially in North America with many construction projects already completed (Benmokrane et al. 2007; El-Salakawy et al. 2005; ISIS Canada 2007; Perry et al. 2007; Rajlic et al. 2010). In addition to deteriorating infrastructure, bridges are also facing increasing standards for load capacity and are now being rendered obsolete. It is imperative now that, with the already substantial and ever growing number of bridges that need repair, engineers look towards these new materials as a solution for replacement and rehabilitation.

In addition to the problem of deteriorating infrastructure, engineers must also find ways to deal with the need for more efficient and economical construction. Population growth and increased traffic demand push for faster overhaul and repair of bridges in order to minimize traffic interruptions. One method being used to address this issue is prefabrication. This construction method is used in many different applications but with bridge building it is especially effective since all the major components of a bridge such as the superstructure members, bridge deck and bridge barriers can be prefabricated leaving a minimal on site construction effort. Prefabricated sections can be sent to the site as needed and joined together using relatively small amount of in-situ casting. This reduces the construction time and may provide advantages in urban areas where storage space is limited. Quality control is also enhanced since members are constructed in a controlled factory setting rather than

outdoors where environmental conditions are constantly changing. Engineers also prefer the use of this method since it simplifies the design process. For these reasons prefabricated bridge construction is expected to comprise a large portion of the overhaul and repair of the current infrastructure (Shah et al. 2006; 2007; Perry et al. 2007).

In recent years there have been many developments in the industry where GFRP reinforcements are manufactured with different surface conditions, ribbed or spiral wound geometry, and a higher tensile modulus. High modulus (HM) GFRP rebars have a much higher tensile strength and modulus of elasticity. Due to its recent development there is little to no research work published on this topic. The superior qualities of HM GFRP rebar may prove to be an even better replacement than its low or standard modulus predecessors provided that their improved properties are worth the additional cost. This new material definitely has the potential to help solve the current infrastructure deterioration/deficiencies and will be the basis for this research.

Ultra high performance concrete (UHPC) is another emerging technology that is being used with prefabrication methods. Casting UHPC around the lapped protruding reinforcement and steam/heat-treating it for faster strength development is one method used to join adjacent sections. UHPC is usually steel fibre reinforced and consists mainly of fine material both of which add to the compressive strength and tensile capacity of the concrete matrix around reinforcement. The added strength allows for the use of smaller splice lengths and thus narrower joint widths. Reducing joint widths can significantly reduce the amount of concrete that needs to be produced on site. UHPC is preferable to traditional coarse aggregate concrete due to its higher strength, response to heat treatment, ability to fill tight spaces without the need for extensive consolidation methods and superior durability. The enhanced durability of UHPC is a result of reduced crack widths from fibre bridging, increased toughness and abrasion resistance, and reduced permeability due to the superior microstructure created by the composition of fine materials (Graybeal 2006a).

The use of UHPC with narrower joint widths has given rise to the concept of a high performance bridge joint (HPBJ). HPBJs have been used in several construction projects but mainly with steel rebar (Harryson 2003; Perry and Royce 2010). The reason being that the bond between concrete and steel reinforcement benefits far more from a higher concrete strength than does GFRP rebar since pullout failures with steel are governed mainly by

concrete crushing around the steel ribs (Lee et al. 2008). The use of UHPC has shown to reduce joint widths by about 50-75% using this application (Harryson 2003). This method has not been widely adopted with GFRP reinforcement, however initial attempts at using UHPC with GFRP reinforced precast bridge decks have proven successful (Perry et al. 2007).

Current design codes do not include provisions for the design of such members with GFRP. There is also a lack of research involving the bond of GFRP rebar with UHPC as well as their performance in tensile lap splices. As a result it is necessary to assess the behaviour of GFRP reinforcement splices within UHPC in order to stay ahead of the changing industry and construction methods so that future precast bridge projects can benefit from the enhanced properties of these new materials. The main idea is to see whether or not it is possible to use enhanced materials such as a higher modulus GFRP rebar and UHPC to produce a HPBJ suitable for use in prefabricated bridge decks.

1.2 Problem Statement

The purpose of this study is to examine the structural, serviceability and durability characteristics of HM GFRP in reduced tension lap splices embedded in UHPC by means of experimental testing and theoretical predictions. The performance of experimental test specimens will be evaluated on the above aspects using the relevant design codes. Conclusions will then be made about the practicality and feasibility of using these materials for the particular application of HPBJs. Recommendations for the current design codes will also be included based on the experimental results.

1.3 Objectives

The general approach is to replicate a section of slab that has similar dimensions and loading conditions as a bridge deck. A tensile lap splice with variable length using HM GFRP rebar will be introduced at mid-span for each slab/beam specimen. Splice lengths will be chosen by imposing a reduction on commonly used standard joint widths and examining the performance using strength and serviceability criteria. Static or fatigue loading will be applied to the specimens in order to achieve the main objectives. Pullout specimens will also be used to assess the bond performance of GFRP bars under aggressive environments. The

main objective of this research is to determine the behaviour of reduced GFRP tensile lap splices embedded in UHPC based on these criteria:

- Ultimate Capacity / Maximum Applied Load
- Bar Force Development and Average Bond Stress
- Bar Strain Distribution Versus Load
- Load Deflection Behaviour
- Effect of Concrete Strength/Splice Length on the Bond Behaviour
- Fatigue Behaviour
- Crack Patterns / Propagation
- Failure Modes
- Bond Strength Versus Embedment Length
- Bond Performance Under Aggressive Environments (Freezing/Thawing)
- Theoretical Modeling of Bond Stress Distribution and Ultimate Bar Stress
- Code Comparisons

1.4 Thesis Overview

This thesis contains 7 main chapters and the following is a breakdown of each.

Chapter 1 - Introduction

The introduction briefly discusses the topic of GFRP rebar and UHPC. It also serves to introduce the method of construction known as HPBJ for prefabricated sections and how HM rebar and UHPC can be used together as a solution to the problem of deteriorating infrastructure.

Chapter 2 - Literature Review

The literature review will cover various aspects of this project through previous research and published design codes. This information will help to outline the research methodology, test parameters and overall design of the specimens and test mechanisms.

Chapter 3 - Experimental Program

This chapter will discuss the materials, specimen design and testing method used in this research. It will also outline the procedures used to construct each specimen type, to administer fatigue testing, and to conduct environmental testing on the necessary specimens.

Chapter 4 - Experimental Results and Discussion

This will present the results through the perspective of the main objectives explained earlier. A discussion and comparison of the results will also be included for each of the objectives.

Chapter 5 - Theoretical Predictions of Bar Stress Distribution in Tension Lap Splices

A theoretical model is presented to predict the performance of tensile lap splices. The model will be fitted with the geometric and material properties of each slab/beam specimen. The theoretical and experimental results will be compared for each specimen to evaluate the validity of the model as well as its deficiencies.

Chapter 6 – Code Comparisons of Critical Splice Lengths

Critical splice lengths will be evaluated using the developed theoretical model and the geometric and material properties of the test specimens. The values obtained will be compared with the code requirements for splices.

Chapter 7 – Conclusions and Recommendations

This chapter summarizes the findings obtained from this research. An overall assessment on the feasibility of using a reduced joint of GFRP and UHPC will be determined. Recommendations and improvements for future research will also be presented.

Chapter 2 Literature Review

2.1 Introduction

The goal of this study is to examine the behaviour of reduced tensile lap splices using HM GFRP rebar and UHPC. The first section will introduce the main construction materials. Both GFRP and UHPC are relatively new to the industry as standard building materials. Their properties and applications are constantly changing and it is necessary to establish a basis for what is currently available and being used in the industry. Information on the composition, manufacturing processes, and material properties will be presented. Next, the concepts of bond stress, development length, and tensile lap splices are established and the current research is investigated on the various factors affecting these concepts. Additional research done on the topics of bridge deck slabs, high performance bridge joints (HPBJ), and performance of GFRP rebar under harsh environments will be examined to gain insight into testing procedures, expected behaviours, etc. Current design methods and failure mode considerations for flexural members reinforced with FRP rebar are also reviewed.

2.2 Glass Fibre Reinforced Polymer Rebar

2.2.1 Material Composition

Like most fibre reinforced polymer products, GFRP rebar is a composite material made up of fibres surrounded by a polymer matrix such as in Figure 2.1. The fibres act to reinforce the matrix by providing high tensile strength and stiffness. Currently, there are three main types of fibres used in construction namely glass, carbon and aramid. Out of the three glass fibres are the cheapest to produce, which is why it has become the most adopted fibre reinforced bar for infrastructure applications. However, glass fibres also have the lowest tensile modulus of elasticity usually in the range of 3 to 4 times less than steel. Glass fibres are manufactured using the direct melt method where fibres ranging from 3 to 25 micrometers are drawn from melted glass. Glass fibres are the heaviest of the three main fibre types used today. The matrix portion serves to combine all the individual fibres together so that forces are more evenly distributed between each. This is achieved by ensuring an even distribution of fibres throughout the cross section and by maintaining a strong chemical bond. It provides rigidity so that the bar retains its shape while also

protecting the fibres from mechanical and environmental damage. It is also important for the matrix to have similar thermal expansive properties as the fibres in order to maintain compatibility through temperature variations. Matrix materials come in three main types classified under thermosetting polymers: epoxies, polyesters, and vinylesters. Due to the chemical bond between the monomeric compounds of the polymer, thermosetting materials cannot be remolded once they have reached initial set and will experience a significant degradation in performance if reheated beyond the glass transition temperature. As a result the shape of the reinforcement must be chosen prior to manufacturing and cannot be easily reversed once the polymer has set (ACI Committee 440 2006; ISIS Canada 2006).

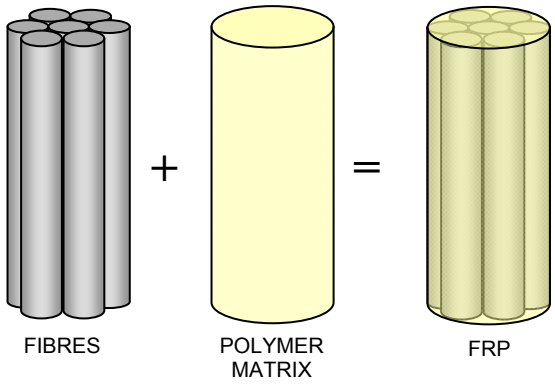

Figure 2.1: Main components of an FRP reinforcing bar (ISIS Canada 2006)

2.2.2 Manufacturing Processes

The fabrication method of fibre reinforced polymer (FRP) products depends very much on the application. The more common methods include the wet lay-up method for applying FRP sheets or wraps in strengthening applications, the filament winding method for hollow members such as pipes and tubes, and the pultrusion method used for making bar type or plate type reinforcements. The pultrusion process illustrated in Figure 2.2 consists of spooling individual fibres off of creels and into a resin bath where they are coated in the matrix polymer. The resin-coated fibres are then pulled through a shaping and heating die where the product takes form and is allowed to set. Here the shape of the member can be chosen whether it is a structural section or a bar. Since the fibres are constantly being pulled in one direction they are aligned uniformly along the section. The behaviour and strength of

the section is thus anisotropic with the higher tensile strength arranged in the fibre direction. The fibre volume fraction of reinforcing bars generally exceeds 55 percent for the added strength and stiffness. The GFRP rebars used in this study were manufactured using this procedure. This manufacturing process provides additional cost savings in that it can be made fully automated (ISIS Canada 2006). An additional surface treatment may also be included to enhance the bond properties and these surface conditions can vary from sand coated, ribbed, spirally wound, helically wrapped and grooved (Baena et al. 2009).

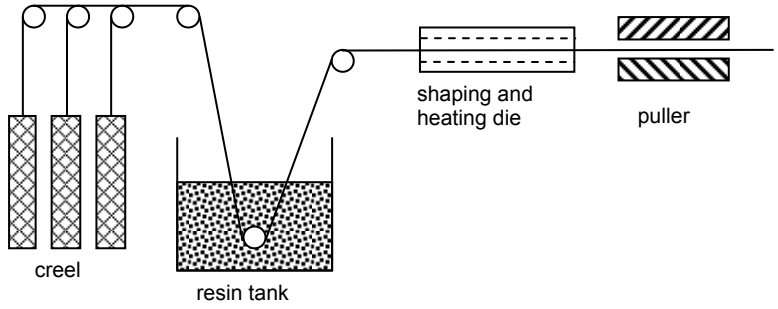

Figure 2.2: Manufacturing process for FRP rebar and structural sections (ISIS Canada 2006)

2.2.3 Material Properties of GFRP and Other Rebar

Table 2.1 shows a comparison of the typical material properties found for bar and tendon type reinforcements of both FRP and steel. Included in the table are the properties of carbon fibre reinforced polymer (CFRP) and aramid fibre reinforced polymer (AFRP) tendons. GFRP gives a tensile strength range that is at the lower bound of the other types of FRP, however it still provides significantly higher tensile strength than steel rebar. FRP materials are generally linear elastic until failure however they do not exhibit yielding. Thus they can experience sudden failure with little warning beforehand whereas strain hardening in steel reinforcement provides additional ductility. GFRP also has a much lower elastic tensile modulus versus the other reinforcement types. The coefficient of thermal expansion (CTE) in the fibre direction shows similar behaviour for both GFRP and steel. This allows GFRP to be a viable replacement for steel in reinforcing concrete structures. GFRP also provides the added benefit of a high tensile strength to weight ratio versus steel even though it is the heaviest out of the three FRP types (ISIS Canada 2006).

Table 2.1: Material properties of various reinforcing bars and tendons (ISIS 2006)

Property	Steel Rebar	Steel Tendon	GFRP Rebar	CFRP Tendon	AFRP Tendon
Tensile Strength (MPa)	483-690	1379-1862	517-1207	1200-2410	1200-2068
Yield Strength (MPa)	276-414	1034-1396	N/A	N/A	N/A
Tensile Elastic Modulus (GPa)	200	186-200	30-55	147-165	50-74
Ultimate Elongation (%)	>10	>4	2-4.5	1-1.5	2-2.6
Compressive Strength (MPa)	276-414	N/A	310-482	N/A	N/A
CTE (10^{-6}/°C)	11.7	11.7	9.9	0	(-1) – (-0.5)
Specific Gravity	7.9	7.9	1.5-2.0	1.5-1.6	1.25

GFRP rebar can be superior to conventional steel reinforcement in many ways but there are some disadvantages that should be accounted for during design. As mentioned earlier FRP materials do not yield and can fail abruptly near the ultimate tensile capacity. Figure 2.3 demonstrates that while FRP materials have a much higher tensile strength, steel has a greater degree of ductility and a superior elastic modulus. To avoid sudden catastrophic failure design codes recommend material reduction factors that limit the allowable stress range of FRP reinforcement even more than for steel or concrete. There is also a minimum requirement for the ultimate capacity of bending members versus their cracking strength to ensure there is enough reserve strength to prevent sudden failure during transfer of tensile forces to the FRP (ACI Committee 440 2006; CSA 2006).

The anisotropic behaviour of GFRP poses some additional dilemmas. The transverse thermal expansion of GFRP rebar is about 21.0 - 23.0 (10^{-6}/°C), for fibre volume fractions of 0.5 to 0.7, which is about twice as much as steel and five times more than concrete. This can lead to problems of splitting cracks in environments where thermal cycling between hot and cold temperatures is an issue. High temperatures and thermal cycling can also enhance the degradation due to environmental effects such as moisture absorption and high alkalinity. Damage due to moisture mainly affects the matrix material and subsequently the shear and compressive properties of FRP until the point of saturation. High alkalinity can react with glass fibres and cause brittleness to occur reducing the strain capacity and strength. The

polymer matrix can be enhanced with additives to help protect against alkaline environments. All FRP materials also experience some degradation in strength due to ultra-violet radiation so precautions must be made to prevent prolonged exposure to sunlight during construction. The fatigue performance of GFRP is not well known but has been shown to be comparable with steel. It is however at a disadvantage due to the high strains caused by the low modulus of elasticity. Larger strains contribute to the degradation of the matrix and matrix-fibre interface. GFRP reinforcements are also prone to a phenomenon called creep-rupture. Premature failure has been known to happen under circumstances where the sustained load is high. This mode of failure is attributed to the visco-elastic behaviour of the polymer matrix and so it does vary with the fibre volume fraction. High temperatures have also been known to amplify the effect of creep. Design codes have imposed a limit on the maximum sustained load to 20-25% of the ultimate strength for FRP materials (ISIS Canada 2006; 2007).

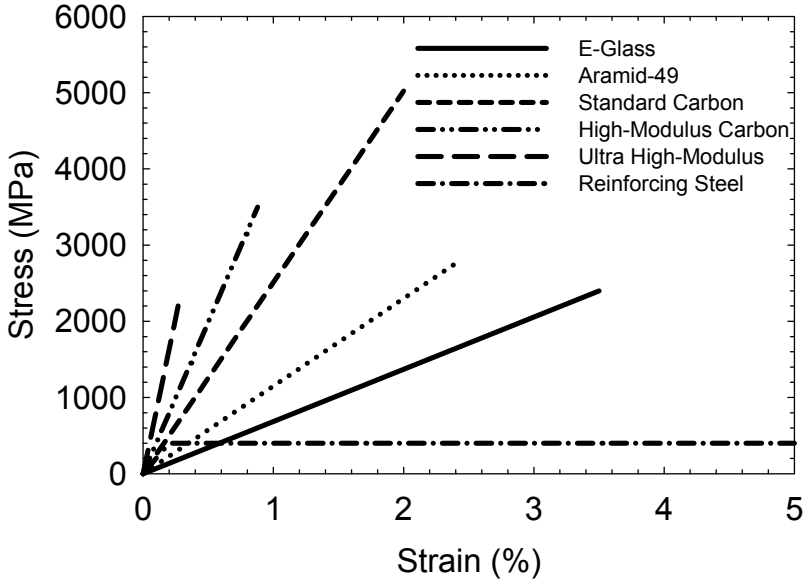

Figure 2.3: Stress strain behaviour of various reinforcing materials (ISIS Canada 2006)

2.3 Ultra High Performance Concrete (UHPC)

2.3.1 Classification of Ultra High Performance Concrete

UHPC has been developed to a point where it has now become a commercial product. The characteristics of UHPC differ from high strength concrete in many respects but the most notable distinctions are the enhanced strength and durability. While there is no solid

standard currently in place to which researchers can refer to it is necessary to provide some classification to which the term UHPC can be used. Some researchers have referred to the Association Française de Génie Civil publication: *Ultra High Performance Fibre-Reinforced Concretes – Interim Recommendations* (AFGC 2002) as a general guideline for UHPC characteristics. This report generally refers to concrete with 147 - 200 MPa compressive strength, 50 - 65 GPa compressive modulus, and some form of fibre reinforcement. Typical characteristics also show a very high flexural tensile strength and toughness compared to normal concrete. Additional guidelines are also found in the 2006, U.S Department of Transportation Federal Highway Administration publication: *Material Property Characterization of Ultra-High Performance Concrete* (Graybeal 2006a). This extensive report includes a multitude of tests using various curing methods on a commercially available UHPC. Both reports share a consensus on the above properties while the latter also incorporates some additional similarities in the mix designs of UHPC as having a low water to cement ratio, use of a superplasticizer, and use of a specialized gradation of fine aggregates such that when combined with the cementing materials will provide an optimized granular structure with little to no voids (AFGC 2002; Graybeal 2006a; Okuma 2006).

2.3.2 Material Composition, Mixing and Curing Procedures

Typical UHPCs incorporate fine sand, Portland cement, silica fume, steel fibres, water and a superplasticizer into the mix design. The fine sand commonly consists of silica sand and in some cases ground quartz. General use Portland cement and silica fume are the main cementing materials while some researchers have also reported the use of metakaolin as a supplement. Steel fibres can vary in strength, dimensions, and deformities however some of the more widely used fibre types for UHPC application are 12.7-13.0 mm in length, 0.16-0.20 mm in diameter, have a minimum tensile strength of 2600 MPa, and an average tensile modulus of elasticity of up to 205 GPa. The length and diameter of the steel fibres are chosen to be compatible with the small particle size of the other dry components such that sufficient bond is achieved at the microscopic level and the fibres are able to act as reinforcement. Fibres are typically added at a fibre volume fraction of about 2%. The use of a water reducing admixture or superplasticizer helps to reduce the water/cementing materials

ratio to levels below 0.22 for most UHPCs. In some cases an accelerator may be added to the mix to reduce the initial set time (Graybeal 2006a; Tafraoui 2009).

Mixing procedures and times can vary depending on the type of water reducing admixture, overall mix design, volume of mix, mixer capabilities, and temperature of the surrounding environment. All the dry materials, excluding the steel fibres, are mixed in a vertical shaft mixer until homogeneous. Water and half the superplasticizer are combined and added while mixing. The mix is allowed to develop a paste like consistency before the addition of the remaining superplasticizer. After the mix has become fluid the fibres are evenly distributed throughout the mix by sprinkling over the surface during the final stage of mixing. A more detailed procedure is presented in the materials section of Chapter 3. Curing procedures can vary for different types of UHPC. UHPCs have the ability to develop considerable strength in response to heat and steam treatments. The design strength can be obtained through curing at temperatures of 90˚C – 150˚C with 95% relative humidity for the first 2-3 days after demoulding. Even when no curing procedures are implemented these concretes can still achieve significant strength gain within 28 days provided that moisture loss is prevented during initial set (Graybeal 2006a; Tafraoui 2009).

2.3.3 Material Properties

Table 2.2 shows typical ranges for strength and durability characteristics of a commercial UHPC as provided by the manufacturer. These values are likely to be for fully cured or steam treated specimens. Untreated test values will vary from these ranges even after 28 days. Due to the large amount of cementitious material and very low water content, much of the strength and durability of untreated specimens can still be developed even beyond 28 days. Studies conducted on this commercial UHPC have shown compressive strengths of up to 225 MPa with steam and heat treatments while untreated cylinder tests demoulded at an age as early as 28 hours showed average 28 day strengths as low as 99 MPa. The age of the premix is also thought to have an effect on the strength development within the first few days. Results also show an increase in the modulus of elasticity with an increase in strength.

Table 2.2: Material properties of a commercially available UHPC (Graybeal 2006a)

Material Property	Range
Compressive Strength (MPa)	180-225
Modulus of Elasticity (GPa)	55-58.5
Flexural Strength (MPa)	40-50
Chloride Ion Diffusion (m^2/s)	1.9×10^{-14}
Carbonation Penetration Depth (mm)	< 0.5
Freeze-Thaw Resistance (RDM)	100%
Salt-Scaling Resistance (kg/m^2)	< 0.012
Entrapped Air Content	2-4%
Post-Cure Shrinkage (microstrain)	0
Creep Coefficient	0.2 – 0.5
Density (kg/m^3)	2,440 – 2,550

Extensive research conducted on cylinder and cube specimens of various sizes appears to be in good agreement with the following equation proposed by Graybeal (2006a, 2007) relating the compressive strength with the modulus of elasticity:

$$E_c = 3840\sqrt{f'c} \quad \text{.....(2.1)}$$

where E_c and $f'c$ are the modulus of elasticity and compressive strength of concrete in MPa respectively. This equation can be applied to UHPC with similar composition between compressive strengths of 25 and 195 MPa with sufficient accuracy Graybeal (2006a, 2007). Figure 2.4 shows how the overall behaviour of concrete changes with compressive strength through their stress-strain curves. Clearly the compressive modulus increases with compressive strength and so does the linearity of the ascending branch. There is also a corresponding increase in the strain at peak stress however the descending branch after peak becomes more brittle (Collins and Mitchell 1997; Graybeal 2006a; Mendis 2003). A linear stress-strain relationship allows for a simplified triangular stress distribution over the traditional parabolic distribution for the compression region of a concrete beam. (High Performance Concrete Delivery Team 2005; Mendis 2003). Other researchers agree that the compressive stress of UHPC in flexural design can be assumed linear up to 85% of the maximum stress (Graybeal 2006b; Okuma 2006).

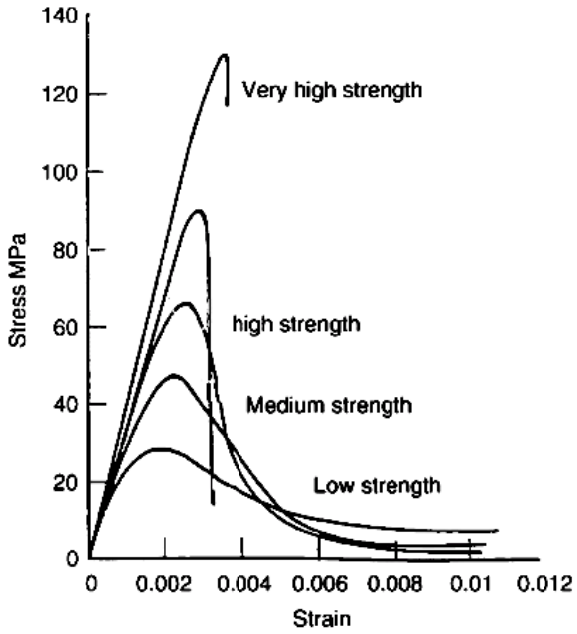

Figure 2.4: Stress strain distributions for normal to ultra high strength concretes (Mendis 2003)

2.4 Bond Stress and Development Length

2.4.1 Introduction to Bond Stress and Development Length

Bond stress is defined as the shear force per unit area between two surfaces. In reinforced concrete bond stress is the mechanism that acts at the interface between the reinforcing bar and the concrete matrix. Due to its inherent weakness under tension it is necessary for concrete to transfer tensile forces to some form of reinforcement by means of bond. There are three main mechanisms that provide bond between a straight reinforcing bar and concrete namely: chemical adhesion, mechanical interaction or bearing resistance, and friction. During the initial loading of a concrete member the bond force between a reinforcing bar and the concrete matrix are by means of chemical adhesion. Through repeated or increased loading the chemical bond will be lost and the forces will be transferred through bearing forces acting on the surface deformations of the reinforcement. When either the concrete or the reinforcement interface can no longer withstand the bearing forces significant slip and typically failure occurs. Any residual forces will then be due to friction between the two interfaces (Hao et. al. 2009; Tighiouart et al. 1998).

Bearing forces that act at an angle towards the bar are the main resisting forces present throughout the service life of a structure and can be broken down into two components as shown in Figure 2.5. For most deformed bars, i.e. surface treated with either ribs, lugs, sand coating, helical wrapping, etc. the bearing forces can be broken down to a longitudinal force acting along the length of the bar and a radial force acting outward from the center. The longitudinal force is what is interpreted as the bond force, which restrains the bar from being pulled out of the concrete, while the radial component is the outward force that is exerted on to the ring of concrete surrounding the bar shown in Figure 2.6. The outward force is the source for tensile splitting failure in this ring (MacGregor and Wight 2005; Tepfers 1982; Tepfers and De Lorenzis 2003).

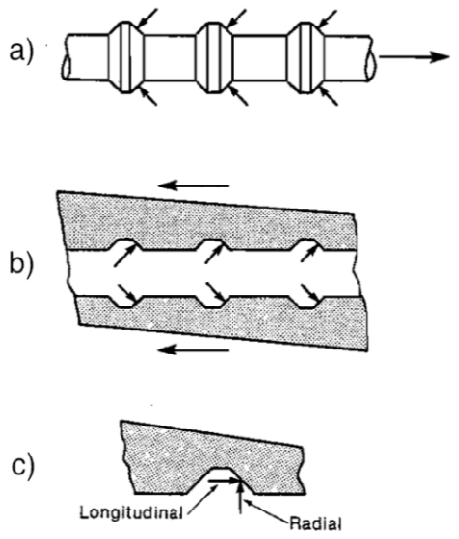

Figure 2.5: (a) Bearing force on a reinforcing bar; (b) bearing force on concrete; (c) main components of bearing force (MacGregor and Wight 2005)

In Figure 2.6a the effective cover, c_e, around a bar of diameter, d_b, makes up the concrete ring resisting the splitting tensile forces. A free body diagram of half the concrete ring shows the balance of forces necessary to maintain the splitting force on the concrete (Fig. 2.6b). Although a non-linear tensile stress distribution is present in the concrete, this may be simplified into a linear distribution for analysis of the splitting tensile capacity of the ring (MacGregor and Wight 2005).

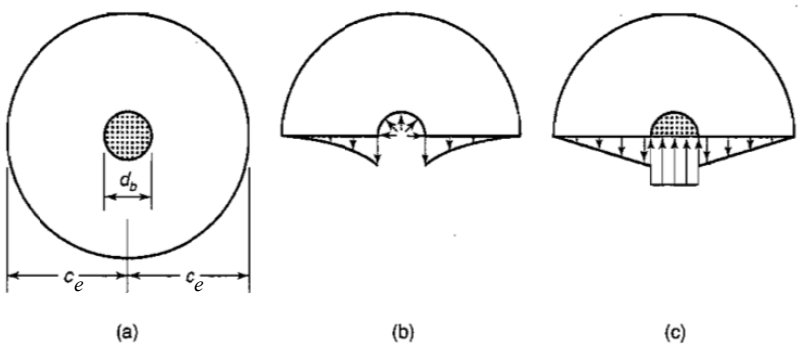

Figure 2.6: (a) Effective concrete ring surrounding a reinforcing bar; (b) radial components of bearing force and concrete tensile stress distribution; (c) simplified tensile resisting forces from the concrete ring and opposing bearing force components (MacGregor and Wight 2005)

The simplest representation of the bond stress on a reinforcing bar is given by equation 2.2 which gives the average distribution over an embedment length.

$$\tau_{avg} = \frac{\sigma_b A_b}{\pi d_b l_e} \quad \text{.....(2.2)}$$

where τ_{avg} is the average bond stress, A_b is the bar area, and σ_b is the bar stress at the loaded end, d_b is the diameter of the bar, and l_e is the embedment length. This equation gives an idealized uniform bond stress distribution throughout the entire embedment length. In reality the bond stress is not constant and the stress at the loaded end is much higher than at the free end of the bar especially for longer embedment lengths. The bond stress given by equation 2.2 is often referred to in design due to the simplicity in its application. A more general relationship between the bar force and bond stress distributions is given by equation 2.3a or 2.3b.

$$\frac{dF}{dx}\frac{1}{u} = \tau \quad \text{.....(2.3a)}$$

$$u\int \tau \, dx = F \quad \text{.....(2.3b)}$$

where u is the perimeter of the reinforcing bar, x is some distance from the free end of the

embedment, τ is the bond stress as a function of x, and F is the force in the bar at location x. The tensile force at the loaded end of an embedded bar is gradually transferred to the concrete through bond until there is zero bar stress at the free end. In order for the bar force to reach its ultimate capacity for a given bond stress distribution the embedment length l_e must be sufficiently long. This value is referred to as the development length or l_d. The term is often referred to by codes and design manuals as the shortest embedment length necessary to develop the full bar force from an initial zero load given a specific set of geometric and material properties (MacGregor and Wight 2005).

2.4.2 Bond Test Methods

Various methods have been developed to determine the maximum bond stress that a reinforcing bar can develop. These methods, shown in Figure 2.7 (ACI Committee 440 2004), vary in the way that load is applied and how the bar is embedded. The forces transferred from the concrete to the bar will have different distributions and subsequently the values obtained for maximum bond stress may not be the same.

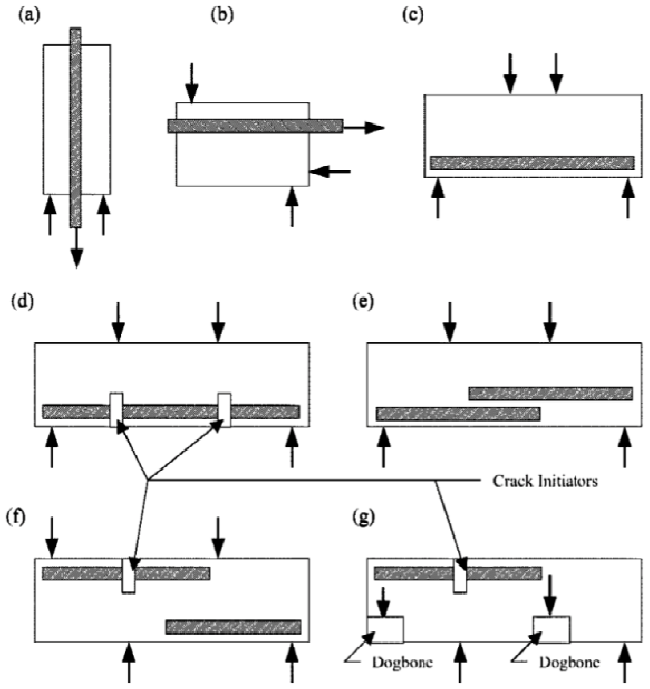

Figure 2.7: Bond test methods for reinforcing bars (a) pullout test; (b) beam-end test; (c) simply-supported beam test; (d) cracked beam test; (e) spliced beam test; (f) cantilever beam test; (g) cantilever beam test with dogbones (ACI Committee 440 2004)

Pullout specimens (Figs. 2.7a, b) are known to provide results that are greater than the bond stresses that will develop in a flexural member since the concrete surrounding the bar is in compression. Beam specimens give a more accurate representation of a flexural member since the surrounding concrete is also in tension and will be subjected to flexural and shear cracks (JSCE 1997; MacGregor and Wight 2005; Tighiouart et al. 1998, Tastani and Pantazopoulou 2006). Despite the drawbacks to pullout tests they still remain a common method for bond strength due to its low cost, simplicity, and direct approach for determining the bar force and bond stress (Davalos et al. 2008). Preliminary testing for new reinforcements is typically done in this fashion. The consistent use of the simple pullout test has also given rise to the "modified" pullout test that allows the concrete to be under tension during loading by restraining the specimen at the free end with additional embedded bars (Aiello et al. 2007; Tastani and Pantazopoulou 2006). Figure 2.8 shows a typical configuration for a modified pullout test.

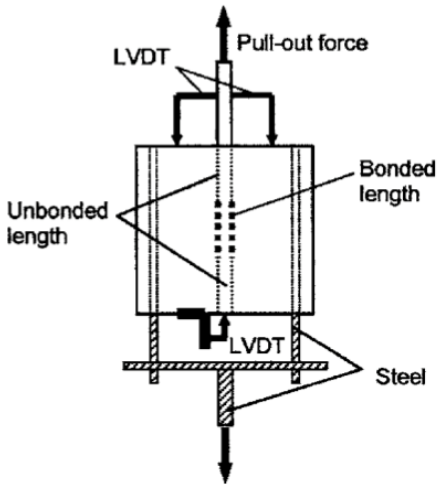

Figure 2.8: Modified pullout test for simulating conditions of concrete under tension (Aiello et al. 2007)

The RILEM Technical Committee provides an additional testing procedure with a hinged beam specimen shown in Figure 2.9. The two ends of a reinforcing bar are embedded into concrete blocks while the compression zone is connected with a steel hinge. The tension and compression forces in the reinforcement and hinge, respectively, can then be calculated directly using simple mechanics and equilibrium. The goal is to mimic the loading

configuration of an actual beam test while simplifying the calculation for bar force. Additional reinforcements are also provided within each block to prevent premature shear, tension, and splitting failure (RILEM 1994).

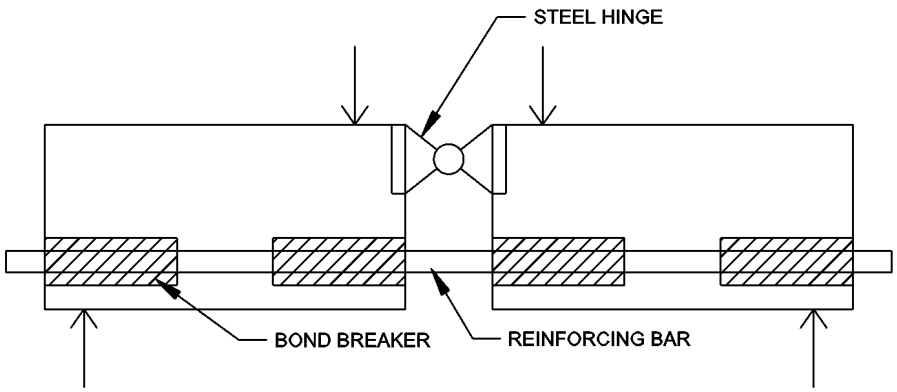

Figure 2.9: RILEM hinged beam test for bond strength of reinforcing bars (RILEM 1994)

2.4.3 Bond Failure Modes of Embedded Bars

When the embedment length is less than the development length one of pullout or splitting failure modes will occur. Pullout failure happens when the tensile resistance of the concrete ring, including the resistance provided by any confining reinforcement, is greater than the bar's circumferential radial forces. The tensile resisting force is governed by a concrete ring surrounding the bar with a radius equal to the least of either the concrete cover or half the bar spacing. When sufficient cover, spacing or confinement is provided then failure occurs at the concrete rebar interface and the bar is pulled out. For deformed steel reinforcement pullout failure is synonymous with the crushing of concrete around the bar's deformations due to the significantly higher strength of steel. However, with FRP reinforcement pullout failure can occur by crushing of concrete or by delamination of the surface between the fibre core and the resin coating. The failure interface largely depends on the concrete strength. A higher strength concrete prevents crushing failure and induces delamination and vice versa (Tepfers 1982; Tepfers and De Lorenzis 2003). Tests on sand coated GFRP rebar have shown that there is a direct correlation between the concrete strength and the amount of sand coating that is removed after pullout failure (Lee et al. 2008). Just prior to failure the bulk of the bond stress has also been known to shift towards

the free end due to significant loaded end slip (Brzev and Pao 2006; Chaallal and Benmokrane 1996).

Splitting failure takes place when there is insufficient cover or confinement such that the radial forces from the bar exceed the tensile resistance of the concrete ring. Partial cracking within the interior concrete initiates around the bar and eventually full splitting cracks occur longitudinally at the location where the cover is thinnest. The bond stress developed when splitting occurs is typically less than that of a pullout failure and is the most common type for design purposes. This mode of failure is also considered more brittle due to the sudden loss of bond strength when the concrete cover breaks off. When splitting occurs the bar stress in confined concrete has been shown to approach a linear distribution meaning the bar stress is roughly uniform at maximum load (MacGregor and Wight 2005; Tepfers 1980; 1982; Tepfers and De Lorenzis 2003). Figure 2.10 shows various types of splitting failure.

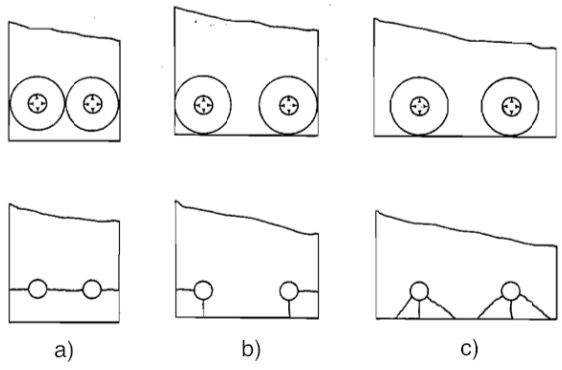

Figure 2.10: (a) Splitting due the side cover and bar spacing; (b) splitting due to side and bottom cover; (c) splitting due to bottom cover (MacGregor and Wight 2005)

2.4.4 Investigation of the Bond Behaviour of GFRP and Other Reinforcing Bars

Several factors are known to affect the bond stress development of a reinforcing bar. The rebar type, rebar modulus, concrete strength, embedment length, bar surface conditions, bar diameter, concrete cover, confining reinforcement, casting height, specimen type, and presence of reinforcing fibres in concrete are all major design parameters that influence the bond characteristics and failure mode. Some additional factors having to do with the changing environment and service conditions include degradation of the concrete due to severe temperature changes and moisture, degradation of the FRP due to high alkalinity, and

damage caused by fatigue loading. The following is a review of current research on the effects of various design parameters on the bond behaviour of GFRP and other reinforcing bars including the effect of extreme temperature cycling. The effect of various chemical conditions is beyond the scope of this research and will not be investigated.

2.4.4.1 Rebar Type and Modulus

Okelo and Yuan (2005) conducted 151 pullout tests using the three major FRP bar types along with steel rebar. It was found that the bond strength of an FRP bar can be 40-100% that of steel rebar when failure is by pullout. It was also found that the change in bar modulus due to the various fibre types of glass, carbon, and aramid can also influence the bond properties. Larralde and Silva-Rodriguez (1993) also had similar findings with the bond strength of spiral wound GFRP being 0.73-0.96 times the bond strength of steel rebar. Results from this study also showed that the bearing forces developed by GFRP bars were likely to be lower than steel due to the lack of splitting cracks around the bar. Tighiouart et al. (1998) agrees and concludes that it is mainly the adhesion and friction that govern the bond strength of GFRP bars. Chaallal and Benomkrane (1996) conducted bond tests using sand coated helically wrapped GFRP bars in RILEM beams and found bond strengths of 0.60-0.90 times that of steel depending on the bar diameter. Moon et al. (2008) used a mixture of milled glass fibres and epoxy resin to formulate a ribbed surface structure for GFRP fibre cores and obtained 56-90% the bond strength of steel rebar with similar diameter. Meanwhile, RILEM beam tests conducted by Okelo (2007) showed that CFRP provides 85% the bond strength of steel while the bond strength of GFRP bars with a reduced modulus was even lower. Baena et al. (2009) conducted 88 pullout tests and showed that the lower modulus of GFRP increased the slip at the same loads versus CFRP and steel rebar. A similar trend was also observed when comparing just GFRP bars with different bar moduli. It was also found that an increase in the concrete strength and modulus had a more noticeable effect on the bond stiffness when the bar modulus was low owing to the similarity in the material stiffness of GFRP and concrete. This trend was also observed by Larralde and Silva-Rodriguez (1993). Furthermore, Pecce et. al (2001) noted that due to the lower modulus of GFRP bars the loaded end slip of pullout tests was substantially greater than the free end slip as opposed to steel. This trend should also be taken into account during any

bond slip analysis and modeling. The influence of concrete strength on the failure modes of sand coated GFRP was observed by Lee et al. (2008) with failure occurring increasingly more in the sand coating layer with an increase in concrete strength. This also had the effect of reducing the ductility of failure of GFRP bars. The rate of increase of GFRP bond strength with concrete strength was found to be much less than steel. Additional research is necessary to establish the bond behaviour of HM GFRP bars since the majority of the current research is based on a standard / low modulus (LM) range of 40-55 GPa.

2.4.4.2 Concrete Strength

Okelo and Yuan (2005) conducted numerous pullout tests in concretes ranging from 30-60 MPa and identified concrete strength as having an effect on the failure mode of embedded FRP bars. Stronger concretes increased the bond to the point where splitting failure governed for short embedment lengths while weaker concretes allowed splitting failure for longer embedment lengths. Their research also led them to the conclusion that the bond strength of FRP bars in normal strength concrete was a function of $\sqrt{f'c}$. On the other hand pullout tests conducted by Ehsani et al. (1997) using ribbed GFRP bars in concrete strengths of 28 and 56 MPa showed that this increase was not proportional to $\sqrt{f'c}$. Similar concrete strengths at about 28 and 52 were used by Baena et. al (2009) for pullout tests of various bar types. A change in failure mode from the concrete surface to the sand coating layer was noted for concretes beyond 30 MPa indicating that the bond strength becomes more dependent on the bar properties as concrete strength increases. Increasing concrete strength also influenced the initial bond stiffness of GFRP bars. Pullout tests conducted by Lee et al. (2008) using sand coated GFRP bars embedded in concrete strengths ranging from 26-92 MPa were in contradiction with the previous conclusion. Although the failure mode shifted more to the sand coating layer with higher concrete strengths, a steady increase in bond strength was observed for sand coated GFRP bars. Furthermore, it was found that the average percent of sand coating removed after pullout failure increases from 27% at the lowest concrete strength to 97% at the highest concrete strength. This indicates that with purely pullout failures of GFRP there is a gradual transition of the failure interface with increasing concrete strength rather than a sudden peeling off of the entire sand coating beyond a certain concrete strength. The rate of increase of bond stress with concrete strength

was shown to be less than steel with the increase being proportional to $(f'c)^{0.3}$. An increase in the bond strength due to concrete strength was also observed by Won et al. (2008) using ribbed GFRP bars in 55-103 MPa concrete pullout tests while Pecce et al (2001), using a novel beam test with 37-55 MPa concrete, also noted the influence of concrete strength on specimens failing by pullout. The results obtained for bond strength of GFRP in high strength concrete are not in agreement and requires further investigation. Design codes are also divided in this regard with CSA-S806-02 (2002) and CSA-S6-06 (2006) design codes for FRP limiting the contribution of concrete strength to development length while ACI 440.1R-06 (2006) does not. Furthermore, the bond strength of GFRP bars in UHPC has yet to be investigated.

2.4.4.3 Embedment Length

Pullout tests of varying embedment length from 5-9 times the bar diameter, d_b, by Okelo and Yuan (2005) showed a decrease in the average bond stress as embedment length increased for both FRP and steel. This was attributed to the non-uniform bond stress distribution and concentration of bond force at the loaded end of the splice. However, an increase in the bar force was observed with longer embedments indicating that the bond stresses were still being developed at the free end. Similar results were also found by Larralde and Silva-Rodriguez (1993) using spiral wound GFRP bars when embedment lengths increased from 3 to 5 inches. Modified beam tests conducted by Pecce et al. (2001) using ribbed GFRP bars showed decreasing average bond stress only after 10 d_b of embedment length suggesting that there may be a significant concentration of stress within the initial portion of embedment. These findings were also verified by Chaallal and Benmokrane (1996) by use of strain gauges attached at different locations along the embedment length of several GFRP bars. The variation of bond stress distribution was found to indeed be non-uniform while the tensile stress was nonlinear. A concentration of bond stress was found to exist at the loaded end and gradually migrate towards the free end as loads increased and slip initiated at the loaded end. The same observations were found for spiral wound GFRP RILEM beam tests conducted by Tighiouart et al. (1998) and spliced beam tests by Tighiouart et al. (1999). Very few results have been reported using sand

coated GFRP rebar especially in high strength and UHPC. Results using HM GFRP are also not present in the current research and needs further attention.

2.4.4.4 Bar Surface Condition

Aiello et al. (2007) conducted modified pullout tests using sand coated, ribbed, and spiral wound GFRP and CFRP bars. Results showed that spirally wound CFRP bars had almost four times the maximum bond strength of similar sand coated bars while spiral wound and ribbed GFRP bars showed about three times that of similar sand coated bars. This was attributed to the contribution of mechanical interlock with larger deformations even after peak stress and damage to the ribs of deformed bars. Ribbed GFRP bars showed also showed improved bond/slip behaviour versus spiral wound bars. Baena et al. (2009) found that the opposite was true for CFRP rebar with results for sand coated bars providing the higher bond strength. Results for GFRP bars also showed that larger spiral wound deformations performed better than ribbed and sand coated bars due to a higher protruding rib area to rib spacing ratio. Pullout tests by Lee et al. (2008) showed that the bond strength of helically wrapped GFRP bars is similar to sand coated bars. However, the slip at maximum bond stress is much higher for helically wrapped bars while the post peak behaviour of sand coated bars is more brittle. Esfandeh et al. (2009) found that the bond strength of sand coated helically wound bars was overall better than just sand coating or helical windings alone. Although sand coated bars showed similar bond strengths depending on the embedment length. Bars with only helical windings suffered from delamination of the ribs causing failure to occur at smaller loads versus other surface conditions. Hao et al. (2009) showed that the bond strength varies substantially with the dimensions of surface deformations or ribs and that optimal rib geometries were necessary to improve bond strength. The large variation in the relative bond strengths of different bar surface conditions can be attributed to the lack of accountability in the geometry of bar deformations. Furthermore the bond mechanisms of FRP bars are constantly improving and so results for the same type of bar can vary dramatically over a very short time span. These factors should be taken into account during investigations and analysis (Tepfers and De Lorenzis 2003).

2.4.4.5 Bar Diameter

A decrease in bond strength with larger bar diameters was observed by Baena et al. (2009) but only for higher concrete strengths of about 52 MPa. No significant change was found for a weaker concrete of about 29 MPa. Several factors were said to influence this behaviour. First was the general need to increase development lengths since larger bars can provide more tensile force. The non-uniform distribution of bond stress then causes a reduction in the average bond stress giving the impression of reduced bond strength for larger diameters. The second factor was due to the Poisson effect, which causes a greater net diameter reduction versus a smaller bar thus reducing the mechanical interlock of surface deformations by that much more. A third reason was due to the energy absorption and release of a larger bar diameter that causes failure modes to be more sudden. Results by Tastani and Pantazopoulou (2006) agree with the trend that larger bar diameters have the effect of reducing the average bond strength for sand coated GFRP bars. However, no significant change was noted for sand coated helically indented GFRP bars. Tighiouart et al. (1998) attributed the reduction in bond strength to the increased surface area of larger bars that causes additional bleed water to accumulate under the bar. Bleed water inside the concrete eventually leads to voids that reduce the effective contact area. Results from Okelo (2007) show similar behaviours with respect to bar diameter for GFRP and CFRP bars.

2.4.4.6 Concrete Cover and Confining Reinforcement

Okelo and Yuan (2005) demonstrated using pullout tests with a variety of rebar types that the cover thickness governs the failure mode. Reduced clear cover induces the occurrence of splitting failure. Code equations for development length place a large emphasis on the effective cover due to the prominent splitting failure mode found in most design applications. Ehsani et al. (1997) also found that reducing the cover increases the slip. The appearance of cover cracks will also reduce the initial stiffness of the bond. For ribbed GFRP bars a cover of one bar diameter was consistent with splitting failure while two d_b initiated pullout failures depending on the embedment length. Changes to the concrete cover affects the thickness of the concrete ring that resists circumferential radial forces caused by bearing. Increasing the cover enhances the tensile splitting capacity of the concrete surrounding the rebar (MacGregor and Wight 2005; Tepfers 1982; Tepfers and De Lorenzis

2003). Confining reinforcement benefits the bond strength by providing additional restraint against splitting failure (Brzev and Pao 2006). Some design codes provide provisions to include the presence of confinement in the development length equations for FRP bars. The contribution to bond strength is measured by the effective confining reinforcement crossing the plane of splitting within the development length (CSA 2006).

2.4.4.7 Casting Height

The height at which a reinforcing bar is cast in a specimen affects the amount of bleed water and voids that accumulate under it. More fresh concrete being cast below a reinforcing bar causes a larger amount of accumulation that will eventually lead to voids. Voids reduce the effective bond area of a reinforcing bar thus causing a reduction in bond strength (ACI Committee 440 2006). Ehsani et al. (1997) conducted pullout tests on spiral wound GFRP bars at casting heights of 8, 24, and 40 inches in 28 MPa concrete. The results showed the bond strength of the bottom bars was between 1.04 and 1.23 times the bars higher up. No significant change was noted for casting heights of 24 and 40 inches. Esfahani et al. (2005) conducted pullout tests with sand coated GFRP in normal and self-consolidating concrete. Self-consolidating concrete showed a larger discrepancy than normal concrete with bottom to top bar ratios of 1.51 and 1.29, respectively. The failure mode of all specimens in this study was by splitting. The combined effect of small cover and void accumulation under the bar caused additional change in the bond strength for top bars. Similar tests conducted by Tighiouart et al. (1998) showed an average factor 1.29 for the top bar effect. ACI 440.1R-06 (2006) recommends a factor of 1.5 for horizontal bars cast with more than 300 mm of concrete below it. A factor of 1.3 is recommended by CSA design codes for FRP (CSA 2002; 2006).

2.4.4.8 Specimen Type and Loading Configuration

As shown previously there are a number of test specimens and loading configurations that can be used to assess the bond performance of reinforcement. Most researchers agree that the presence of compression in a pullout test is beneficial to the bond since it increases the friction due to compression stress fields within the concrete, prevents transverse cracking, and adds additional restraint at the loaded end due to the force of the bearing plate. As a

result modified pullout tests and beam tests are expected to develop less bond strength (Ehsani et al. 1997; JSCE 1997; MacGregor and Wight 2005, Tastani and Pantazopoulou 2006; Tighiouart et al. 1998). However, Aiello et al. (2007) has found that this trend can vary depending on the bar type and surface condition. Both normal pullout and modified pullout tests were conducted to using ribbed, spiral wound, and sand coated reinforcing FRP bars. A comparison between the two tests methods showed that normal pullout tests favored ribbed or deformed bars while spirally wound bars showed enhanced bond strength with modified pullout tests. Sand coated FRP bars showed no variation between the two specimen types. The decrease in bond strength due to beam tests seem to only affect tests with ribbed or helically wrapped type reinforcements where bond stress is transferred through bearing forces concentrated at the rib locations. If tensile cracks were to occur at a rib location some bond loss will occur because that rib will have no concrete to act upon and for that portion of the bar until the next rib there will be no bond. Whereas for sand coated rebar a tensile crack will only affect the bond directly at the crack location while the rest of the sand coating around it will still retain its bond. This reduces the effect of bond degradation due to tensile cracking. Further research is necessary to establish the bond behaviour of sand coated GFRP reinforcing bars in beams versus pullout tests.

2.4.4.9 Fibre Reinforced Concrete

Won et al. (2008) conducted pullout bond tests using ribbed CFRP and GFRP rebar. The concrete contained various proportions of hooked steel (20 or 40 kg/m^3) or synthetic fibres (4.55 or 9.1 kg/m^3). The target concrete strengths were 50, 70 and 90 MPa. The results showed an increase in bond strength of 5-70% with an increase in fibre content. The normalized bond strength showed that regardless of concrete strength the concrete with highest steel fibre content provided the best bond performance. Very few tests have been conducted in this area. The use of fibre reinforced concrete can provide significant improvements on the bond performance of reinforcing bars. Fibres can enhance the tensile capacity of concrete thus increasing the resistance to splitting failure and localized cracks along the bar. They effectively act as confining reinforcement. Further investigation into this area is necessary to understand the improved bond behaviour of GFRP with other surface conditions in the presence of fibre reinforced concrete.

2.4.4.10 Environmental Effects

Davalos et al. (2008) conducted pullout tests for GFRP and CFRP bars after exposure to various extreme environments. The concrete strength for the pullout blocks were on average 60 MPa prior to conditioning. The surface condition for GFRP bars were either sand coated or helically wrapped with sand coating while CFRP bars were sand blasted. One of three types of treatments were applied to the specimens: 90 days submerged in room temperature tap water, 90 days in 60˚C tap water, or 30 days of cycling in air between +60˚C and -20˚C with 6 hours at each temperature limit and 6 hours for temperature ramping in between (one cycle per day). Failure was by pullout and the GFRP suffered damage mainly on the resin rich layer surrounding the fibre core for both treated and untreated specimens. Sand coated GFRP showed a reduction of about 20%, 5%, and 18% after each treatment type respectively. Concrete strengths showed a significant reduction of 17-24% only after treatment in 60˚C tap water while no substantial degradation was found after the other treatments. However, no clear correlation was found between bond strength and concrete strength within the range of specimens tested. The lack of bond strength degradation for treatment in 60˚C water was attributed to increased moisture absorption and swelling of the bar that enhanced the mechanical interlock. The greater reduction in concrete strength had little effect since failure was mainly in the resin layer of the GFRP bars. The extensive bond loss for thermal cycling was attributed to micro-cracking in the concrete as well as damage to the GFRP bar itself. Similar thermal cycling regimes were employed by Laoubi et al. (2006) to evaluate the sustained load performance of sand coated GFRP reinforced concrete beams. The temperature limits were set at +20˚C and -20˚C for 6 hours each with 50% humidity. These limits have also been used by Chen et al. (2007) in conjunction with full immersion and chemical testing with FRP bars.

2.5 GFRP Tensile Lap Splices

2.5.1 Introduction to Tensile Lap Splices

Tensile lap splices are necessary due to construction stoppages and limitations on rebar lengths. They also provide means to facilitate many forms of precast construction. Splices are used in joints to transfer forces from one reinforcing bar to the next enabling structural continuity within a member. The most widely used form of splicing is the lap

splice where forces are transferred across adjacent discontinuous bars by means of the concrete in between them. Lap splices require that the bars be sufficiently close and have enough overlap that the necessary amount of force can be transferred without bond failure. The stress fields generated within a splice are a combination of bearing forces acting in opposite directions. Bearing forces between two adjacent bars form compression fields that help to transfer load as shown in Figure 2.11a. Increasing the spacing between two spliced bars reduces the effectiveness of these compression fields. The crack pattern shown in Figure 2.13b generally follows the stress fields in that compressive struts are formed between the bars at the points between the deformations. Splices also have the tendency to form transverse cracks at the ends due to the discontinuity of reinforcement. Due to the increased bearing stresses acting on the concrete, splices also have a tendency to exhibit the splitting mode of failure and require the support of confining reinforcement (Brzev and Pao 2006; MacGregor and Wight 2005; Tepfers 1980; 1982).

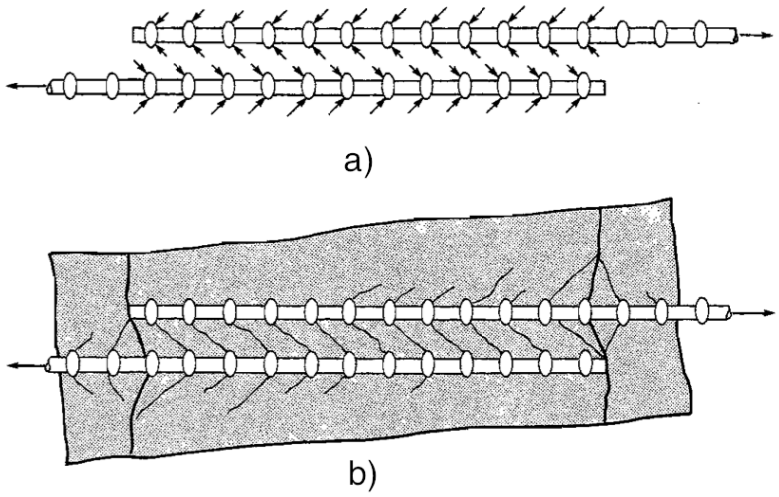

Figure 2.11: (a) Tensile lap splice stress fields in concrete around a reinforcing bar; (b) crack pattern around a tensile lap splice (MacGregor and Wight 2005)

2.5.2 Investigation of the Behaviour of GFRP Tensile Lap Splices

Choi et al. (2007) conducted unconfined splice tests using a surface coated GFRP lap spliced at the center span of 4 m long normal strength concrete beams. The concrete strength was 23.0 MPa and the GFRP bars had a modulus of elasticity and tensile strength of 37.2 GPa and 690 MPa respectively. The bars had a diameter of 12 mm and were tested in splice

lengths ranging from 15 - 60 times d_b. Effective cover thickness ranged from 19.1 to 36.4 mm with the number of spliced bars ranging from 3 to 5. The cross section was constant for all specimens, 300 x 400 mm (width x height), but the reinforcement ratio ranged from 0.31% to 0.51% while the calculated balanced ratio was 0.34%. Strain gauges were applied at the ends of the splice for verification. An additional beam was cast using three full-length bars for comparison. Beams were tested under four point loading with a total span of 3600 mm and a shear span of 1000 mm. Shear reinforcement was provided just in the shear region so as to give the most conservative bond behaviour in regards to splitting failure, which was the only mode of failure exhibited by the spliced beams. The beam with continuous bars failed under tensile rupture of the GFRP bar. Beams with splice lengths of 30 and 60 bar diameters had a load capacity of only 48.5% and 66.4% of a similar beam with continuous reinforcement. Cracking typically began at the ends of the splice then continued increasing in length and number while also accompanied with stiffness degradation. Longitudinal cracks along the bar height signified the onset of splitting failure. Typical load deflection behaviour showed a stiff climb up to the cracking load followed by a loss of stiffness but linear increase in load until the point of failure.

Tighiouart et al. (1999) also conducted spliced beam tests using ribbed GFRP rebar of 12.7 mm and 15.9 mm diameters. The various splice lengths, between 460 and 1545 mm, were chosen as values between 0.6 and 1.6 times the development length. An effective span of 3000 mm and a shear span of 1000 mm were used under a four point loading configuration. The concrete strength was 31 MPa and the clear cover was 30 mm. Mild steel stirrups were used throughout the beam including the splice as well as two steel bars at the top for compression. Beam dimensions were either 200 x 300 mm or 230 x 450 mm (width x height) depending on the bar size and splice length. Failure of specimens was by splitting off of the concrete surrounding the splice or by compression failure in the case of one beam. Cracking generally began at the ends of the splice due to the discontinuity of reinforcement and propagated outwards even beyond the pure bending region. For the longest embedment length cracks generally stayed within the pure bending region and only occurred at the ends of the splice after much higher loads were reached. It was noted that for shorter embedment lengths splitting cracks occurred early on while for longer embedment lengths splitting did not occur until after the midpoint of loading. This was attributed to the larger bond stresses

associated with a shorter embedment length. The strains measured at center splice of the tensile rebar were shown to have a good bond and transfer of forces due to the similarities in the load strain distributions. According to the results a minimum of 1.6 times the development length was predicted to develop the full strength of the GFRP bar while a factor of 1.3 was deemed sufficient since material restrictions were generally imposed on FRP reinforcement ultimate capacities for design.

Harajli and Abouniaj (2010) conducted splice tests using beams of 1800 mm span under four-point loading. Each beam had two spliced bars and steel stirrups as shear reinforcement in the shear region. Two types of surface conditions were used namely helically wrapped and ribbed. Additional steel specimens were cast for comparison. The three splice lengths ranged from 15 to 30 bar diameters. Concrete cover ranged from 1.25 to 2.0 times the bar diameter. Some specimens also had additional transverse reinforcement in the pure bending region. The applied loads were spaced in such a way that the entire splice length would be in the pure bending region. The concrete strength was between 48 and 52 MPa. Strain gauges were also applied just outside the spliced region to verify the maximum bar force. The mode of failure for ribbed rebar including steel was by splitting with a complete loss of load capacity immediately after the maximum load was reached. On the other hand threaded bars experienced a more ductile failure with a gradual pullout of the rebar. This also had the effect of increasing crack widths to more than 20 mm at the end of the splice. Furthermore, due to the friction between the bars and concrete after initial bond loss, a substantial load capacity still remained even through large deflections until failure. Threaded GFRP bars developed a capacity between 27 and 36% of the ultimate tensile strength while the ribbed GFRP bars developed 42 - 67%. A reduction in the bond strength was noticed, even more so for thread wrapped bars versus ribbed bars, with an increase in the splice length however an increase in the bar force was still achieved. An increase in the cover showed little improvement on the bond strength for ribbed GFRP bars with no increase shown for thread wrapped bars. However, a considerable increase in the bond strength was observed with the presence of confining reinforcement for both types of GFRP.

Aly (2006) conducted spliced beam tests on sand coated CFRP and GFRP bars. The concrete strength was 40 MPa. The bar diameters were 15.9 and 19.1 mm for GFRP and 9.5 and 12.7 mm for CFRP. The dimensions of the beam were 250 mm width and 400 mm depth

while the shear span was 1000 mm with a 1600 mm constant moment region. Shear reinforcement was provided throughout the shear span at a spacing of 100 mm and an increased spacing of 150 mm within the constant moment region. Splice lengths for the study ranged from 500 mm to 1400 mm. An additional full bar beam was cast for comparison using GFRP rebar. The clear cover to the bar was 40 mm. Strain gauges were also mounted at various locations along the splice for verification. The strain behaviour showed that little force is carried by the bar prior to cracking of concrete followed by a steady increase in load afterwards until failure. The strain distribution of the bar showed that bond stress is not constant but rather more concentrated at the loaded end. Just prior to failure, however, the bar strain distribution becomes more linear. This was due to the splitting failure mode which predominately occurred for the larger bar diameters. Larger diameter bars typically showed weaker bond stress. Theoretical predictions of the neutral axis depth using the ultimate strength method were very similar to that obtained from strain compatibility from the concrete and bar strain measurements. Similarly, the strain measurements matched with those obtained from theoretical calculations. Cracks typically occurred at the ends of the splice and then propagated towards the center. Results also showed that a linear variation exists between the maximum developed bar force at the end of the splice versus the length of the splice. It was concluded that only a couple of spliced beam tests were necessary to form a relationship for predicting the critical splice length. Critical splice length predictions ranged from 40 and 50 bar diameters for the 15.9 and 19.1 mm GFRP bars respectively while critical bond stresses within the splice were predicted to be 4.1 and 3.0 MPa respectively. Due to the consistent splitting failure mode of the splice the concrete tensile strength was deemed essential in enhancing the bond strength of splices.

Aly (2007) conducted further theoretical analysis using the modulus of displacement theory to predict the bond stress distribution and bar force distribution for some of the tests in the previous study. The previous research showed that the contribution of the confining reinforcement allowed a constant bond stress along the length of the bar while for unconfined splices the bond stress was non-uniform. The modulus of displacement theory was adopted from Tepfers (1980) for analysis. Additional pullout tests conducted using the free end slip showed that the modulus of displacement for 19.1 mm GFRP rebar was in the range of 300 N/mm^3 and 30 N/mm^3 for tangent and secant modulus, respectively. Theoretical predictions

were compared with values from the strain gauges using three stages. The first stage prior to cracking includes the contribution of concrete in the tensile region. The second stage ignores this due to the presence of cracking. While the third stage, up to failure, uses a reduced modulus of displacement due to the plastification of concrete ring surrounding the rebar. The reduced modulus of displacement ranged from 5 to 30 N/mm^3. The results from strain gauges showed a good agreement with the theory.

Choi et al. (2008) tested one-way slabs using four-point loading and spirally wound GFRP rebar. The two concrete strengths used were 26.5 and 33.2 MPa with 30 or 50 mm cover. Steel shear reinforcement was used only in the shear region. The bars surface condition was spirally wound and the nominal diameter was 13 mm. Strain gauges were applied at the ends of the splice. The dimensions of the slab were 750 mm x 250 mm (width x height) with 5 or 9 spliced bars in the tension region. The total span was 3600 mm with a shear span of 1200 mm. The main failure mode for all spliced slabs was by splitting of the bottom and side cover. The bond strength ranged from 2.1 to 4.8 MPa with the smaller bond strength occurring with smaller bar spacing. Similarly, reductions in cover and increases in embedment length reduced the average bond strength.

Although, previous studies have suggested that bearing forces and subsequently radial splitting forces were much lower with FRP bars (Larralde and Silva-Rodriguez 1993; Tighiouart et al. 1998), splitting failure is still the dominant failure mode of spliced FRP bars. Further research in the area of tensile lap splicing of FRPs in UHPC would be beneficial since the use of a higher tensile strength concrete will reduce the occurrence of splitting failure and improve the bond conditions of splices.

2.6 Flexural Behaviour of GFRP Reinforced Beams

Theriault and Benmokrane (1998) conducted beam tests using deformed GFRP bars of 12.3 mm diameter. Each beam was 130 x 180 mm (width x height) with 20 mm cover and was designed with various reinforcement ratios giving compression failure. The beams used 6 mm steel compression and shear reinforcements. The span was 1500 mm and the load was applied in 20 kN increments using a four point loading configuration. Concrete strength ranged from 53.1 - 97.4 MPa. Results showed a decrease in the crack widths and height with an increase in reinforcement ratio. The change in concrete strength showed negligible effects

on crack spacing, and stiffness. Crack spacing typically reached a minimum at about 80 mm. An increase in the moment capacity was noted for both higher concrete strength and reinforcement ratio however the increase was restricted due to the compressive failure mode for most beams. The load-deflection behaviour was initially very stiff prior to cracking after which a reduction in stiffness was observed with a linear load-deflection response up to failure. Specimens that were subjected to several cycles of repeated loading with increasing applied load also showed increasing residual deflection. The strain behaviour of concrete and reinforcing bars was also linear after cracking up to failure.

Alsayed (1998) also conducted beam tests using GFRP and found similar load deflection behaviour. A sudden increase in deflection was also noted after cracking which was attributed to the low modulus of elasticity of GFRP bars. Small jumps in deflection were also observed during the linear portion after cracking due to the breaking of fibres from the shear lag effect. A value of 35% of the ultimate capacity of a similar steel reinforced beam was used as an indication of the service load limit. A larger deflection of about double was observed for GFRP reinforced beams versus a similar steel reinforced beam at the service load. It was also found that the ultimate strength design method could accurately predict the load capacity of concrete beams over reinforced with GFRP. The deflection at failure of GFRP beams was in some cases more than 40 mm even for concrete crushing thus demonstrating the ductility of an over-reinforced member using GFRP.

Benmokrane et al. (1995) found similar differences in load-deflection behaviour versus steel. Steel reinforced beams exhibited smaller deflections and had a much higher stiffness after cracking than GFRP beams. Similarly the deflection at maximum load was much higher than equivalent steel beams providing some ductility in spite of the sudden failure mode exhibited during tensile rupture of GFRP. In some cases up to three times the deflection was observed during service load levels versus equivalent steel beams with similar load capacity. Crack widths and heights were also more severe with GFRP beams. Improvements on the serviceability behaviour of GFRP beams versus steel were observed for lower span to depth ratios.

Issa et al. (2011) studied the effect of various fibre types and concrete strengths on the serviceability behaviour of GFRP reinforced concrete beams. Three types of fibres were used: polypropylene, glass, and steel. Two target concrete strengths were also included at 25

and 65 MPa. The cross section of the beams was 150 x 150 mm with a 1500 mm span. A four point loading configuration was used to apply load until failure. Fibres were added at 0.5% volume fraction for all mixes containing fibres. Steel stirrups were used in the shear region while 12 mm sand coated GFRP bars were used as the main tension reinforcement. Significant improvements on the ultimate load were observed for glass and steel fibres while polypropylene fibres improved a small amount. The addition of fibres also increased the concrete compressive strain and deflection at maximum load. Steel showed the most improvement in terms of ductility. The change in stiffness due to the addition of fibres was inconclusive due to the significant differences in concrete strength for each fibre type. Evaluations were however conducted based on the deformability factor for each beam as a measure of the ductility. The presence of fibres significantly improved the deformability of GFRP reinforced beams and is recommended in the case of non-ductile behaviour.

2.7 Fatigue Behaviour of GFRP Reinforced Slabs

El-Ragaby et al. (2006; 2007) conducted fatigue tests on 5 full-width GFRP bridge deck slabs under simulated tire loads. Each specimen was 3000 x 2500 x 200 mm (length x width x height) and had main reinforcement of LM No. 19 sand coated GFRP bars at 150 or 180 mm spacing. Reinforcement was also provided in the transverse and top locations. The target concrete strength was 37 MPa while a cover of 38 mm was used for all specimens. An additional steel reinforced slab was constructed for comparison. All slabs were subjected to one year in an outdoor environment prior to testing. The ends of the slabs were restrained to the supporting girders spaced at 2000 mm on center using steel bolts and structural channels. Load was applied using a stroke actuator through a steel plate and neoprene sheet with dimensions of a Canadian Highway Bridge Design Code (CHBDC) truck tire (250 x 600 mm) (CSA 2006). For comparison, a finite element model was derived from previous static testing of similar slabs to evaluate the static load capacity of the current slabs. The maximum load capacity ranged from 731 to 750 kN. Two fatigue regimens were implemented one using a constant amplitude maximum load of 122.5 kN at 4 Hz and the other using varying maximum loads of 122.5 – 490 kN for 100,000 cycles or until failure each at 2 Hz. The peak load of 122.5 kN was obtained using the maximum truck tire load of 87.5 kN factored for dynamic load allowance. The failure mode of slabs subjected to varying

peak loads was by punching shear during the final maximum loading scheme. The steel reinforced deck slab failed during fatigue testing prior to reaching the last peak load stage. The better performance of GFRP was attributed to the similarities between the reinforcing bar and concrete modulus. The single slab tested using constant amplitude withstood 4,000,000 cycles without failure. This slab also showed acceptable cracking and deflection performance even after fatigue loading with a residual deflection of about 1.4 mm and a service load deflection of 1.8 mm. Furthermore, the residual crack width increase was negligible while service load crack width was about 0.4 mm.

2.8 High Performance Bridge Joints

The concept of HPBJ was first developed at Chalmers University of Technology in Sweden with the use of an UHPC called Compact Reinforced Composite (CRC) (Harryson 2003). This concrete had typical compressive strengths of 150 MPa with a 6% volume fraction of steel fibres. The purpose of this joint is to allow faster construction by reducing the amount of onsite casting and facilitating the use of prefabrication for slab elements. This application of UHPC and steel reinforced precast sections allows joint widths of as little as 100 mm with the use of a shear key. Tests have shown that the joints behave continuously with the adjacent members. Similarly, the shear capacity of the joint is higher than the surrounding material. Some key points were noted from bending tests as critical in preventing pullout failure in the reinforcement: sufficient UHPC cover, presence of transverse reinforcement consisting of straight bars placed on top of the splice within the joint for load distribution and longitudinal crack bridging, and sufficient lap length. The steel reinforcement used in the precast segments had a yield stress of 564 MPa and ultimate stress of about 660 MPa. Flexural testing under a four point loading configuration led to crushing failures beyond the yield point of steel except for the specimens with 80 mm lap lengths or no transverse reinforcement. Fatigue testing showed a fatigue bending failure in slabs with a smaller reinforcement ratio after 400,000 - 500,000 cycles. Higher reinforcement ratios showed that it was possible to withstand more than 800,000 cycles. Cracks that propagated throughout the specimen during fatigue did not reach the joint fill CRC material. Figure 2.12 shows a typical 100 mm joint used in this application (Harryson 2003).

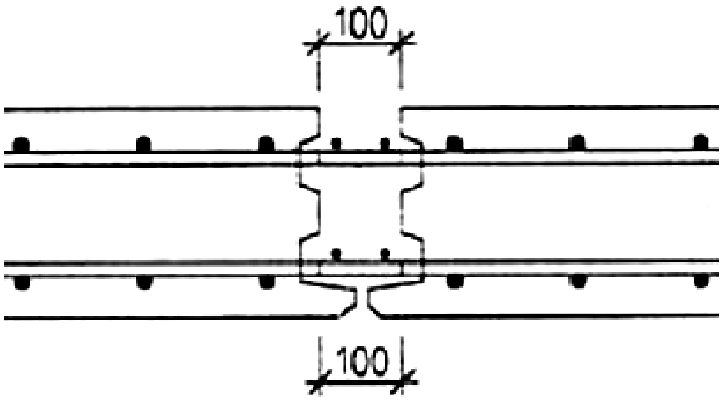

Figure 2.12: CRC joint fill HPBJ design (Harryson 2003)

HPBJs using steel reinforcement have also been applied in the field in Oneonta, NY. The precast sections were reinforced with galvanized steel while the joint reinforcement consisted of overlapping hairpin bars with two transverse reinforcing bars passing through them. A lap length of 100 mm was used with a total joint width of 152 mm. UHPC was cast in the joint and left to cure for 3 days up to 100 MPa before opening to traffic. No consolidation was necessary since the concrete was self-settling. Figure 2.13 shows the configuration and dimensions of the joint. A second application using lapped straight galvanized steel rebar was also implemented in a bridge deck in the Village of Lyons, NY (Perry and Royce 2010).

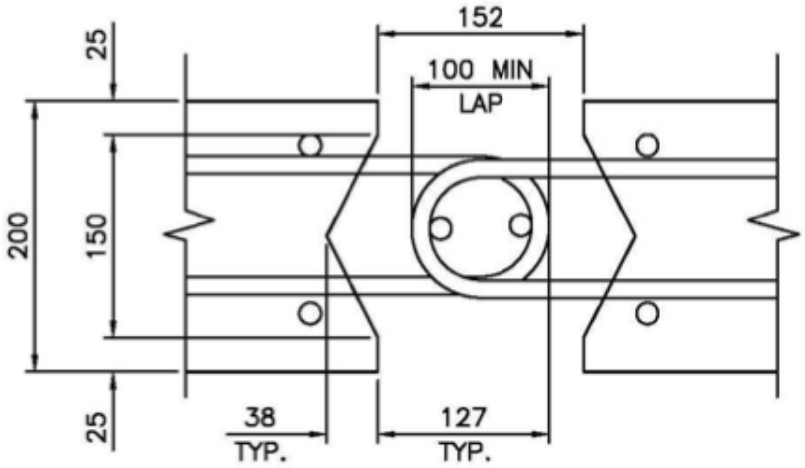

Figure 2.13: Details of the Oneonta, NY HPBJ using hairpin steel bars (Perry and Royce 2010)

In Rainy Lake, Ontario this application has also been extended to the use of sand coated LM GFRP however only in the top layer of reinforcement (Perry et al. 2007). The joint widths were 210 mm with a lap length of 190 mm for GFRP. Two joints were necessary for this project the first was a transverse joint using 16 mm GFRP and the second was a longitudinal joint in negative bending cast over the steel girders using 19 mm GFRP. The longitudinal joint also acted as a shear key with shear studs also being cast within it. One transverse bar was also placed across the overlapping bars at mid-splice. Steel reinforcement was provided in the bottom layer of precast sections and in the joint. These consisted of 15M bars spliced at 90 mm in the transverse joint and 190 mm in the longitudinal joint. Preliminary testing showed that a 190 mm splice length was sufficient in resisting the design tensile forces. Foam strips were placed between the concrete slab and steel girder to facilitate the casting. UHPC cast within the joint was allowed to cure for 4 days to the 100 MPa mark before opening to traffic. Figure 2.14 shows the details of the longitudinal joint for this application (Perry et al. 2007).

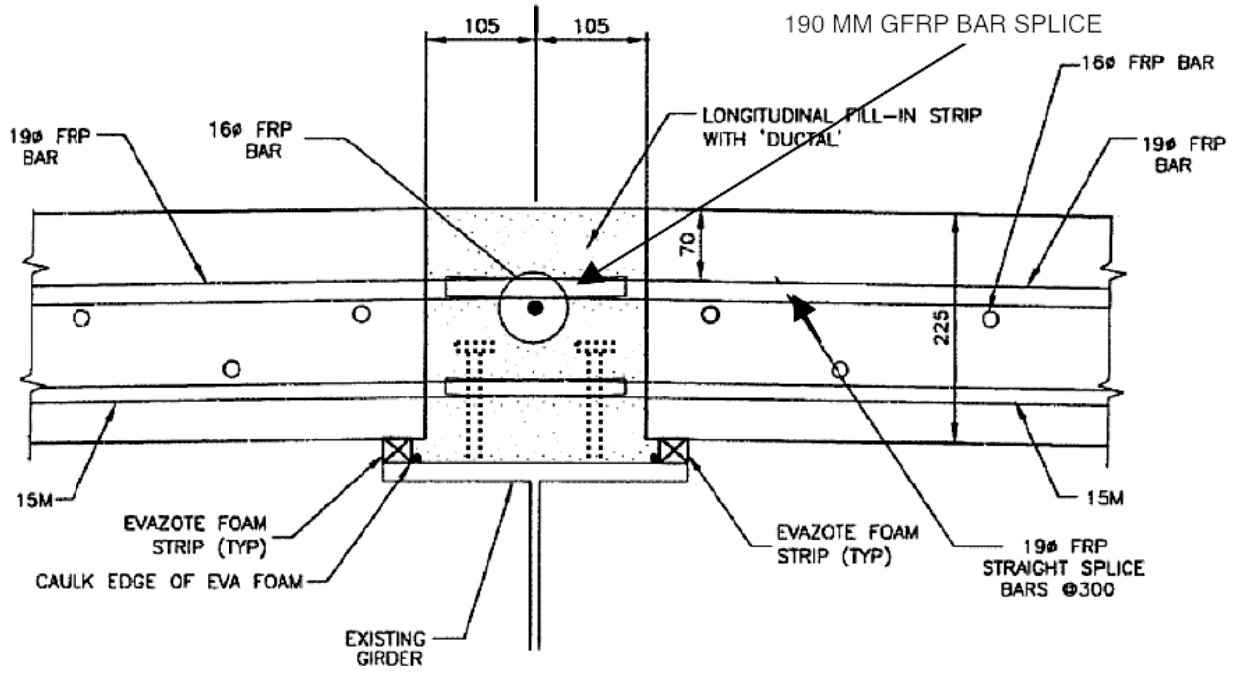

Figure 2.14: Details of the longitudinal bridge deck joint at Rainy Lake, Ontario (Perry et al. 2007)

2.9 Design of FRP Reinforced Flexural Members

The same flexural design philosophy used for steel reinforced concrete has also been adopted for FRP. The concept of linear strain compatibility applies to the cross section and the assumption is also made that zero slip has occurred so the strain in concrete has the same strain as the reinforcing bar a given location. Analysis is conducted on a cracked section neglecting the tensile contribution of concrete. The FRP in this case gives a linear response however no yielding occurs and the bar exhibits sudden failure. As a result design manuals recommend an over-reinforced section since the concrete crushing failure mode is typically more ductile. Tension failure modes are permitted however is sufficient envelope is sufficient factor of safety is provided.

2.9.1 Balanced Condition

The balanced condition is where simultaneous crushing of concrete and tensile failure of the reinforcing bar at the extreme fibre location occurs. Through equilibrium of forces and a linear strain distribution the following relationship is obtained for the balance reinforcement ratio (ISIS 2007):

$$\rho_{frpb} = \alpha_1 \beta_1 \frac{\phi_c}{\phi_{frp}} \frac{f'c}{f_{frpu}} \left(\frac{\varepsilon_{cu}}{\varepsilon_{cu} + \varepsilon_{frpu}} \right) \quad \text{.....(2.4)}$$

where ρ_{frpb} is the balanced reinforcement ratio, α_1 is the ratio between the average concrete strength of a rectangular stress block versus the concrete compressive strength, β_1 is the ratio of the depth of the rectangular stress block to the depth of the neural axis, ϕ_c and ϕ_{frp} are the material resistance factors for concrete and FRP, $f'c$ is the compressive strength of concrete, f_{frpu} is the ultimate tensile strength of the reinforcing bar, ε_{cu} is the ultimate compressive strain of concrete (typically -0.0035) and ε_{frpu} is the ultimate tensile strain of the FRP bar. The balance reinforcement ratio gives the dividing line between a compression failure and a tension failure. A larger reinforcement ratio will lead to compression failure and vice versa. The values for α_1 and β_1 can be found using the following equations for normal to high strength concretes (CAC 2006).

$$\alpha_1 = 0.85 - 0.0015 f'c \geq 0.67 \quad (2.5)$$

$$\beta_1 = 0.97 - 0.0025 f'c \geq 0.67 \quad (2.6)$$

The stress strain curves for concrete under compression can also be used to find additional rectangular stress block factors for UHPC. The compression and tension forces in concrete and reinforcement are found using the following equations (ISIS 2007):

$$C = \alpha_1 \phi_c f'c \beta_1 c b \quad (2.7)$$

$$T = A_{frp} \phi_{frp} f_{frp} \quad (2.8)$$

where C and T are the compression and tension forces respectively, A_{frp} is the area of FRP reinforcement, c is the depth of the neutral axis, f_{frp} is the stress in the FRP reinforcement, and b is the width of the section. The moment resistance can be found as the product of either the compression or tension force and the distance between their centroids such as in the following equations.

$$M_r = C\left(d - \frac{\beta_1 c}{2}\right) \quad (2.9a)$$

$$M_r = T\left(d - \frac{\beta_1 c}{2}\right) \quad (2.9b)$$

where M_r is the resisting moment of the section and d is the effective depth (ISIS 2007).

2.9.2 Compression Failure

When a beam has more reinforcement than the balance ratio concrete compression failure will occur and the concrete reaches -0.0035 strain (ε_{cu}) at the extreme compressive fibre before rupture of the FRP occurs. To find the moment resistance of such a beam trial and error can be used to estimate the depth of neutral axis that gives force equilibrium across the section while the extreme compression fibre is at the limit. The following equations can also be used to compute the stress in the FRP at failure.

$$f_{frp} = 0.5E_{frp}\varepsilon_{cu}\left[\left(1+\frac{4\alpha_1\beta_1\phi_c f'c}{\rho_{frp}\phi_{frp}E_{frp}\varepsilon_{cu}}\right)^{1/2}-1\right] \quad \text{.....(2.10)}$$

$$\rho_{frp} = \frac{A_{frp}}{bd} \quad \text{.....(2.11)}$$

where E_{frp} is the modulus of elasticity of the FRP, ρ_{frp} is the reinforcement ratio, while all other variables remain the same. The stress in the FRP at failure can be used to compute the tension force and subsequently the moment resistance using equation 2.9b (ISIS 2007).

2.9.3 Tension Failure

Tension failure of an FRP reinforced concrete beam is different from a steel reinforced beam due to the non-yielding behaviour of the FRP. Under these circumstances the compressive strain at the extreme concrete fibre may not reach -0.0035 and thus the values for α_1 and β_1 from equations 2.5 and 2.6 may give inaccurate results. In this case values for rectangular stress block factors may be determined using the stress strain curves of concrete in compression for maximum strains smaller than -0.0035. From these values the same trial and error approach should be implemented as before where the neutral axis depth is varied to balance the forces across the section given a known tensile strain at ultimate for the reinforcement. Equation 2.9 can then be used to determine the moment resistance (ISIS 2007).

2.10 Review Summary

GFRP reinforcement is a constantly changing industry with a growing number of applications and advancements. This review of literature has identified several areas that require further investigation. The bond performance of sand coated GFRP rebar with improved tensile properties, such as a higher modulus and tensile strength, have yet to be investigated. The application of UHPC to bridge deck joints has allowed reduced joint widths and requires further research when used with GFRP rebars. Tensile lap splice joint construction using prefabricated bridge decks with GFRP is an important topic due to the combined benefits of faster and more efficient construction with high corrosion resistance.

However, there is currently a lack of research pertaining to the bond performance of sand coated HM GFRP under spliced conditions especially with UHPC. In general, the bond and flexural performance of UHPC members reinforced with FRPs is a growing topic that requires further attention. Additional research will provide improvements to the use of code equations for development/splice length requirements of FRP rebars in UHPC members. Further research is also necessary to understand the load/deflection, and fatigue behavior of such members. The superior durability characteristics of UHPC can also provide improvements to the bond performance of FRP reinforcements subjected environmental degradation but has not been examined in the current literature. The current research is a timely and important initiative to investigate the bond performance of sand coated HM GFRP reinforcing bars in tension lap splices with UHPC. Additional insight provided on the flexural and fatigue behaviour of GFRP reinforced UHPC members will contribute to the improvement of existing technology. This study will also include the effect of environmental loading on the bond performance of sand coated GFRP bars in UHPC.

Chapter 3 Experimental Program

3.1 Introduction

A total of ten tensile lap spliced GFRP reinforced concrete slab/beams were tested in addition to nine pullout specimens for bond tests that were subjected to environmental loading under freeze/thaw treatments. The main parameters for the slab/beam tests were splice length and concrete strength. Two UHPC mixes and one high strength concrete (HSC) mix were used to obtain the different strengths. Three groups differentiate the 10 slab/beams. Groups 1 and 2 consist of one type of UHPC each with three splice lengths and an additional slab/beam for fatigue testing giving a total of 8 specimens (four per group). These 8 slab/beams are referred to as full cast slab/beams since the entire slab/beam consists of one concrete type. The third group contains two specimens constructed from HSC precast sections joined with an UHPC fill and spliced reinforcement representing a construction joint in a bridge deck slab. One was used for static testing and the other for fatigue. Slab/beams in the third group are referred to as precast slab/beams since they were constructed using precast sections. Static testing of slab/beams were tested under four-point loading with a constant loading rate until failure. Fatigue tests were conducted under cyclic loading for a specified number of cycles before loading to failure. For clarity the general program and specimen types for slab/beam tests are shown in Figure 3.1. The designation of each slab/beam specimen begins with a letter D, R, or P denoting the concrete type, either D or R, for full cast slab/beams (D and R) or that the slab/beams were made from precast sections of type K concrete with a UHPC construction joint (P). The number represents the splice length in millimeters and the last letter differentiates between a static (A) or fatigue (B) test specimen. For example D150A means concrete type D was used with a 150 mm splice on a static test specimen. Specimens without A or B are by default static tests. The nine pullout tests were subjected to freeze/thaw treatments with humidity before being tested. Pullout tests are also divided into three groups each constructed using one of the three different concrete types. Each group contains specimens with both high modulus and low modulus GFRP bars. Pullout test results will be compared to identical specimens without environmental treatment conducted in a related study at the university (Ametrano 2011; Hossain et al. 2011). The pullout test program is shown in Figure 3.2. Additional details

about the materials, test specimen design, loading configuration/ procedures, test setup, and instrumentation are provided in the following sections. The concrete compressive strength ($f'c$) shown in each group in Figures 3.1 and 3.2 were the target concrete strengths.

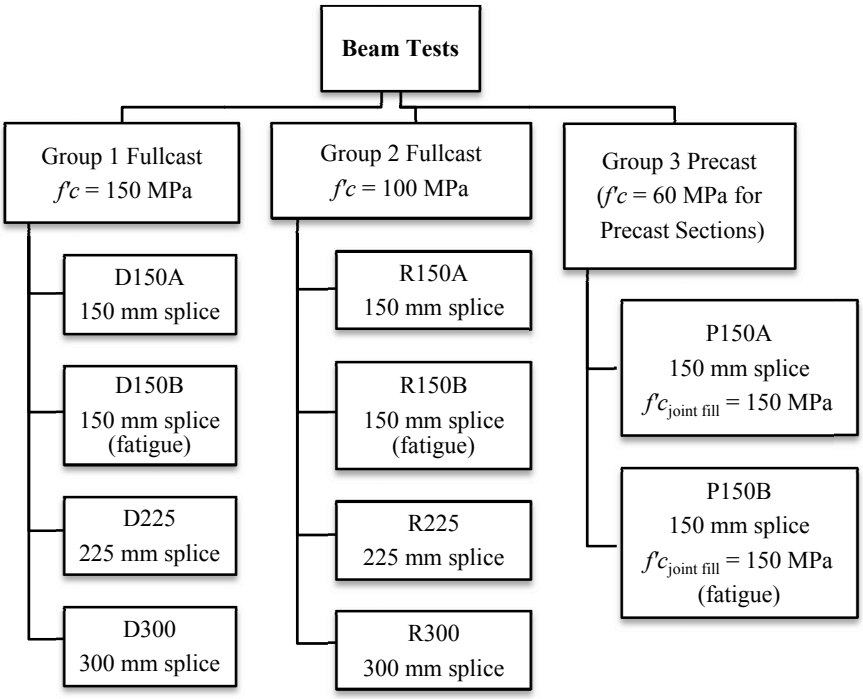

Figure 3.1: Slab/beam test experimental program

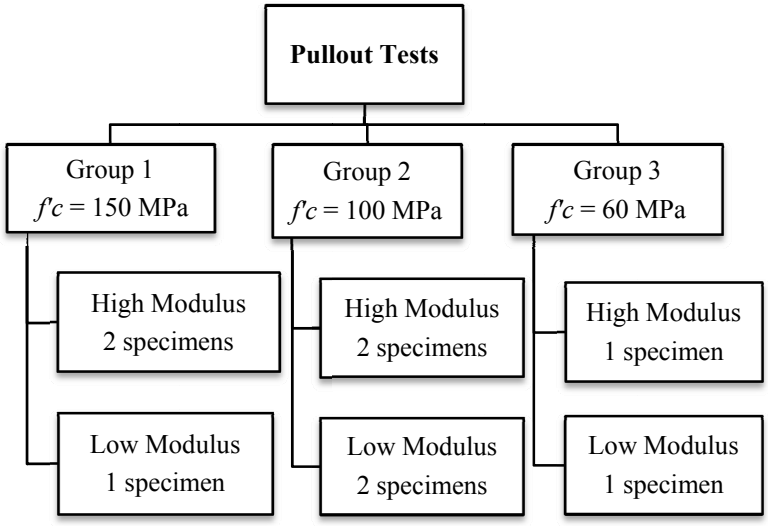

Figure 3.2: Freeze/Thaw pullout experimental program

3.2 Materials

3.2.1 Concrete

Three types of concrete were used throughout this study. Hereafter they will be denoted with the letters "D", "R" and "K" for Groups 1, 2 and 3 respectively. The target 28-day concrete compressive strengths are shown in Figures 3.1 and 3.2. Type D concrete was also used as the joint fill material for the precast slab/beam specimens in Group 3. Both D and R type mixes are classified as UHPC with steel fibre reinforcement while K is considered a HSC. Although the target concrete strength for type R was not in the range of typical UHPC as discussed in Section 2.3.1, it is still classified as such since the constituent materials and mix design are able to produce concrete in that range depending on the curing procedures. This concrete continued to cure even in plain laboratory environment beyond the 28-day mark and was found to have reached UHPC strength as shown in some of the specimens. The following sections describe the mechanical properties, mix designs, and mixing/curing procedures used for each type of concrete.

3.2.1.1 Mechanical Properties

The compressive properties (strength and modulus of elasticity) were tested in reference to ASTM Standard C39 (2009) using standard cylindrical specimens with a diameter of 100 mm and length of 200 mm. The surface finish and expected compressive strength for type K allowed the use of a sulfur capping compound to provide an even stress distribution from the head and table of the compression machine. However, for UHPC mixes, the cylinders required surface preparation using a diamond tipped rock saw such that the ends were perpendicular to the longitudinal axis within 0.5˚ or 1/100 mm as required by the standard to provide an even surface for testing. The ends of these particular cylinders were cut down about 10 mm -12.5 mm per side thus giving a total length of 175-180 mm during testing. The rate of loading was kept at the minimum allowable by the compression machine. This generally was within the limit of 0.25 MPa/s, however it was not possible to maintain this load rate during the latter portion of loading due to stiffening of the specimen. The loads were taken and averaged over the cross sectional area of the cylinder to obtain the compressive strength. A minimum of 3 cylinders were broken per mix on the day of testing for each pullout or slab/beam test with more being done in the case of larger variance. As

mentioned earlier the compressive strength of some mixes, especially with type R, attained a much higher compressive strength than the target due to complications with the lab scheduling and equipment that prevented testing of the slab/beam specimens at 28-days. The actual compressive strengths for each slab/beam and pullout specimen are shown in Table 3.1. Since conventional concrete models are not suited for UHPC (Collins and Mitchell 1997), some additional investigation was required to determine the stress-strain behaviour for this concrete.

Table 3.1: Actual specimen concrete strengths and compressive moduli

	Specimen	Concrete Compressive Strength (MPa)	Modulus of Elasticity Compression (MPa)	Precast Concrete Strength (MPa)
Slab/beams	D150A	148.5	46793	N/A
	D150B	169.5	49998	N/A
	D225	140.0	45435	N/A
	D300	140.0	45435	N/A
	R150A	153.4	47559	N/A
	R150B	150.0	47024	N/A
	R225	100.9	38572	N/A
	R300	108.3	39969	N/A
	P150A	168.1	49787	61.3
	P150B	183.2	51975	69.5
Pullout	Group 1	164.9	N/A	N/A
	Group 2	101.7	N/A	N/A
	Group 3	65.7	N/A	N/A

The modulus of elasticity for UHPC was predicted using the empirical equation proposed by Graybeal (2006a; 2007), which relates the compressive strength of UHPC concrete to the modulus of elasticity. The equation is restated here as equation 3.1 for convenience:

$$E_c = 3840\sqrt{f'c} \quad \text{.....(3.1)}$$

where E_c and $f'c$ are the modulus of elasticity and compressive strength of concrete in MPa respectively. This equation can be applied to UHPC between compressive strengths of 25 MPa and 195 MPa with sufficient accuracy (Graybeal 2006a; 2007). Additional cylinders were tested in conjunction with ASTM Standard C469 (2002) to verify this relationship. After the necessary end preparation, the cylinders were fitted with two horizontal and two vertical strain gauges with a gauge length of 50.8 mm. Each strain gauge was applied at mid-height at the half points with vertical and horizontal gauges diametrically opposite the gauge with the same orientation. Figure 3.3 shows the orientation of the strain gauges on a typical cylinder.

Figure 3.3: Horizontal and vertical strain gauges attached to cylinder specimen

The loading rate was kept constant at 0.241 MPa/s using an MTS testing machine while a data acquisitions system took 10 scans per second to record strain and load during loading history. The loading rate and gauge length/position were chosen in accordance with the standard. Some deviations from the standard were made due to limitations of the testing apparatus and instrumentation. These include applying only a single loading rather than several consecutive loadings to the specimen as well as using a limited load strain distribution due to premature failure of the specimen. The conventional cylinder compression machine was not able to provide a steady loading rate so the test had to be conducted using an MTS machine fitted with many steel spacers. This setup, as shown in Figure 3.4, did not provide ideal end loading conditions and as a result the cylinders failed prematurely due to stress concentrations and internal shear forces. With the exception of one

of the samples, the typical failure loads were about half of the expected load obtained from cylinders tested from the same batch on the same day. The modulus of elasticity was thus obtained using the slope of the line of best fit passing through the obtained data. The experimental results for modulus of elasticity showed reasonable correlation with equation 3.1 (Fig. 3.5). This relationship was found to have been the best fit across the entire range of UHPC used in this study versus other equations proposed by Graybeal (2006a; 2007).

Figure 3.4: MTS setup for testing modulus of elasticity of concrete

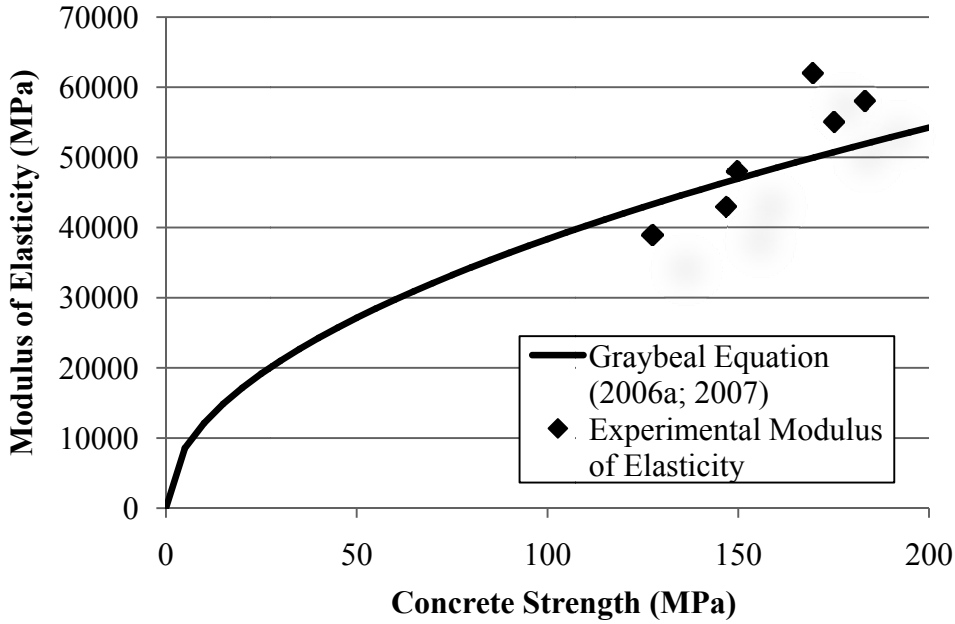

Figure 3.5: Relationship between compressive strength and modulus of elasticity

Another characteristic of UHPC important to this study is the convergence to full linearly elastic behaviour as concrete strength increases. The parabolic nature of normal concrete is commonly associated with the longitudinal cracking induced at the weak points between paste and aggregates (Collins and Mitchell 2007). However, in the case of UHPC there are no coarse aggregates and subsequently no inherent weak points. Moreover, any cracks that are initiated in the matrix are quickly bridged by the steel fibre reinforcement. The result is an increasingly linear response as the concrete paste becomes stronger and steel fibres become more effective. This stress-strain behaviour is useful for simplifying beam analysis with UHPC since a linear stress-strain relationship can be approximated for the compression block. Linearity in the UHPC used in this study is demonstrated in Figure 3.6, which shows the stress strain behaviour for the gauge fitted cylinder that reached its expected compressive strength. This behaviour has also been noted by previous researchers on this topic (Mendis 2003; Graybeal 2006a; Okuma 2006).

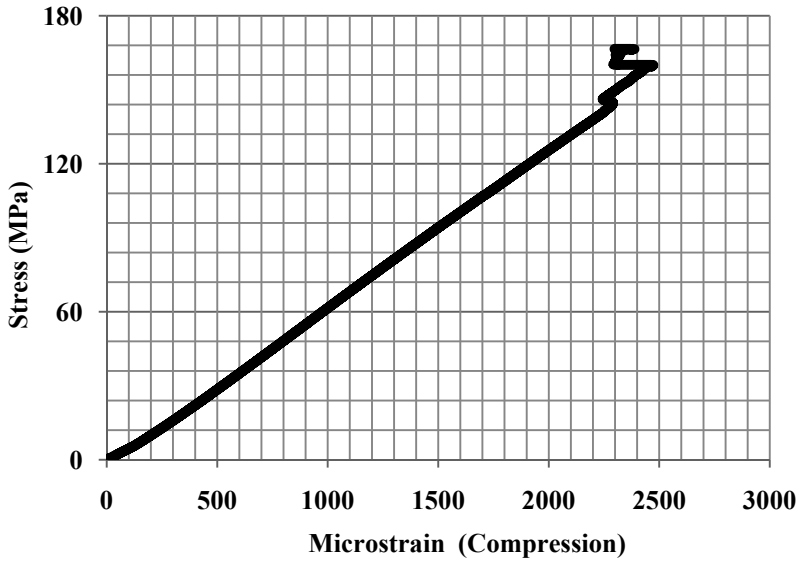

Figure 3.6: Stress strain behaviour of UHPC Type D

The modulus of rupture was also investigated for the two types of UHPC in accordance to ASTM Standard C78 (2009). Prism specimens were cast in steel moulds with cross-sectional dimensions of 75 x 75 mm and length of 305 mm. Four-point loading was applied at a constant rate of 0.027 kN/s as recommended by the standard. The specialized

loading apparatus was secured to the top and bottom platen of an MTS machine with a 100 kN load capacity. The total span was 225 mm with a shear span equal to the depth (also 1/3 span). Beams were turned onto their side relative to the direction of casting before being put into the testing machine. Load was applied until failure of the specimen. Figure 3.7 shows the flexural tests before and after failure of the specimen. Failure was characterized by a sudden loss of load capacity in the specimen and would typically result in the failure mode shown in the figure where all the steel fibres are pulled out and exposed. This was due to the load application being a function of force rather than displacement control.

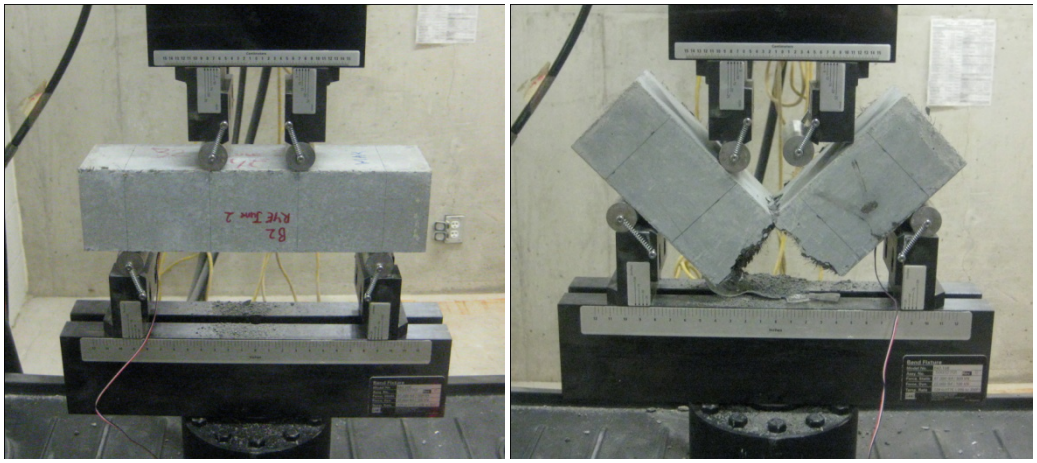

Figure 3.7: Flexural test before (left) and after (right) failure

All specimens failed within the pure bending region, so the simplified equation proposed by the standard based on the maximum load and geometry of the specimen was used to determine the tensile stress at the bottom of the prism. Approximately 2-3 cylinders per prism were also tested to determine the compressive strength versus modulus of rupture. The results showed that type R concrete had a significantly lower flexural strength versus type D concrete even though the compressive strengths were in some cases comparable. This was probably due to the enhanced microstructure of type D concrete from the use of ground quartz in the mix that allowed better bond between the steel fibres and the concrete matrix. Furthermore, the steel fibres in type D concrete were deformed with a slight spiral along the length thus adding additional mechanical interaction. Figure 3.8 shows the flexural strength values versus the concrete compressive strength for both R and D type concretes. The results

for flexural strength for type R concrete was between 6.9 MPa and 16.5 MPa for compressive strength between 90.9 MPa and 146.8 MPa. For type D concrete flexural strength ranged between 21.4 MPa and 27.1 MPa for compressive strength between 139.3 to 205.1 MPa.

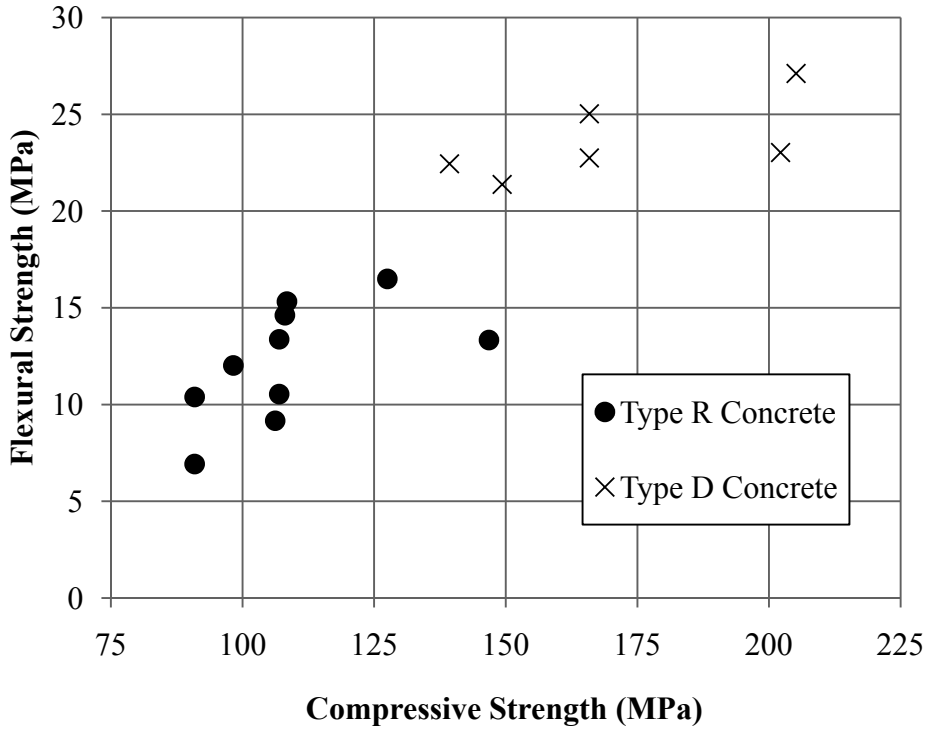

Figure 3.8: Flexural strength of UHPC versus compressive strength

3.2.1.2 Mix Designs

Type D Concrete

This UHPC is a commercial product named Ductal® produced by Lafarge and it consists of a premix (includes all dry materials), an accelerator, a high-range water reducing admixture, steel fibres, and water. The manufacturer provided all the necessary constituent materials as well as the mixers for this product. The premix is composed of Portland cement, silica fume, silica sand and quartz sand. The proportions shown for the premix in Table 3.2 were obtained from publications on the manufacturer's website (Graybeal 2006a) and are here factored to fit the current mix design. The amounts for water, accelerator, superplasticizer, and steel fibres can be changed to obtain a wide range of properties, however, the actual amounts used in this mix are shown in the table. The accelerator and

superplasticizer were also provided as a single mixture. The typical values for particle size are also shown in Table 3.2 in order to demonstrate the relative magnitude of the different materials versus themselves and the steel fibres. The steel fibres were made of high tensile strength steel strand with a minimum design tensile strength of 2600 MPa. This mix had a 2% steel fibre content by volume. The diameter of the steel fibres was 0.2 mm and the length was 12.7 mm. The fibres used in this concrete had a spiral along the length to improve the mechanical interlock with the concrete matrix.

Table 3.2: Type D concrete mix design (Graybeal 2006a)

Material	Quantity (kg/m^3)	Percent by Weight	Particle Size (μm)
Portland Cement	719	28.4	15
Fine Sand	1029	40.6	150-600
Silica Fume	233	9.2	0.5*
Ground Quartz	213	8.4	10
Superplasticizer + Accelerator	30	1.2	N/A
Steel Fibres	156	6.2	N/A
Water	155	6.1	N/A

*(Holland 2005)

Type R Concrete

This UHPC was produced by the research team at Ryerson based on the mix design proportions proposed by Tafraoui et al. (2009). Each constituent material was selected from a variety of manufacturers and tested to determine their compatibility with the mix. This mix essentially contains the same base materials as type D however no ground quartz or accelerator was necessary. The selected materials and their proportions are shown in Table 3.3. The silica fume used in this mix was undensified and the superplasticizer was a polycarboxylate based ASTM C494 Type F and ASTM C1017 Type I plasticizer. A steel content of 2.1% by volume was used in this concrete. The steel fibres were made from the same manufacturer as Type D but instead had no deformities. Each material came individually packaged and was proportioned out based on the required volume for the mix.

Table 3.3: Type R concrete mix design (Tafraoui 2009)

Material	Quantity (kg/m^3)	Percent by Weight
Portland Cement – Type 10 (Lafarge North America Inc.)	818	35.1
Silica Sand - F-110 Natural Grain (U.S. Silica Company)	899	38.5
Silica Fume - Microsilica Grade 971-U (Elkem Materials Inc.)	204	8.7
Superplasticizer – ADVA® Cast 575 (Grace Construction Products)	26	1.1
Steel Fibres– Dramix® OL 13/0.2 (Bekaert)	164	7.0
Water	221.8	9.5

Type K Concrete

This high strength concrete is a second commercial product classified as HP-S10 that also comes in a bagged premix form. HP-S10 is produced by King Packaged Materials Company. The main constituent materials are Portland cement, silica fume, air-entraining admixture, and 10 mm stone. Additional materials are also included but are not revealed by the manufacturer. The mix design is given as 2.4 liters of water per 30 kg bag of premix with an approximate yield of 0.014 m^3. This works out to be 2142.9 kg/m^3 and 171.4 kg/m^3 for premix and water respectively (KPM Industries 2011).

3.2.1.3 Mixing, Casting and Curing Procedures

Full cast slab/beam specimens required a minimum of 108 liters of either type R or D concrete with an additional 20-30 liters for control specimens and allowance. The average batch size per slab/beam was 132 liters. Each precast section required a minimum of 48.6 liters of type K concrete in addition to cylinders and allowance so the average batch size was 70 liters. The joint fill concrete required 10.8 liters and was casted together with the pullout specimens.

Type R and D Concrete

The mixing procedure and times for types R and D concrete are generally the same but can vary slightly depending on the volume of the mix and temperature of the surrounding

environment. Mixing times did not exceed 20 minutes. The procedure for mixing these UHPC generally followed this format for volumes between 80-140 liters:

- All dry materials were combined at the correct proportions (excluding the fibres) into the mixer and mixed for 3-5 minutes depending on the quantity until homogeneous. If the dry materials were provided in a premix such as with commercial products then these materials were placed in the mixer at the correct proportions and mixed for about 2-5 minutes to ensure an even distribution of materials.
- Half of the required superplasticizer (with combined accelerator, if applicable) was then mixed with the correct amount of water and this mixture was added to the dry materials over the course of 1-2 minutes while the mixer was still running.
- Mixing continued for another 5-7 minutes, depending on the temperature and volume, until the mixture had the consistency of a dry paste.
- The other half of the superplasticizer was then added over the course of 1-2 minutes while mixing.
- Mixing continued for another 5 minutes or until the mixture became fluid.
- The fibres were added by lightly sprinkling them over the surface of the mixture while mixing. This was to avoid any clumping and to improve the fibre distribution.
- Once all of the fibres were evenly incorporated the mix was ready for casting.
- The mixer was left running until casting was finished.

A Mortarman® 750 mixer, produced by IMER U.S.A, was used for all UHPC casting. This vertical shaft mixer (Fig. 3.9) provides the optimal mixing action for this type concrete by use of a horizontal stirring motion with paddles that reduces the entrapped air during mixing versus a folding motion produced by rolling barrel mixers. The optimal volume range for this mixer was between 80-150 liters. Smaller volumes did not incorporate well while large batches would not allow the ideal mixing speed. Consolidation methods were not used since these concretes were self-settling. However, pouring of the concrete was done in such a way that the fibres would align in the main tensile direction. In the case of the full cast slab/beams, pouring of the concrete was done from the end of the specimen so it would flow longitudinally to the other end thus aligning the fibres in that direction. Pullout specimens were poured from the side so that fibres would be transverse to the bar so as to prevent splitting failure. An effort was also made to avoid pouring directly over the

reinforcement since this caused clumping and segregation of the steel fibres. Instead the concrete was allowed to gradually flow upwards as the depth of concrete increased allowing a more even distribution of the fibres. Once the control cylinders had been cast every effort was made to prevent any mechanical disturbances in order to keep the fibres suspended in the concrete matrix.

Figure 3.9: IMER Mortarman 750 vertical shaft mixer

The full strength development of UHPC was not necessary for this research and so steam/heat treatments were not used. Instead all specimens were cured in a laboratory environment using wet burlap and plastic sheets as moisture barriers. Type R concrete required a full seal around the moulds for both the specimen and control cylinders due to excessive high heat of hydration caused by the large volume of concrete that would have caused the majority of the water to evaporate from the specimen. Wet burlap was also laid over the surface of all type R specimens after initial set to provide additional moisture. Type R control cylinders were demoulded after 2 days and placed under the moisture barrier with the slab/beam specimens. The burlap was kept continuously wet during the curing period. The plastic sheets were removed after 21 days since the concrete had obtained the desired strength and the specimen was demoulded. Specimens were left in the same laboratory environment until testing. Type D concrete had a much slower initial set, in some cases as much as 3 days, so the temperature change due to heat of hydration was much lower. Wet burlap was used only with the slab/beam specimens to prevent plastic shrinkage. A moisture barrier was formed over the tops of all the moulds and cylinders using plastic sheets (Fig.

3.10) and plywood as a weight. After three days and initial set, type D specimens were demoulded and left in a laboratory environment for at least 28 days before testing. It was found that even in a plain lab environment the UHPC would still gain significant strength beyond 28 days and thus some of the specimen strengths were affected.

Type D concrete was also used for the joint fill application. The joint surface of the precast sections was prepared by scouring with a wire brush to enhance the bond with the UHPC. A clean wet cloth was used to wipe the surface clean from any dust or residue. After the joint was prepped and the moulds were constructed, Type D concrete was then poured into the joint from the side of the slab/beam aligning the fibres in the transverse direction so as to prevent splitting. Additional concrete was added beyond the height of the specimen and was enclosed using taped cardboard strips to allow excess for settlement. When the surface had set the area was covered using wet burlap and plastic to prevent moisture loss and shrinkage. The joint was allowed to set for 3 days before the plastic and moulds were removed. It was then left for at least 28 days before being moved or tested.

Figure 3.10: Full cast type D slab/beam specimen under plastic sheets (left) and control cylinder specimens under plastic sheets (right)

Type K Concrete

This concrete was mixed in a separate high shear vertical pan mixer with a capacity of 75 liters. The mixing procedure was as follows for a typical 70 liter mix (KPM Industries 2011):

- 75% of the required water was first added into the mixer.
- All the dry materials were then introduced and mixing was initiated.
- The remaining water was slowly introduced during mixing once the original contents had been thoroughly incorporated.
- Mixing continued for a minimum of 5 minutes until a paste like consistency was achieved.

Casting of the specimen was done over a vibrating table to improve consolidation. A tamping rod was also used to help place the concrete in tight spaces. Control cylinders were cast in two layers with vibration as per ASTM Standard C192 (2007). Due to the lack of space in the curing room these specimens were also cured in a laboratory environment using wet burlap and moisture barriers. The burlap was kept continuously wet during the curing period of 21 days after which all burlap and plastic sheets were removed. Precast specimens were left in the lab environment until the joint fill application. Figure 3.11 shows how the precast sections were cured.

Figure 3.11: Precast slab/beams under moisture barrier and wet burlap

3.2.2 Glass Fibre Reinforced Polymer Rebar

Two types of V-Rod® GFRP rebar were provided by Pultrall Inc. for use in this study namely high modulus and low modulus. The bars are composed of a vinyl ester resin at a volume fraction of 35% with E-glass fibres impregnated within at 65%. A sand coating is applied to the surface of the bar by use of a resin in order to improve the bond capacity. The

nominal bar diameter was 15.9 mm for both bar types. The tensile properties of both high modulus and low modulus GFRP are provided in Table 3.4 along with some other characteristics relevant to this study (Pultrall 2011).

Table 3.4: GFRP reinforcing bar properties (Pultrall 2007; 2008)

Bar Description	High Modulus GFRP	Low Modulus GFRP
Nominal Bar Diameter (mm)	15.9	15.9
Nominal Bar Area (mm^2)	197.9	197.9
Modulus of Elasticity (GPa)	64.1	48.2
Design Tensile Strength (MPa)	1259	683
Nominal Tensile Strength (MPa)	1439	751
Nominal Tensile Strain (%)	2.24	1.56
Longitudinal Coefficient of Thermal Expansion (10^{-6}/°C)	6.4	6.4
Transverse Coefficient of Thermal Expansion (10^{-6}/°C)	24.9	29.1
Poisson's Ratio	0.25	0.25

3.2.3 Mild Steel Reinforcement

Additional 6.35 mm diameter smooth steel bars were necessary to provide shear reinforcement as will be explained in the next section. The relevant properties of these bars are given in Table 3.5. Due to the lack of surface deformations the bars were bent to form hooks in order to provide the required mechanical interlock.

Table 3.5: Mild steel reinforcing bar properties (Riley et al. 2007)

Bar Description	Mild Steel
Bar Diameter (mm)	6.35
Bar Area (mm^2)	31.7
Modulus of Elasticity (GPa)	200
Yield Strength (MPa)	250
Yield Strain (%)	0.125
Coefficient of Thermal Expansion (10^{-6}/°C)	11.9

3.3 Design of Test Specimens

3.3.1 Full Cast Slab/beams

All full cast slab/beams were designed as a spliced beam test with dimensions representative of a strip of bridge deck slab. The depth of each slab/beam was 200 mm while the width was 270 mm. The total length was 2000 mm with a span of 1800 mm and shear span of 600 mm. Type D and type R concretes were used to cast four slab/beams each with concrete strengths of 150 and 100 MPa, respectively. The reinforcement details were chosen based on empirical recommendations by the Canadian Highway Bridge Design Code (CHBDC) for the design of internally restrained cast-in-place bridge decks reinforced by FRP bars. The following guidelines were used to design the reinforcement for each slab/beam as shown in Figure 3.12 (CSA 2006):

- Clause 8.18.2 – The slab thickness shall not be less than 175 mm.
- Clause 8.18.4.2(b) – When the slab is supported on parallel beams, the reinforcement bars closest to the top and bottom of the slab are laid perpendicular to the axes of the supporting beams or are laid on a skew parallel to the lines of beam supports.
- Clause 16.8.8.1(a) – The deck slab shall contain two orthogonal assemblies of FRP bars, with the clear distance between the top and bottom transverse bars being at least 55 mm.
- Clause 16.8.8.1(b) – For the transverse FRP bars in the bottom assembly, the minimum area of cross-section in mm^2/mm shall be equal to $500d/E_{frp}$; where d is the distance from the top of the slab to the centroid of the bottom transverse FRP bars (mm) and E_{frp} is the modulus of elasticity of the FRP bar (MPa).
- Clause 16.8.8.1(c) – The longitudinal bars in the bottom assembly and the transverse and longitudinal bars in the top assembly shall be of GFRP with a minimum reinforcement ratio of 0.0035.

It is important to note that, according to the CHBDC, the main tensile reinforcement is referred to as the transverse bars since they cross the axis of the supporting beams. However, from the point of view of this study the main reinforcement is referred to as being in the longitudinal direction due to the large length to width ratio of the specimen and will hereafter be referred to by this term. Any reinforcement transverse to this direction is thus referred to as transverse reinforcement. Based on the guidelines the following reinforcement details

were used as shown in Figure 3.12:

- Bottom Assembly
    - 2 x 15.9 mm high modulus longitudinal (main) reinforcement at 135 mm spacing.
    - 5 x 15.9 mm low modulus transverse reinforcement at 400 mm spacing.
- Top Assembly
    - 2 x 15.9 mm low modulus longitudinal reinforcement at 135 mm spacing
    - 5 x 15.9 mm low modulus transverse reinforcement at 135 mm spacing
- A top clear cover to the longitudinal GFRP bars of 31 mm.
- A bottom clear cover to the longitudinal GFRP bars of 50 mm.
- A clear distance between top and bottom longitudinal reinforcement of 87 mm (clear distance of 55 mm between assemblies).

Low modulus (LM) GFRP bars were used as a low cost substitute for high modulus (HM) bars in the minor reinforcement assemblies so HM rebar was only used for the main tensile reinforcement. A clear cover of 50 mm was chosen based on pullout tests with clear cover of 40 and 60 mm (Ametrano 2011; Hossain et al. 2011). Results from these tests showed no splitting failure for the smaller cover when using UHPC and thus 50 mm was deemed sufficient to ensure pullout bond failure in the specimen. Furthermore, since the main purpose was to test the splice performance, the opposing longitudinal bars in the top and bottom assemblies were offset half a bar diameter in opposite directions and lapped using either a 150, 225 or 300 mm splice length (Fig. 3.12). The splice lengths were based on joint widths used in recent HPBJ applications using LM GFRP and steel rebar (Harryson 2003; Perry and Royce 2010; Perry et al. 2007). The transverse reinforcement was also arranged according to recent designs by ensuring that at least one bar in each spliced assembly crossed the main reinforcement (Harryson 2003; Perry et al. 2007). The presence of transverse bars in the splice helps to prevent longitudinal splitting failure at the minimum cover location, provides a more even distribution of load across the splice, and prevents local cone failures (Harryson 2003). A pure bending region of 600 mm was chosen to represent the width of a typical 600 x 250 mm CL-625 truck tire print while ensuring that the spliced region was also fully encompassed and exposed to maximum moment. The 270 mm width of slab also fits well with the dimension of the tire print.

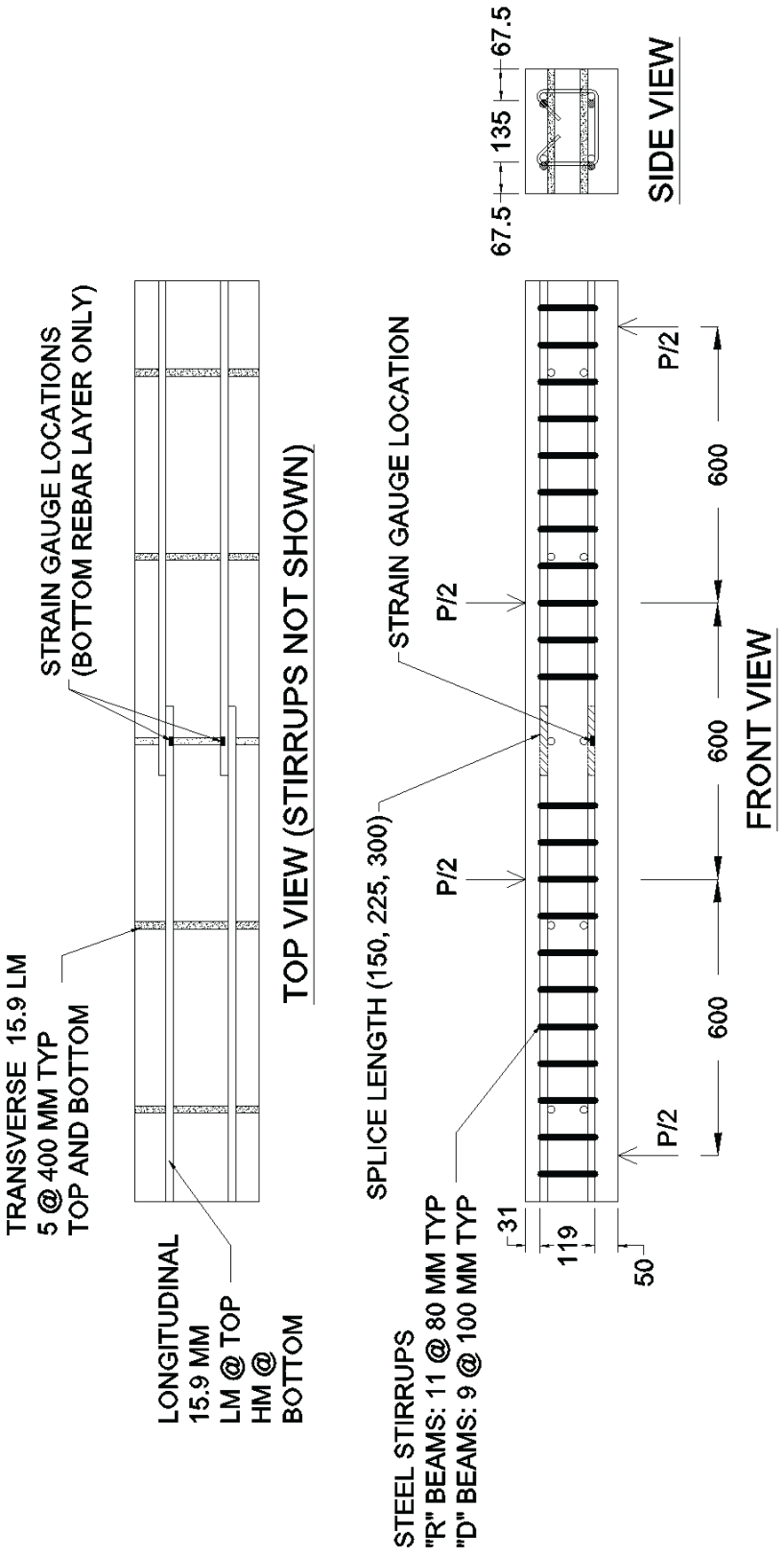

Figure 3.12: Full cast slab/beam specimen design (dimensions in mm)

The slab/beams were also checked according to CSA A23.3-04 (2006) concrete code for shear strength. It was found that these slab/beams were prone to shear failure depending on the strength of the splice, which is consistent with the punching shear failure of concentrated loads applied to full width slabs (El-Ragaby et. al 2006). Thus additional shear reinforcement was fabricated using 6.35 mm mild steel bars. Stirrups were anchored around the longitudinal reinforcement using 135˚ hooks extending at least 60 mm beyond the longitudinal bar (Fig. 3.13). This stirrup and anchorage design is in accordance with the following standards (CAC 2006; CSA 2009):

- CSA A23.3-04 Cl.12.13(a) – For 15M and smaller bars, transverse shear reinforcement provided for shear shall be anchored by a standard stirrup hook around longitudinal reinforcement.
- CSA A23.3-04 Cl.7.1.1 – Standard hooks and bends shall comply with Clause 6.6.2 of CSA A23.1.
- CSA A23.3-04 Cl.7.1.2 – Stirrups shall be anchored by standard stirrup hooks. The standard stirrup hooks shall have a bend of at least 135˚ unless the concrete cover surrounding the hook is restrained against spalling, in which case a bend of at least 90˚ shall be permitted.
- CSA A23.1 Cl.6.6.2 – Standard hook design requires a minimum extension of 60 mm or 6 bar diameters, whichever is larger, beyond the longitudinal bar.

The dimensions of the final stirrup design are shown in Figure 3.13. Type D slab/beams were expected to develop a higher concrete strength and so a stirrup spacing of 100 mm was used. This allowed a total of 9 stirrups with 6 placed in the shear span. Two were extended into the pure bending region but did not enter the spliced region. The first stirrup in shear span was placed at one half the spacing or 50 mm. Type R slab/beams had stirrups spaced at 80 mm allowing 11 in total with 7 stirrups placed in the shear span.

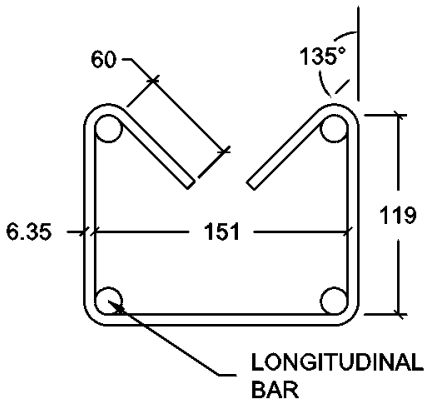

Figure 3.13: Stirrup design using 6.35 mm mild steel bars (dimensions in mm)

Various photographs of the slab/beam moulds are shown in Figure 3.14. An additional two steel loops were placed on top of the load points before casting for lifting purposes (Fig. 3.14a). All the bars were fastened together using plastic zip ties (Fig. 3.14b). The spliced bars were also tied together for full contact of opposing bars (Figs. 3.14b, c). The moulds were constructed using a 19 mm thick plywood base with 200 mm wide wood planks at the sides. The ends were secured using steel bolts passing through additional 50 x 50 mm wood braces that were screwed into the wood planks (Fig. 3.14d). Furthermore 16 mm diameter holes were drilled into the sides of the slab/beam moulds at the GFRP bar locations so that all the reinforcement could be held at the correct position without the use of plastic seaters (Fig. 3.14d). This also provided additional restraint against floating due to the lower density of GFRP bars. The holes were then sealed using a silicone caulking to prevent any leaks. The interior of the moulds was coated with a polyurethane varnish to help prevent against damage and moisture absorption. An additional coating of petroleum jelly was applied prior to assembling the reinforcement to help ease demoulding. Each mould was designed to be shared between two simultaneously cast slab/beams due to the tight casting schedule and need to reduce construction costs. The hydrostatic pressure from the wet concrete on the dividing wall would be balanced on both sides when two slab/beams were simultaneously cast (Fig. 3.14e). An additional wood frame was constructed to provide additional support to the outer walls of the moulds. The wires from the strain gauges were suspended above the specimen using a cross wire (Fig. 3.14f).

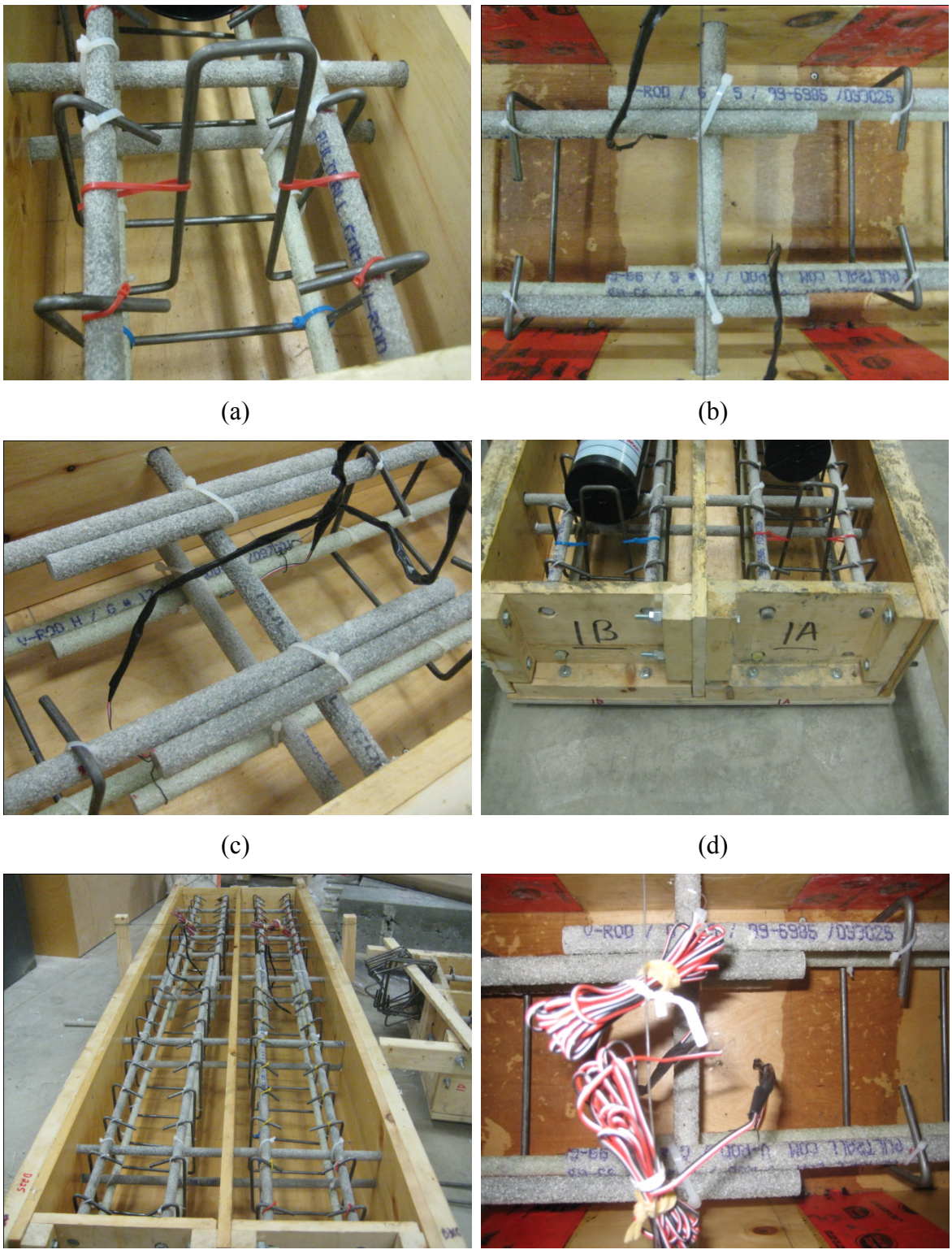

(a) (b)

(c) (d)

(e) (f)

Figure 3.14: (a) Steel loop for lifting, (b) top view of 150 mm splice, (c) 225 mm splice, (d) slab/beam mould end pieces, (e) full view of slab/beam moulds, (f) strain gauge wires

3.3.2 Precast Joint Slab/beam Specimens

The reinforcement configuration of precast slab/beam specimens was identical to the full cast slab/beams with the exception that there were no stirrups. Shear reinforcement was not provided in order to examine real slab behaviour more closely as well as the flexural performance of the joint versus the shear capacity of a slab strip. Two specimens were cast both using 150 mm splices thus allowing a 200 mm joint width which is similar to what has been implemented in previous HPBJ (Perry et al. 2007). Longitudinal reinforcement would protrude 175 mm out from the precast section providing the lap length of 150 mm (Fig. 3.15). The joint interface was designed using a flat surface transverse to the slab/beam direction rather than a shear key. This gave the worst case scenario in terms of bonding surface area and shear capacity at the interface.

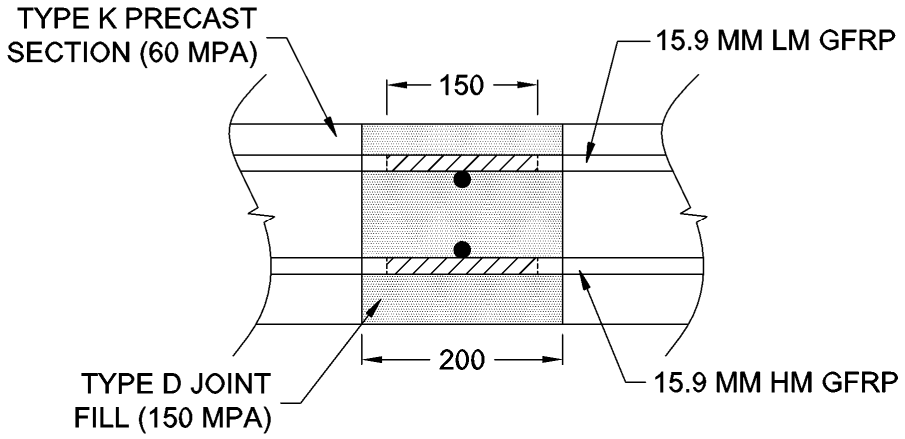

Figure 3.15: Precast joint interface design (dimensions in mm)

Each precast section had the same cross-sectional dimensions as the full cast slab/beams (200 mm x 270 mm) but the length was 900 mm each. Again the total length of the specimen would be 2000 mm as shown in Figure 3.16. Each precast section was constructed individually using HSC (Fig. 3.17a). After the precast sections had reached the target strength they were arranged according to the design in Figure 3.16 to facilitate the joint fill application (Fig. 3.17b). The sections were placed with two specimens side-by-side similar to the full cast slab/beams while clamps were used to secure the walls of the joint mould (Fig. 3.17c). Transverse bars within the joint region were placed accordingly and tied down using plastic zip ties (Fig. 3.17d). Once the moulds were constructed, Type D concrete

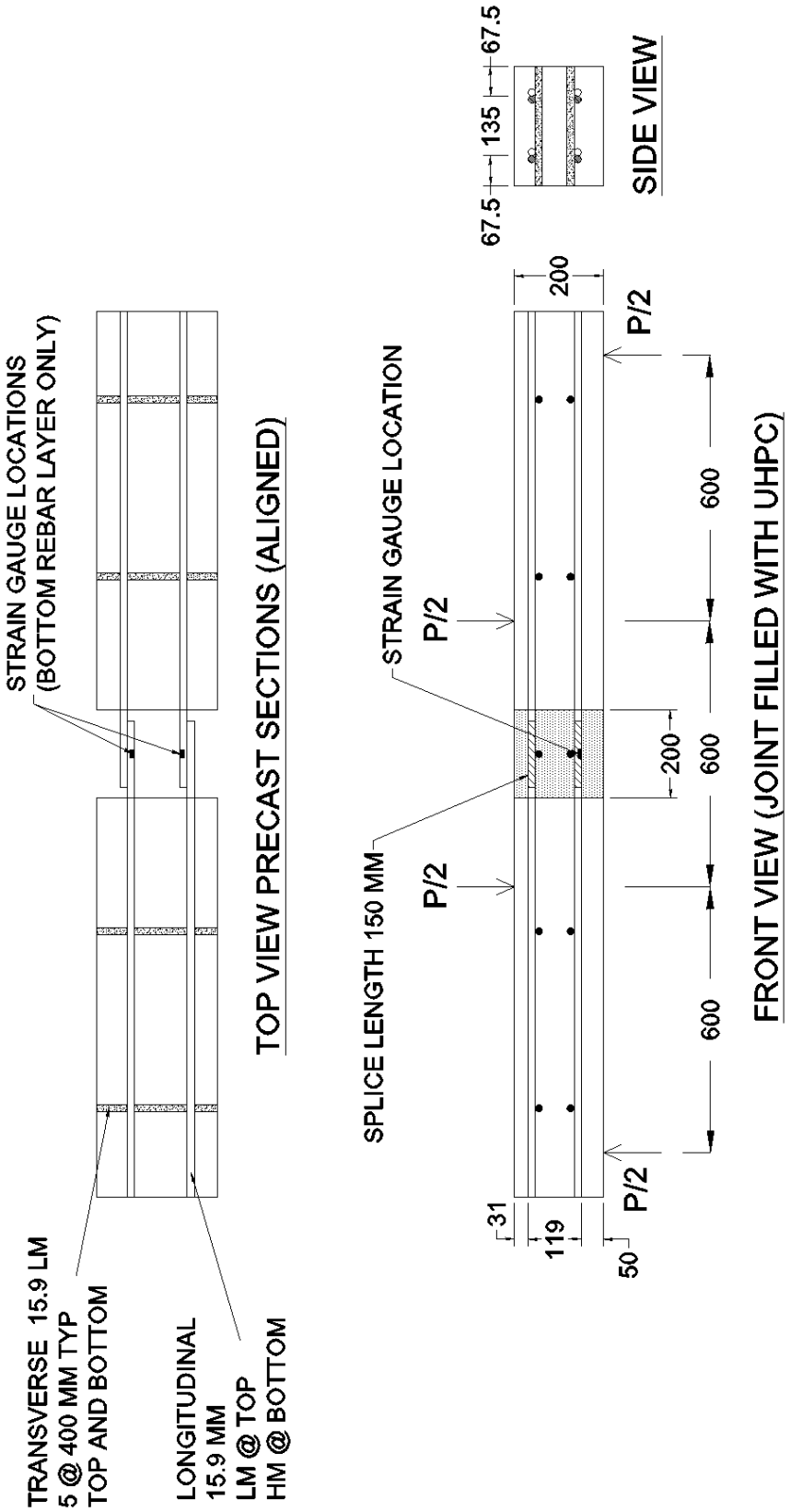

Figure 3.16: Precast slab/beam specimen design (dimensions in mm)

was filled into the joint (Fig. 3.17e) using the casting procedures stated in previous sections. The target strength for these slab/beams was 60 MPa for the precast sections and 150 MPa for the joint fill material.

(a) (b)

(c)

(d) (e)

Figure 3.17: (a) Precast section with protruding GFRP reinforcement; (b) precast sections arranged with joint moulds; (c) two specimens arranged side by side with wood clamps; (d) single joint with transverse bars secured at mid-splice; (e) finished UHPC joint

3.3.3 Pullout Specimen Design

Pullout specimens were designed based on CAN/CSA-S806-02 Annex D: Test Method for Development Length of FRP Reinforcements (CSA 2002). The cross-sectional dimensions were 150 x 150 mm while the total length was 120 mm. The initial 25 mm length at the loaded end was left unbonded by use of foam pipe insulation secured with zip ties. This was to counteract the frictional restraint imposed by the bearing force on the contact surface of the block. Both HM and LM 15.9 mm sand coated GFRP bars were used in the investigation with embedment lengths of 5 bar diameters, approximately 80 mm. The remaining 15 mm of the embedded length was also covered using foam to create the effective bond length. The total length of the bar was 1.0 m with a 100 mm portion protruding out the free end of the block to accommodate an LVDT. The bars were placed eccentrically such that the clear cover was 40 mm at the bottom of the specimen. These details are shown in Figure 3.18 and the pullout moulds are shown in Figure 3.19. All three concrete types were included in this investigation with the target strength ranging from 60 MPa to 150 MPa. The specimens were cast horizontally while the concrete was poured from the side of the specimen and not over the bar. A total of nine pullout specimens were subjected to freeze/thaw cycles and humidity prior to being tested. The results will be compared to identical pullout tests conducted in a related study that were not subjected to harsh environmental testing. Details about environmental testing and loading are presented in a later section.

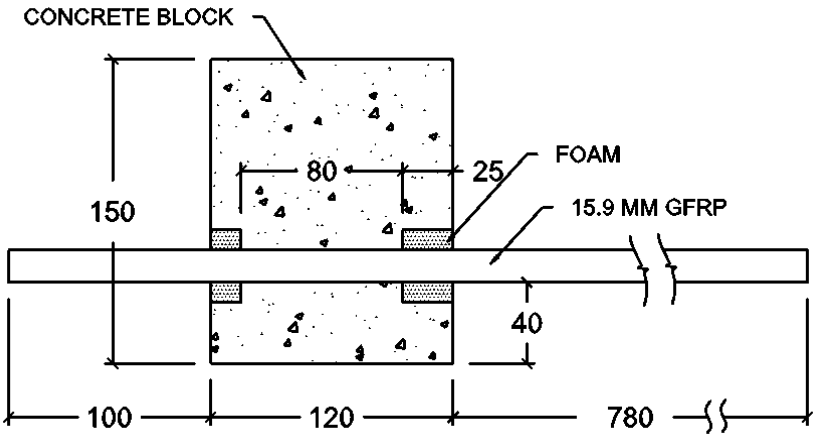

Figure 3.18: Pullout specimen design

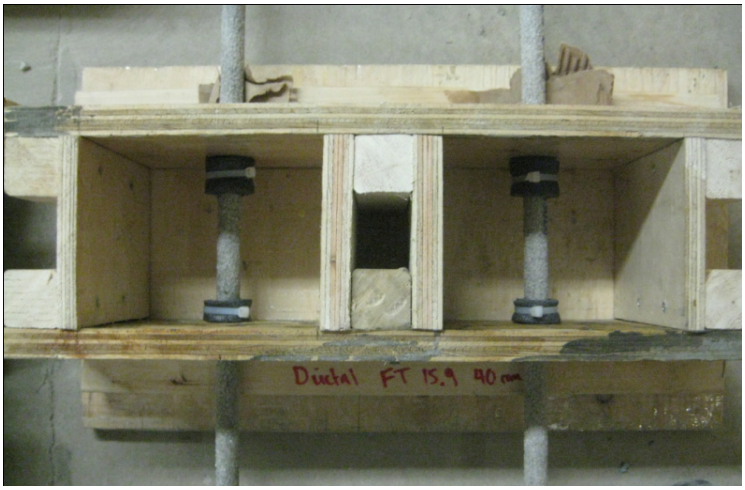

Figure 3.19: Pullout moulds

3.4 Testing Procedures, Setup and Instrumentation

This section discusses the procedures, test setups, and instrumentation used in each of the experiments. Tests procedures will include details on loading rates, cyclic load frequencies, etc. for slab/beam tests as well as the freeze/thaw regime and loading details for pullout testing. The design of the test apparatus and load mechanisms are also included. Details about the instrumentation and measuring devices used during each test will also be discussed.

3.4.1 Static Slab/beam Tests

Testing Procedures

Static slab/beam tests were conducted with a maximum loading rate of 5 kN/minute until failure. At every 10 kN interval the load increment was paused to examine crack propagation. This continued until all the major cracks had formed and was then stopped due to safety issues during failure. Failure occurred when a sudden explosive noise was heard followed with a large jump in deflection. Two setups were used for static testing. The first utilized a manually controlled hydraulic jack so the loading rate was controlled using a stopwatch and by monitoring the load from the data acquisition system. The second testing apparatus used an MTS machine, which applied the load at the correct rate through the entire test until failure.

Test Setup

Each static slab/beam test was conducted under four-point loading with a total span and shear span of 1.8 m and 0.60 m respectively. The slab/beams were elevated over a rigid slab using hollow steel sections with roller supports. A loading frame was constructed using two structural steel threaded rods secured to the support slab and a hollow steel cross beam mounted at the top. A hydraulic jack was secured to the bottom of the cross beam to apply the load. The load was applied through a load cell on to a steel spreader beam with two welded roller supports spaced at 600 mm that distributed the load to two points on the slab/beam. The test slab/beam was positioned at the mid-point of the cross beam to ensure the load was evenly distributed. This setup is shown in Figure 3.20.

Figure 3.20: Static slab/beam test setup

Instrumentation

Several of the measuring devices used for static testing can be seen in Figure 3.20. Static tests required the load deflection behaviour at various locations along the length of the slab/beam. Three LVDTs accurate to 0.01 mm were mounted on steel supports and were directed downwards onto horizontal clamps attached to the slab/beam at mid-span and mid-shear span. A load cell accurate to 0.01 kN was placed between the spreader beam and hydraulic jack to measure the total applied load. All instruments were connected to a data acquisition system taking 10 scans per second. Two embedded strain gauges were also

mounted on the inner opposing tension bars at mid-splice (the two bars closest to the middle of the slab/beam coming from opposite directions) to measure the load strain behaviour. Special arrangements had to be made to apply each strain gauge. Each bar had the sand coating removed on a 10 mm x 20 mm rectangle using a grinder. The area was then smoothed using 400 grit sand paper and prepped as recommended by the strain gauge manufacturer. Figure 3.21 shows bars used for various splice lengths with strain gauges mounted at the mid-splice position. M-Bond 200 adhesive was used to adhere the gauge longitudinally along the bar surface. An additional moisture barrier was applied over the strain gauge along with a layer of silicone caulking for mechanical protection. The strain gauge wires were tied to a crosswire suspended above the specimen during casting. The strain gauges were accurate to the microstrain level and were also connected to the data acquisition system. The positioning of the strain gauge relative to the neutral axis of the bar cross section was also important and so they were placed in the moulds facing sideways (at the neutral axis) to minimize the effects due to bending of the bar.

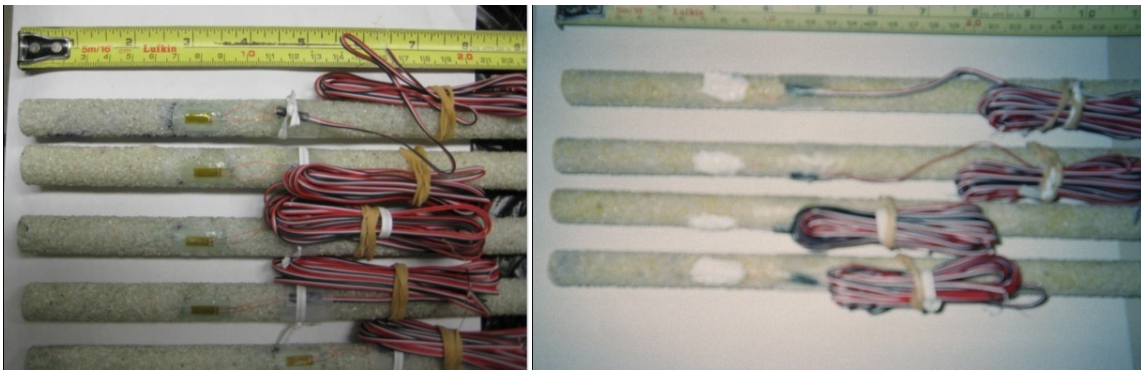

Figure 3.21: GFRP bars with strain gauges prior to moisture barrier application (left) and GFRP bars after silicone applied (right)

3.4.2 Fatigue Slab/beam Tests

Testing Procedures

Fatigue slab/beam tests were first loaded to cracking before the cycles were applied. The cracking load was determined from the load deflection curves of the identical static tested specimens. The end of the initial stiff portion of the curve when the slope would abruptly change is where cracking is assumed to have occurred. This value was generally

within the modulus of rupture range for each of the concretes with type D slab/beams having a higher cracking load. Cracking load was applied with the same 5 kN/min rate of loading as with static tests. A serviceable load range was estimated based on the live load factors and material resistance factor for GFRP. The ultimate limit state has a factor of 1.7 for live load while the fatigue limit state has a factor of 1.0. A material resistance factor of 0.5 is also given to GFRP as concrete reinforcement. By dividing the ultimate capacity of the equivalent static slab/beam test by the live load factor and multiplying by the material resistance factor an estimated service range of 30% of the ultimate capacity for the slab/beam is obtained. The minimum load was set at 5 kN to account for sustained loads such as bridge barriers and wearing surfaces as well as to offset the lack of sensitivity of the loading apparatus at small loads. For the last fatigue specimen (R150B) an additional 5 kN was added to the minimum load to help address this issue. The final load range would then begin at the minimum load (5 or 10 kN) and then move up an additional 30% of the expected ultimate capacity. The desired loading frequency was to be 2 Hz as used by other researchers on GFRP bridge decks (El-Ragaby et. al 2006). However, the MTS machine did not apply load from a top moving crosshead so such a high frequency could not be achieved. Instead, each slab/beam had to be optimized to give the maximum possible frequency based on the required loading range. Each load cycle was applied using a sinusoidal waveform. The final load ranges and frequency for each fatigue test specimen is provided in Table 3.6. The original program was to apply cycles until failure of the specimen occurred but due to the extremely low frequency this was not feasible. The actual number of cycles applied to each fatigue specimen are also shown in Table 3.6.

Table 3.6: Fatigue testing details

Specimen	Cracking Load (kN)	Frequency (Hz)	Minimum Load (kN)	Maximum Load (kN)	Cyclic Loading (# of Cycles)
P150B	35	0.125	5.0	25.5	100,000
R150B	90	0.1	10.0	50.3	100,000
D150B	100	0.1	5.0	45	60,000

D150B was the first specimen to be tested under cyclic loading and was cut short due to complications with the loading apparatus that had to be changed. After the specified number of cycles had been reached the slab/beam was loaded to failure at 5 kN/min. The results for load capacity, bond strength, and deflection are then compared with static test results.

Test Setup

The loading apparatus for fatigue testing and some of the static tests were done on an MTS machine. Two steel beams were bolted together to form the support beam that was then mounted to the bottom platen of the machine. Two thick steel rollers were welded to the top of the steel support beam at a 1.8 m span giving enough elevation to prevent contact with the steel beam prior to failure. Four-point loading with a shear span of 0.6 mm was also used so the same spreader beam from static testing was placed on top of the concrete slab/beam once it was positioned correctly. The loading rate, load range, and frequency were controlled nearby through a computer and the MTS software. The machine applied loads by lifting the entire apparatus up to the contact plate at the top of the machine. Figure 3.21 shows the fatigue test setup.

Figure 3.22: Fatigue test setup

Instrumentation

An additional two LVDTs were required to account for the deflection of the steel support beam. These were placed directly under the roller supports and interpolation was used between these two values to determine the effect at various locations along the slab/beam. A 87.5 x 37.5 mm wood cross member extending the full length of the slab/beam was clamped to the midpoint of the setup. The midpoint is where deflection is assumed zero since this was supported directly above the bottom platen of the machine. All five LVDTs were mounted on the wood cross member and were directed upwards to the bottom of the slab/beam at mid-span, mid-shear span and under the roller supports. An external load cell was not required for this setup since one was already built into the MTS machine. Two embedded strain gauges were also mounted at mid-splice as per the static tests. All external instrumentation was connected to a data acquisition system taking 10 scans per second.

3.4.3 Environmental Pullout Tests

Testing Procedures

The pullout specimens in this study were first subjected to freeze/thaw cycling prior to being loaded. Identical control specimens were also cast from the same batch and cured using the same procedure and environment, respectively. Testing was done at approximately the same age for both control and freeze/thaw pullout specimens. The ultimate capacities of pullout specimens exposed to environmental effects are then compared with the pullout capacity of the control specimens not subjected to freeze-thaw cycles. The purpose of this test is to investigate any potential bond degradation due to extreme heat and extreme cold with the presence of humidity. Splitting cracks may occur in the surrounding concrete at high temperatures as a result of the larger transverse coefficient of thermal expansion of GFRP rebar versus steel (ISIS Canada 2006; 2007). Furthermore, the added moisture and freezing temperatures may cause degradation in the sand coating of the rebar or to the fibre core itself due to the expansion of the absorbed moisture (Laoubi et al. 2006). The freeze/thaw regime used here was derived from similar studies on GFRP reinforced concrete beams (Davalos et al. 2008; Laoubi et al. 2006). A maximum temperature of 60˚C and a minimum temperature of -30˚C were used with 50% humidity whenever possible. Each cycle consisted of a ramp up to the maximum temperature, which was then maintained for six

hours, and then a ramp down to the minimum temperature for another six hours. Figure 3.22 demonstrates the temperature variation during one cycle. A total of 50 cycles were applied to each specimen using an environmental chamber that controlled the temperature and humidity. Figure 3.23 shows an image of the specimens in the chamber after testing. The specimens were kept elevated using a steel grating to maximize the surface area exposed to humidity and temperature change.

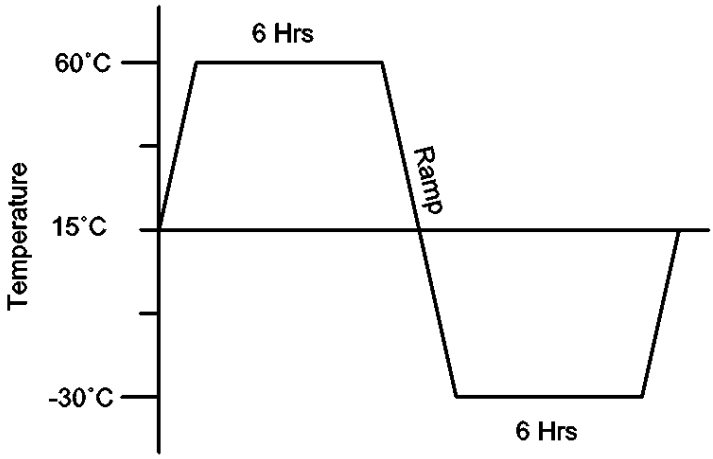

Figure 3.23: A single freeze/thaw cycle for pullout tests (50 of these cycles were used for environmental treatment)

Figure 3.24: Environmental chamber for freeze/thaw application

Once 50 cycles were completed the pullout specimens were left in a plain laboratory environment to let dry and return to room temperature prior to being loaded. Each pullout specimen was loaded to failure at a rate of 250 MPa/min or approximately 50 kN/min for a 15.9 mm bar. The bar was marked at the free end where it met with the concrete so that failure could be visually confirmed since the steel grips at the loaded end were susceptible to failure before pullout. This was further verified by a loss of load capacity and by a slip distance at the free end equal to the bar's diameter. This procedure is based on the CAN/CSA-S806-02 Annex D pullout test method (CSA 2002).

Test Setup and Instrumentation

The loading apparatus, shown in Figure 3.24, was designed similar to that proposed in CAN/CSA-S806-02 Annex D and was constructed using an annular hydraulic jack, steel grips (anchor), v-grips (secondary anchoring device), steel plates (spacers), annular load cell, LVDT, and clamps. The steel grips, also shown in Figure 3.24, were designed in accordance with the code by providing centric load transfer without torsion, an even load distribution along the perimeter of the bar to prevent premature failure within the anchorage, and no chemical or mechanical alteration within the gauge-length of the bar (CSA 2002). Each of these consists of two steel blocks large enough to accommodate two structural steel bolts and the GFRP rebar through the middle. A hole was drilled through the block and the block was cut in half to form a clamp. Two of these were used during each test. Each bolt was pretensioned using a pneumatic wrench to provide the necessary frictional force on the bar. An LVDT is attached at the free end using clamps to measure the load slip response. A circular steel plate was then used around the bar at the loaded end to act as a load distributor and spacer. The annular load cell was then applied followed by the hydraulic jack and two steel grips. Additional spacers were also provided so that the v-grips could be used at the very end of the bar as a backup anchorage device. The annular load cell (accurate to 0.01 kN) and LVDT (accurate to 0.01 mm) were connected to a data acquisition system set at 10 scans per second. Additional spacers were provided under each component whenever necessary to provide the correct elevation with the bar to eliminate any eccentric loading.

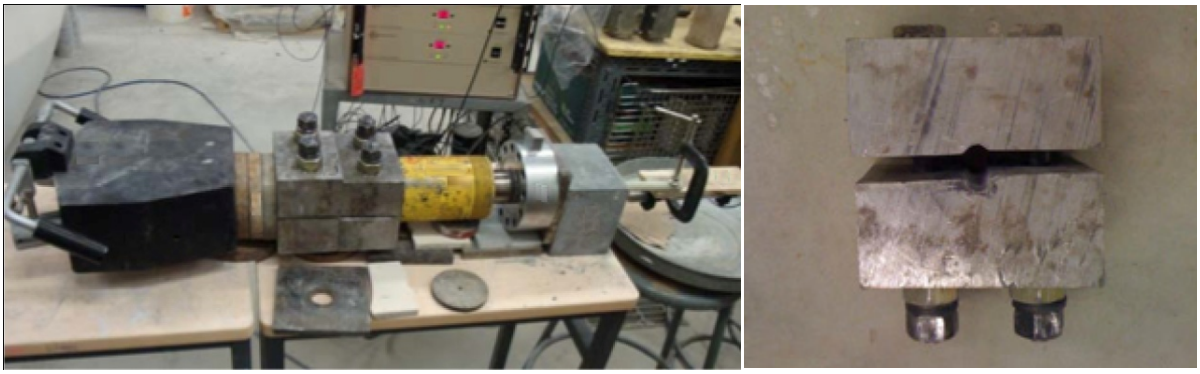

Figure 3.25: Pullout test setup (left) and steel grips (right)

Chapter 4 Experimental Results and Discussion

4.1 Introduction

The following sections will present the results obtained from experimental testing as they pertain to the research objectives and main parameters. To establish an understanding of the behaviour of sand coated GFRP tensile lap spliced beams in UHPC the results will first be analyzed based on the ultimate capacity and bond behaviour of each slab/beam. This will provide information on the effect of various splice lengths and concrete types on the bond strength of splices. Results for bar force will be further verified and compared with the strain readings obtained at mid-splice. The strain readings will provide some additional insight on the effects of each parameter. Following this comparison the load deflection behaviour of each slab/beam will be presented for the various concrete types to see any differences in stiffness and ductility for the spliced slab/beams. Results from fatigue testing are also evaluated based on the damage caused to various aspects of the performance. Additional sections will also present the crack propagation, failure modes, and environmental durability.

4.2 Ultimate Capacity and Bond Strength

In order to determine the bond strength obtained from each splice, beam design theory and concrete material models were first used to determine the maximum bar force. Two methods were devised based on the specimen type. Both methods incorporated strain compatibility however the main difference was the linear material model used for UHPC (full cast) slab/beams versus the non-linear concrete model used for precast slab/beams. The analysis carried out in this chapter negates the use of material resistance factors so the actual bar force could be calculated directly. The slab/beams also failed mainly due to pullout and not by concrete compression or GFRP bar rupture so the use of these factors would not be appropriate. All full cast slab/beams failed in the tension region with some specimens experiencing some simultaneous crushing of concrete. Due to the nature of the failure and the non-yielding behaviour of GFRP, traditional concrete beam design using code determined stress block factors cannot be used. Tensile failure of GFRP reinforced concrete beams does not always allow the extreme compression fibres of concrete to reach the maximum strain so typical concrete design stress block factors may provide inaccurate results (ISIS 2007).

Furthermore common concrete design codes have no design equations for UHPC. In order to circumvent these issues a simplified analysis method was devised using the strain compatibility of beam theory and the linear elastic stress-strain behaviour of both UHPC and GFRP rebar. A linear strain distribution is assumed to exist across a transverse section of a beam under bending. Since UHPC exhibits linear stress-strain behaviour the compression region will also have a linear stress distribution as shown in Figure 4.1.

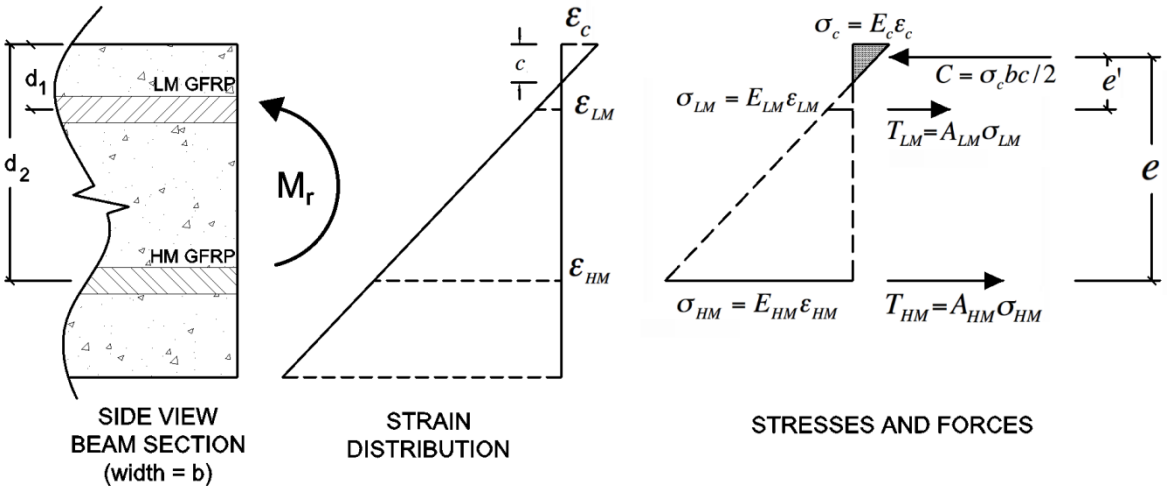

Figure 4.1: Stress and strain distribution across beam section (Brzev and Pao 2006)

During this analysis it was found that, at failure, the steel fibre reinforcement in UHPC contributed negligible amounts to the tension region due to the excessive crack widths associated with GFRP reinforcement (Mak et al. 2011). Initially, it was thought that the tensile contribution of the concrete could be estimated using the modulus of rupture along with a stress-crack opening displacement relationship for the response up to and beyond cracking. However, calculations that included some form of residual tensile strength from concrete after cracking severely underestimated the bar forces at the critical section which did not correlate well with strain gauge data. Furthermore, upon examination of the crack at the critical section, it was noted that for the majority of the tensile region of the slab/beam the fibres were pulled out almost entirely. There was also no appearance of multi-microcracking usually associated with strain hardening fibre reinforced concrete in tension (Kanda et. al 2000; Wille et. al 2010). This indicates that a stress discontinuity exists across the tension portion of the concrete cross-section. For the small portion higher up in the slab/beam cross

section where crack widths were not so intense it could be said that once the maximum bond force was reached within a fibre and slip had initiated, very little force would be transmitted between cracks. Each fibre would already be in its descending branch of load slip behaviour. Thus the tensile force of concrete was neglected when conducting ultimate strength calculations. The assumption was also made that no slip had occurred between the bars and concrete such that the strain in concrete was equal to the strain in the bar at that location (Collins and Mitchell 1997). Preliminary calculations also showed that the top LM reinforcing bars were actually in tension during the latter portion of loading due to excessive strain in the main tension bars (Mak et al. 2011). Their contribution to the moment capacity will be included in the calculations. Using this model and Figure 4.1, force equilibrium across the section can be used to solve for the neutral axis depth. The quadratic in equation 4.1 was derived using this approach for sets of two reinforcing bars.

$$c^2 b E_c - 4E_{LM} A_b (d_1 - c) - 4E_{HM} A_b (d_2 - c) = 0 \quad \text{.....(4.1)}$$

where c is the neutral axis depth, b is the section width, E_c; E_{LM}; E_{HM} are the moduli of elasticity for concrete; LM GFRP; and HM GFRP respectively, A_b is the area of one reinforcing bar, and d_1 and d_2 are the depths of LM GFRP and HM GFRP respectively. Since the concrete stress distribution is triangular, equation 4.2 can then be used to find the concrete strain (ε_c) at the extreme compression fibre corresponding to the maximum resisting moment (M_r).

$$\varepsilon_c = \frac{M_r}{2A_b\left(E_{LM} e' \frac{d_1 - c}{c} + E_{HM} e \frac{d_2 - c}{c}\right)} \quad \text{.....(4.2)}$$

where d_1 and d_2 are the depths to the top and bottom longitudinal reinforcing bars respectively and the eccentricities e' and e of each bar to the centroid of compression are found from equations 4.3 a and b respectively.

$$e' = d_1 - \frac{c}{3} \quad (4.3a)$$

$$e = d_2 - \frac{c}{3} \quad (4.3b)$$

The bar strains can then be calculated from equation 4.4a and 4.4b for LM and HM bars respectively which in turn are converted to stresses using the modulus of elasticity for each bar.

$$\varepsilon_{LM} = \varepsilon_c \left(\frac{d_1 - c}{c} \right) \quad (4.4a)$$

$$\varepsilon_{HM} = \varepsilon_c \left(\frac{d_2 - c}{c} \right) \quad (4.4b)$$

Precast slab/beams failed in shear near the support so the full bond strength in the splice was not achieved. Since these slab/beams utilized concretes with strengths ranging from 60-70 MPa in the precast regions, the attained bar force at failure can be calculated by the method proposed by the *ISIS Design Manual No. 3: Reinforcing Concrete Structures with Fibre Reinforced Polymers* (2007). This method utilizes traditional concrete compression models but incorporates sub-ultimate concrete strains during a tension zone failure. Rectangular stress blocks can be used to represent the concrete stress distribution for varying strains below peak strain using generalized stress strain curves for normal to high strength concrete. The following general relationship for the compressive behaviour of concrete was proposed in Collins and Mitchell (1997):

$$\frac{f_c}{f'_c} = \frac{n_f (\varepsilon / \varepsilon_p)}{n_f - 1 + (\varepsilon / \varepsilon_p)^{n_f k}} \quad (4.5)$$

where ε is the concrete strain, ε_p is the concrete strain corresponding to peak compressive stress, f_c is the concrete stress corresponding to strain ε, f'_c is the peak compressive stress obtained from cylinder tests, n_f is a curve fitting factor, and k is a factor to increase the post

peak decay in stress (equal to 1.0 for $\varepsilon < \varepsilon_p$ and a value greater than 1.0 for $\varepsilon > \varepsilon_p$). In lieu of comprehensive material testing additional equations have been derived to solve for ε_p, n_f, and k when just the compressive strength of the concrete is known. The following relationships were also presented in Collins and Mitchell (1997):

$$n_f = 0.8 + \frac{f'c}{17} \quad (4.6)$$

$$\varepsilon_p = \frac{f'c}{E_c}\frac{n_f}{n_f - 1} \quad (4.7)$$

$$E_c = 3320\sqrt{f'c} + 6900 \quad (4.8)$$

$$k = 0.67 + \frac{f'c}{62} \ (\text{for}\ \varepsilon > \varepsilon_p) \quad (4.9)$$

where $f'c$ and E_c are given in MPa. Equation 4.5 was broken down into a piecewise function for numerical analysis since the post peak behaviour changes relative to the concrete strength by the decay factor k. Higher concrete strengths tend to have a more brittle post peak behaviour. Equation 4.5 can be used to find the centroid of a given concrete compressive stress distribution relative to the maximum strain which can then be translated into a factor β representing the depth of the effective rectangular stress block. The same approach is also used to find the factor α that relates the average stress across the stress block to the ultimate concrete compressive stress. By these definitions equations 4.10 and 4.11 can be used to obtain distributions for α and β at various strain values for a variety of concrete strengths.

$$\beta = 2\left[1 - \frac{1}{\varepsilon_c}\left(\frac{\int_0^{\varepsilon_c} \frac{n_f(\varepsilon^2/\varepsilon_p)}{n_f - 1 + (\varepsilon/\varepsilon_p)^{n_f k}} d\varepsilon}{\int_0^{\varepsilon_c} \frac{n_f(\varepsilon/\varepsilon_p)}{n_f - 1 + (\varepsilon/\varepsilon_p)^{n_f k}} d\varepsilon}\right)\right] \quad (4.10)$$

$$\alpha = \frac{1}{\varepsilon_c \beta}\left[\int_0^{\varepsilon_c} \frac{n_f(\varepsilon/\varepsilon_p)}{n_f - 1 + (\varepsilon/\varepsilon_p)^{n_f k}} d\varepsilon\right] \quad (4.11)$$

Figures 4.2 and 4.3 show various distributions of α and β for concrete strengths ranging from 60 – 100MPa.

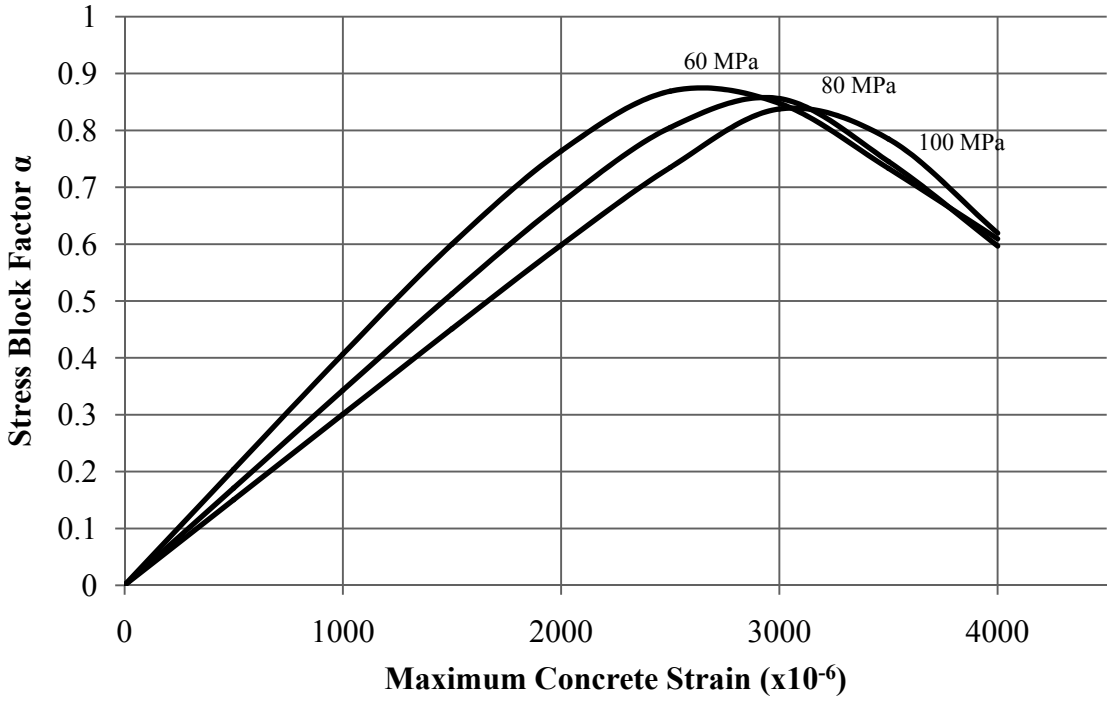

Figure 4.2: Stress block factor α (Equation 4.11)

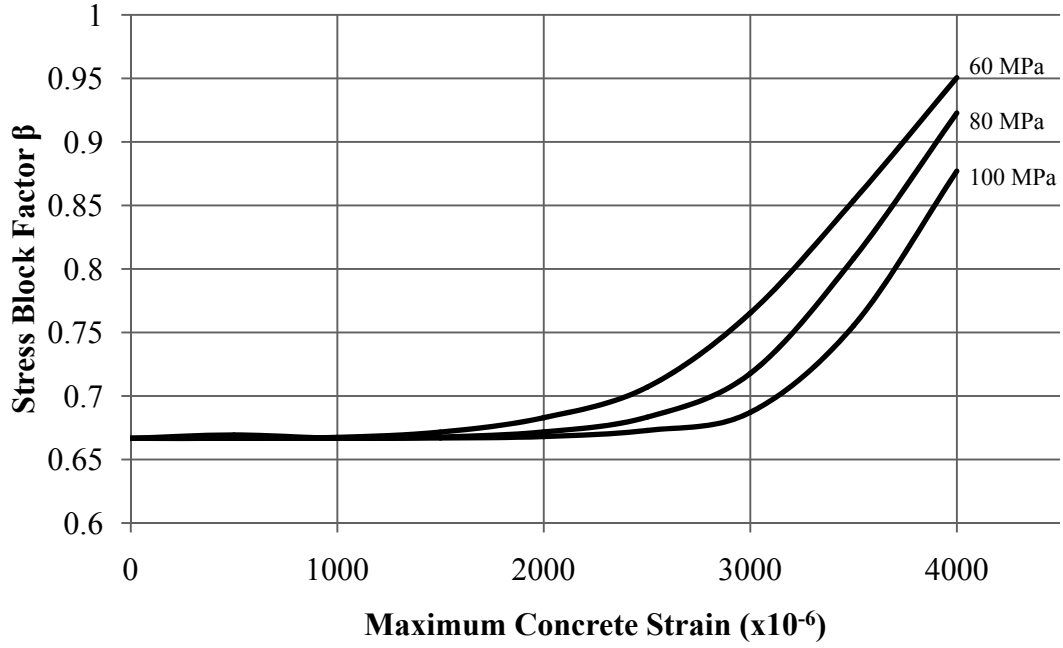

Figure 4.3: Rectangular stress block factor β (Equation 4.10)

An iterative procedure was then implemented to determine the bar force by varying the neutral axis depth and concrete strain until the resisting moment was equal to the applied moment in the pure bending region for precast slab/beams. Force equilibrium was also necessary. This concept is illustrated in Figure 4.4 for an arbitrary beam cross-section.

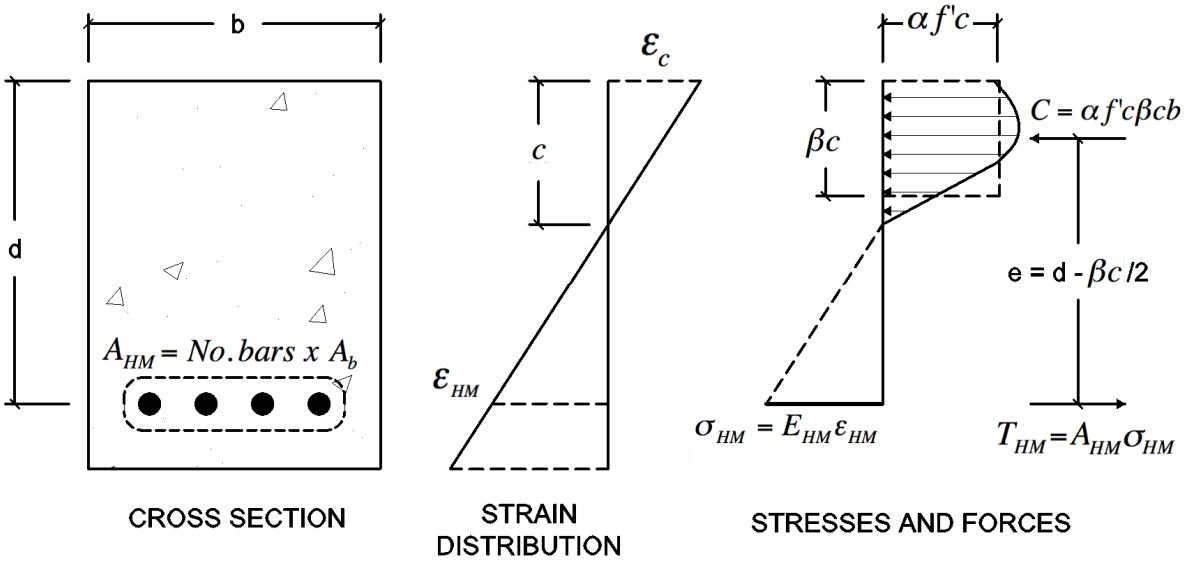

Figure 4.4: Non-linear concrete stress distribution for beam theory (Brzev and Pao 2006)

When using the linear concrete compression analysis method for UHPC, both R225 and R300 showed concrete stresses near or exceeding the peak stress in the compression region given by the modulus of elasticity from equation 3.1. This implies that some strain hardening of the concrete in the extreme compression region may have occurred which may also explain the slight crushing of concrete at the top surface of the critical section at failure. The more comprehensive stress block factors were used to further verify the values calculated from the linear concrete approach for these two slab/beams. Use of the generalized concrete stress-strain response would also incorporate some strain hardening and non-linearity near the peak strain. The results obtained from both methods were almost identical in terms of neutral axis depth and calculated bar force as shown in Table 4.1 even though the formulation used for modulus of elasticity was slightly different. This verifies that the use of a purely linear elastic distribution for concrete strengths above 100 MPa

would provide suitably accurate results. Once the bar forces were known the following equation was used to calculate the average bond stress:

$$\tau_{avg} = \frac{\sigma_b A_b}{\pi d_b l} \quad \text{.....(4.12)}$$

where τ_{avg} is the average bond stress over the embedment length, σ_b is the stress in the reinforcing bar at the loaded end of the splice, A_b is the bar area, d_b is the bar diameter, and l is the splice length. The calculated bar forces, bond stresses, concrete strains, and neutral axis depths for each slab/beam are also shown in Table 4.1.

The range of splice lengths were between 10 - 20 d_b and provided a maximum bar stress within the range of 57.3% – 71.7% of the design tensile strength of the HM GFRP bar. As most research has shown, an increase in embedment length will decrease the average bond strength due to an uneven bond stress distribution with higher stresses occurring near the loaded end. This was true among the set of results for average bond stress as shown in Table 4.1 with a 40%-50% decrease overall when splice lengths doubled. Even though type D slab/beams generally had the higher compressive strength, the decrease was more noticeable in type D slab/beams with a 49.8% reduction versus type R with a 43.4% reduction of the average bond strength corresponding to an increase in splice length from a 150 mm to 300 mm. Moreover, this discrepancy is further demonstrated among the calculated bar forces with type D slab/beams showing a negligible increase of 5.3% after doubling the bond length versus a moderate increase of 19.0% with type R slab/beams.

Overall, type R slab/beams with a weaker concrete performed better in terms of ultimate capacity and bond strength versus their type D equivalents. Although this trend may appear as a result of variance among slab/beams with arguably small differences, a more centered comparison across concrete types between the 225 and 300 mm spliced slab/beams shows better performance with a significantly weaker concrete. This trend is believed to be associated more with the flexural tensile strength of the concretes than with the compressive strength. The lower modulus of rupture for type R concrete actually helped contribute to the bond capacity versus type D slab/beams with a higher modulus of rupture and more brittle bond behaviour. GFRP bars develop significant strain when bar forces are high due to a

much lower stiffness versus traditional steel reinforcements. In order for these bars to maintain a good bond this strain must be accommodated or slip is likely to occur with delamination of the sand coated resin layer. For the case of type R slab/beams this strain was incorporated through transverse cracking that occurred within the splice due to the weaker flexural tensile capacity of the concrete. The results of preliminary material testing showed that the average modulus of rupture of type D concrete was 93.3% higher than type R. The theoretical concrete tensile stress developed within the spliced regions of D slab/beams was thus much lower than the modulus of rupture. So while transverse cracking was prevented, slip and bond loss was permitted resulting in a reduced ultimate capacity. This phenomenon mainly comes into effect when sufficient cover is provided such that splitting failure is prevented and any additional concrete tensile strength would contribute negligible benefits towards splitting.

The brittleness and inability for type D slab/beams to accommodate large bar strains while still maintaining bond is the primary reason for the lack of strength development after 150 mm. So much of the bond stress is concentrated within the initial 150 mm of the embedment near the loaded end while very little contribution is made to the development of bar force after 150 mm because bond stresses are smaller there. Thus through the entire range of splice lengths, type D slab/beams showed very similar ultimate capacities because only about 150 mm of the splice was being used effectively at any given time.

A comparison was also made between the calculated maximum concrete strain (ε_c) in the slab/beam versus the theoretical peak strain (ε_p) for each concrete. With the exception of R225 and R300 all slab/beams remained well below the peak concrete strain and would not have been accurately analyzed if code values for rectangular stress block factors for maximum concrete strain at -0.0035 were used. However, use of the linear concrete method showed that R225 and R300 had exceeded the theoretical peak (given by the ratio $f'c/E_c$) and was in the descending portion of the load strain behaviour. A more comprehensive analysis using the generalized concrete stress strain curve provided by equation 4.5 allowed some strain hardening just prior to the peak stress. Maximum concrete strains were found to be lower than the peak strains using the more accurate method as seen in Table 4.1. Both methods however gave almost identical results and since the rest of the full cast slab/beams stayed well below the peak strain a linear approach was satisfactory.

Table 4.1: Results and analysis for slab/beam tests

	Specimen	l_d (mm)	P (kN)	M_r (kNm)	$f'c$ (MPa)	ε_p x 10^{-6}	E_c (MPa)	ε_c x 10^{-6}	ε_{HM} x 10^{-6}	σ_{HM} (MPa)	c (mm)	F_{HM} (kN)	τ_{avg} (MPa)	Failure Mode
Linear Concrete Method	D150A	150	131.3	39.4	148.5	-3173	46793	-2168	11252	721	22.9	143.2	19.1	Pullout
	D150B	150	138.3	41.5	169.5	-3391	49998	-2202	11821	758	22.3	150.5	20.1	Pullout
	D225	225	140.6	42.2	140.0	-3081	45435	-2361	12066	773	23.2	153.6	13.7	Pullout
	D300	300	138.1	41.4	140.0	-3081	45435	-2319	11850	760	23.2	150.8	10.1	Pullout
	R150A	150	137.0	41.1	153.4	-3225	47559	-2242	11733	752	22.8	149.3	19.9	Pullout
	R150B	150	145.9	43.8	150.0	-3189	47024	-2403	12500	801	22.9	159.1	21.2	Pullout
	R225	225	147.5	44.2	100.9	-2616	38572	-2712	12735	816	24.9	162.1	14.4	Pullout
	R300	300	163.4	49.0	108.3	-2711	39969	-2946	14091	903	24.6	179.3	12.0	Pullout
Rectangular Stress Block Factor Method	R225	225	147.5	44.2	100.9	-2944	40249	-2680	12727	816	24.7	162.0	14.4	Pullout
	R300	300	163.4	49.0	108.3	-3036	41450	-2930	14052	901	24.5	178.8	11.9	Pullout
	P150A	150	70.0	21.0	61.3	-2411	32894	-1420	6104	391	26.8	77.7	10.4†	Shear
	P150B	150	89.3	26.8	69.5	-2527	34578	-1760	7743	496	26.3	98.5	13.1†	Shear

* Values for linear concrete method are calculated using equations 4.1- 4.4.

* Values for rectangular stress block factor method are calculated using equations 4.5- 4.11.

* Resisting moment was calculated from $M_r = 0.6P/2$ using the shear span and applied load.

* Calculations for R225 and R300 using the simplified linear concrete method provides a maximum 0.28% and 0.81% difference for bar force and neutral axis depth versus the rectangular stress block factor method.

† Bond strength of precast beams was determined using the applied moment at shear failure and does not imply bond failure.

The calculated neutral axis depths were very shallow staying within the top 25% of the slab/beam for all full cast slab/beams and just slightly below for precast slab/beams. These small values can be attributed to the low tensile stiffness of HM GFRP which require large bar strains to develop at high loads. The concrete strength and modulus of elasticity showed no significant difference to the neutral axis depth although a slight increase is noted for weaker concretes.

Precast specimens failed in shear at about 52.9% and 67.1% of the maximum bond strength exhibited by an average 150 mm splice with type D slab/beams. This comparison is made only with D slab/beams since the joint infill concrete is of the same type. Overall the bond performance within a short splice length of only 150 mm has allowed the development of enough bar stress to exceed the ultimate tensile stress of a conventional steel rebar (400 MPa).

4.3 Bar Strain Behaviour Under Static Loading

Strain gauges were placed on two opposing tensile GFRP bars for each slab/beam at mid-splice. There are several important points to note prior to the discussion of these results. The deflection behaviour showed clear similarities with the strain distributions and will be discussed in more detail in the next section. R300 experienced technical difficulties during the test and had to be reloaded after nearly reaching the ultimate capacity. The residual effects of fatigue loading are also present in the results of D150B, R150B and P150B with the strain and deflection curves beginning larger than zero strain at no applied load. Overall, both strain gauges in each slab/beam showed very similar values throughout the majority of loading until the maximum load was reached indicating a good transfer of force across the splice.

The strain behaviour of full cast slab/beams can be characterized with a tri-linear distribution as shown in Figure 4.5, but with some variations due to concrete type and splice length. The first branch demonstrates a relatively higher stiffness in strain and deflection due to the contribution of concrete in the tension region. The start of the second branch coincides with cracking of the concrete in the tension region while the beginning of the third branch typically coincides with strain separation of the two opposing bars, a significant reduction in load-strain slope, and the maximum load. The third branch is very ductile sustaining large

strain and deflection without a significant loss of load capacity. The end of the third branch is the critical point when complete failure occurs and the beam experiences a large jump in deflection with significant bar slip within the splice (Mak et al. 2011).

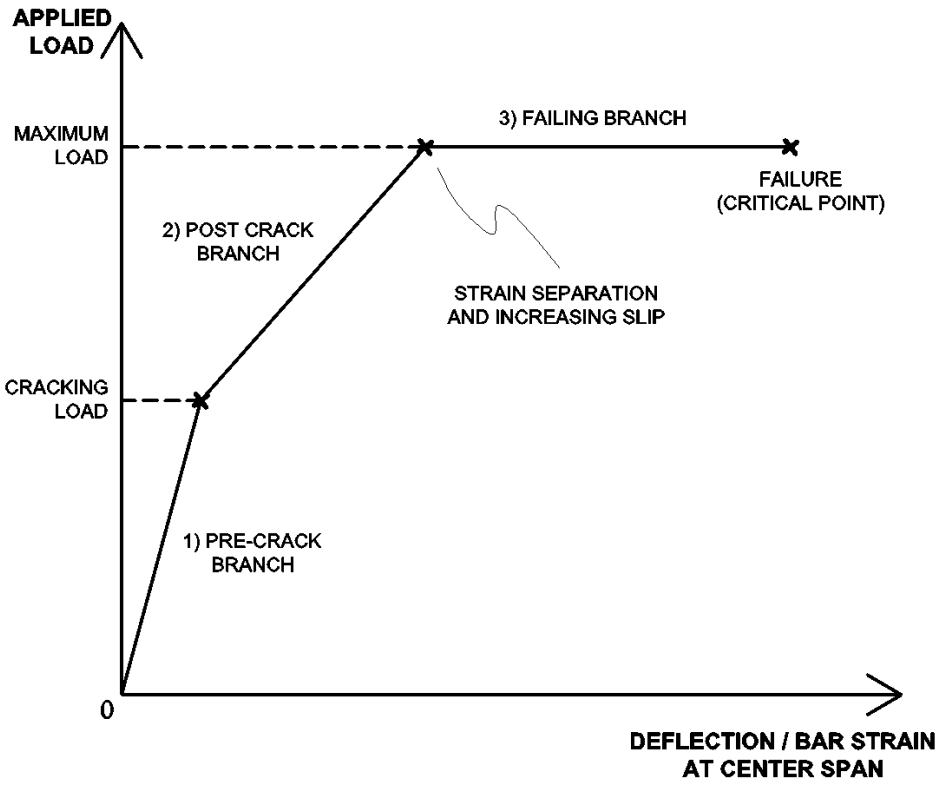

Figure 4.5: Tri-linear load strain/deflection distribution

The load strain curve for each full cast specimen is shown in Figures 4.6 - 4.13 while the curves for precast specimens are shown in Figures 4.14 -4.15. The fatigue specimens are shown in Figures 4.7, 4.11, and 4,14 for D150B, R150B, and P150B, respectively. The relationship between the experimental strain behaviour at mid-splice and the generalized curve are discussed throughout for each specimen.

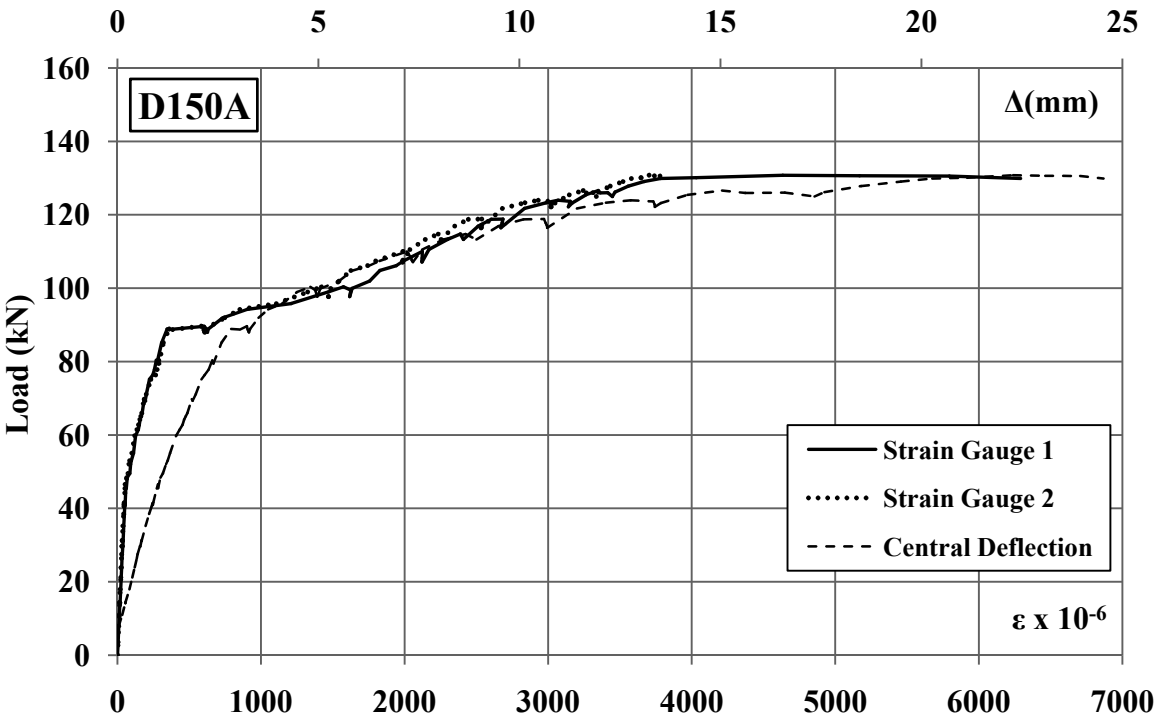

Figure 4.6: D150A load-strain and deflection curves

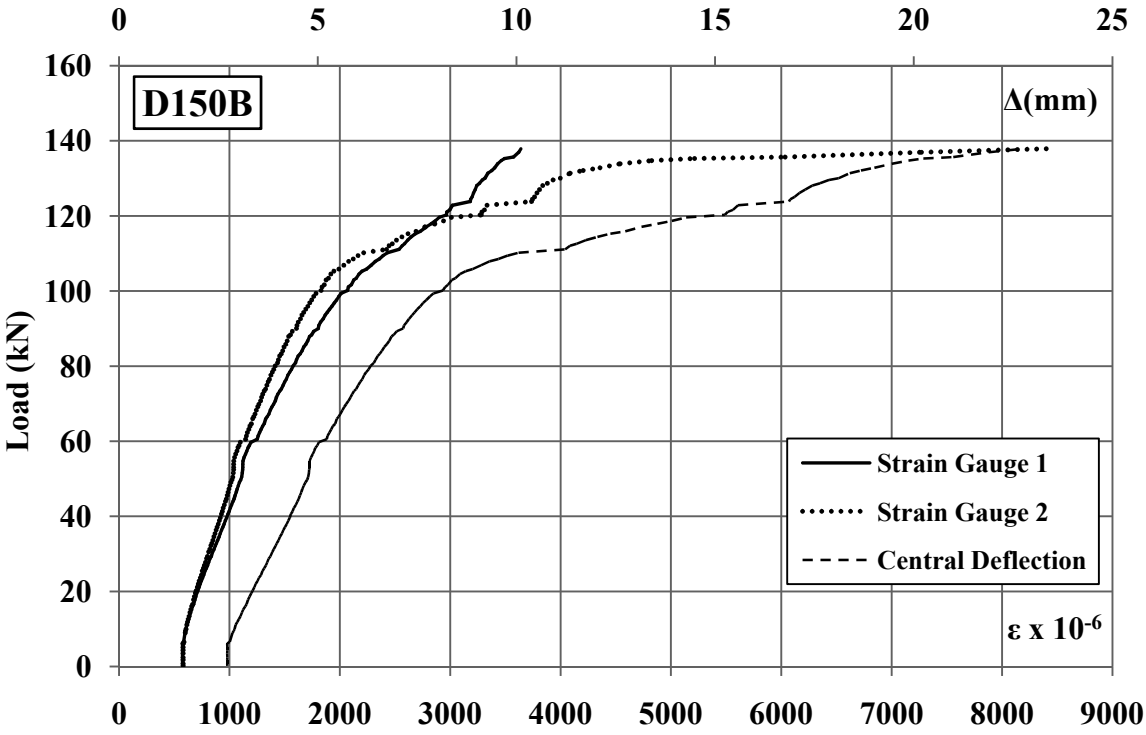

Figure 4.7: D150B load-strain and deflection curves after fatigue loading

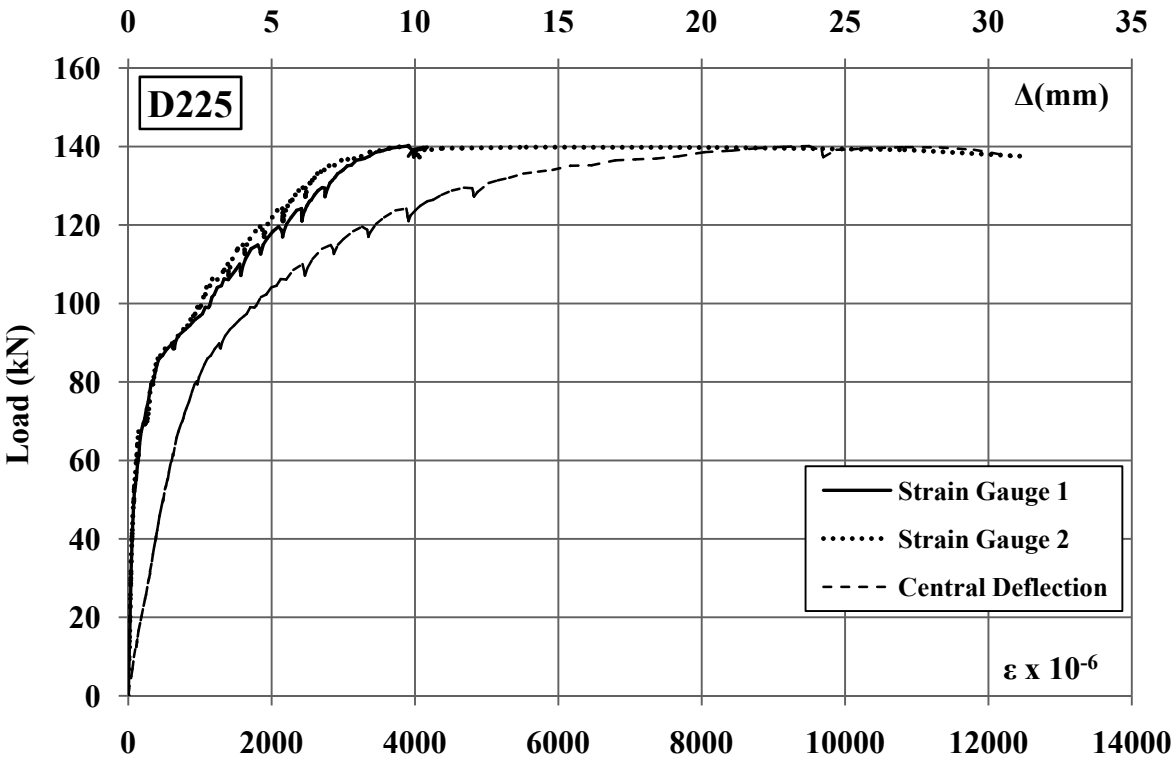

Figure 4.8: D225 load-strain and deflection curves

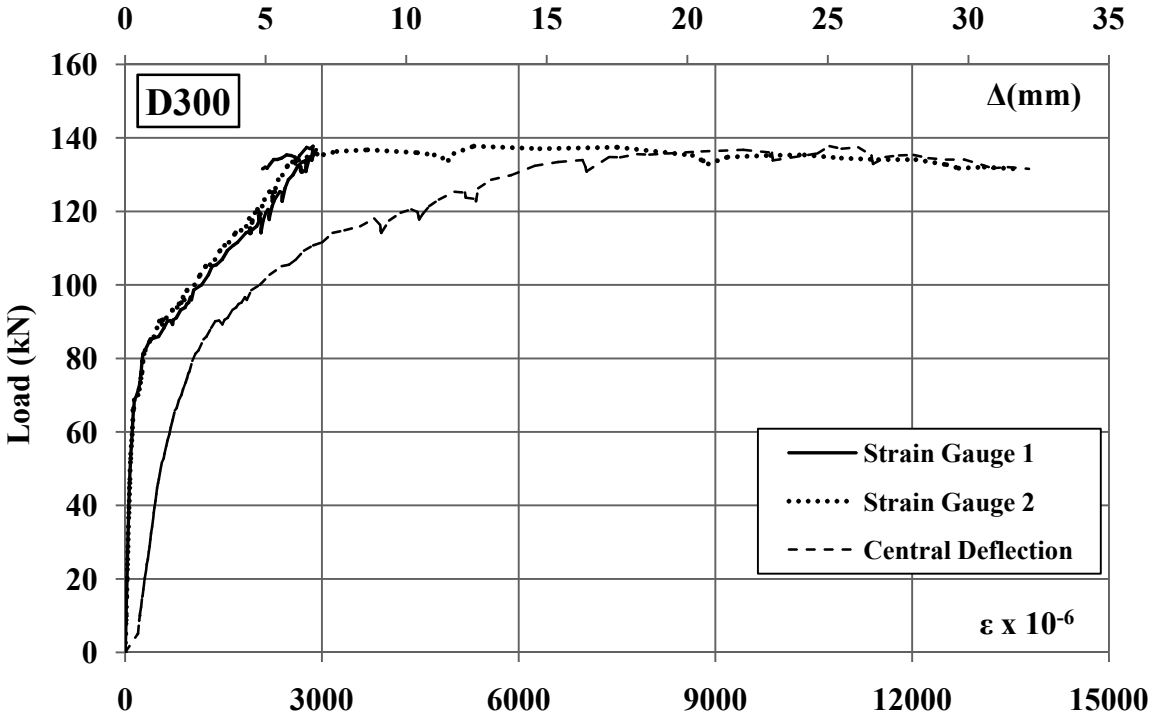

Figure 4.9: D300 load-strain and deflection curves

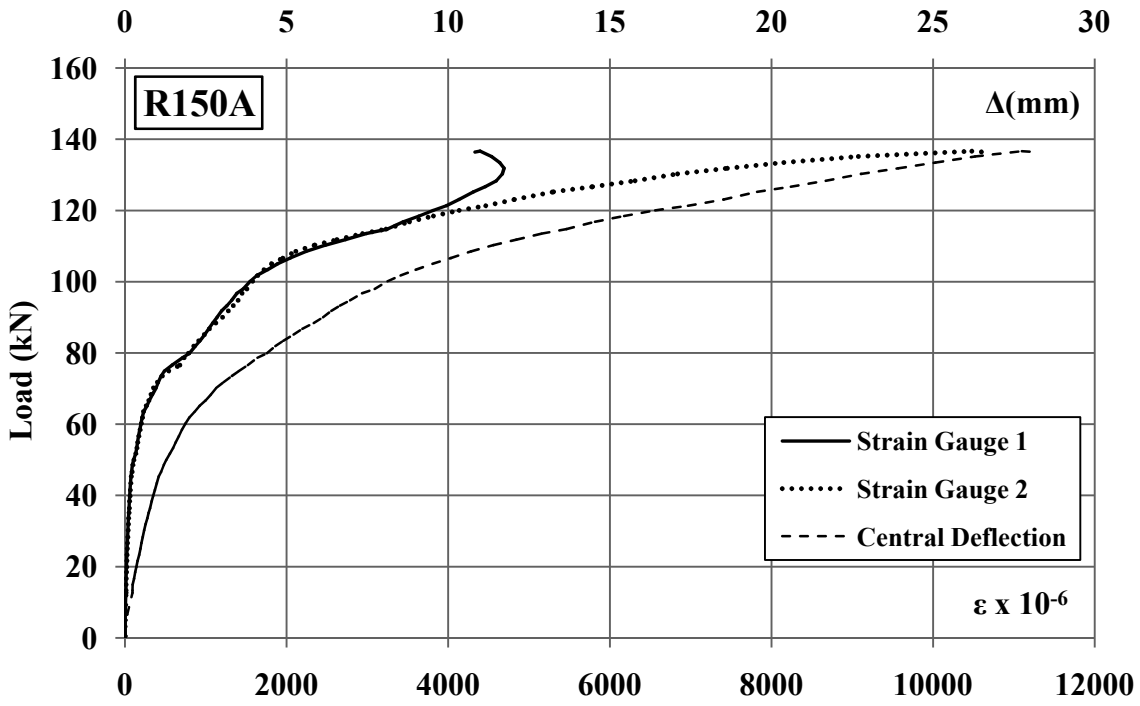

Figure 4.10: R150A load-strain and deflection curves

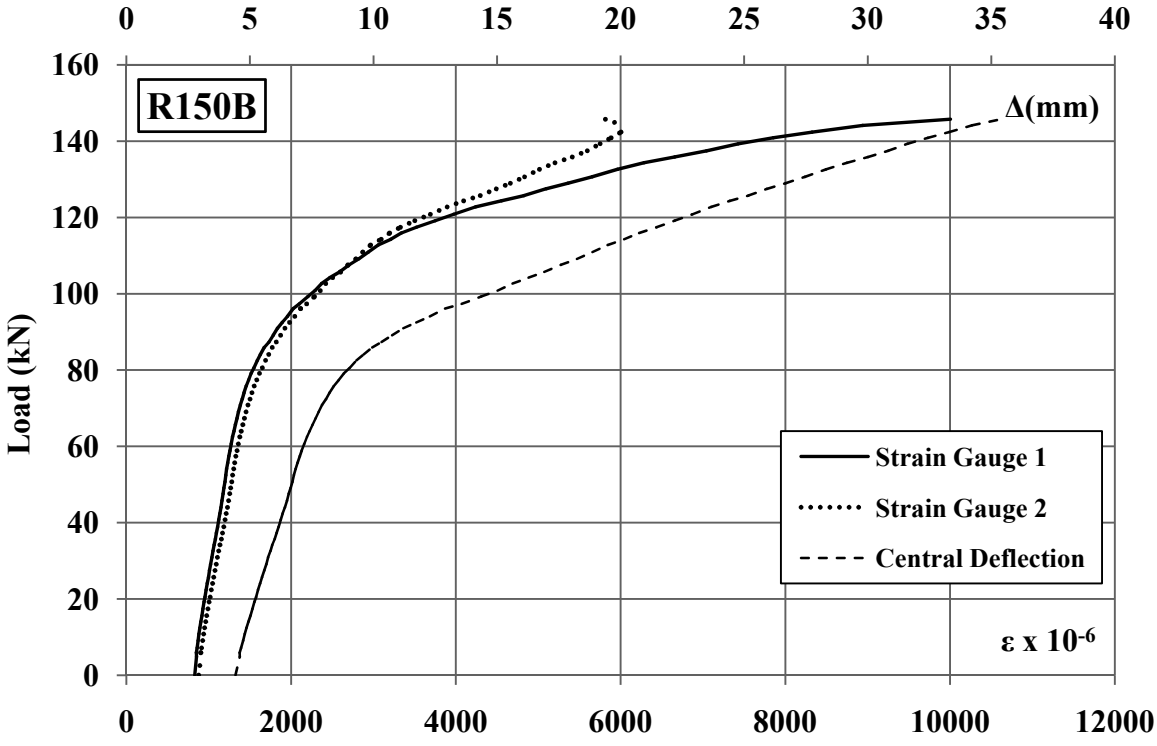

Figure 4.11: R150B load-strain and deflection curves after fatigue loading

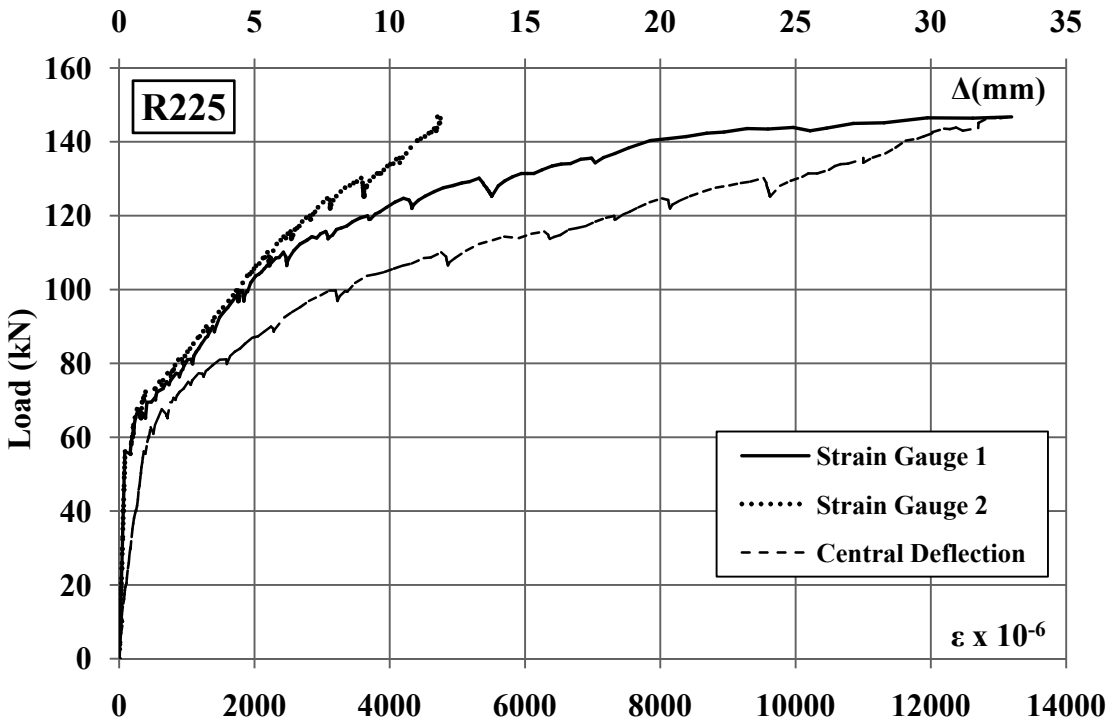

Figure 4.12: R225 load-strain and deflection curves

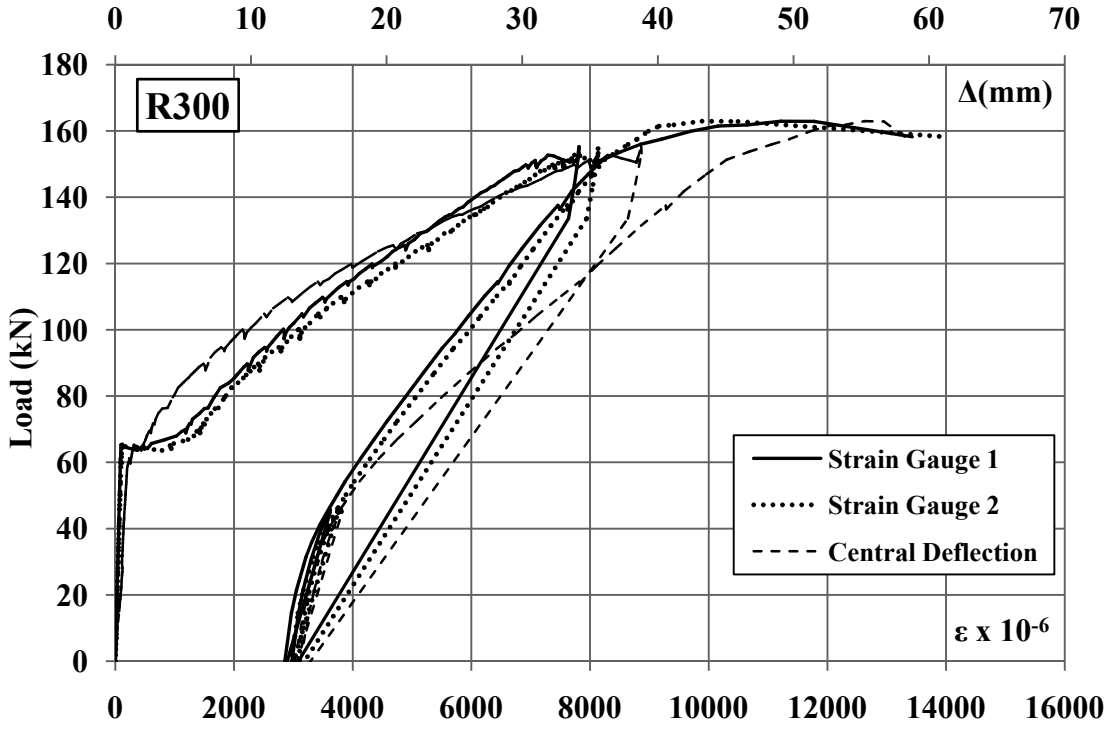

Figure 4.13: R300 load-strain and deflection curves

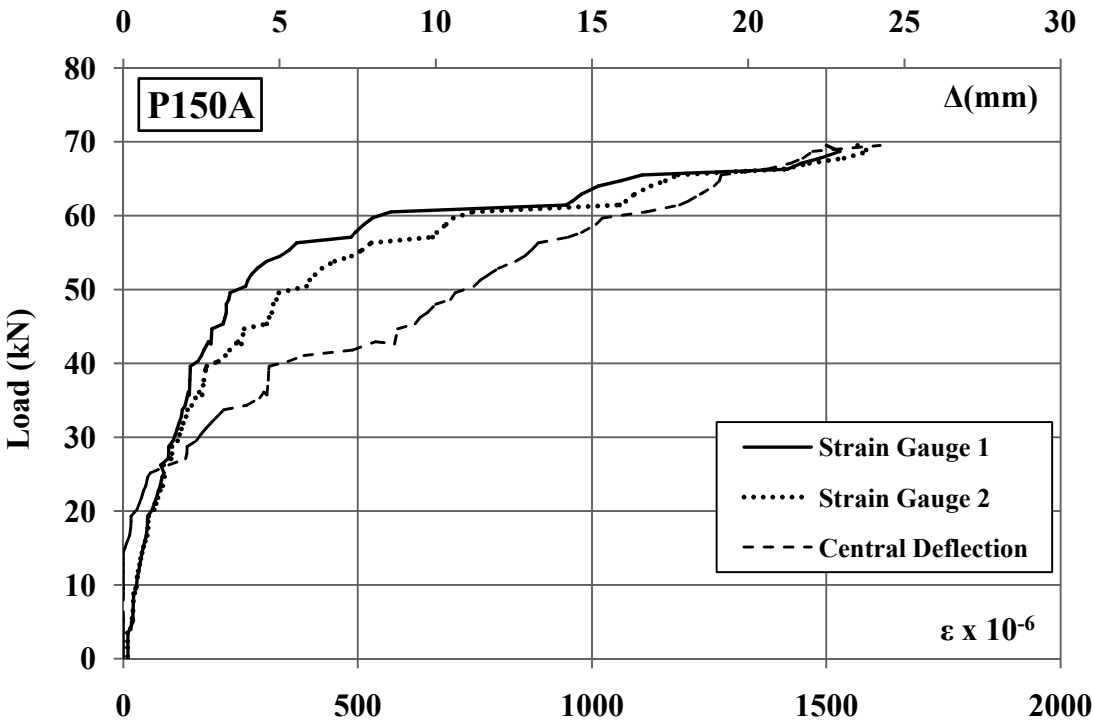

Figure 4.14: P150A load-strain and deflection curves

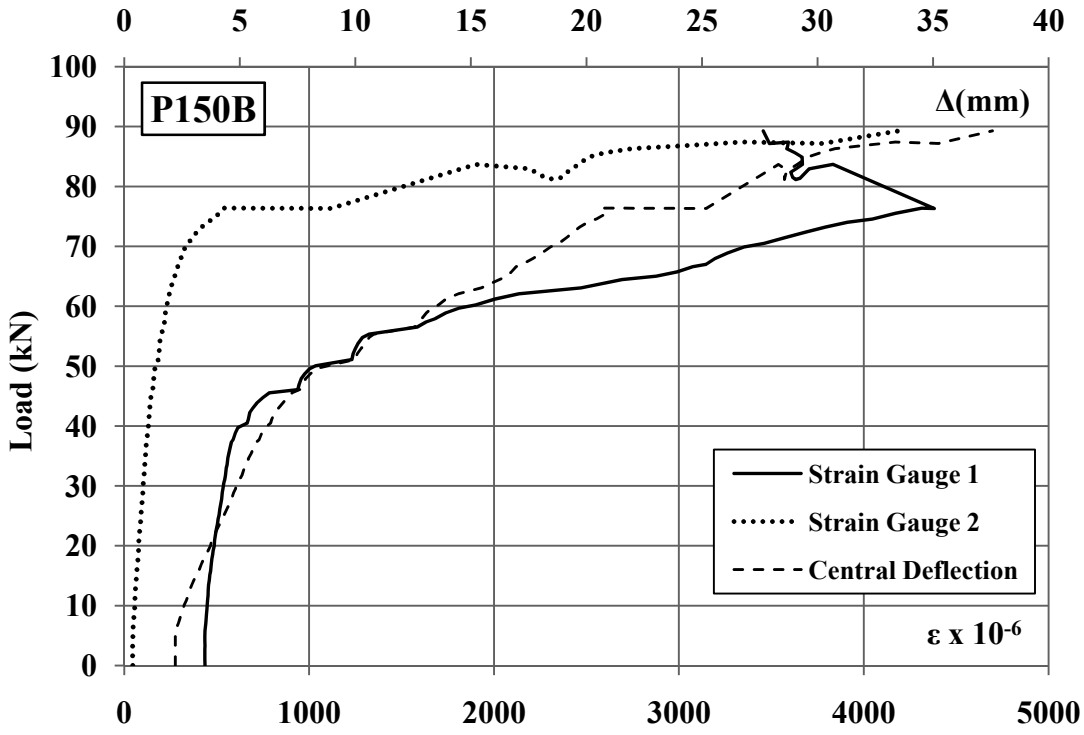

Figure 4.15: P150B load-strain and deflection curves after fatigue loading

With the exception of the fatigue slab/beam specimens (Figs. 4.7 and 4.11), they each begin with an initial stiff portion prior to cracking where very little load was taken by the reinforcing bars (Figs. 4.6, 4.8-4.10, 4.12-4.13). This branch of the curve had a very steep slope until the cracking load was attained (Mak et al. 2011). The cracking load was higher for type D slab/beams at approximately 90 kN (Figs. 4.6, 4.8, 4.9), versus type R slab/beams at about 65 kN (Figs. 4.10, 4.12, 4.13). When using the gross second moment of area for the slab/beam cross-section these values correspond to a cracking tensile stress of 15.0 and 11.7 MPa for type D and R concretes respectively. These values were slightly lower than expected for type D concretes but was typical for type R concrete based on flexural test results (Fig. 3.8). Similar cracking loads were applied to the fatigue tests prior to cyclic loading.

The second branch changes with a significant reduction in the slope sometimes with a sudden jump in bar strain just after cracking (Figs. 4.6, 4.13). This part of the curves shows a steady increase in the strain with load until the maximum load is reached (Mak et al. 2011). The second branch is not always entirely linear sometimes showing some form of curvature (Figs. 4.10-4.13) which can be explained by the presence of steel fibres still having some effect. Typically the bar strain behaviour after cracking would be followed with a large enough jump in the strain from a tensile force transfer such that with the new slope of this second branch the vertical intercept would return to zero load or somewhere below due to some residual stress after cracking (Tighiouart et al. 1999). However, because the strain gauges were located at mid-splice the readings did not adhere to that expectation. The strain only begins to increase substantially after a certain load has been reached after cracking. The vertical intercept of the second branch does not cross at zero or below but actually at some point above it (Figs. 4.6-4.13). This is largely because of the uneven distribution of bond stress in the splice. Since there is a concentration of bond stress at the loaded end the bar stress diminishes fairly quickly such that the strain at mid-splice does not experience any noticeable change until a certain load is reached even when cracking has occurred at the end of the splice. Increasing the load within this range adds to the residual strain and contributes to the plastic damage from cracking as shown from the load strain curves of the fatigue specimens and the reloading of R300 (Figs. 4.7, 4.11, 4.13). Any consecutive loadings within this range below the maximum from the load history should still behave elastically

returning to the same residual deflection when the load is removed. In this load range the bar should still maintain a good bond with the concrete, with minimal slip while the strain only increases when enough bar force is developed. If the strain gauge were located elsewhere for example at a crack location just outside the splice, the second branch would begin with a larger jump in strain such that the intercept of the tangent would be closer to zero. The second branch usually continued with approximately the same slope until the maximum load was reached and the third branch began (Figs. 4.6-4.13).

The third branch normally occurs after the maximum load was attained and no more additional load could be applied. This behavior is more evident in type D slab/beams (Figs. 4.6-4.9). For the majority of the full cast slab/beams, with the exception of R300, the maximum load also corresponded to the initiation of strain separation between the two gauges (Figs. 4.6-4.12). Thus one strain gauge would remain at approximately the same value obtained at maximum load while the opposing bar strain would continue to increase even with no additional load applied. The slope of this portion was very close to zero but for only one bar. This portion of the curve can be explained by localized bond loss at the loaded end of the splice and the progression towards critical failure. When the maximum bond stress is reached at the loaded end of the splice localized bond failure will occur. The lack of strain accommodation at high bar stresses, bond stress concentration at the loaded end, and failure of the sand coating around the bar are the mechanisms that allow this to happen. When there is a localized loss of bond the full force of the bar is transferred further into the splice to where bond still exists (Mak et al. 2011). This explains the significant increase in strain for one of the bars even when no additional load could be applied (Figs. 4.6-4.12). This bar was gradually getting pulled out. Pullout tests conducted by Chaallal and Benmokrane (1996) showed similar behaviour with bond stresses migrating more towards the free end of the embedment length as loads increased. As a result the deflection within this branch of the curve also increased in the same manner (Figs. 4.6-4.13). This continued until the critical point where the remaining bonded portion was no longer able to withstand the bar force and the slab/beam failed (Mak et al. 2011).

Although for each slab/beam this tri-linear behaviour was the general case, the different concrete types, R and D, showed slight variations due to the strengths of each concrete. Due to the weaker flexural tensile strength of type R concrete, some of these

slab/beams were allowed to crack transversely within the splice as will be explained in Section 4.6. This allowed additional bar strain to develop at the gauge location. As a result the third branch was essentially a continuation of the second branch but with a gradually decreasing slope (Figs. 4.10-4.13). Even after the bar strains began to separate some additional load could be applied and the strain continued to increase but not at the same rate as with the second branch. Transverse cracking is what allowed type R slab/beams with weaker concrete to withstand more load than type D (Table 4.1). This type of cracking allows additional bond forces to develop further into the splice away from the loaded end (Mak et al. 2011). Type D slab/beams on the other hand showed a clear transition between the second and third branch because they were not able to accommodate the additional bar strain (Figs. 4.6-4.9). Instead, once localized bond failure had initiated, no more bar force could be developed and the load capacity remained the same throughout the third branch. Transverse cracking is the main reason why R300 was able to maintain similar bar strain values throughout the entire stretch of loading until failure (Fig. 4.13).

Different splice lengths also had an effect on the strain behaviour of each slab/beam. For longer splice lengths such as in D300 (Fig. 4.9) the slope of the second branch was slightly higher since the strain gauge was deeper in the splice and the effect of loading on the bar strain took longer to reach the gauge. With shorter splices the strain at mid-splice would naturally increase faster with the loading because it is closer to the loaded end and the effects of bond stress concentrations are less (Figs. 4.6-4.8). This trend is less noticeable with type R slab/beams due to transverse cracking within the splice (Figs. 4.10-4.13). Longer splice lengths also increased the length of the third branch by providing additional bond length for when localized failure progressed down the splice (Figs. 4.6, 4.13). When more embedment is provided the slab/beam experiences more ductility and the full bar force can progress further into the splice causing the strain at the center to increase more than with shorter splices.

The effects of fatigue are also present within the strain diagrams of D150B and R150B (Figs. 4.7, 4.11). Once loaded beyond the cracking point there was residual strain leftover at zero load equal approximately to the sudden increase in bar strain after cracking. Any subsequent loading not exceeding the maximum from the load history adds negligible amounts to the residual strain. The slab/beam remains elastic within this second branch with

the slope of the load strain curve equal to some value between the slope of the pre-crack loading and the slope of the second branch. If the load is increased to a new maximum then the residual strain at zero load is also increased and the reloading curve is shifted accordingly to the right. This behaviour can be seen in both full cast fatigue specimens (Figs. 4.7, 4.11) and R300 (Fig. 4.13) when compared to the non-fatigue equivalents (Figs. 4.6, 4.10). After being loaded to the cracking load all subsequent load cycles for fatigue remained below this value. When the slab/beam was finally loaded to failure the load strain curve still remained steep indicating that there was still a lag in the strain response at mid-splice and the bond at the loaded end still existed (Figs. 4.7, 4.11). The load increased with a steep slope in the curve until the maximum load from the load history and from there would continue on with the second branch (Figs. 4.7, 4.11). The load history determines the state of the bar force within the splice. If the load is increased to a new maximum then some additional cracking and steel fibre pullout will take place causing the bar force and subsequently the bar strain at mid-splice to increase due to a force transfer to the bar. Since the initial ascending branch of D150B and R150B (Figs. 4.7, 4.11) loading to failure was still steep the bond within the splice should still be intact. So while increasing the load may cause an increase in the residual strain due to cracking, as long as the maximum load history remains within the second branch then subsequent loadings should still be elastic because the bond within the embedment length still exists.

The first two branches of the tri-linear distribution (Fig. 4.5) can also be applied to the precast specimen in Figure 4.14. The first branch is the initial stiff portion prior to cracking. Cracking initiates at a much smaller load at around 35-40 kN than with the fibre reinforced concretes after which the load strain curve shifts into the second branch. Because this slab/beam failed in the shear failure mode the third branch of loading could not be reached. Sudden increases in the bar strain were observed throughout the second branch corresponding to various instances of cracking that caused increases in the bar force. Cracking at the joint interface may have also been the cause of the increased strain. Both strain gauges maintained similar values throughout the entire loading and did not deviate very far from one another. The ultimate tensile capacity of the splice is expected to be much higher than what was observed from the precast slab/beam tests.

Fatigue effects were also observed in the strain diagram for P150B (Fig. 4.15). Cyclic loading caused two types of cracking around the joint area. On one side of the slab/beam longitudinal splitting cracks began to occur along the bar in the precast concrete. There was also some debonding at the interface between the joint fill and precast material. As a result the tensile force was not distributed evenly amongst the two bars. A lack of force transfer occurred around the bar where the concrete had split longitudinally while the other bar began to take majority of the load. This is why after cyclic loading P150B showed a considerable discrepancy between the two bars in terms of strain (Fig. 4.15). The bar taking more load initially, here now referred to as bar 1 corresponding to strain gauge 1 in Figure 4.15, accumulated more residual strain at mid-splice versus the second bar from the opposing side. Furthermore, the bar with longitudinal splitting, referred to as bar 2, developed a sudden increase in strain at mid-splice only after about 80% of the ultimate capacity when large deflections (20 mm) and significant cracking had occurred. Meanwhile, bar 1 without longitudinal cracking showed increasing bar strain at about 45% of the ultimate capacity. However, when bar 2 began to take effect in resisting some tensile force, bar 1 showed a reduction of bar strain at mid-splice signified by the shift back to a lower strain after about 75 kN. Bar 2 quickly develops its bar force and strain at mid-splice and eventually both bars attain similar strain values at failure.

Figure 4.16 shows a secondary visualization of the three branch strain behaviour and localized bond failure using D300. This graph shows the bar strain values at different stages of loading marking the beginning and end of each branch of the curve. The free end bar strain is always zero by inspection and the loaded end strain was calculated using the same bar force calculation in the previous section. The strains at mid-splice were taken from the gauge readings at the same loads. From the zero load up to cracking a very small increase in bar strain is observed at mid splice meanwhile a large bar force is generated at the loaded end. As the applied load is increased the strain at mid-splice receives a more noticeable increase but still remains relatively small. After the maximum load the mid-splice strain increases dramatically until the critical point where the slab/beam fails. This graph clearly shows that a bond loss occurred between mid-splice and the loaded end during the third branch of loading because the strain values at mid-splice exceed the calculated bar strain at the loaded end.

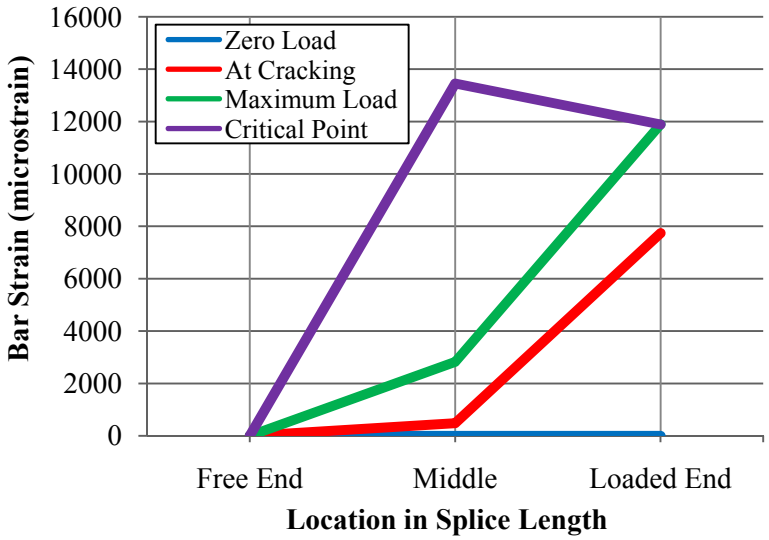

Figure 4.16: Bar strain distributions at various load points for D300

4.4 Load Deflection Behaviour

Figures 4.17-4.20 show comparisons between the load deflection curves at center span of similar slab/beams. The same tri-linear behaviour was observed for the load deflection curves of all type D slab/beams but only some from type R. An initial stiff branch exists up to the cracking load where the slope changes dramatically. Cracking loads also coincide with the change in slope observed from the load strain curves with type D slab/beams having a higher pre-crack load capacity. The pre-cracking stiffness for both R and D slab/beams are very similar (Figs. 4.17-4.19). The second branch has a reduced slope and generally continues on to the maximum load. For most slab/beams this branch is not entirely linear due to the presence of steel fibres and crack bridging. This curvature is more noticeable for type D slab/beams due to a better bond between the concrete matrix and steel fibres versus type R (Figs. 4.17-4.19). Increasing the load within this region contributes to the plastic damage and cracking of the slab/beam however the GFRP reinforcing bar still maintains a good bond with the concrete with minimal slip. The degradation in stiffness is mainly due to crack propagation. Much like the strain diagrams (Figs. 4.6-4.13) the third branch will continue beyond the maximum load with a very small slope. Large deflections are formed with little to no increase in load capacity. This portion of the curve is where the GFRP bar begins to pullout from the spliced region and the loss of stiffness is a combination of localized bond failure, rebar slip, crack propagation, and crack widening. This portion of

the curve will contribute significantly to the plastic damage of both the concrete and rebar bond. Ultimately, at the critical point when the rebar runs short on the bond length due to localized bond failure the slab/beam will fail.

As with the strain diagrams some differences are observed between type D and type R concretes (Figs. 4.17-4.19). Type R slab/beams tend to exhibit a lack of a third branch due to the consistent increase in load capacity and so the point of maximum load also corresponds to slab/beam failure. This again is a result of the added bond capacity of type R concrete from transverse cracking and strain accommodation at high bar forces. Type R slab/beams also exhibited better ductility especially with R300 having almost twice the deflection at maximum load versus D300 (Fig. 4.19). Due to the higher cracking load and stiffer load deflection response, type D slab/beams initially showed better performance in terms of energy absorption. However, if the entire loading is taken into account type R slab/beams performed better overall. Aside from increasing the load capacity of type R slab/beams, longer splice lengths also contribute to the ductility for all full cast slab/beams when comparing the load-deflection curves of 150 mm spliced slab/beams (Fig. 4.17) to those with a 300 mm splice (Fig. 4.19). This comparison between the maximum deflections at failure shows a steady increase as the splice length increases. This can be explained by the localized bond failure phenomenon. With a longer splice length, the bar is able to accommodate more slip prior to total bond failure thus contributing more to the ultimate deflection.

The effect of cyclic loading on the load deflection behaviour of full cast beams (Fig. 4.17) was also very similar to the load strain behaviour (Figs. 4.7, 4.11). After the cracking load was applied some residual deflection remained at unload corresponding to a residual strain. Pre-loading and cyclic loading reduced the steel fibre bond at the extreme tension fibres of the concrete and as a result the reloading curve became smoother. This also had the effect of transferring more load to the reinforcing bars due to a loss of stiffness across the concrete cross section. Since the bond between the reinforcement and concrete remained rigid the reloading curve, also referred to as the load to failure curve, has an ascending branch with a relatively high stiffness almost equal to the pre-crack stiffness as shown in Figure 4.17. By cracking and transferring additional load the reinforcing bar there was some residual deflection however the stiffness with respect to the new zero load deflection location is higher than the typical second branch of loading explained in Figure 4.5. As long as the

maximum load history remains within this second branch the subsequent reloading should still have a stiff elastic response because the GFRP bond within the splice remains and very little slip has occurred. While cyclic loading stayed within the second branch of the original loading curves of both D150B and R150B (Fig. 4.17), R300 (Fig. 4.19) on the other hand nearly reached the end of phase two, which had an effect on the subsequent reloading. The initial stiff portion is much shorter during the second loading due to the initiation of localized bond failure at the loaded end of the splice. Once slippage of the bar occurred the overall stiffness of the slab/beam is reduced thus the ascending branch of the second loading is cut short followed with a reduced slope that begins earlier than normal.

Due to the shear failure mode of precast slab/beams the third branch was not observed in their load deflection curves (Fig. 4.20). Precast slab/beams showed a staircase like deflection curve with sudden increases in deflection due to the appearance of more cracks without the restraint of steel fibre bridging. Two branches can be observed in the behaviour of precast slab/beams. The first branch has a higher stiffness than the rest of the curve until the onset of cracking, after which the slope decreases dramatically where the slab/beam takes on more deflection. This second branch generally continued until shear failure occurred. Similar to the strain behaviour of precast beams (Fig. 4.15), cracking leaves behind a residual deflection from which the slab/beam behaves linear elastically as long as the load does not exceed the maximum from the load history. If this value is exceeded then the curve continues on with the second branch. This behaviour is clearly shown in Figure 4.20 where a comparison is made between the fatigue and non-fatigue slab/beams. After the cracking load and fatigue cycles were applied, the slope of the first branch of P150B appears to be some value between the pre-crack slope and the slope of the second branch of a non-fatigue slab/beam. Once the highest load from the load history was passed it continued on with the second branch of the original loading curve. The second branch is where additional cracks are formed and crack lengths and widths are increased. Similar to full cast slab/beams (Figs. 4.7, 4.11, 4.13), however, additional load will then be taken by the GFRP reinforcement and while the residual deflection increases the stiffness is maintained. This is why P150B has a clearly defined ascending branch (Fig. 4.20). The end of the second branch is where failure occurred however the bond stress within the splice was nowhere near the pullout failure stress (Table 4.1).

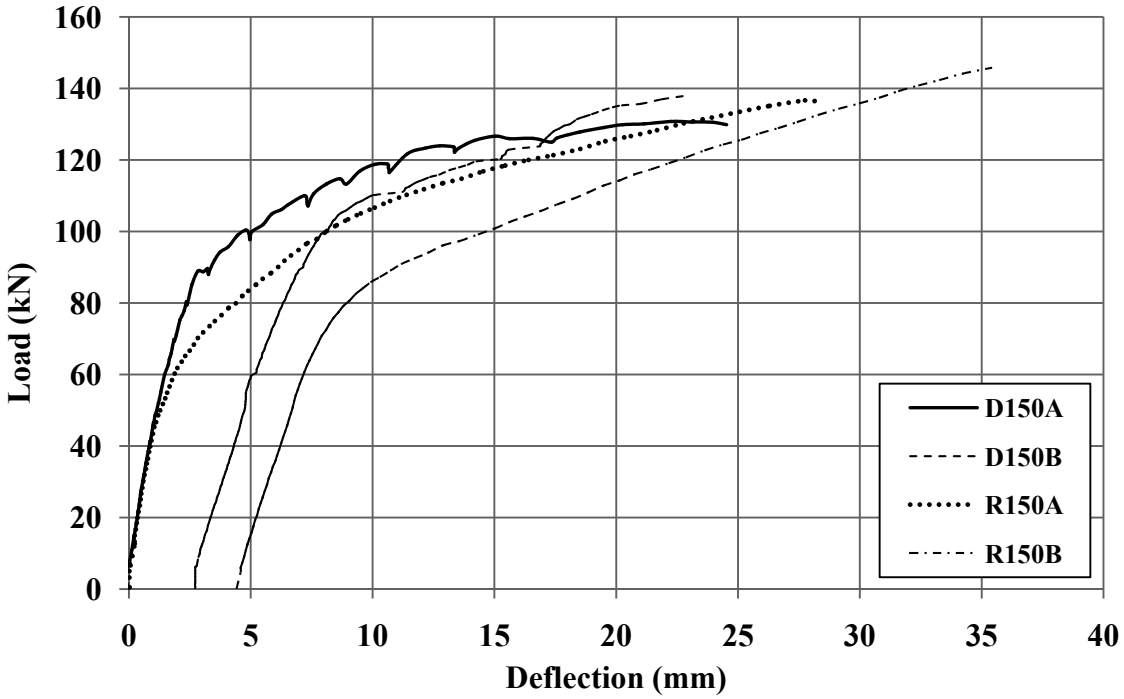

Figure 4.17: Mid-span load deflection curves for 150 mm spliced full cast slab/beams (after fatigue loading for "B" specimens)

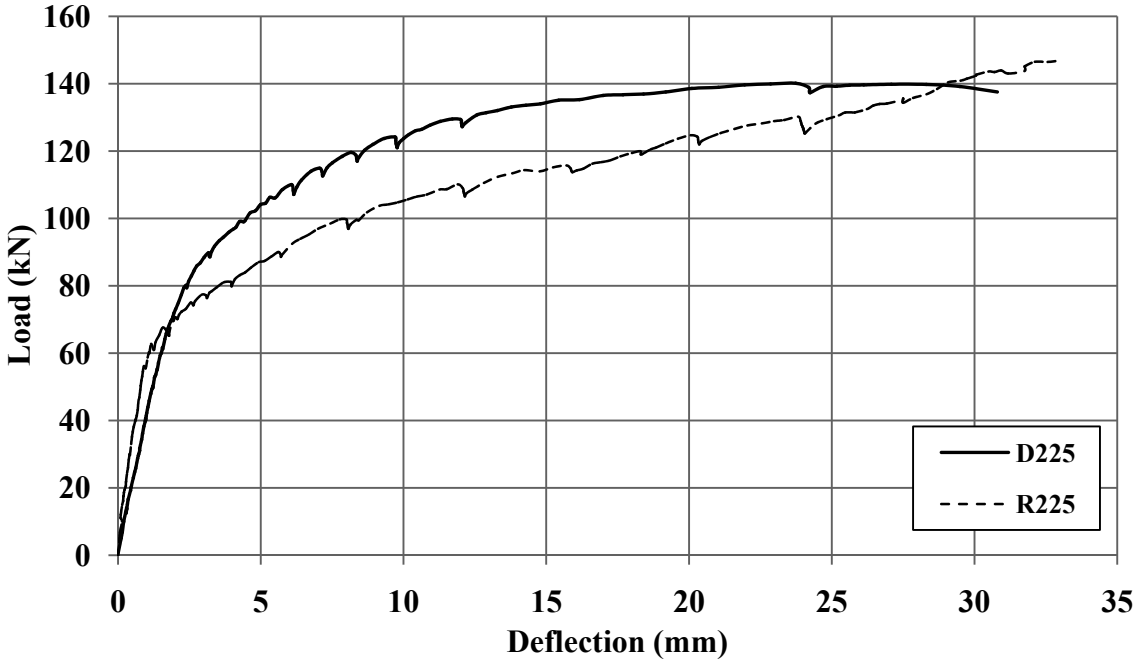

Figure 4.18: Mid-span load deflection curves for 225 mm spliced full cast slab/beams

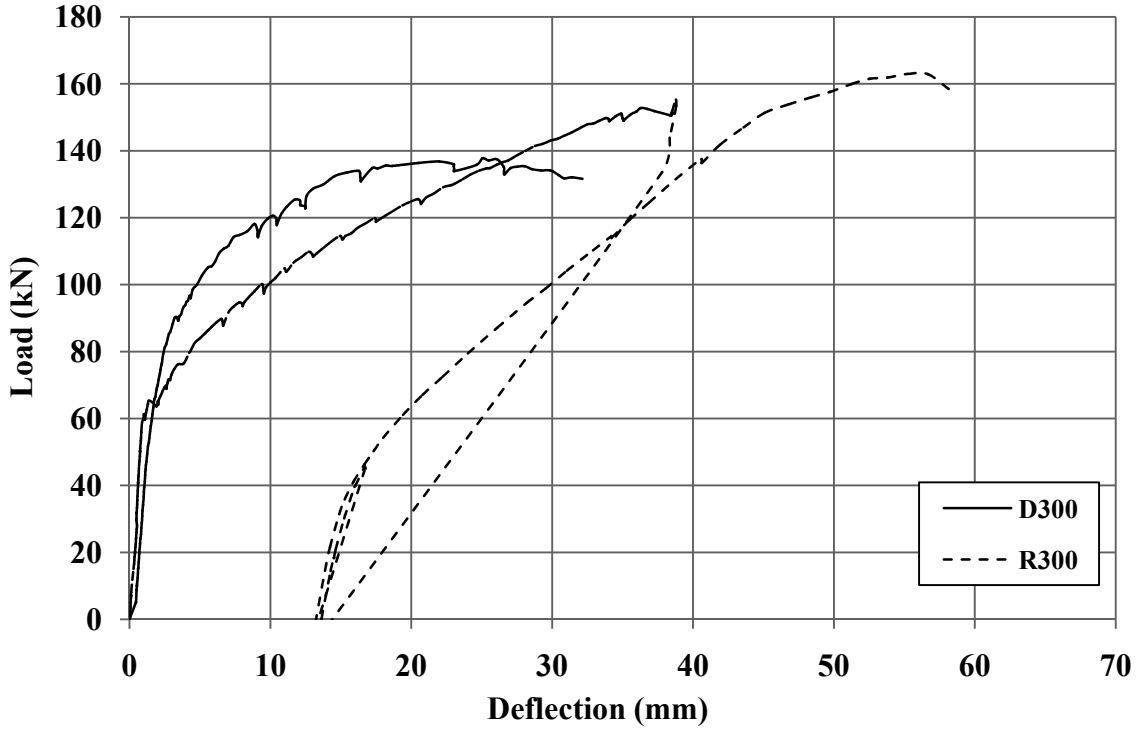

Figure 4.19: Mid-span load deflection curves for 300 mm spliced full cast slab/beams

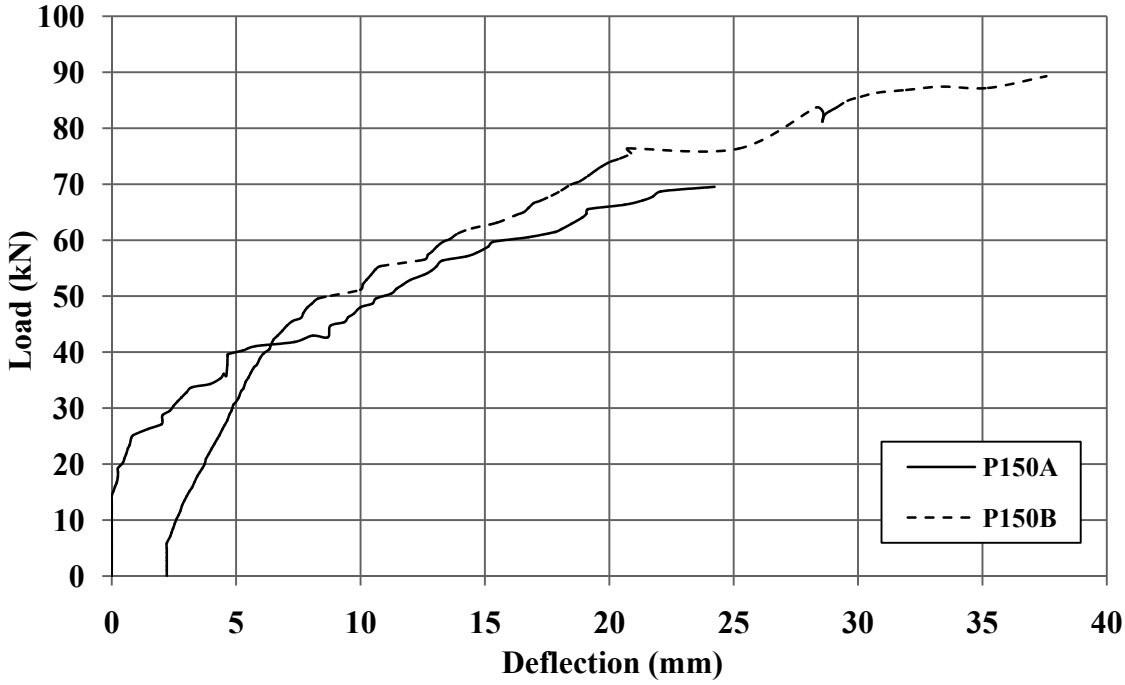

Figure 4.20: Mid-span load deflection curves for 150 mm spliced precast joint slab/beams (after fatigue loading for "B" specimen)

4.5 Fatigue Behaviour and Damage Analysis

Table 3.6 from the experimental program shows the cyclic loading parameters used for fatigue testing. Each slab/beam was loaded to the cracking load shown in the table at a rate of 5 kN/min. A loading range of 30% of the expected ultimate capacity was used for each load cycle with a minimum load of 5-10 kN. The maximum frequency allowable for the testing apparatus was applied to each slab/beam. After the required number of load cycles each slab/beam was loaded to failure at the same rate. Throughout each test the applied load, bar strain, and deflection were recorded. The following is a discussion of the results and observations.

To begin discussing the fatigue results it is important to first explain the progression of the fatigue test setup from the first slab/beam test, D150B, to the last, R150B. Several complications were identified as having a direct effect on the results. Some measures were taken to mitigate these effects thus the overall behaviour of the later slab/beam tests were slightly different than D150B. The first complication was due to the low frequency allowed by the MTS machine. The target of 2 Hz was not possible and instead the machine had to be optimized based on the loading requirements for each slab/beam. The actual frequency shown in Table 3.6 did not allow for a large number of cycles to be applied to the slab/beam within a reasonable amount of time. Testing had to take place over the course of several weeks to a month while the number of cycles had to be cut short. Secondly, the machine had to be turned off daily due to safety concerns with leaving the test unattended. The first test, D150B, was broken down into approximately 20 load sessions each consisting of several thousand cycles. Between each session the machine was turned off and the slab/beam was unloaded. It was found that unloading the slab/beam had a significant effect on the measurements obtained for deflection and strain. Figure 4.21 shows the progression of the residual deflection for D150B during the fifth load session, which had approximately 4500 cycles. For the first 2500 cycles the residual deflection accumulates fairly quickly after which the rate of increase diminishes due to the stiffening effect of fatigue loading. It is believed that the latter portion of this curve, after several thousand cycles, is the region that causes the most plastic damage to the slab/beam. The effects of the initial phase are considered elastic and will generally rebound once the slab/beam is unloaded and has been

left for 10-12 hours between sessions. Essentially only a portion of each load session actually contributed to the fatigue damage when the load cycles were interrupted.

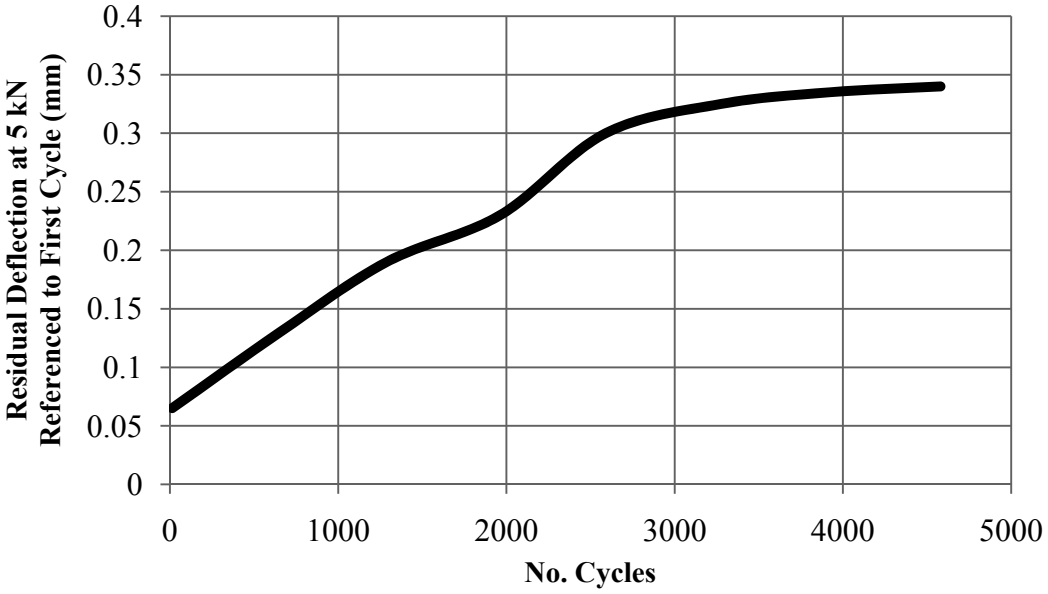

Figure 4.21: Residual deflection for D150B cyclic loading session number 5

The residual deflection and strain readings for D150B were consequently very erratic and did not show a consistent accumulation. Fatigue testing for D150B was cut short to 60,000 cycles so that modifications to the testing apparatus could be made to improve the safety and stability of the steel support beam. These modifications were made prior to the fatigue testing of P150B and were shown to provide the necessary improvements. However, authorization was required before continuous uninterrupted testing was permitted and this required observation of the testing apparatus during load application. Thus the first half of P150B was also inconsistent after which clearance was given to leave the test running continuously. R150B was allowed to run continuously throughout all 100 000 cycles with the exception of a power outage in the lab that caused some rebounding of the slab/beam halfway through testing. The results for R150B were more consistent than the rest of the tests.

Figures 4.22 - 4.24 show the load deflection curves at 20,000 cycle intervals. Also shown on each graph is the final load session where the slab/beam was loaded to failure plotted within the same load interval. The line of best fit is graphed through each load cycle

and a comparison is made between the slopes and x-intercepts obtained from the equations. The slope gives an indication of the relative stiffness degradation versus the first cycle and the x-intercepts show any changes to the residual deflection at unload. The slope of the load deflection curve for when the slab/beam is loaded to failure is a lot shallower than during the load cycles because the loading rate was much slower (5 kN/min compared to the cyclic load range/half the period of each cycle). The higher loading rate gives a slightly higher stiffness due to dynamic effects. Each load cycle starts with a steep, almost vertical, portion where the slab/beam first accelerates upwards. The diagonal part is where the slab/beam responds gradually with the loading and increases linearly in deflection and load. The vertical drop is where the load starts to be released but due to dynamic effects again the slab/beam does not immediately respond and the deflection remains for a short time while the load decreases. Then similar to the ascending branch the slab/beam returns to its original position with a linear descending branch of the same slope. Each graph shows the progression in residual deflection for each slab/beam, however R150B shows a more consistent accumulation versus the other slab/beams due to the continuous cyclic load application.

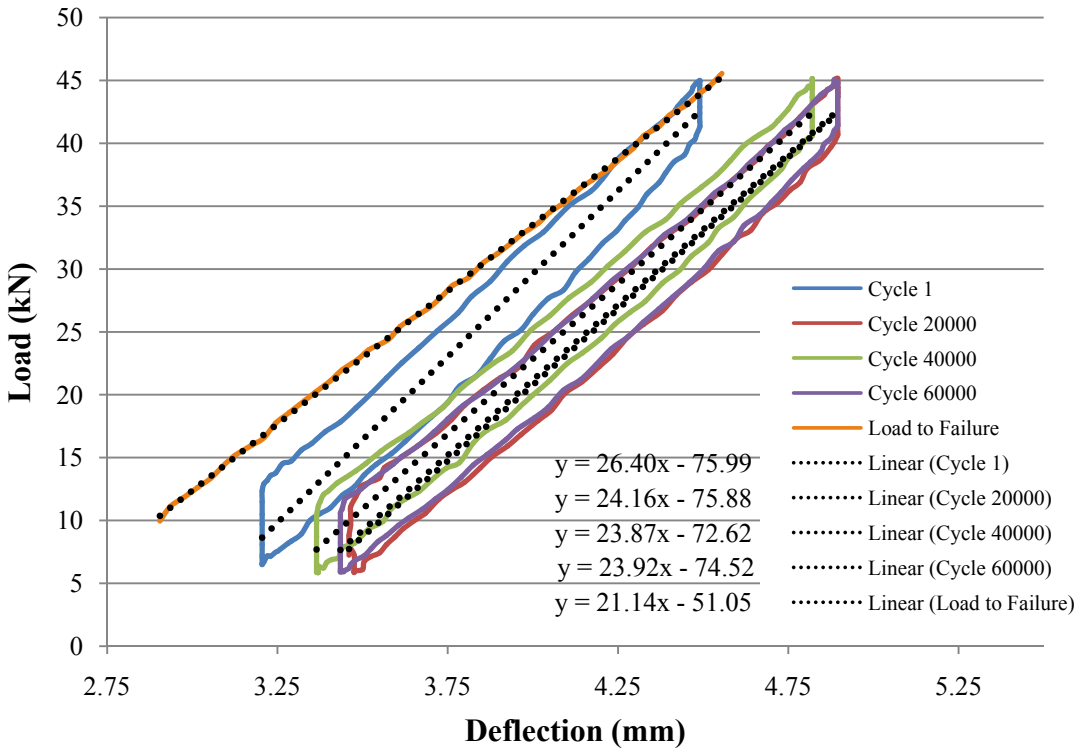

Figure 4.22: D150B cyclic load deflection curves

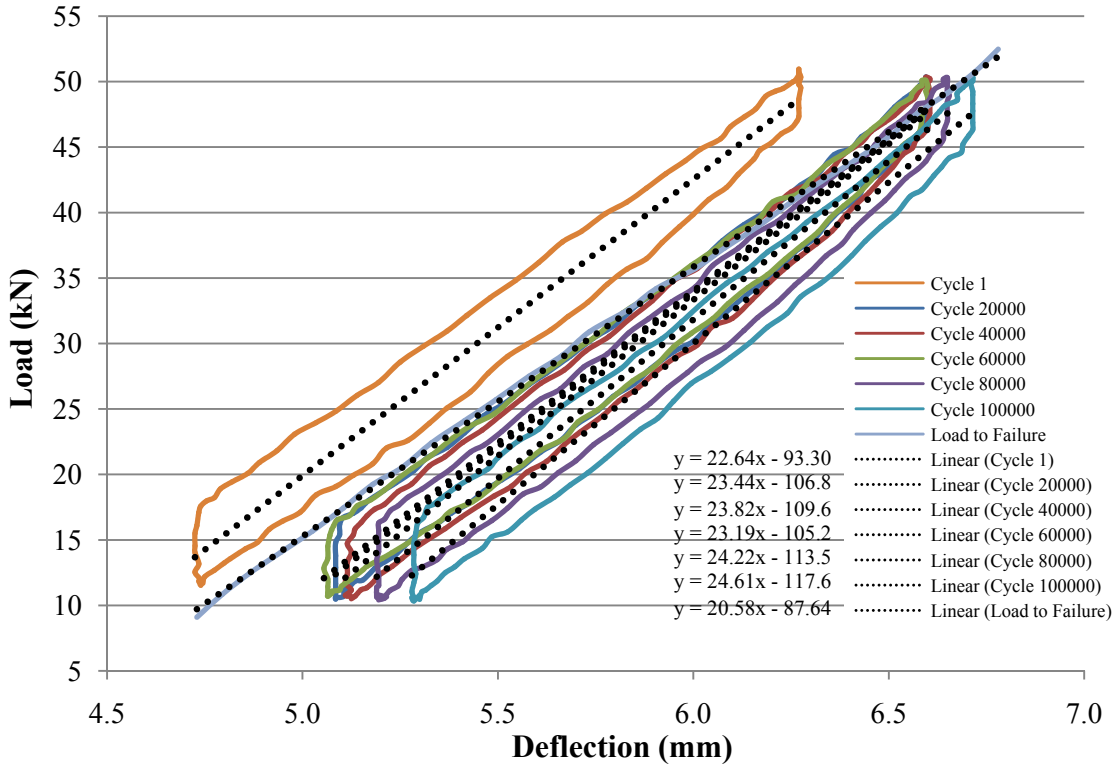

Figure 4.23: R150B cyclic load deflection curves

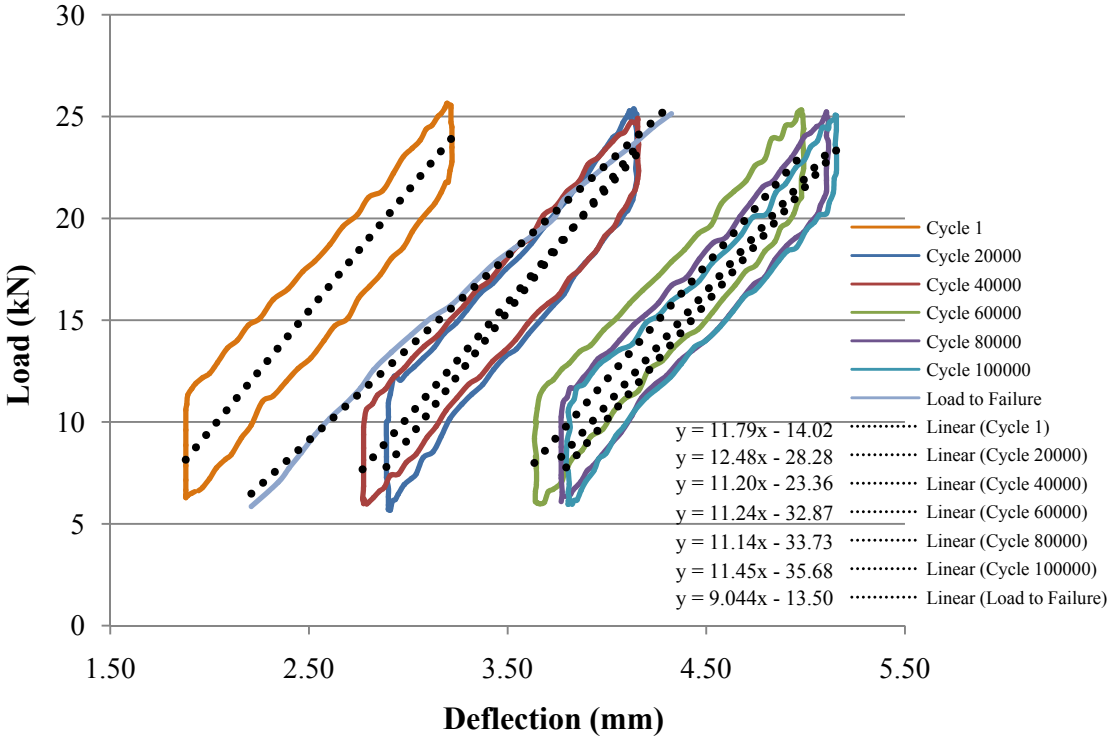

Figure 4.24: P150B cyclic load deflection curves

The results for slope and residual deflection were converted into damage factors to evaluate any changes due to fatigue loading. Whenever possible some cracks were also monitored for changes during each interval of cycles. Each factor is a ratio of the observed value after a given number of cycles to the value measured from the first cycle. These factors are presented in Table 4.2 for each interval of 20,000 cycles. An additional factor is given at the end of all the cycles as a ratio of the ultimate capacity after cyclic loading to that of an equivalent slab/beam without fatigue effects.

The stiffness degradation factor, γ_1, is the ratio of the slope of the load deflection curve at a given cycle to the slope from the first cycle. This factor showed a decrease by about 9.4% for D150B and an increase of 8.7% for R150B after the respective number of cycles. This discrepancy is due to the difference in continuous and non-continuous cyclic loading. The longer the load session, i.e. more consecutive cycles, the more plastic damage is incurred by the slab/beam. Examples of this are increasing crack width and length, steel fibre pullout, and bar slip. As more plastic damage is incurred more load is transferred to the reinforcing bar while a minute amount of bar slip is also induced such that any voids between the GFRP bar surface deformations and the surrounding concrete are closed. Similar to the strain and deflection curves the stiffness is maintained due to the stiff bond between the rebar and concrete however the residual deflection increases with plastic damage.

The residual deflection factor, γ_2, is the ratio of the x-intercept of the line of best fit passing through the load deflection curve at a given cycle to the x-intercept of the first cycle. Accumulation of plastic damage increases the residual deflection, but also give the appearance of improved stiffness relative to the new slab/beam position. This is demonstrated by the increase in both the stiffness and residual deflection damage factors for R150B. If, however, the load sessions are shorter and non-continuous then there will be an apparent decrease in stiffness with no clear change in residual deflection. After letting the specimen rest and rebound, the first 1000-2000 cycles in each session must redistribute the load back to the bar and since the original effective cross-section has already been damaged beyond the current state a reduction of stiffness is observed. This second type of behaviour is observed for D150B.

P150B showed an overall decrease in stiffness combined with an increase in residual deflection. Both of these are the result of additional cracking at the interface between the

joint fill material and precast sections as well as the onset of longitudinal cracking around the bar. Transverse cracking increases the residual deflection while the longitudinal cracking impedes proper load transfer to the bar causing a corresponding decrease in stiffness.

The crack width factor, γ_3, is the ratio between the crack widths at a given cycle to the crack width after the first cycle. Crack widths were measured mainly from the initial crack location for D150B and R150B since no other cracks appeared during fatigue loading. The initial crack widths were 0.22 mm, 0.20 mm and 0.30 mm for D150B, R150B and P150B respectively. These crack widths were measured using a handheld crack scope when the load had been removed and not during load application. This factor shows that for the two full cast slab/beams no significant increase was observed after the initial 20,000 cycles. Since crack widths could only be accurately observed while the slab/beam was unloaded this may have caused the lack of an increase in this factor. Steel fibre bridging would have also contributed to the moderate crack widths. P150B showed a significant increase in crack width from the first cycle at the first observed crack location. Additional cracking at the joint interface was also noted however measurements could not be taken at this location due to the orientation of the setup.

The load capacity factor, γ_4, is the ratio between the ultimate load capacity of each fatigue slab/beam to the non-fatigue slab/beam equivalents. All slab/beams showed an increase in load capacity with P150B showing the largest overall increase. The shear failure mode of P150B benefited directly from the 13.4% increase in concrete strength versus P150A. An overall increase in the compressive strength was expected for all fatigue specimens due to the length of testing required. Although, R150B showed a small 2.2% decrease in concrete strength, attributed mainly to variance, it still showed a 6.5% increase in load capacity. D150B showed a clearer increase in concrete strength with a 14.1% jump between D150B and D150A and a corresponding 5.3% increase in load capacity. While fatigue loading contributed to the degradation in stiffness and deflection, no damage was observed in terms of ultimate capacity. This is mainly due to the low frequency of cyclic loading, relatively small number of cycles, and elastic cyclic load range that allowed the bond between the GFRP and concrete to remain intact. With P150B the loading range was well below the load at which shear cracks became dominant.

Table 4.2: Fatigue loading damage factors

D150B	No. of Cycles				
Damage Factor	20000	40000	60000		
γ_1	0.915	0.904	0.906		
γ_2	1.091	1.057	1.082		
γ_3	1.50	1.50	1.50		
γ_4	N/A	N/A	1.053		
R150B	**No. of Cycles**				
Damage Factor	20000	40000	60000	80000	100000
γ_1	1.035	1.052	1.024	1.070	1.087
γ_2	1.106	1.117	1.101	1.137	1.160
γ_3	1.25	1.25	1.25	1.25	1.25
γ_4	N/A	N/A	N/A	N/A	1.065
P150B	**No. of Cycles**				
Damage Factor	20000	40000	60000	80000	100000
γ_1	1.059	0.950	0.953	0.945	0.971
γ_2	1.906	1.754	2.459	2.546	2.62
γ_3	1.00	1.00	2.33	2.333	2.333
γ_4	N/A	N/A	N/A	N/A	1.276

γ_1 = Ratio of the slope of the load deflection curve to the slope from Cycle 1.
γ_2 = Ratio of the residual deflection to the residual deflection at Cycle 1.
γ_3 = Ratio of the measured crack width to that from the initial cracking load.
γ_4 = Ratio of the ultimate capacity to that of the duplicate "A" specimen.

In future, cyclic load application should be done using a linear actuator rather than an MTS machine. This would allow continuous cycle application at a higher frequency better simulating the load experienced by a real bridge deck. More cycles could also be applied within a shorter time frame.

4.6 Crack Propagation and Failure Modes

For all the slab/beams the first cracks appeared near or directly under the load points at the start of the maximum moment region. The presence of transverse reinforcement also acted as crack initiators with many cracks passing through their locations. The crack patterns for each slab/beam are shown in Figures 4.25 and 4.26. For all full cast slab/beams the location of the major crack generally occurred near the end of the splice. For precast slab/beams the major crack was a diagonal shear crack extending from the support to the load point. Each diagram shows the locations of transverse reinforcing bars, load application, supports, splice lengths, and joint material for precast slab/beams. The location of the major crack is also differentiated using thicker line weight. The height range to where the cracks

extended to at the critical section for full cast slab/beams was between 165-185 mm. This observation corresponds with the neutral axis depths obtained from the bar force calculations.

Type D slab/beams had similar cracking characteristics for all three splice lengths (Fig. 4.25). Of the few cracks that occurred within the splice none of them reached the bottom of the slab/beam indicating that the tensile stress within the concrete still existed. As the load approached the ultimate capacity the GFRP bar began to slip out of the splice at the location of the major crack. This caused a significant increase in crack width at the critical section but also prevented any additional cracks from forming beyond the maximum load even though the deflection increased. For the same reason cracks that did not form at the critical section stayed relatively small. The higher modulus of rupture for type D concrete also contributed to the lack of crack development throughout the slab/beam. It is also clearly visible, from the crack diagrams (Fig. 4.25), the location of where the compression zone ended and the tension zone began due to the forking of the vertical crack in the compression region. There was no significant change in crack behaviour between fatigue and non-fatigue specimens of this concrete type. Crack widths at the critical section after failure were about 12 mm for D150 slab/beams and 20-25 mm for D225 and D300 slab/beams. The larger crack widths correspond with the longer splice lengths because more pullout length was provided before failure. The location of the major crack for type D slab/beams was generally at the same location within the vicinity of the end of the splice. It is believed that the location of the steel stirrups within the pure bending region greatly affected the major crack location.

Type R slab/beams showed significantly more cracking as the splice lengths increased (Fig. 4.26). This is the result of a weaker modulus of rupture for this concrete type as well as a constantly increasing load capacity up to failure. Type R slab/beams allowed more bar force to develop through transverse cracking within the splice so localized slip at high bar forces was not as intense helping to resist the widening of the cracks at the critical section. The steady load increase up to failure allowed tensile stresses to develop throughout the concrete creating a more even distribution of cracks. An increase in the overall crack distribution was observed with the larger splice lengths. Most cracks for type R slab/beams continued in a vertical fashion upwards in the slab/beam with no clear indication of where the compression region began (Fig. 4.26). Because type R slab/beams were able to develop a

larger bar force the curvature was slightly higher causing the cracks to remain vertical. The increased curvature also resulted in a small amount of concrete crushing for R225 and R300 which was also verified by the calculated concrete strains at failure. Fatigue testing on R150B initiated some additional cracking at the load point and around the major crack versus R150A. The crack width at the critical section for R slab/beams ranged from 10 mm to 15 mm.

Precast slab/beams did not experience as much cracking in the constant moment region however there was noticeable debonding at the interface between the precast section and the joint material (Figs. 4.25-4.26). Some longitudinal cracking did occur at the height of the bar in that region as well, which may indicate localized splitting failure in the precast concrete section. Aside from those, most of the cracks propagated outwards starting as vertical tension cracks directly under the load point and gradually becoming diagonal shear cracks until the critical load was reached and the slab/beam failed in shear. During cyclic loading of the fatigue specimen the only cracks that occurred other than those observed after initial cracking of the slab/beam were the ones at the joint interface. No cracks were observed within the joint fill material.

The failure mode of all full cast slab/beams was by tension failure caused by rebar pullout. A typical full cast beam after failure is shown in Figure 4.27a. Type D slab/beams began to fail gradually by localized bond failure and slip after reaching the maximum applied load. This had the effect of widening the major crack at the critical section while reducing cracking throughout the rest of the slab/beam and within the splice (Fig. 4.27b). Bar strains at mid-splice just prior to failure for the longer splice lengths reached values greater than the calculated bar strains at the end of the splice indicating that bond failure had indeed occurred (Fig. 4.5). Type R slab/beams were able to accommodate additional bar force through transverse cracking within the splice (Fig. 4.27c) that helped to redistribute bond forces to the latter part of the splice away from the loaded end. This allowed type R slab/beams to have a consistently higher load capacity than type D slab/beams while reducing the crack widths at failure and increasing the overall distribution of cracks. This difference meant that type R slab/beams were also more ductile than type D slab/beams taking on more deflection and load at failure. The larger splice lengths for type R slab/beams, namely R225 and R300, also showed some slight crushing of concrete due to the increasingly large curvature of the

slab/beam at higher loads (Fig. 4.27d). Precast slab/beams were able to resist the tensile forces exerted on the joint but failed due to a lack of shear reinforcement. The major crack extended directly from the support to the point of load application (Fig. 4.27e). The concrete encompassed by this crack crumbled into smaller chunks and in the case of P150B exposed the tensile reinforcing bars. This failure mode was very sudden and brittle but was preceded by many loud explosive noises as cracks propagated out towards the support (Mak et al. 2011).

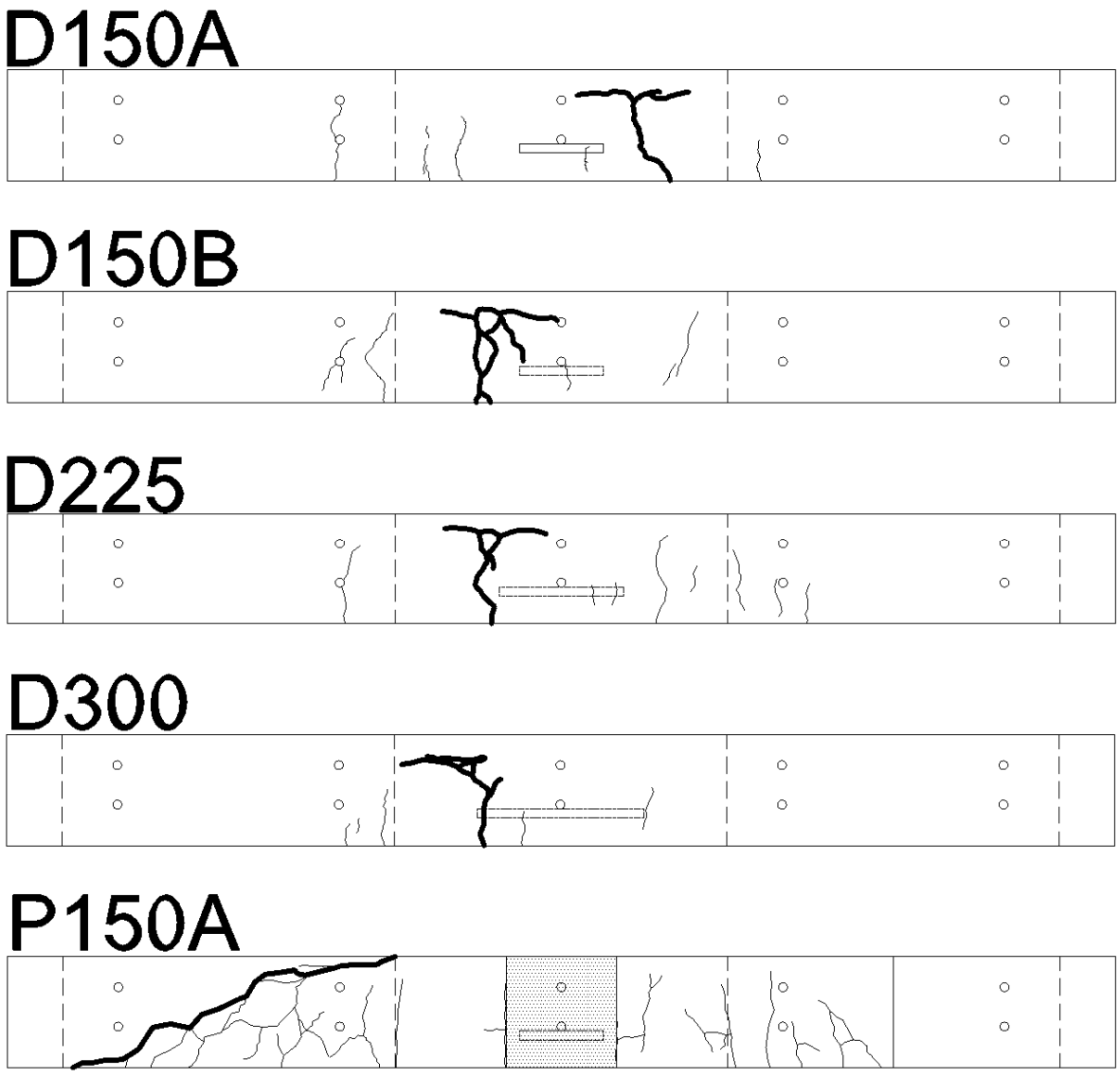

Figure 4.25: Crack diagrams of type D and P150A slab/beams

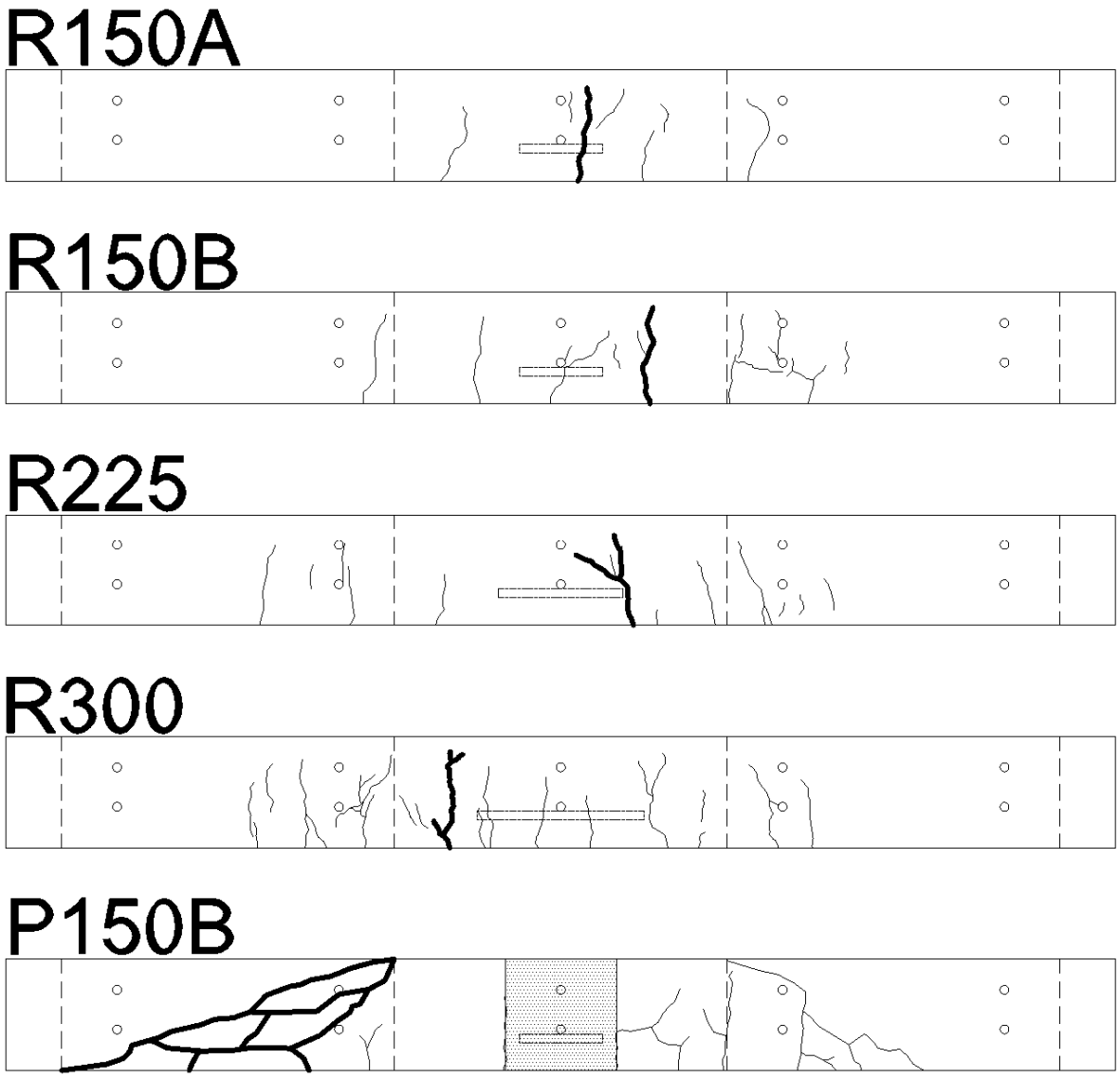

Figure 4.26: Crack diagram of type R and P150B slab/beams

(a)

(b)

(c)

(d)

(e)

Figure 4.27: (a) Typical full/cast beam failure, (b) D300 splice region after failure, (c) transverse crack at mid splice for R150B, (d) concrete crushing of R300, (e) shear failure mode of P150B

4.7 Bond Performance Under Aggressive Environment

A limited study was conducted on the effects of freeze/thaw with humidity on the bond performance of GFRP with various types of concrete. Duplicate pullout specimens were exposed to 50 cycles of +60˚C and -30˚C temperature with 50% humidity. The results were compared with 20 control specimens without freeze-thaw (F/T) cycles conducted by a research group at Ryerson University (Ametrano 2011; Hossain et al. 2011) using the same concrete types and dimensions. Control test results are included in the database of results in the Appendix. The embedment lengths for all pullout tests were 5 d_b and the clear cover was 40 mm. The results are shown in Figure 4.28 for each concrete type (K, R, and D). Each graph shows the maximum bond stresses obtained from both HM and LM tests versus their respective freeze/thaw tests. In future a larger number of pullout tests should be included to balance the effect of variance in the results.

Table 4.3 summarizes the results by comparing the averages from each group of pullout tests. A substantial decrease in bond performance was observed with type K pullout specimens especially with the low modulus rebar. The loss of bond strength was most likely due to the greater transverse expansion of the GFRP bar versus concrete during the high temperature portion of the test combined with the expansion of moisture absorbed by the bar during freezing. The transverse coefficient of thermal expansion of GFRP is about 5 times larger than concrete (ISIS Canada 2006). Transverse expansion of the bar would have added additional radial forces to the surrounding concrete and may have initiated local splitting cracks around the bar. The lack of confining steel fibres surrounding the rebar in type K concrete prevented the specimen from bridging any longitudinal cracks that formed along the bar at failure. Overall both R and D concretes with fibres performed better in terms of bond. The better performance is a result of the enhanced confinement from the steel fibres. By preventing the concrete from expanding radially, it forces more of the sand coating to fail under direct shear, which provides a more effective load resisting mechanism than being pulled away from the bar during any form of splitting. Furthermore, R and D concretes would have provided superior chemical adhesion to the sand coated surface while also providing enough compressive strength to prevent crushing of concrete. Similar tests by Lee et al. (2003) showed a larger portion of the sand coating was peeled off the fibre core of sand coated GFRP as concrete strengths increased. These phenomena are what benefited type R

and D concretes after freeze/thaw. The high humidity and temperature from environmental loading would have increased the strength of these concretes thus giving a stronger and stiffer confinement to the GFRP bars. This forced the failure to occur entirely by shear within the sand coating layer rather than being pulled away from the bar during splitting failure or by simultaneous crushing of concrete and debonding of sand coating as with weaker concretes. After freeze thaw, Type D concrete showed approximately 40% and 63% increase in bond strength for LM and HM bars respectively, which is quite substantial. LM rebar performed better with type R concrete showing a 27% increase versus about 4% for HM bars. The enhanced performance of Type D concrete versus Type R may be attributed to higher strength development after treatment. Type D concrete contains a larger percentage of fine cementitious material (Graybeal 2006a) that improved the strength development when exposed to additional heat and moisture.

Table 4.3: Comparison of pullout testing with aggressive environmental treatment

Specimen Type	Control Avg. Bond (MPa)	F/T Avg. Bond (MPa)	Percent Change (%)
Type K LM	11.6	9.0	-22.4
Type K HM	10.4	10.0	-3.8
Type R LM	14.3	18.2	27.3
Type R HM	13.3	13.8	3.8
Type D LM	13.3	18.6	39.8
Type D HM	10.0	16.3	63.0

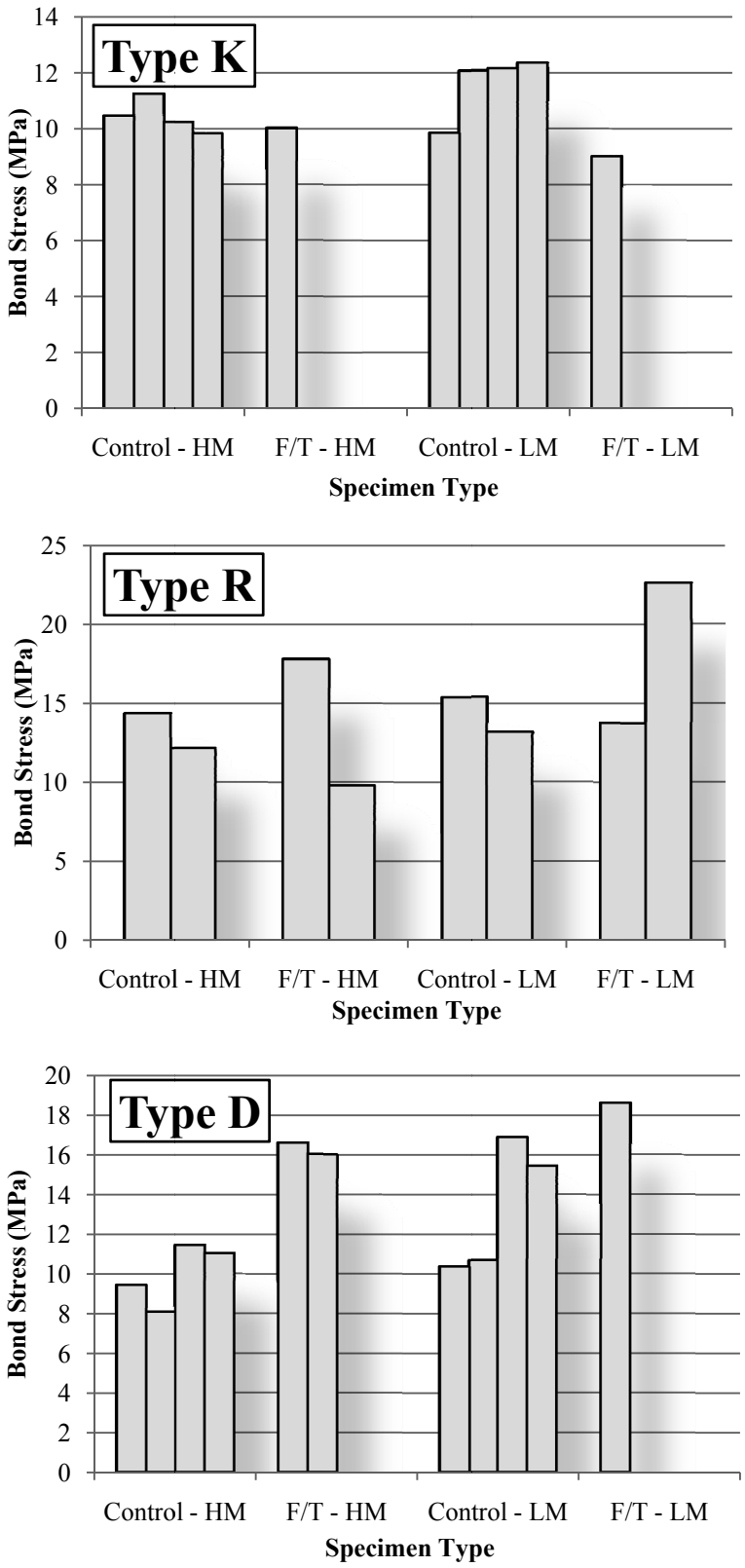

Figure 4.28: Bond strength of pullout testing before and after aggressive environmental treatment

4.8 Comparison Between Pullout Tests and Slab/beam Tests

Most literature suggests that the bond strength from pullout tests will generally be higher than the values obtained from flexural beam tests (Ehsani et al. 1997; JSCE 1997; MacGregor and Wight 2005; Tastani and Pantazopoulou 2006; Tighiouart et al. 1998). This behavior has mainly been attributed to the state of compression within the concrete surrounding the rebar versus the tensile stresses within a beam. However, the results from this study show that the opposite can be true for sand coated GFRP rebar. Researchers have also shown that that the compression in a normal pullout test can cause a decrease in the bond strength using sand coated spiral wound rebar while improving the bond strength for ribbed reinforcement (Aiello et al. 2007). As explained in previous sections the lower modulus of elasticity for GFRP requires that the concrete accommodate greater strain at high bar forces. Placing the surrounding concrete in compression would prohibit the concrete from deforming with the bar thus adding to the stress concentration at the loaded end. A comparison of the bond strength between pullout and spliced slab/beam test results in Figures 4.28 show that even at a much longer embedment length and the presence of splicing the bond strength of spliced slab/beam tests are equivalent to or exceed that of pullout testing from a significantly shorter embedment length. This is a clear contradiction of the results found from the above literature stating that pullout tests provide better bond conditions for both GFRP and steel rebar. Furthermore, the results from RILEM beam testing show consistently higher bond strength than the pullout tests. The results for RILEM beam tests and pullout tests in Figure 4.28 use both LM and HM GFRP sand coated rebar of 15.9 mm diameter embedded in UHPC exceeding 100 MPa with steel fibre reinforcement. The data set used for this figure is included in the Appendix.

Several trends are also observed from Figure 4.28. The first is the decreasing average bond strength with embedment length as expected for similar specimen types. The second is the relatively higher average bond strength of spliced beam tests versus the HM RILEM beam tests with a significantly shorter embedment length. This may have been the effect of having a very high stiffness in the matrix surrounding the GFRP bar in relation to the axial stiffness of the bar itself. RILEM beams contain both steel fibers and shear and tensile steel bars that dramatically increase the confinement in both vertical and horizontal directions directly surrounding the embedded portion of the GFRP bar. This acts to stiffen the concrete

preventing bond stresses to develop further away from the loaded end much like the effects of compression in a pullout test. The slab beams, however, do not contain as much restraint around the bar location allowing relatively more bond stresses to develop along the bar. A minimum bond stress of 10 MPa was achieved at splice lengths of up to 300 mm for slab/beams. The third trend is the lower bond strength of HM bars in both RILEM beam tests and pullout tests versus LM bars. This has been attributed to issues with the manufacturing of the sand coating layer.

Overall, beam tests provide a better representation of the actual bond performance in flexural members since the concrete surrounding the bar is subjected to flexural tension, shear cracking, and transverse cracking.

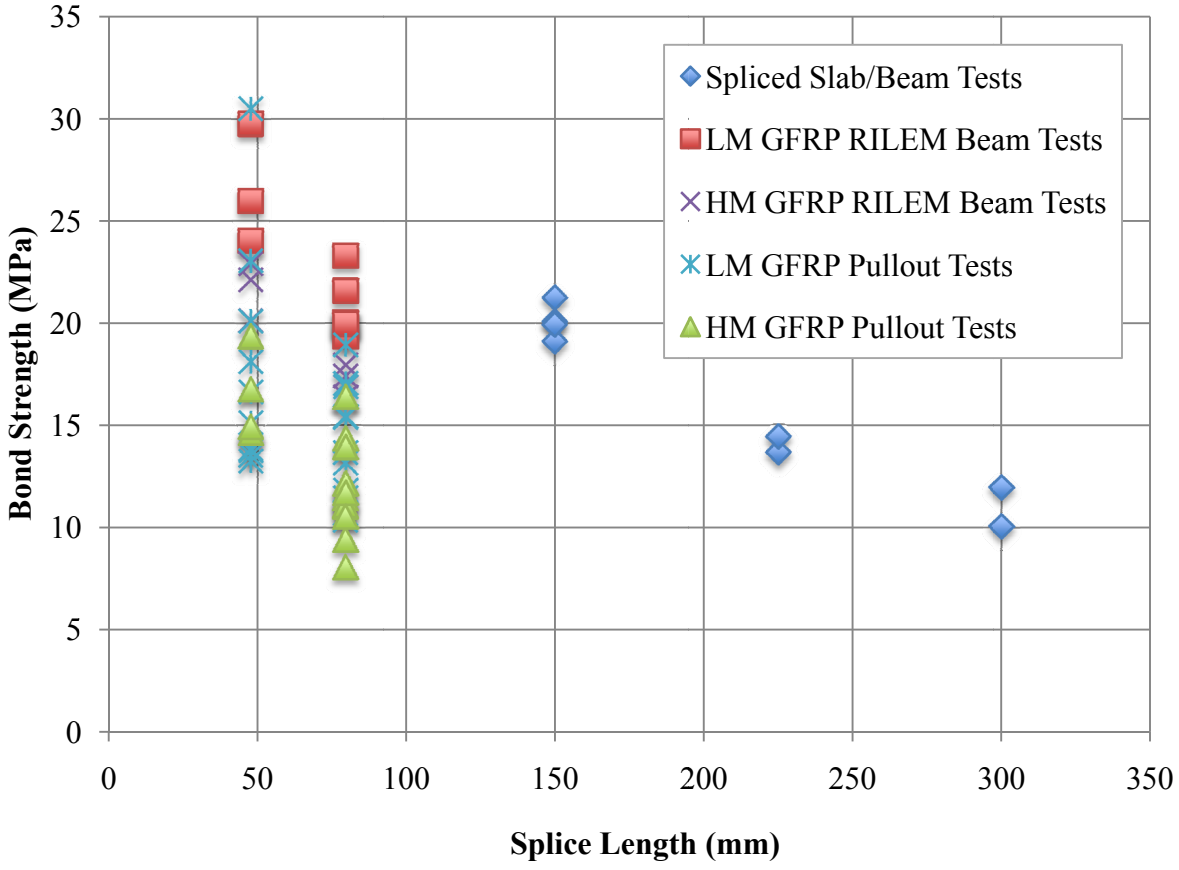

Figure 4.29: Bond strength versus embedment length for various specimen types using sand coated 15.9 mm GFRP rebar

Chapter 5 Theoretical Predictions of Bar Stress Distribution in Tension Lap Splices

5.1 Introduction to the Modulus of Displacement Theory

Many researchers have employed different methods for analyzing the bond strength of traditional steel reinforcement to that of GFRP. This chapter aims to utilize the modulus of displacement theory (MDT) originally derived for steel rebar for the analysis of sand coated HM GFRP splices in UHPC. This method has successfully modeled the bar stress distributions of sand coated LM GFRP and CFRP reinforcing bars in normal strength concrete (Aly 2007). The main objective is to predict the maximum tensile bar stress that can be developed by a splice and subsequently the maximum average bond strength. A comparison is then made between the theoretical predictions and the experimental results to verify the model's validity. If the test results show good agreement with the model then projections will be made on the bond strength of longer splice lengths and the minimum required for developing the full strength of a HM GFRP bar. Tepfers (1980) utilized the concept of a constant modulus of displacement to derive the relationships between bond stress, longitudinal bar stress, and concrete stress within a splice length of known material and geometric properties. A constant displacement modulus gives the relationship between the slip and the shear bond stresses between two materials. In this case the GFRP rebar is bonded to a concrete matrix. It is also necessary for both materials to exhibit linear elastic behaviour according to Hooke's law within the range of analysis in order to maintain accuracy. Several other assumptions must also be satisfied in regards to the geometry and loading of the spliced region and they are as follows (Tepfers 1980):

- The spliced region must be contained within a constant moment region such that no shear is present and the tension forces are equal at the ends of the splice.
- Concrete cracking has already occurred at the ends of the splice caused by the sudden change in reinforcement ratio in that region as shown in Figure 5.1.
- Opposing bars are assumed to have the same dimensions and thus occupy the same area at the ends of the splice.
- Reinforcing bar stresses are zero at the free ends of the splice and reach a maximum tensile force σ_{frp0} at the loaded end.

- The governing equations must follow a consistent co-ordinate system based on their derivation. For the equations presented herein the main variable x represents some distance from the center of the splice in the longitudinal bar direction and l is the splice length.
- The current notation specifies that frp_1 represents the bar with loaded end (maximum bar stress σ_{frp0}) at the negative x direction (Fig. 5.1) and vice-versa for frp_2.
- The effective area of concrete providing tensile resistance in the spliced region is governed by the minimum cover dimension according to concrete ring splitting theory for reinforcing bars as shown in Figure 5.2.

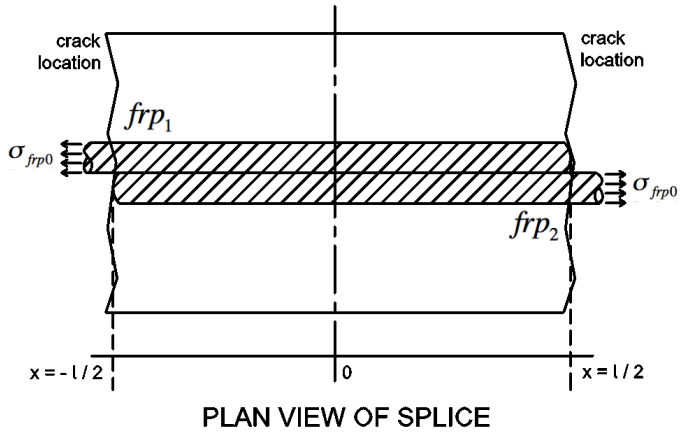

Figure 5.1: Plan view of a single splice confined between two cracked regions (Tepfers 1980)

Tepfers (1980) begins the derivation by equating the change in tensile concrete stress to the change in longitudinal stresses for both spliced bars. The bond stress, also a varying quantity along the splice, is included in this equation for establishing the relation between concrete and reinforcement. The concrete stress is assumed to act over the effective area of concrete surrounding the bar (Fig. 5.2). A constant modulus of displacement is introduced to relate the strain difference of concrete and rebar to the change in bond stress along the rebar. Equilibrium of the splice at any point between the two cracked ends allows the previous equations to be combined to eliminate the bond stress and thus leaving a differential equation for concrete stress. The solution to this final equation gives the variation of concrete stress, which can then be used to determine the bond stress and bar stress variations. Each equation is a function of the main variable x and the constants are made up of the modulus of

displacement, the maximum bar stresses at the loaded end of the splice and the various geometric properties representing the bar and concrete tensile region. The final equations as presented in Tepfers (1980) are as follows:

For concrete tensile stress in the direction of the reinforcement:

$$\sigma_{ct} = \frac{\sigma_{frp0}}{1+2n\rho}\frac{\rho}{\cosh(\kappa_1 l/2)}\left[\cosh\frac{\kappa_1 l}{2} - \cosh(\kappa_1 x)\right] \quad \text{.....(5.1)}$$

For longitudinal bar stresses:

$$\sigma_{frp1} = -\frac{\sigma_{frp0}}{2}\frac{\sinh(\kappa_2 x)}{\sinh(\kappa_2 l/2)} + \frac{\sigma_{frp0}}{2(1+2n\rho)}\left[\frac{\cosh(\kappa_1 x)}{\cosh(\kappa_1 l/2)} + 2n\rho\right] \quad \text{.....(5.2)}$$

$$\sigma_{frp2} = \frac{\sigma_{frp0}}{2}\frac{\sinh(\kappa_2 x)}{\sinh(\kappa_2 l/2)} + \frac{\sigma_{frp0}}{2(1+2n\rho)}\left[\frac{\cosh(\kappa_1 x)}{\cosh(\kappa_1 l/2)} + 2n\rho\right] \quad \text{.....(5.3)}$$

For bond stresses along the spliced bars:

$$\tau_1 = \frac{A_b}{u}\left[-\frac{\sigma_{frp0}\kappa_2}{2}\frac{\cosh(\kappa_2 x)}{\sinh(\kappa_2 l/2)} + \frac{\sigma_{frp0}\kappa_1}{2(1+2n\rho)}\frac{\sinh(\kappa_1 x)}{\cosh(\kappa_1 l/2)}\right] \quad \text{.....(5.4)}$$

$$\tau_2 = \frac{A_b}{u}\left[\frac{\sigma_{frp0}\kappa_2}{2}\frac{\cosh(\kappa_2 x)}{\sinh(\kappa_2 l/2)} + \frac{\sigma_{frp0}\kappa_1}{2(1+2n\rho)}\frac{\sinh(\kappa_1 x)}{\cosh(\kappa_1 l/2)}\right] \quad \text{.....(5.5)}$$

and the constants κ_1 and κ_2 are equal to:

$$\kappa_1 = \sqrt{\frac{uK}{E_{frp}A_b}(1+2n\rho)} \quad \text{.....(5.6)}$$

$$\kappa_2 = \sqrt{\frac{uK}{E_{frp}A_b}} \quad \text{.....(5.7)}$$

where l is the length of the splice (mm); x is the distance from the center of the splice with respect to the longitudinal bar axes (mm); σ_{frp0} is the loaded end bar stress (MPa); σ_{frp1}, σ_{frp2} are the bar stresses at some point x along the splice (MPa); σ_{ct} is the concrete tensile stress at

some point x along the splice (MPa); τ_1, τ_2 are the bond stresses for opposing bars frp_1 and frp_2 at some point x along the splice (MPa); n is the modular ratio between the reinforcement and the concrete; ρ is the reinforcement ratio of reinforcing bar area to effective concrete area; u is the perimeter of the reinforcing bar (mm); E_{frp}, E_c are the FRP bar and concrete elastic moduli (MPa) respectively; A_b, A_c are the reinforcing bar and effective concrete areas respectively (mm^2), and K is the modulus of displacement (N/mm^3).

5.2 Determining the Geometric and Material Constants

The constants used in equations 5.1 to 5.7 must represent the characteristics of the experimental tests specimens. Table 5.1 shows the values that will be used in this analysis for each of the full cast specimens. These values will be explained in the following sections as necessary.

Table 5.1: Constants used for modulus of displacement analysis

Constants	D150A	D150B	D225	D300	R150A	R150B	R225	R300
u (mm)	50.0	50.0	50.0	50.0	50.0	50.0	50.0	50.0
A_c (mm^2)	6209.0	6209.0	6209.0	6209.0	6209.0	6209.0	6209.0	6209.0
A_b (mm^2)	198.6	198.6	198.6	198.6	198.6	198.6	198.6	198.6
d_b (mm)	15.9	15.9	15.9	15.9	15.9	15.9	15.9	15.9
E_{frp} (MPA)	64100	64100	64100	64100	64100	64100	64100	64100
E_c(MPA)	46793	49998	45435	45435	47559	47024	38572	39969
n	1.37	1.28	1.41	1.41	1.35	1.36	1.66	1.60
K (N/mm^3)	8.436	8.436	8.436	8.436	8.436	8.436	8.436	8.436
ρ (%)	0.0320	0.0320	0.0320	0.0320	0.0320	0.0320	0.0320	0.0320
l (mm)	150	150	225	300	150	150	225	300
κ_2^2 ($1/mm^2$)	3.31E-05	3.31E-05	3.31E-05	3.31E-05	3.31E-05	3.31E-05	3.31E-05	3.31E-05
κ_1^2 ($1/mm^2$)	3.60E-05	3.58E-05	3.61E-05	3.61E-05	3.60E-05	3.60E-05	3.66E-05	3.65E-05
κ_2 (1/mm)	5.75E-03	5.75E-03	5.75E-03	5.75E-03	5.75E-03	5.75E-03	5.75E-03	5.75E-03
κ_1 (1/mm)	6.00E-03	5.99E-03	6.01E-03	6.01E-03	6.00E-03	6.00E-03	6.05E-03	6.04E-03
τ_{max}(MPa)	21.9	23.0	21.4	21.4	22.1	22.0	19.3	19.7

According to Tepfers (1980, 1982) the effective area of concrete A_c can be computed as the equivalent of the concrete ring necessary for providing the radial and tangential bond forces on a reinforcing bar minus any overlapping portion due to splicing. Thus the thinnest region of concrete surrounding a single rebar governs the maximum radial force allowed by the concrete ring necessary to prevent tensile splitting in the longitudinal direction. In this case the minimum cover for a single bar is 50 mm and the radius is approximately 8 mm. For two lapped bars the effective area is then given by equation 5.8 with reference to Figure 5.2 (Tepfers 1980, 1982):

$$\pi(c_y + r_b)^2 \left(1 - \frac{\cos^{-1} \dfrac{r_b}{c_y + r_b}}{180} \right) + r_b \sqrt{(c_y + r_b)^2 - r_b^{\,2}} \quad \text{.....(5.8)}$$

where c_y is the smallest clear cover to the tensile reinforcing bars and r_b is the radius of one reinforcing bar.

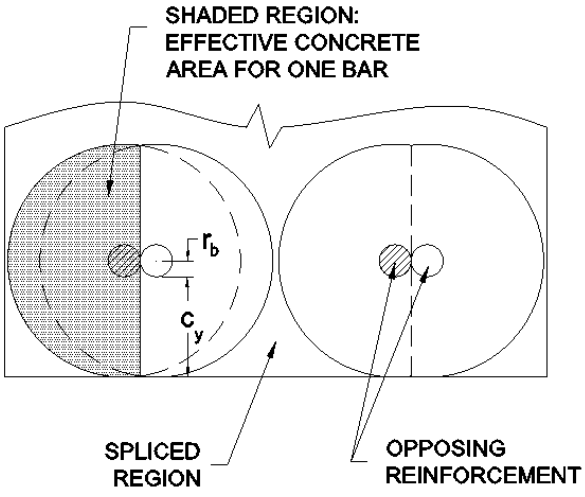

Figure 5.2: Effective concrete area for modulus of displacement analysis (Tepfers 1982)

Based on the areas for concrete and reinforcing bar, a reinforcement ratio can be established. The reinforcing bar tensile modulus and concrete compressive modulus was provided by the manufacturer or through standardized testing and was discussed earlier in Chapter 3. The resulting modular ratio can be obtained from these values. The length of the splice varies

with each specimen either as 150, 225, or 300 mm. The maximum allowable bond stress, τ_{max}, that could be developed at the end of the splice was obtained through RILEM beam tests from a related study (Ametrano 2011; Ametrano et al. 2011; Hossain et al. 2011). Additional testing and research was also required to determine a suitable value for the modulus of displacement, K, and will be discussed in the next section.

5.3 Modulus of Displacement Values

The modulus of displacement, K, is defined as the stress per unit slip between two bonded materials. Tepfers (1980) provides some values and ranges for steel reinforcing bars that can be used for the analysis of conventional steel splices. The bond stress/slip curves obtained from pullout specimens were used to determine these values. This concept requires that the pullout tests have a small embedment length such that the bond stress distribution across the bond length is near constant. An increased embedment length gives higher variation of the bond stress due to stress concentrations at the loaded end of the bar. Thus shorter embedment lengths give values that are more representative of a constant modulus of displacement (Abrishami and Mitchell 1996; Chaallal and Benmokrane 1996; Tepfers 1980, 1982).

Similar to obtaining the modulus of elasticity for a non-linear material, different applications can yield different modulus values depending on which portion of the curve provides a more accurate estimate of the load range. Two types of readings can be obtained from a single curve and they are called the tangent modulus or the secant modulus. From a bond stress/slip curve the possible range is then defined by the initial tangent modulus from the start of the curve where zero slip occurs and the secant modulus to the maximum stress location. The latter provides a value that incorporates more slip and is thus less stiff (lower) than the former. This is due in part to the yielding or plastification of the concrete and bond interface at higher stress values (Tepfers 1980; 1982).

In addition to the possible variation of displacement modulus due to higher and lower stress ranges it is proposed that GFRP may have an increased variation due to the difference in slip between the loaded end and the free end of a pullout test. Due to the low tensile modulus of GFRP, the slip recorded at the loaded end is normally significantly higher than at the free end. As the GFRP bar reaches higher tensile stresses the larger strain from the

loaded end must be accommodated either by excessive slip or some other form of bond degradation. Aside from total pullout failure or bar rupture this can mean either of four things for a modified pullout test as shown in Figure 5.3. The concrete directly surrounding the bar may (a) have a localized cone failure as shown in Tastani and Pantazopoulou (2006), (b) have localized debonding if the splitting tensile capacity of the concrete is stronger than the bond such as the case with steel fibre reinforced concrete, (c) have partial splitting failure if the cover is not sufficient in withstanding the radial forces exerted by the bar onto the concrete noted in Tepfers and De Lorenzis (2003), or (d) the concrete may crack transversely due to excessive longitudinal tensile stress part way into the embedment.

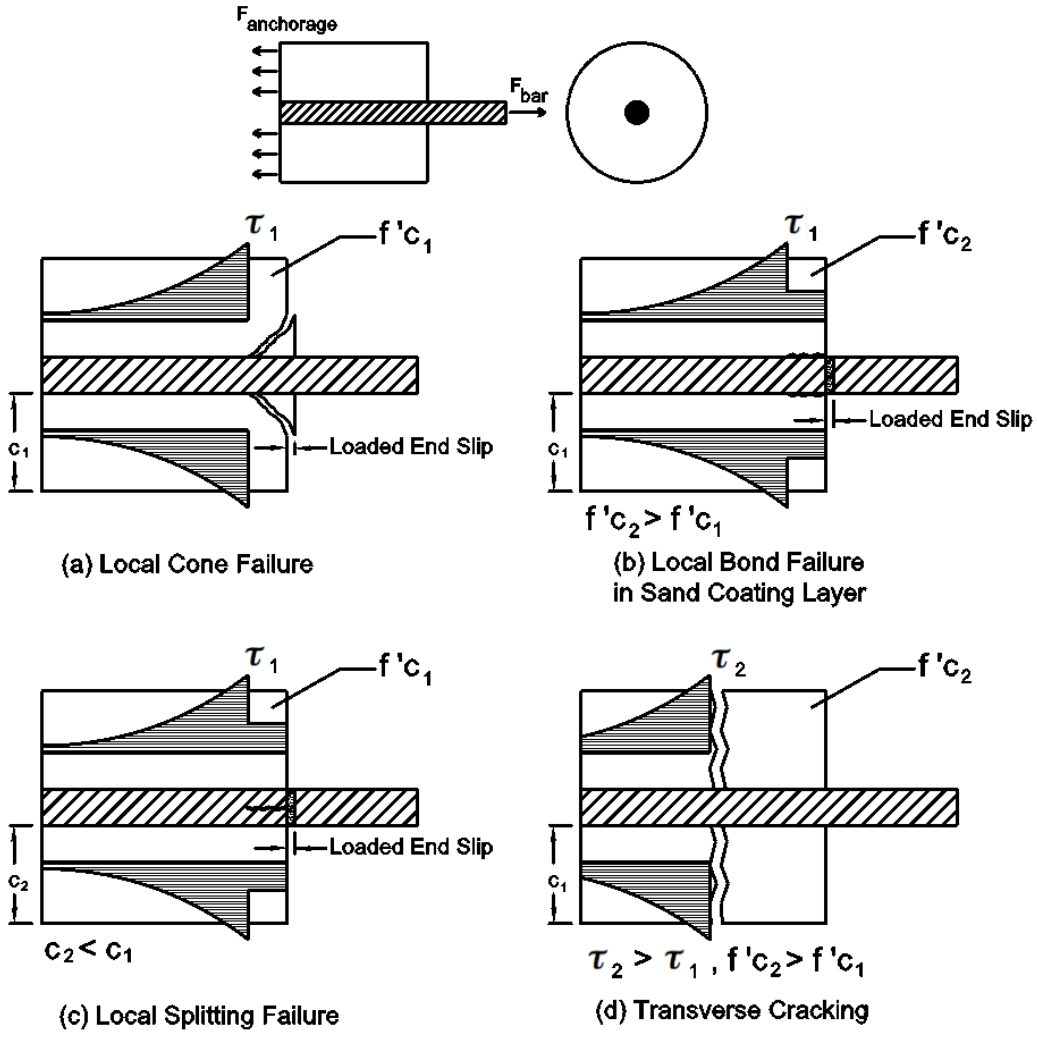

Figure 5.3: Various types of failure modes and excessive loaded end slip conditions for modified pullout tests

Both scenarios (b) and (c) cause slip readings to increase dramatically at the loaded end while still maintaining high bar forces and without any external indication that the bond had deteriorated in that region. This would also be the case for scenario (c) if longitudinal cracks have not yet reached the surface of the specimen. If sufficient concrete cover is provided, preventing longitudinal splitting failure, then scenarios (a) and (b) are more likely to occur. Modified pullout tests conducted on sanded coated GFRP reinforcing bars embedded in normal strength concrete (no fibres) with a clear concrete cover of approximately $3.5d_b$ have shown localized cone pullout failures at the loaded end (Tastani and Pantazopoulou 2006). Even when the embedment length is as low as $3d_b$ the variation of loaded end versus free end slip is still quite high. The last form of strain accommodation for lower tensile modulus GFRP bars is by scenario (d) transverse cracking. If the bond strength and cover are enough to limit local bond or splitting failures then the tensile forces developed in the concrete further into the embedment length may cause cracking across the section.

It is then necessary to determine a suitable range for the modulus of displacement that takes into account the overall variation. An upper bound for the range will be determined using the free end slip from pullout and RILEM beam tests conducted from a related study at Ryerson University by Ametrano (2011), Ametrano et al. (2011) and Hossain et al. (2011) as well as other studies by the following researchers: Aiello et al. (2007), Baena et al. (2009), Lee et al. (2008). The lower bound range will use the loaded end slip behaviour of tests conducted by Aiello et al. (2007) and Baena et al. (2009) since these measurements were not obtained among the results in this study.

Pullout tests using high and low modulus GFRP rebar and high to ultra high strength concrete were tested in a related study and bond stress/slip curves were obtained (Ametrano 2011; Hossain et. al 2011). These tests are similar to those tested with freeze/thaw cycles. The test results provide the upper bound for the modulus of displacement since only the free end slip was obtained. Results from these pullout tests include an embedment length of $3\text{-}5d_b$ for sand coated high and low modulus GFRP rebar with clear cover of 40-60 mm. The concrete strength range was mainly between 100 MPa and 169 MPa, however some additional specimens using lower strength concrete from 45 MPa to 71 MPa were also included from this study to show any differences in the free end slip between high strength and ultra high strength concrete. Bond stress/slip data from RILEM beam tests of short

embedment length are also included for comparison and for the maximum bond strength. Results for concrete strength ranging from 40 MPa to 92 MPa were also included from Lee et al. (2008).

Additional results from Aiello et al. (2007) and Baena et al. (2009) were required in order to obtain the lower bound for the range based on the loaded end slip at maximum bond stress. These results all come from sand coated GFRP pullout tests where pullout failure was reported. The concrete strength range was 52-54 MPa. Due to the difficulty in obtaining the loaded end slip from pullout tests as well as the relatively recent adoption of GFRP by the industry, there is a significant lack of research with sand coated GFRP rebar where bond/slip test results have been reported in detail. An even larger gap exists with HM rebar embedded in UHPC. While it would be ideal to use test results with similar concrete strength and tensile reinforcement properties as the slab/beam specimens themselves, it was not possible to do so. However, the use of higher strength concretes showed that failure occurs mainly in the resin between the sand coating layer and the fibre core (Lee et al. 2008). It is believed the resulting bond slip behaviour would share some similarities given that the resin governs the bond strength for both HM and LM bars. Moreover, since we are looking for a lower bound for the modulus of displacement, the use of normal strength concrete with a low modulus bar would only increase the slip at maximum bond stress and would thus provide a range that is inclusive of more accurate results.

Results included in the database are of failure by pullout or by peeling off of the sand coating only and not by splitting. This is to keep the failure mode and slip behaviour consistent with the slab/beam specimens. Figure 5.4 shows these results graphed and categorized based on free end and loaded end slip. The slip values were obtained at maximum bond stress. Due to the large variation of maximum bond stress obtained from this data set a line of best fit was used with the free end slip and loaded end slip results at peak stress and slip to represent the upper bound and lower bound, respectively, for K (Fig. 5.4). The specific details of this data set are shown in the Appendix.

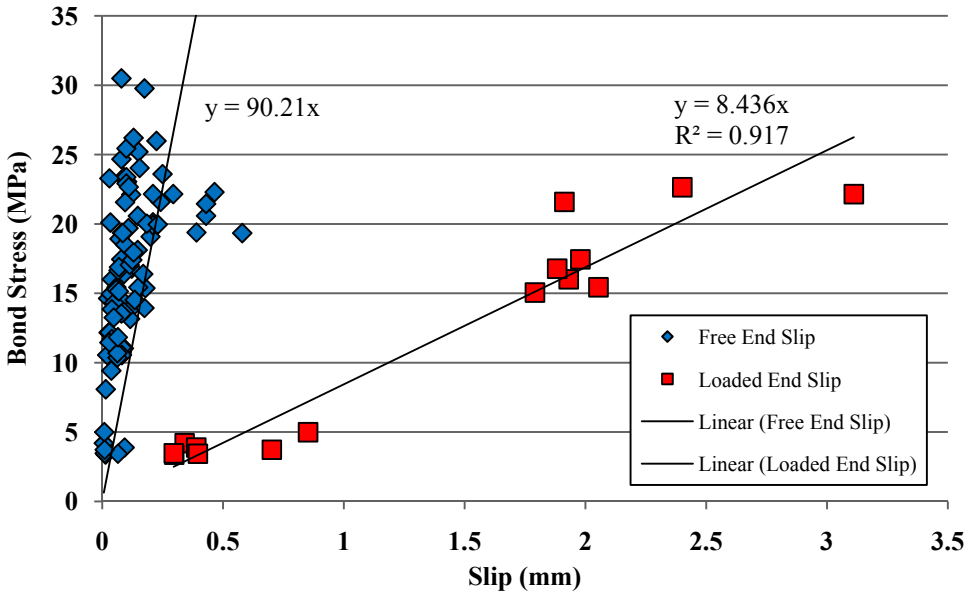

Figure 5.4: Range of variation for modulus of displacement K

Each group of tests was plotted with a line of best fit crossing through the origin. The slope of each line represents possible limits for K. As shown in Figure 5.4 the range for K is quite large with the upper bound of 90.21 N/mm^3 equal to 10.7 times the lower bound of 8.436 N/mm^3. This type of behaviour has also been reported by Aly (2007) where pullout tests for various types of sand coated FRP showed an upper bound of 10 times the lower bound. However, it is expected that the lower bound values for displacement modulus would provide the most accurate representation of the bond stress distribution at failure since it incorporates a higher degree of ductility and slip similar to the behaviour of the slab/beams in this research. Furthermore, the loaded end slip is based more accurately on higher stress levels since the majority of the stress is concentrated within the loaded region due to the low tensile modulus of the GFRP bar. Free end slip measurements, although are significantly lower than the loaded end, are based on a much smaller magnitude of bond stress due to the uneven distribution of bond stress. Using such a high value for K increases the bond stress concentration developed at the loaded end in order for the concrete to remain connected to a highly strained bar. Aly (2007) also reports that due to the lower tensile modulus of GFRP relative to steel, it is not accurate to use a single modulus of displacement throughout the entire loading range up to failure. Rather when small loads are applied the initial tangent modulus can be used since the slip values are much lower due to lower bar strains. As load

increased to the point of failure it was reported that reduced values for the modulus of displacement, on the order of 5-30 N/mm^3, better predicted the stress distribution due to an excess of localized slip. This type of stress slip behaviour is critical to accurately predicting the bond stress distribution at failure. Both the full cast slab/beams and the pullout specimens in the current study demonstrate this type of localized behaviour at large stress values as explained earlier. The spliced bond/bar stress distribution at failure should then be predicted using the smallest expected value for modulus of displacement so as to incorporate the additional localized slip. The analysis carried throughout this chapter shall assume a value of 8.436 N/mm^3 in lieu of better results using high modulus bars.

5.4 Bar Stress/Bond Stress Prediction Using Modulus of Displacement Theory

5.4.1 Uncracked Splice

Based on the theoretical equations for bar stress and bond stress it should be possible to combine the modulus of displacement for an expected load range with the ultimate bond capacity from pullout or hinged beam tests of short embedment length to predict the maximum bar force that can be developed within a splice of known dimensions and material properties. The comparisons shown here neglect the possibility of longitudinal splitting failure due to the confining action of the steel fibres in the concrete. If analysis is to be conducted with regards to splitting failure then the ultimate bond stress and modulus of displacement should be based on tests results of that failure mode.

Ultimate bond stress capacities, τ_{max}, obtained from pullout and or hinged beam tests can be substituted into equations 5.4 and 5.5 for τ_1 and τ_2 to obtain the maximum bar force σ_{frp0} that can be developed. The assumption is that once the maximum bond stress has been reached at the loaded ends of the splice, then localized bond failure will occur and only frictional forces will remain between the bar and the concrete in that region. The bar force must then be transferred back into the splice in order to maintain the same load. Progressive localized bond loss and slip will continue if the load is not released resulting in complete failure of the splice. The maximum capacity of the splice is then the bar force calculated when the loaded end first reaches the ultimate bond strength, τ_{max}.

Hinged RILEM beam tests with short embedment length ($3d_b$) will be used to obtain the maximum bond stress (Hossain et al. 2011). Hinged beam tests better predict the actual

flexural behaviour of members under bending versus pullout tests since the location of the embedment is also under tension (Tighiouart et al. 1998). Table 5.2 shows several values for maximum bond stress obtained from such beam tests. These values were also included in the data set for determining modulus of displacement. The concrete strengths shown here approximate those of the full cast slab/beam tests fairly well. An average value between two specimens was used for the last entry in Table 5.2. Maximum bond stress values (τ_{max}) used for theoretical predictions are presented in Table 5.1 and were extrapolated from these two points based on the concrete strength of each slab/beam in lieu of more test results.

Table 5.2: Bond stress values from hinged beam test specimens

Bar Type	*f'c* (MPa)	Bar Diameter (mm)	Embedment Length (mm)	No. Bar Diameters Embedded	Surface Condition	Maximum Bond Stress (MPa)
High Modulus	115.5	15.9	47.7	3	Sand Coated	20.1
High Modulus	160.0	15.9	47.7	3	Sand Coated	22.5

Based on the failure mode of each slab/beam specimen, it is assumed that the bond stress at the loaded end of the splice will reach a maximum value equivalent to the ultimate bond stress obtained from RILEM beam specimens of short embedment length. Once this value has been reached at the loaded end of the splice, no more load can be applied to the bar without localized bond failure occurring at the loaded end. Continuous loading will then lead to progressive failure of the embedment. Thus the values in Table 5.1 and the maximum bond stress values (τ_{max}) interpolated from Table 5.2 will be used with equations 5.4 and 5.5 to determine the maximum bar stress (σ_{frp0}) that can be applied at the loaded end. The maximum bar stress can then be used in equations 5.1-5.3 to determine the concrete tensile stress distribution as well as the longitudinal bar stress distribution.

In the following sections a comparison will be made with the experimental bar stress variation from the spliced slab/beam tests to verify the validity of this method. By inspection the free end of the splice will have zero bar stress while the loaded end stress is obtained from the beam theory calculations in Chapter 4. Further verification will be from the strain readings at mid-splice converted to stress using the tensile modulus of the GFRP bar.

5.4.2 Cracked Splice

The equations presented previously apply only to splices that do not have cracks transverse to the reinforcement. If transverse cracks form they will tend to start at the midpoint between the initial two cracks that first appear at the ends of the splice. Additional cracking would then appear at the 1/4 points then the 1/8 points etc as shown in Figure 5.5.

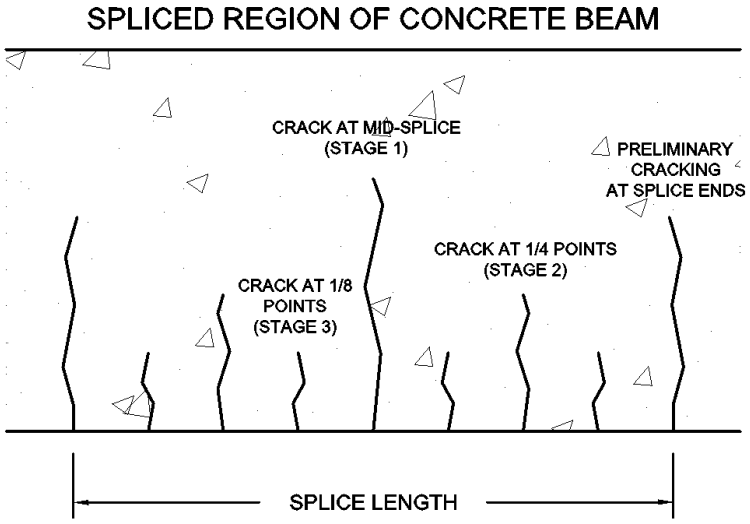

Figure 5.5: Crack progression within a splice

Prior to cracking within the splice the tensile stress in the concrete typically accumulates to a maximum at the mid-point due to the transfer of bond forces from the reinforcement to the concrete (Tepfers 1980). The MDT is based on a constant stress distribution on a cross section of the effective concrete area constituting the concrete ring. This is not true for beam specimens under bending. For beam specimens the concrete stress determined using equation 5.1 actually gives the average concrete tensile stress over the effective area while the maximum concrete stress occurs at the bottom of the beam. To include this additional stress, the assumption must be made that between cracks a linear stress distribution still exists across the section, which is generally true with UHPC. Since both types of GFRP rebar have relatively similar modulus of elasticity as the concrete a good preliminary estimate of the neutral axis depth prior to cracking would be at mid-depth of the beam. The concrete tensile stress from equation 5.1 is assumed to be at the same level as the bar. From the known geometry of the beam we can then predict the maximum tensile stress

at the bottom of the beam where cracking would normally begin by use of a curvature factor. An initial estimate of the maximum curvature factor for this slab/beam is about 2.38 as shown in Figure 5.6. When used at mid-splice prior to cracking, this factor is the ratio of the maximum concrete tensile stress at the bottom of a flexural member to the average tensile stress determined from equation 5.1. The average value of tensile stress is assumed to occur at the level of the bar. The curvature factor is thus obtained as the ratio between the distance from the neutral axis to the bottom of the section and the distance from the neutral axis to the location of the bar. By using the factor of 2.38, we can compare the stress at the extreme tension fibre of concrete to the modulus of rupture and determine if cracking has occurred.

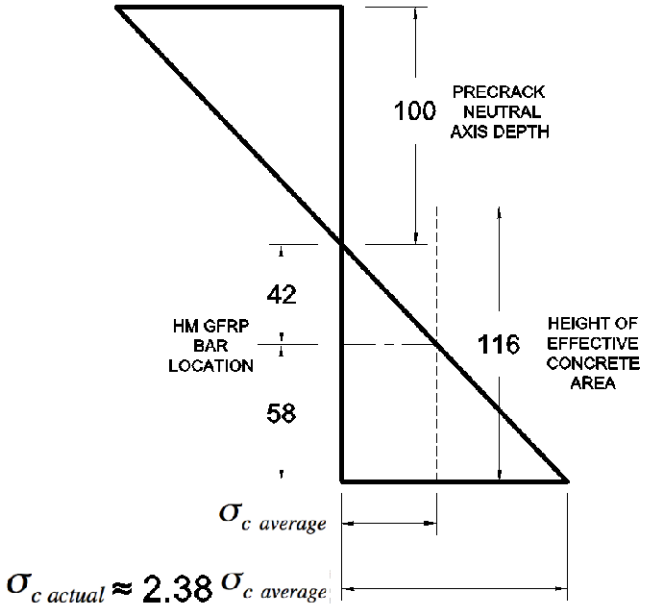

Figure 5.6: Pre-crack UHPC concrete slab/beam stress distribution within the splice

To derive the equations for a single crack at mid-splice, equations 5.9 and 5.10 were used as boundary conditions at mid-splice and end splice to solve for the coefficients A and B in the general equations 5.11 for bar stress distribution and 5.12 for concrete tensile stress distribution. Equations 5.8 and 5.9 were derived assuming zero concrete tensile stress contribution by setting the reinforcement ratio to infinity (Tepfers 1980).

$$\sigma_{frp1} = \frac{\sigma_{frp0}}{2}\left[1 - \frac{\sinh(\kappa_2 x)}{\sinh(\kappa_2 l/2)}\right] \quad (5.9)$$

$$\sigma_{frp2} = \frac{\sigma_{frp0}}{2}\left[1 + \frac{\sinh(\kappa_2 x)}{\sinh(\kappa_2 l/2)}\right] \quad (5.10)$$

$$\sigma_{frp} = A\cosh(\kappa_2 x) + B\sinh(\kappa_2 x) + \frac{\sigma_{frp0}}{2(1+2n\rho)}\frac{\cosh(\kappa_1 x)}{\cosh(\kappa_1 l/2)} + \frac{\sigma_{frp0} n\rho}{1+2n\rho} \quad (5.11)$$

$$\sigma_{ct} = A\sinh(\kappa_1 x) + B\cosh(\kappa_1 x) + \frac{\sigma_{frp0}\rho}{1+2n\rho} \quad (5.12)$$

By differentiating equations 5.9 and 5.10 and multiplying by the ratio of bar area to bar perimeter the equations for bond stress are obtained for zero concrete stress contribution. These equations are as follows (Tepfers 1980):

$$\tau_1 = -\frac{\sigma_{frp0} A_b \kappa_2}{2u}\frac{\cosh(\kappa_2 x)}{\sinh(\kappa_2 l/2)} \quad (5.13)$$

$$\tau_2 = \frac{\sigma_{frp0} A_b \kappa_2}{2u}\frac{\cosh(\kappa_2 x)}{\sinh(\kappa_2 l/2)} \quad (5.14)$$

The following equations are for use with a splice with one transverse crack occurring at mid-splice:

The equation for bar stress is:

$$\sigma_{frp1,\,frp2} = A\cosh(\kappa_2 x) + B\sinh(\kappa_2 x) + \frac{\sigma_{frp0}}{2(1+2n\rho)}\frac{\cosh(\kappa_1 x)}{\cosh(\kappa_1 l/2)} + \frac{\sigma_{frp0} n\rho}{1+2n\rho} \quad (5.15)$$

The equation for bond stress is:

$$\tau_{1,2} = \frac{A_b}{u}\left[A\sinh(\kappa_2 x)\kappa_2 + B\cosh(\kappa_2 x)\kappa_2 + \frac{\sigma_{frp0}\kappa_1}{2(1+2n\rho)}\frac{\sinh(\kappa_1 x)}{\cosh(\kappa_1 l/2)}\right] \quad (5.16)$$

where A is equal to:

$$A = \frac{\sigma_{frp0}}{2} - \frac{\sigma_{frp0}}{1+2n\rho}\left[\frac{1}{2\cosh(\kappa_1 l/2)} + n\rho\right] \quad \text{.....(5.17)}$$

and B for σ_{frp1} for $-l/2 < x < 0$ and $0 < x < l/2$ respectively are:

$$B_{-l/2<x<0} = \frac{\sigma_{frp0}}{1+2n\rho}\frac{\cosh(\kappa_2 l/2)}{\sinh(\kappa_2 l/2)}\left[\frac{1+2n\rho}{2}\left(1 - \frac{1}{\cosh(\kappa_2 l/2)}\right) - \frac{1}{2\cosh(\kappa_1 l/2)} - n\rho\right] \quad \text{.....(5.18)}$$

$$B_{0<x<l/2} = \frac{-\sigma_{frp0}}{1+2n\rho}\frac{\cosh(\kappa_2 l/2)}{\sinh(\kappa_2 l/2)}\left[\frac{1+2n\rho}{2}\left(1 + \frac{1}{\cosh(\kappa_2 l/2)}\right) - \frac{1}{2\cosh(\kappa_1 l/2)} - n\rho\right] \quad \text{.....(5.19)}$$

and B for σ_{frp2} for $-l/2 < x < 0$ and $0 < x < l/2$ respectively are:

$$B_{-l/2<x<0} = \frac{\sigma_{frp0}}{1+2n\rho}\frac{\cosh(\kappa_2 l/2)}{\sinh(\kappa_2 l/2)}\left[\frac{1+2n\rho}{2}\left(1 + \frac{1}{\cosh(\kappa_2 l/2)}\right) - \frac{1}{2\cosh(\kappa_1 l/2)} - n\rho\right] \quad \text{.....(5.20)}$$

$$B_{l/2<x<0} = \frac{-\sigma_{frp0}}{1+2n\rho}\frac{\cosh(\kappa_2 l/2)}{\sinh(\kappa_2 l/2)}\left[\frac{1+2n\rho}{2}\left(1 - \frac{1}{\cosh(\kappa_2 l/2)}\right) - \frac{1}{2\cosh(\kappa_1 l/2)} - n\rho\right] \quad \text{.....(5.21)}$$

For the concrete stresses with a crack at the midpoint:

$$\sigma_{ct} = A\sinh(\kappa_1 x) + B\cosh(\kappa_1 x) + \frac{\sigma_{frp0}\rho}{1+2n\rho} \quad \text{.....(5.22)}$$

where B is equal to:

$$B = \frac{-\sigma_{frp0}\rho}{1+2n\rho} \quad \text{.....(5.23)}$$

and A for σ_{ct} for $-l/2 < x < 0$ and $0 < x < l/2$ respectively are:

$$A_{-l/2<x<0} = \frac{\sigma_{frp0}\rho}{1+2n\rho}\frac{1}{\sinh(\kappa_1 l/2)}\left[1 - \cosh(\kappa_1 l/2)\right] \quad \text{.....(5.24)}$$

$$A_{0<x<l/2} = \frac{\sigma_{frp0}\rho}{1+2n\rho}\frac{1}{\sinh(\kappa_1 l/2)}\left[\cosh(\kappa_1 l/2) - 1\right] \quad \text{.....(5.25)}$$

Transverse cracking allows the embedded bar to have some additional strain at the location of the crack while still maintaining full bond with the concrete. This sudden change in bar strain at the crack location has several effects. The first is that it allows additional bond forces to form further down the splice away from the loaded end past the transverse crack location. Secondly, it reduces the bond stress concentration at the loaded end of the splice. The crack is effectively transferring some of the stress at the loaded end closer to the free end of the splice where little stress had originally existed prior to transverse cracking. This allows a larger bar force to be developed prior to the onset of localized bond failure since the bond stress distribution is more evenly distributed. While transverse cracking within the splice allows for a higher moment capacity it does reduce the serviceability performance by increasing the deflection. Provided that sufficient cover is used to prevent longitudinal cracking along the bar it can be said that a lower tensile strength concrete, that is allowed to have some transverse cracks within the splice, will have a higher pullout capacity than a higher tensile strength concrete that prevents transverse cracks. The latter prevents bond stress from accumulating further into the splice and concentrates it at the loaded end causing localized bond failure to occur.

5.4.3 General Method for Determining the Ultimate Capacity of Spliced GFRP Rebar

To determine the ultimate capacity of a splice the following steps should be followed. The conditions stated in previous sections must be true for accurate results.

1) Given the maximum bond stress from a short embedment length hinged RILEM beam test and the modulus of displacement from the loaded end slip (obtained from pullout tests in lieu of loaded end slip from hinged RILEM beams) determine the maximum bar stress that can be generated using equations 5.4 and 5.5. The assumption must be made that no splitting failure can occur. If splitting is expected then the pullout and hinged beam test results must reflect this mode of failure.
2) Determine the concrete stress distribution from equation 5.1 using the maximum bar stress obtained from step 1.
3) Compare the curvature factored maximum concrete stress at mid-splice (2.38 for the slab/beams in this research) with the modulus of rupture for the concrete. If the factored concrete stress is higher than the modulus of rupture then cracking will occur

and additional bar stress may be possible. Otherwise the ultimate capacity of the splice will be the maximum bar stress determined from step 1.

4) If cracking occurs then repeat step 1 using the bond stress equations 5.16 - 5.21 for cracked concrete at mid-splice to determine the maximum bar stress.
5) Check the resulting concrete tensile stress distribution using the curvature factor and equations 5.22-5.25 to see if additional cracking will occur. If additional cracking will occur then additional equations may need to be derived for additional cracking at the quarter points. If the crack spacing and resulting concrete stresses are sufficiently small then equations 5.13 – 5.14 may simply be used to find the maximum bar stress. Tepfers (1980) concluded that for conventional steel reinforcement cracking tends to halt at a spacing of 50-200 mm.

There is also the case where cracking may initiate some distance away from the ends of the splice due to other factors such as the presence of transverse reinforcement. This was true for the smaller splice lengths of 150 mm in this study where cracking initiated at the location of the last stirrup. The effect of this premature cracking would cause the maximum bar stress to occur away from the end of the splice. Bar forces will then be reduced while concrete tensile stresses are increased due to the transfer of bond forces to the concrete. At the end of the splice the bar stress will be some value less than the maximum. Several things can happen from this point onward if the applied load on the slab/beam is increased. Increasing tensile stresses in the concrete will eventually cause additional cracking to occur directly at the end of the splice due to a sudden change in cross-section such as with R300 or, if the distance between the first crack and the end of the splice is too small, cracking will initiate at mid-splice. Aside from bond stress transfer, the concrete in the second case will also take on additional tensile forces due to the applied bending moment. This was the case with R150 slab/beams.

This method of analysis becomes more accurate with a better understanding of the cracking behaviour of the concrete within the splice. However the results obtained using uncracked concrete are considered to be more conservative since it assumes that bond failure occurs at the loaded end prior to developing additional bond stresses from transverse cracking.

5.4.4 Bond Stress / Concrete Stress Distribution

Figures 5.7 to 5.14 show the theoretical bond stress and concrete stress distributions predicted using the values in Table 5.1 and the previous equations for cracked and uncracked splices. The bond stress distributions presented here are the basis for the ultimate bar force and bar stress distributions obtained in the next section. There are several important things to note from these figures:

- The bond stress distribution is not constant along the splice length.
- Maximum bond stress was assumed to occur at the loaded end first.
- The bond stresses at the free end are significantly lower than at the loaded end and this difference in bond stress increases with splice length.
- The concrete tensile stress is a maximum at center splice when no transverse cracking is present.
- The concrete tensile stress at mid-splice increases with the splice length.
- The concrete tensile stresses should be multiplied by a curvature factor of 2.38 (based on the geometry of the specimen) due to the curvature in the slab/beam in order to determine whether the concrete in the splice will crack.
- Use of the curvature factor with the maximum concrete stress of each specimen prior to cracking shows that D slab/beams had not reached their range for modulus of rupture (Figs. 5.7-5.10) while R300 slab/beam (Fig. 5.14) was well within type R concrete's modulus of rupture range. R150A and R150B showed values that were quite close (Figs. 5.11-5.12). Thus only type R specimens experienced considerable cracking within the splice due to the significantly lower tensile capacity of the concrete while type D slab/beams did not.
- Although, the maximum curvature factored concrete tensile stress for R150A and R150B (Figs. 5.11-5.12) were not directly in their cracking range it is believed that due to the initiation of cracks away from the ends of the splice (from the presence of steel stirrups) additional tensile stresses were taken by the concrete to resist the applied moment. Thus R150A and R150B tests specimens were actually able to achieve a state of transverse cracking and are shown graphed with both stress distributions for cracked and uncracked concrete.

- After cracking takes place concrete stresses are significantly reduced and a stress discontinuity exists at the location of cracking for both the bond stress and concrete tensile stress distributions (Figs. 5.11-5.12, 5.14).
- Bond stresses beyond the crack location are greater in magnitude than the bond stress distribution without cracks (Figs. 5.11-5.12, 5.14).
- At the crack location GFRP bars will take all the tensile force.
- The presence of friction at the loaded end after localized bond stress failure was neglected in this analysis. For longer embedment lengths the frictional component may contribute more pullout resistance than the bond stress at the free end.

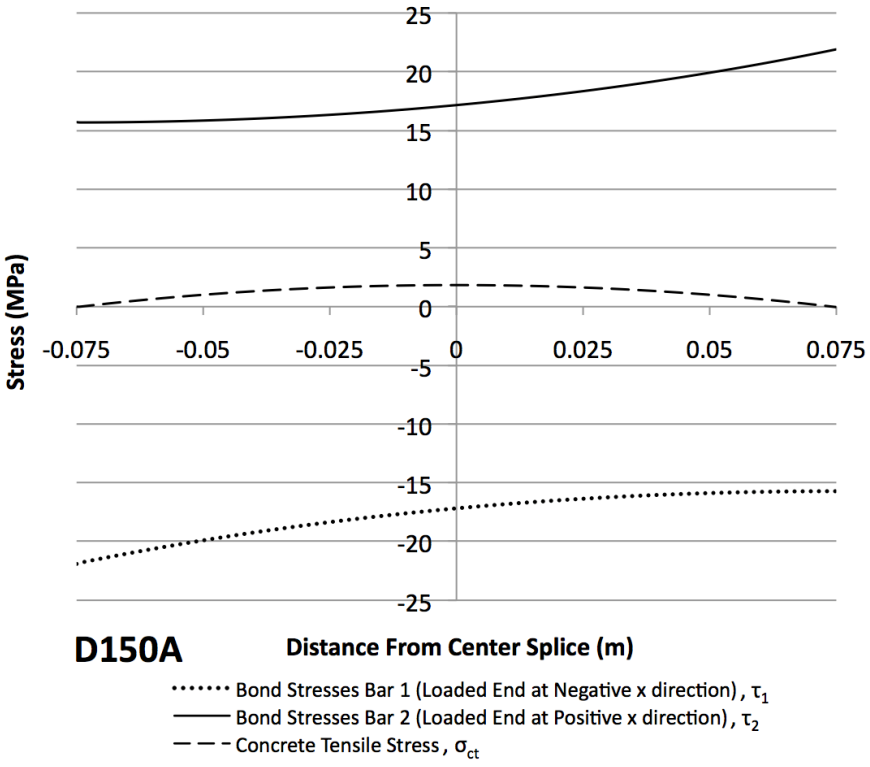

Figure 5.7: D150A theoretical bond stress and concrete tensile stress distribution

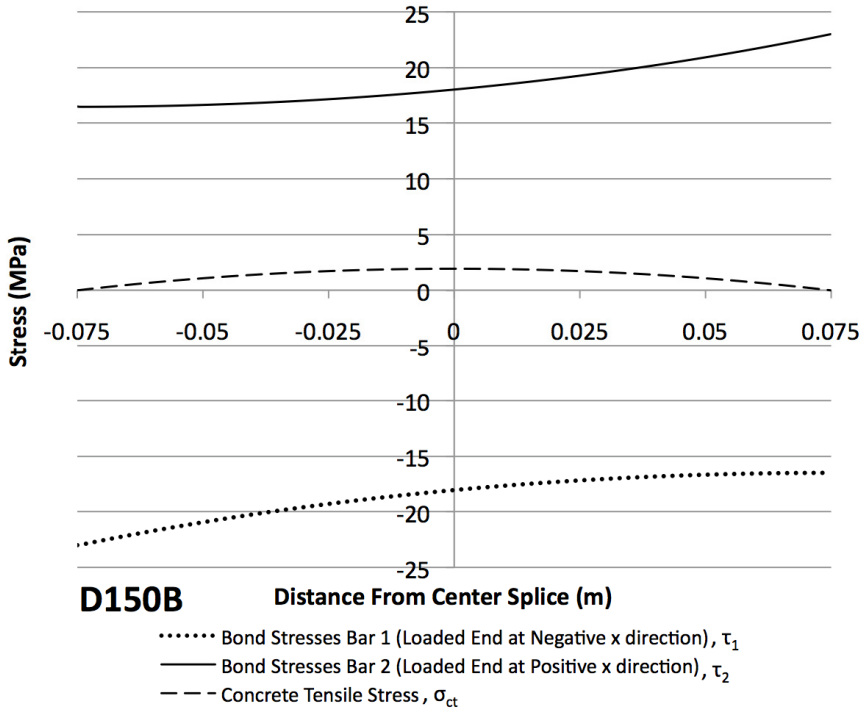

Figure 5.8: D150B theoretical bond stress and concrete tensile stress distribution

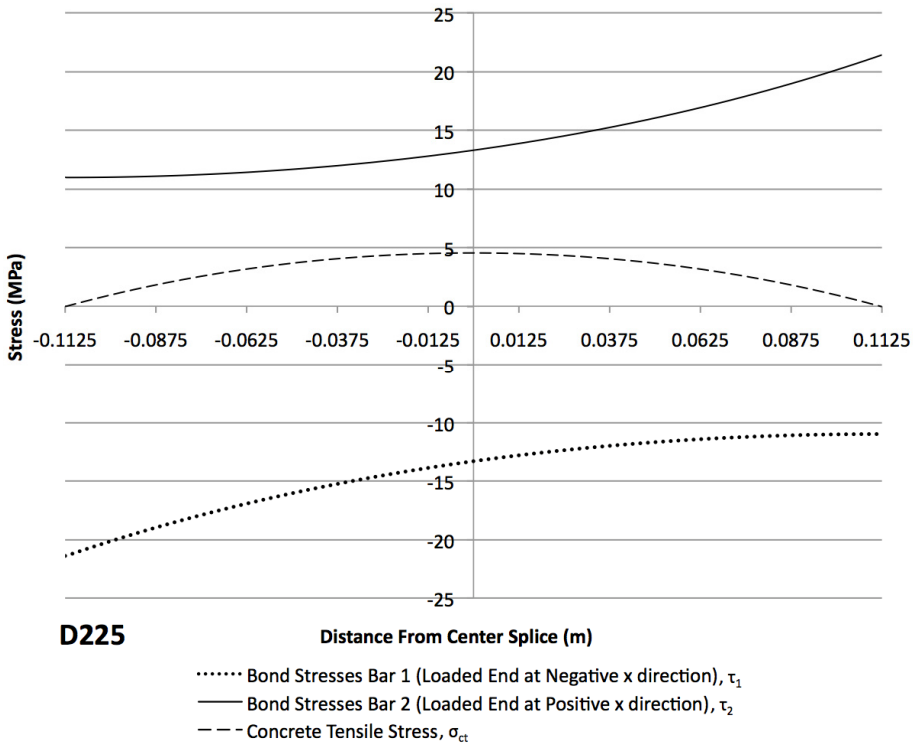

Figure 5.9: D225 theoretical bond stress and concrete tensile stress distribution

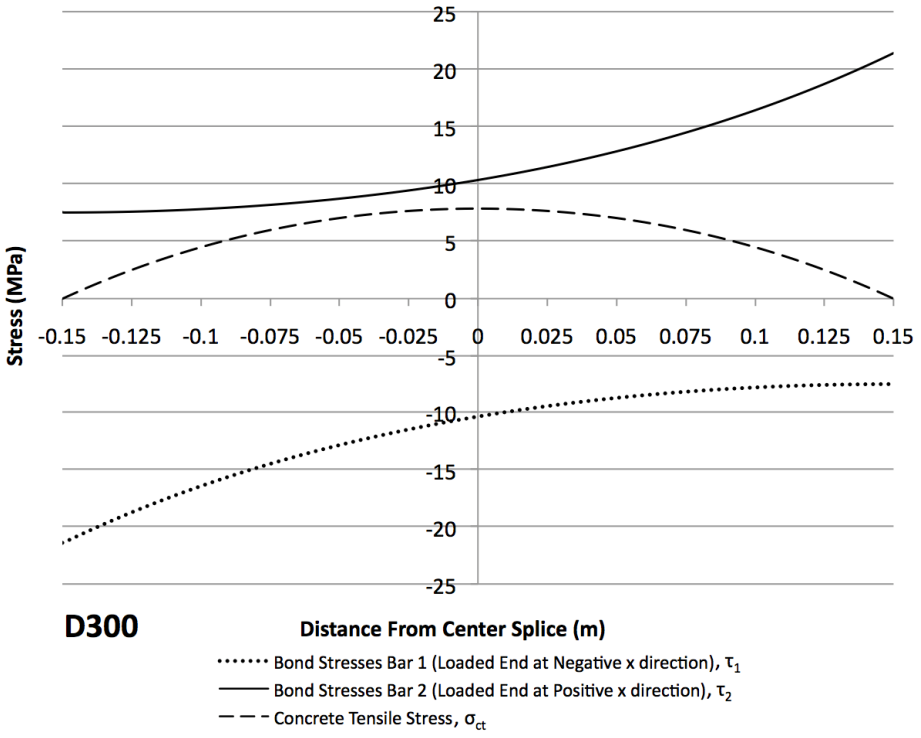

Figure 5.10: D300 theoretical bond stress and concrete tensile stress distribution

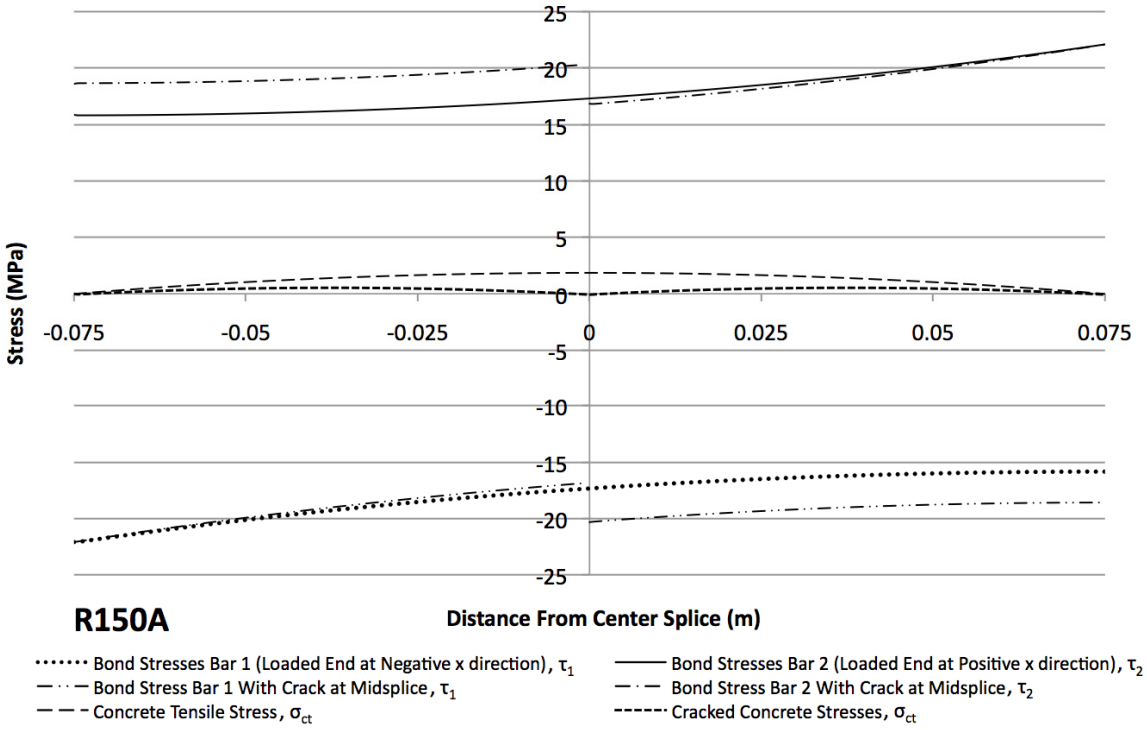

Figure 5.11: R150A theoretical bond stress and concrete tensile stress

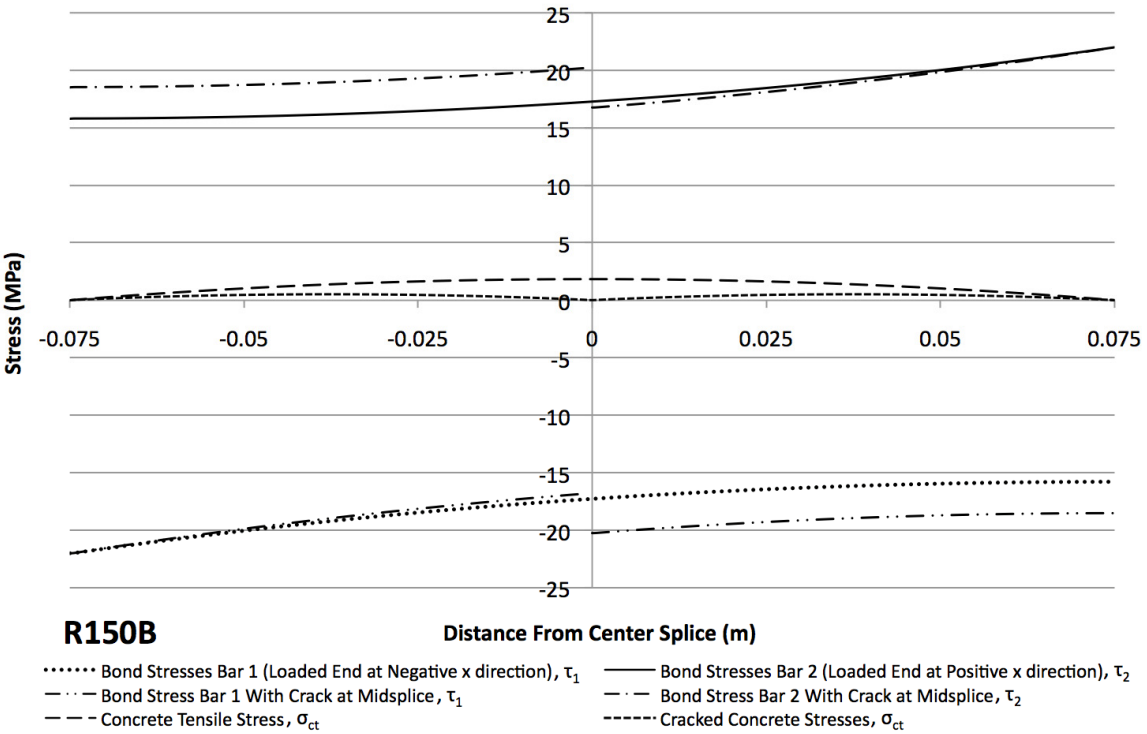

Figure 5.12: R150B theoretical bond stress and concrete tensile stress

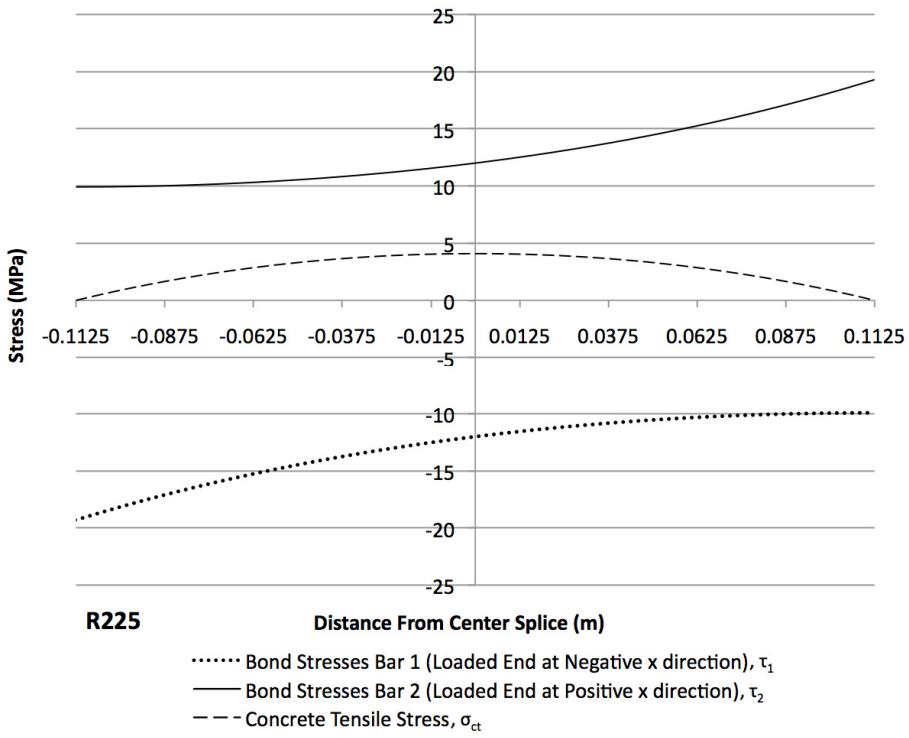

Figure 5.13: R225 theoretical bond stress and concrete tensile stress

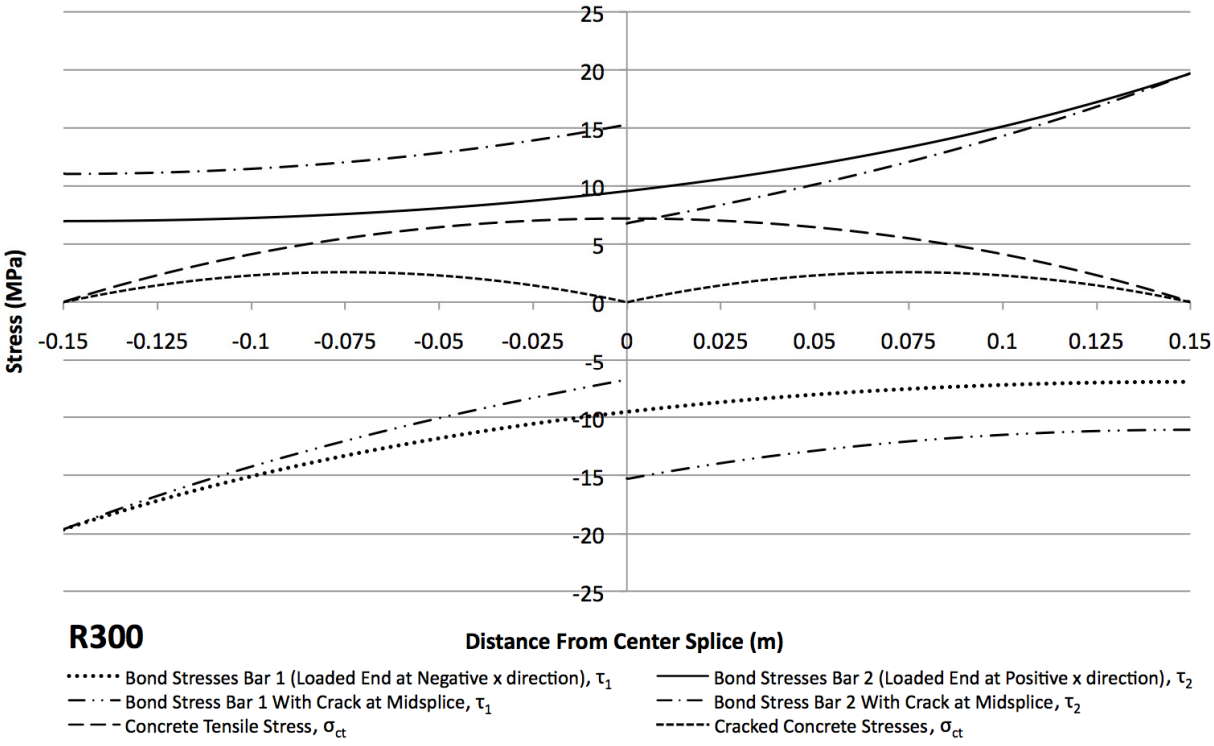

Figure 5.14: R300 theoretical bond stress and concrete tensile stress

5.4.5 Bar Stress Distribution and Comparison of Modulus of Displacement Theory With Experimental Results

The maximum bar stress obtained from the general method proposed in section 5.4.3 are compared with the experimental stress values at the end of the splice. Values predicted for R150A, R150B and R300 using the equations for cracked concrete will be explained in the following discussion. Table 5.3 shows the percent error in the prediction of maximum bar stress by the MDT estimate and the actual maximum bar stress obtained using beam theory at the critical section. With the exception of D300, the predicted values for all full cast spliced beam specimens were within an 11% range of the actual bar stress obtained from experimental tests. This demonstrates the validity of the MDT method for predicting the ultimate capacity of a splice. The mid-splice bar strain will also be compared in the following discussion for further verification.

Table 5.3: Comparison of actual and predicted ultimate bar stress

Specimen	Actual Bar Stress (MPa)	Estimated Bar Stress (MPa)	% Error
D150A	721.2	668.7	-7.3
D150B	757.5	702.2	-7.3
D225	773.6	807	4.3
D300	759.5	882.9	16.2
R150A	751.9	723.5	-3.8
R150B	801.3	720.2	-10.1
R225	816.4	728.2	-10.8
R300	903.1	939.4	4.0

Slab/Beams D150A and D150B

Both D150A and D150B spliced beams shared very similar material properties as well as identical geometric configurations so both had a closely predicted pullout capacity. However the concrete strength for D150B was slightly higher due to a significant concrete age difference. This discrepancy is noticeable in both actual and estimated values showing a slightly higher bar stress for D150B versus D150A (Table 5.3). The small amount of fatigue loading that D150B received showed no effect on the maximum bar stress of the splice. The accumulation of bar strain at mid-splice was not included among the graphs since these effects were not significant in this comparison. The model provides a fairly accurate

prediction of the bar stress distribution along the splice. Figures 5.15 and 5.16 show that mid-splice stress values were quite consistent with the theoretical prediction for both specimens. However, as seen throughout several of the other full cast slab/beams including D150B, one bar reaches a significantly higher stress at mid-splice while the opposing bar stress remains the same. This strain separation occurs at approximately 85% of the ultimate load capacity of D150B and nearly at the ultimate applied load for D150A (Figs. 4.6-4.7). The earlier strain separation of D150B may have been a result of fatigue loading. Beyond this point the third phase of excessive plastic damage occurs. This behaviour is consistent with a large change in deflection but only a very small increase in the load capacity as was explained in the discussion of the results in Chapter 4.

The most likely cause for strain separation is due to localized bond failure at the loaded end of the splice. The high ductility of the splice allowed for significant deflection to occur while still maintaining similar load capacity. The addition of fatigue cycles for D150B would have also contributed to the bond degradation at the loaded end, which reduced the impact that would have occurred from a sudden bond loss. After reaching loads close to the maximum the large deflection and curvature that accumulates at the center of the beam causes bending in the GFRP bar itself. Although the strain gauges were placed level with the neutral axis these bars may have moved during casting causing the gauge to have additional strain from bending.

Referring to the load strain curves for D150A and B (Figs. 4.6-4.7) it is clear that there was very little change in load capacity between the point where the maximum occurs and the point where the mid-splice bar stresses begin to separate due to this plastic deformation. The modulus of displacement model therefore provided an accurate prediction of both the maximum bar stress and overall distribution for both D150A and D150B slab/beams at failure. The initiation of cracking slightly away from the end of the splice would have also enhanced pullout capacity of the reinforcing bars since more bond forces are transferred to the concrete prior to reaching the splice. This contributed to the slight underestimation of the bar force since this was not taken into account during the analysis.

Slab/Beams D225 and D300

A comparison between the larger embedment lengths of D225 and D300 show that D300 had experienced a premature failure. It was expected that D300 would have provided a larger load capacity than the smaller embedment lengths of D225 and D150B. This is one reason for the large over estimation of the maximum bar stress in Table 5.3 for D300. D225 however, with a 225 mm splice, showed an increase in ultimate load capacity versus the smaller embedment lengths of 150 mm as expected. A comparison of mid-splice bar stresses also shows an over prediction by the MDT for both specimens (Figs. 5.17-5.18). This is a drawback from using a constant modulus of displacement to represent the entire embedment length. For shorter embedment lengths such as 150 mm it is expected that a constant modulus of displacement would provide a good estimate of the bond behaviour for the entire length of splice. As the embedment length increases the latter portion of the splice close to the free end will deviate from this modulus and move towards a larger value. The reason is because the lower bound used for the modulus of displacement best represents a bond state that is near plastic with a larger amount of slip. But if the distance from the loaded end increases the bond state will change to a more elastic behaviour with a stiffer modulus. The end result is that less bond stress will be transferred to the latter portion of the splice and the actual bar stress distribution will be lower than predicted. Type D concrete also has a much stiffer and more brittle bond behaviour than the other concrete types used to obtain the modulus of displacement which also contributes to the large overestimation of the maximum bar stress of D300 and is visible in the bar stress distributions of both D300 and D225 in Figures 5.17 and 5.18.

Slab/Beams R150A and R150B

Figures 5.19 and 5.20 show the theoretical prediction for both cracked and uncracked splices of R150 specimens. The prediction of bar stress using cracked concrete does not strictly follow the general method outlined earlier. More accurate predictions can be obtained with a better understanding of the cracking behaviour of the specimens. It is believed that the cracks bordering the spliced region formed some distance away from the ends of the splice due to the reduced cross-section at the stirrup location. This additional bonded length may have been the reason for the underestimation of the maximum bar stress

for these two beams (Table 5.3). Bond stresses developed earlier on in the concrete without the ability to transfer forces directly over to an adjacent bar through compressive struts normally developed between two spliced bars in concrete (Fig. 2.11). By the time the bar enters the splice the tensile stress in the concrete is much higher while the bar stress is reduced. More emphasis is placed on the concrete to directly resist the tensile force from the applied moment, which for the case of R150 slab/beams caused additional cracking at center splice. While the theoretical model does not include methods to predict this type of cracking behaviour, the use of the cracked concrete equations still gives a better representation of the state of the concrete within the splice. When modeled without transverse cracking the maximum bar stress prediction has a much larger discrepancy due to the fact that more of the bond stress is concentrated at the loaded end. A better understanding of the cracking behaviour would definitely improve the accuracy of the predictions.

Similar to D150B the bar coming from the loaded end nearest to the critical section experienced excessive strain at mid-splice. This strain separation at mid-splice occurs at about 82-88% of the ultimate capacity for R150 slab/beams (Figs. 4.10 - 4.11). Beyond 90% of the ultimate capacity is where the third stage of loading begins. At this point the slab/beam reaches a plastic curvature hardening stage where large deformations such as cracking must occur in order to accommodate a small increase in load capacity. The small discrepancies in stress at mid-splice may be due to the small variation of the location where cracks actually occurred in the slab/beam (Figs. 5.19-5.20). In theory transverse cracking should occur first at mid-splice but some variance can be expected. Overall, the MDT showed good agreement with the maximum bar force calculated from the experimental results of R150 slab/beams.

Slab/Beam R225

The MDT predicts the overall bar stress distribution of R225 (Fig. 5.21) and the maximum bar stress very well (Table 5.3). Similar to the other slab/beams the mid-splice stress for the failing GFRP bar began to separate from the opposing bar. The measured strains at mid-splice even exceed the values calculated using beam theory at the critical section. This is clear evidence that some slip had indeed occurred because if the bar force is the same between two points then there should be no bond forces acting between them.

Other factors may have also contributed to the additional strain such as bending of the GFRP bar and the additional curvature induced at the critical section when crack widths widened.

The maximum concrete stress multiplied by the curvature factor was well within the modulus of rupture range for this type of concrete and it was expected that transverse cracking would have occurred. However, since cracking within the splice was prevented, the uncracked concrete model provided the better prediction for the bar stress distribution. Several factors would have influenced the cracking behaviour. The loading rate, which became difficult to control within the third branch of loading, could have caused sudden increases in the applied load preventing the bar forces from redistributing into the concrete. There may also have been a local concentration of steel fibres within that region that enhanced the tensile properties of the splice.

Slab/Beam R300

To demonstrate the effect of progressive bond failure on the bar stress R300 is shown graphed with the experimental bar stress distribution for both 95% and 100% of the maximum load (Fig. 5.22). At 95% the bar stress at mid-splice comes very close to the theoretical prediction using cracked concrete although some discrepancy still exists due to additional cracking throughout the splice. This is because just prior to failure when the loading is within the third branch of the curve a small increase in load equivalent to just 5% of the ultimate capacity caused an increase in the mid-splice bar stress of 20-33%.

From Figure 5.14 it is noted that the factored maximum concrete stress is well within range of the flexural tensile strength of type R concrete and so transverse cracking was present within the splice. Longer splice lengths show a more definitive change in bar stress distribution due to cracking as shown in the theoretical predictions of Figure 5.22 using cracked and uncracked concrete. The mid-splice bar stresses are increased significantly while the bar stresses closer to the free end are also being developed. The MDT also shows considerable increase in maximum bar stress after cracking occurs. The presence of additional cracking throughout the splice allowed both bars to develop a better distribution of bond stresses that remained intact throughout the entire loading. This helped to prevent the occurrence of localized bond failure due to stress concentrations at the loaded ends of the

splice. Opposing bars maintained a good transfer of tensile load across the splice, which is also clearly demonstrated by the load strain curves of Figure 4.13.

Summary

The MDT provides a good estimate for the maximum bar stress that can develop within a splice. However, additional understanding of the overall cracking behaviour is necessary to provide more accurate predictions. For the smaller embedment lengths the predictions were on the conservative side. This was caused by the initiation of cracks some distance away from the splice that essentially added additional embedment length to the bar and improved the overall load capacity. Cracking within the splice was also inconsistent and may have been a result of the loading rate and fibre distribution within the concrete.

Improvements also need to be made in terms of predicting the overall bar stress distribution. The discrepancies noted at mid-splice were a result of initiating pullout failure of the GFRP. According to the general method of Section 5.4.3 the start of bond failure is considered to be the maximum load since the theory is based on the elastic response of all materials and their interactions. Additional load taken through added plastic deformation (i.e. the third branch of loading) should not be included so any strain separation between the two bars would not have been present in the comparison. Doing this would result in predictions that are slightly lower since failure is said to have occurred earlier. However, it is important to note that the modulus of displacement value used in this analysis was taken from pullout tests using LM GFRP and normal to high strength non-fibre reinforced concretes. The modulus of displacement values for HM GFRP embedded in UHPC is expected to be higher meaning a stiffer bond exists between the bar and concrete. Subsequently, the concentration of bond stress at the loaded end would be higher while the bond stress at the free end is reduced. This has the effect of reducing the predicted maximum bar stress since bond failure would initiate sooner at the loaded end. If changes to the modulus of displacement were made to better fit the current conditions and the designation of failure was restricted to the point where strain separation of the two bars began, it is expected that the theory would provide much better predictions of the entire bar stress distribution.

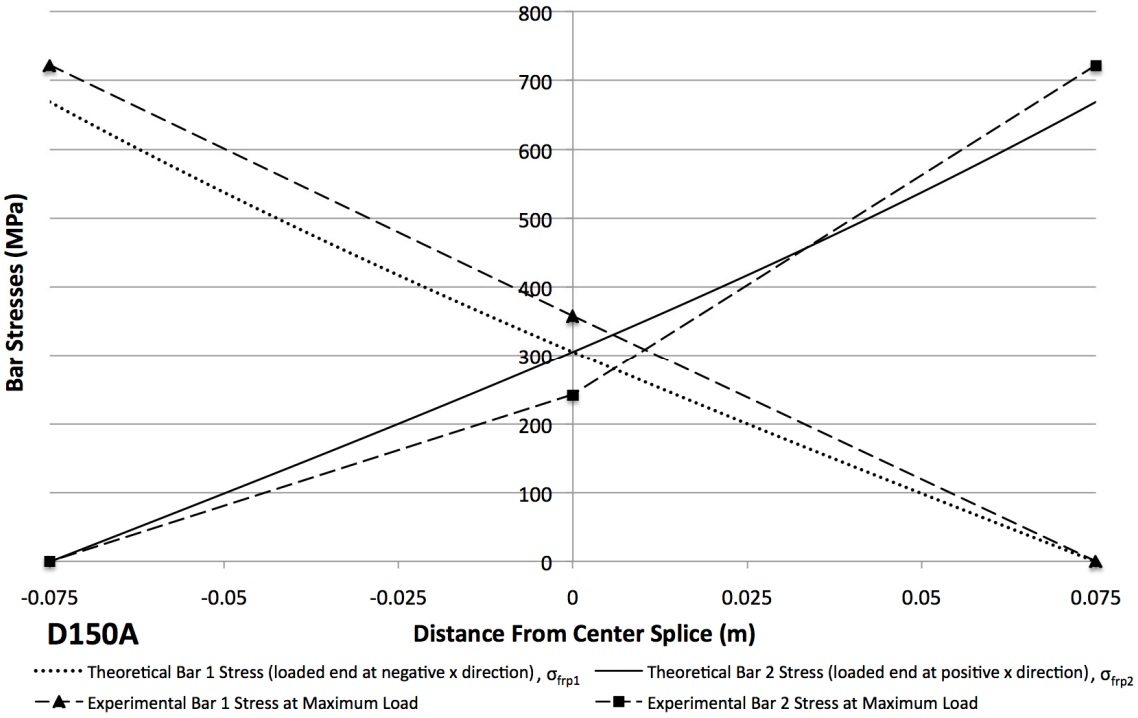

Figure 5.15: D150A in-splice bar stress distribution

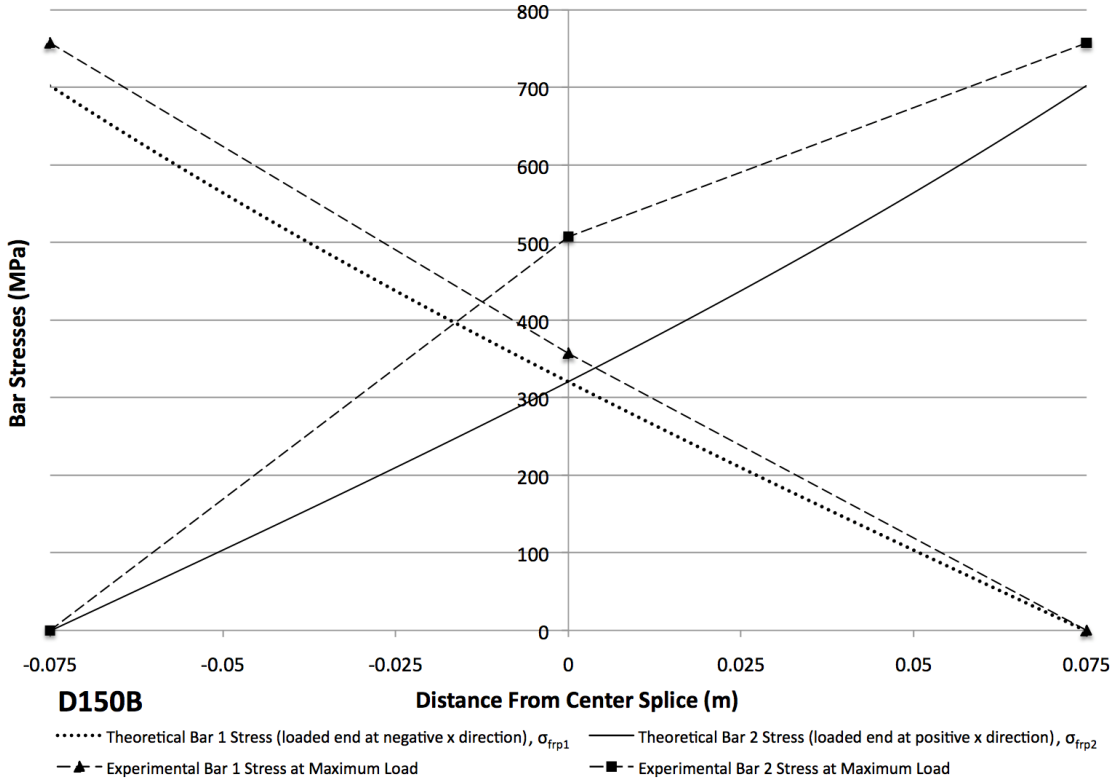

Figure 5.16: D150B in-splice bar stress distribution

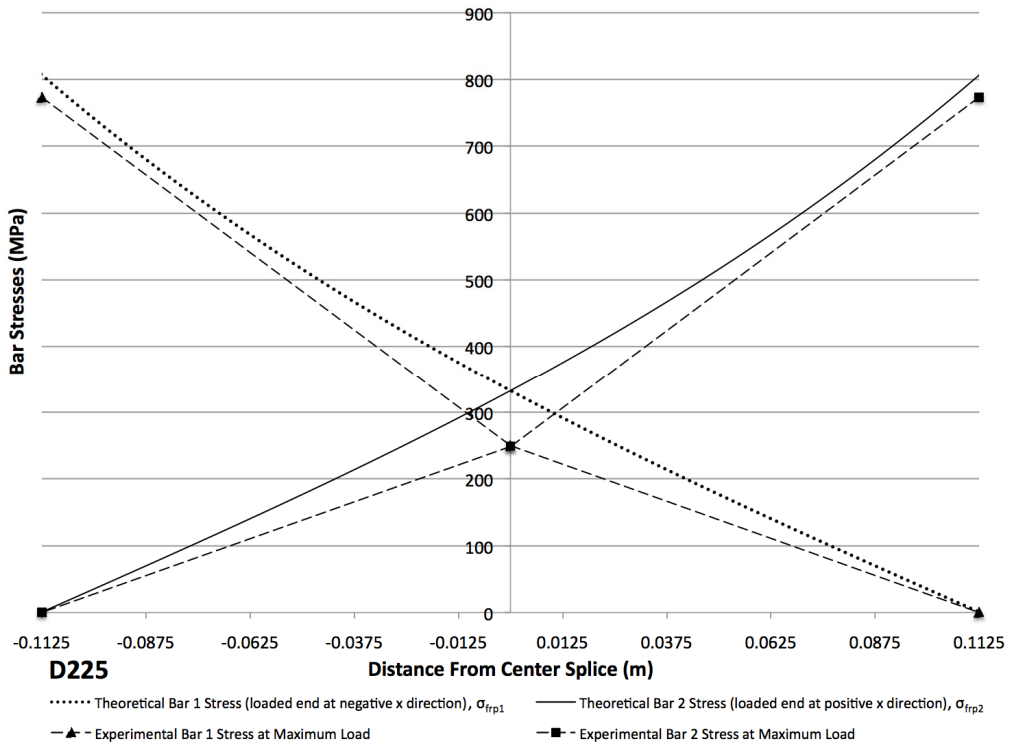

Figure 5.17: D225 in-splice bar stress distribution

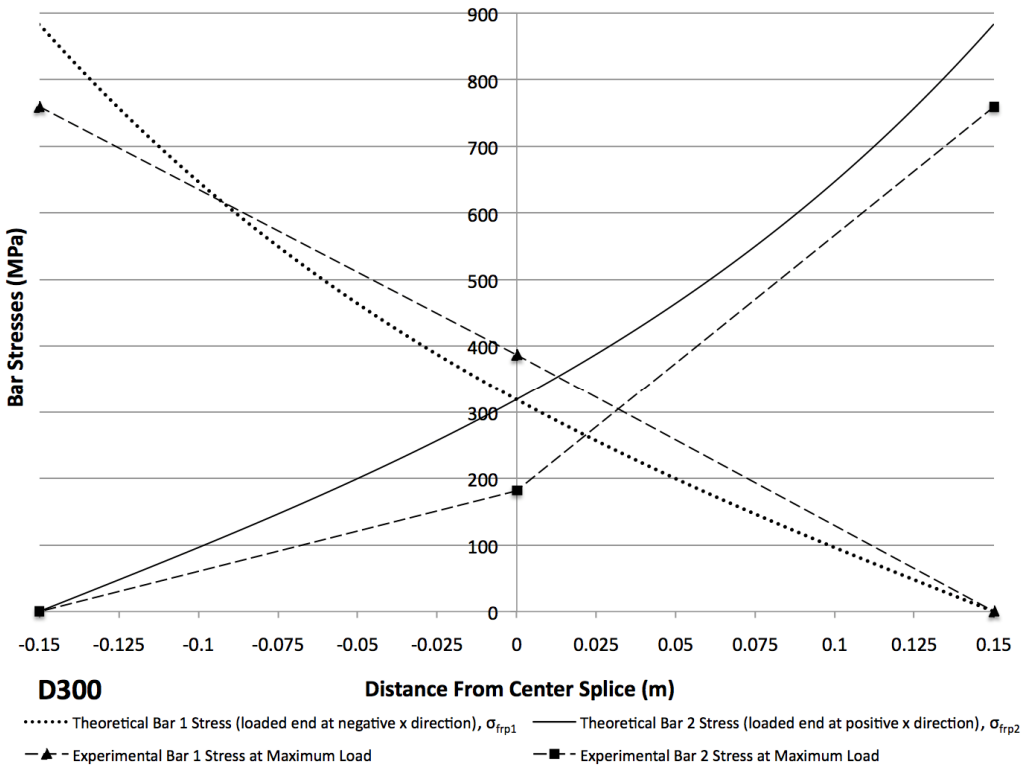

Figure 5.18: D300 in-splice bar stress distribution

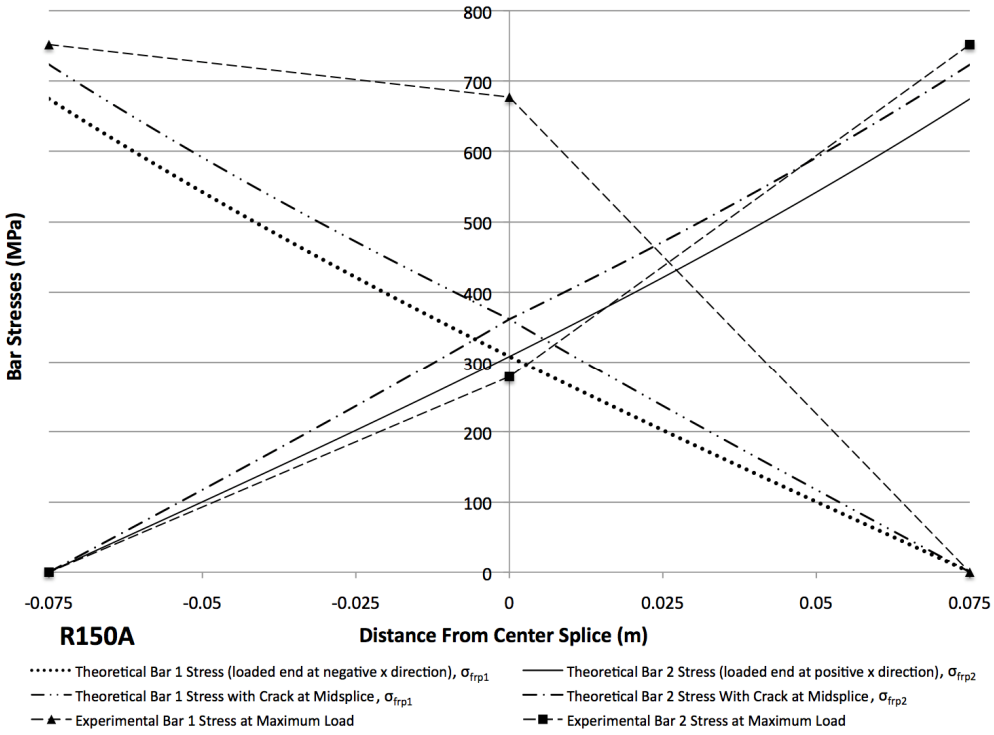

Figure 5.19: R150A in-splice bar stress distribution

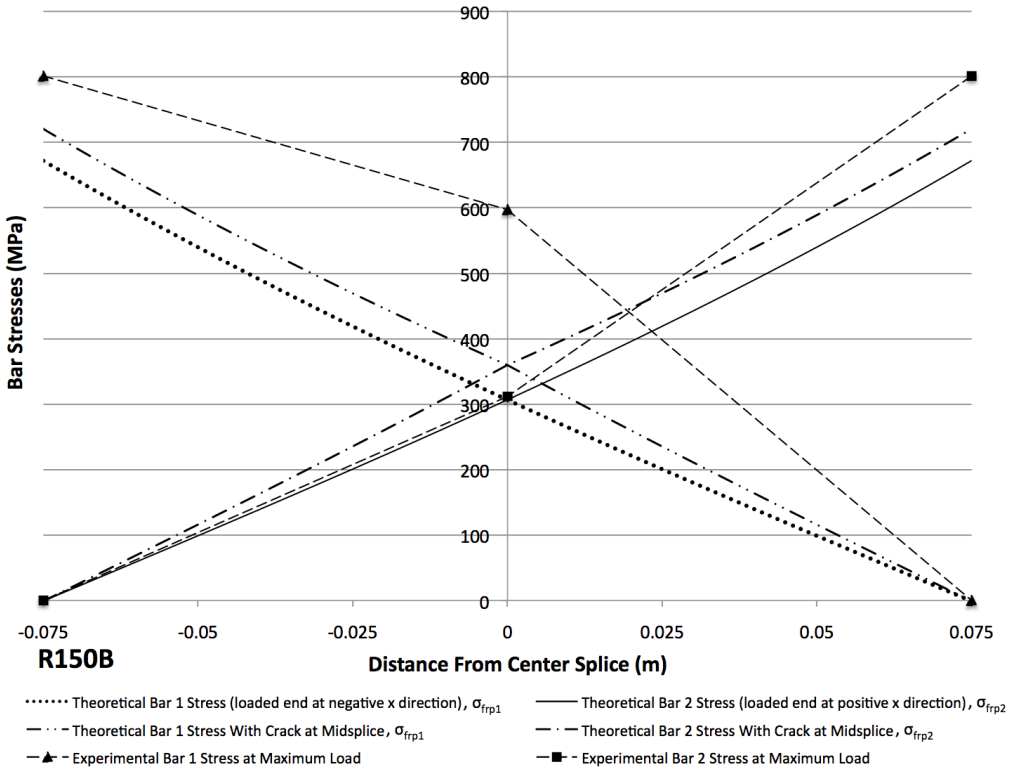

Figure 5.20: R150B in-splice bar stress distribution

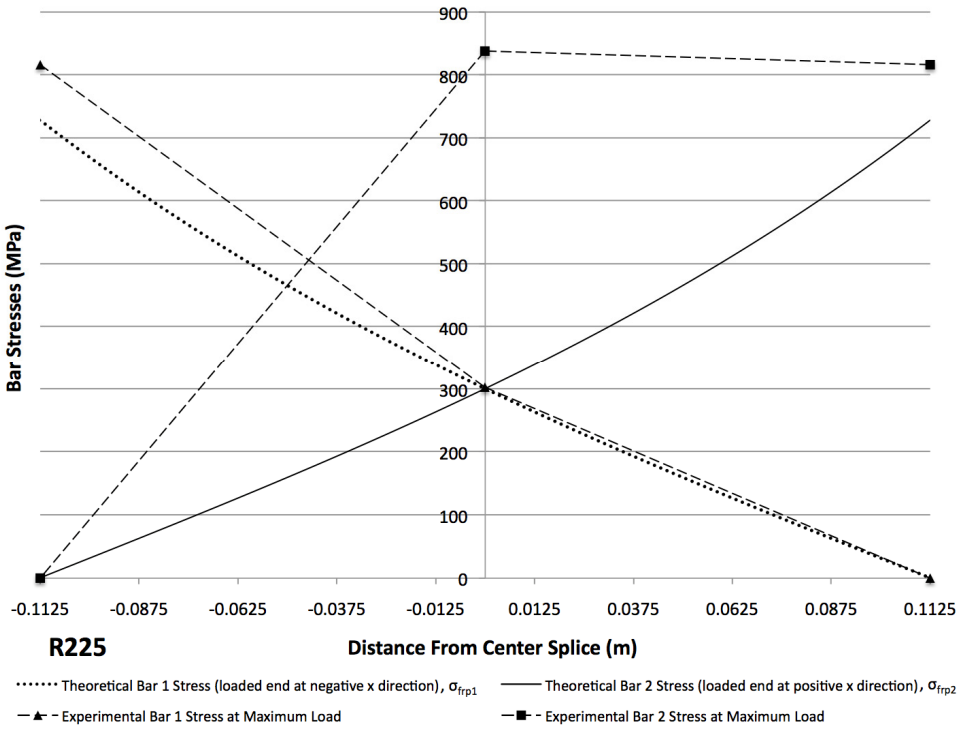

Figure 5.21: R225 in-splice bar stress distribution

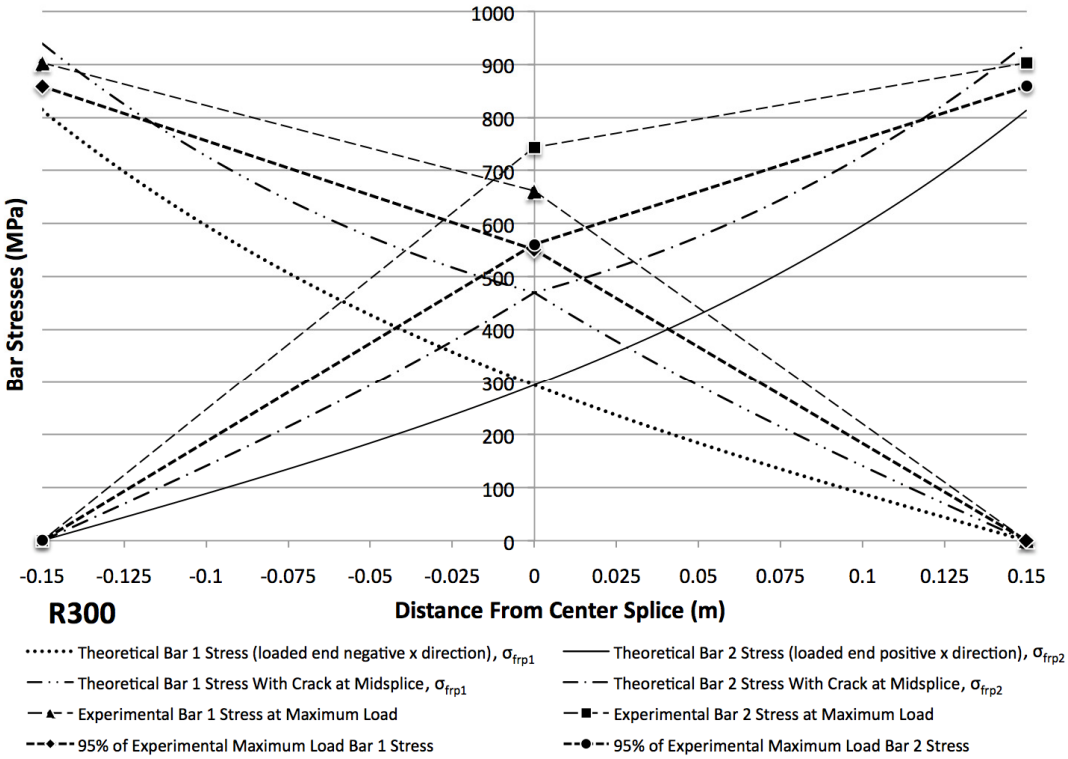

Figure 5.22: R300 in-splice bar stress distribution

Chapter 6 Code Comparisons of Critical Splice Lengths

6.1 Introduction

The current FRP design codes do not provide provisions for the application of UHPC to GFRP reinforcement splices. The greater tensile strength of UHPC concrete reinforced with fibres should be taken into account when dealing with lower modulus reinforcing materials. This chapter presents a comparison between the critical splice lengths ($l_{critical}$) obtained from the MDT using UHPC and the minimum splice lengths recommended by various codes. The general method proposed in Chapter 5 for analysis of splices will be implemented here using idealized concrete values representing that of this research. The progression of the bar stress will be explained along with how the critical splice lengths were obtained. Where applicable the same geometric and material properties used in the experimental testing of the spliced slab/beams will be used with CAN/CSA S6-06 (2006), CSA S806-02 (2002), and ACI 440.1R-06 (2006) design code equations for development length. A splice factor is then applied to determine the minimum required splice lengths. Some recommendations for the code will also be presented.

6.2 Prediction of Critical Splice Length By Modulus of Displacement Theory

The same constants shown in Table 5.1 will be used in this analysis with the exception of those listed in Table 6.1. Following the general method proposed in section 5.4.3. the maximum bar stress will be computed for various splice lengths at the instant where maximum bond stress is obtained at the loaded end of the splice. At each splice length the maximum concrete stress factored for the effects of curvature is compared to the flexural cracking strength. If cracking occurs then the next formulation for bond strength incorporating cracking at the midpoint between the two previous cracks is used to caculate the maximum bar stress. This continues until the design tensile strength of the rebar has been reached. Sufficient concrete cover is assumed to prevent splitting failure.

The experimental results showed that the MDT can provide good results for the bond stress and bar stress distributions of sand coated GFRP splices. Through theoretical analysis and experimental testing it was found that the effective concrete area in relation to the curvature of the slab/beam and flexural tensile strength of the concrete had a significant

effect on the bond characteristics of spliced GFRP bars. These properties played an important role in the bond stress distribution and therefore the maximum bar stress of the splice. By cracking transversely to the bar within the splice bond stresses can be better distributed throughout the splice length. It is important for the concrete to develop cracks within the spliced region due to the high GFRP bar strains that need to be accomodated at higher bar loads. The same clear cover of 50 mm is used so as to keep the effective concrete area the same as in the previous analysis. Two curvature factors will be implemented in this analysis for comparison namely 1.5 and 2.5 thus giving total depths of 193 and 348 mm respectively; typical for slabs and beams. Changing the curvature factor affects the maximum bar force at which the next set of transverse cracks begin to form. The cracking strength is also varied significantly to encompass typical flexural tensile strengths of UHPC as shown in Table 6.1. A total of four beams will be modelled using the two concrete types and two curvature factors.

Table 6.1: Material properties used for critical splice length analysis

Material Property	Type D	Type R
$f'c$ (MPa)	150	100
f_{cr} (MPa)	24	12
f_{frpu} (MPa)	1259	1259
τ_{max} (MPa)	22	20
E_c (MPa)	47030	38400
E_{frp} (MPa)	64100	64100
n	1.36	1.67

Figure 6.1 shows the modulus of displacement predictions for minimum splice lengths of different maximum bar stress. The points at which sudden increases in bar stress occur correspond to the splice lengths where additional transverse cracking is attained before the loaded end reaches maximum bond stress. A redistribution of bond forces also takes place after cracking. From zero to about 20 d_b the increase in bar force is almost linear with increasing splice lengths. For short embedment lengths a more even distribution of bond stresses can be expected. At about 20 d_b cracking is expected to occur for type R concretes

and for shallow members with larger curvature factors. After cracking the maximum bar stress is shown to be decreasing until the next point of transverse cracking occurs. The reason for this is again due to strain accomodation. Large bar stresses require additional cracking or slip to occur. As splice lengths increase beyond the first cracking point the crack spacing also increases causing bond stresses to again be focused near the loaded end. A decrease is shown because bond forces will reach a maximum at the loaded end sooner when the distances between consecutive cracks increases. This progresses until the factored concrete stresses reach the cracking stress again and cracks occur at the 1/4 points casuing another redistribution of bond stresses.

Figure 6.2 shows the average bond strength corresponding to each splice length. The distribution resembles the reciprocal of a power function with a steep decline in average bond stress within the first $50d_b$. Maximum bar force is obtained at an average bond stress of 3-5 MPa while for the bar with indefinite development length the bond strength decreases steadily below 3 MPa after about $100d_b$. Results for average bond stress at the critical splice length were estimated by Aly et al. (2006) as being 4.1 MPa for 15.9 mm LM GFRP bars embedded in 40 MPa concrete. It is clear from the distribution that providing increasingly larger splice lengths will contribute diminishing amounts of bond force. Despite the difference in cracking behaviour the average bond strength distribution generally follows the same trend for all the modelled speciemen types. This is due in part to the constant modulus of displacement used throughout the analysis. It is expected that varying the concrete strength from 100 to 150 MPa would definitely have an effect on the modulus of displacement due to the increased stiffness of the bond and should be considered in future research.

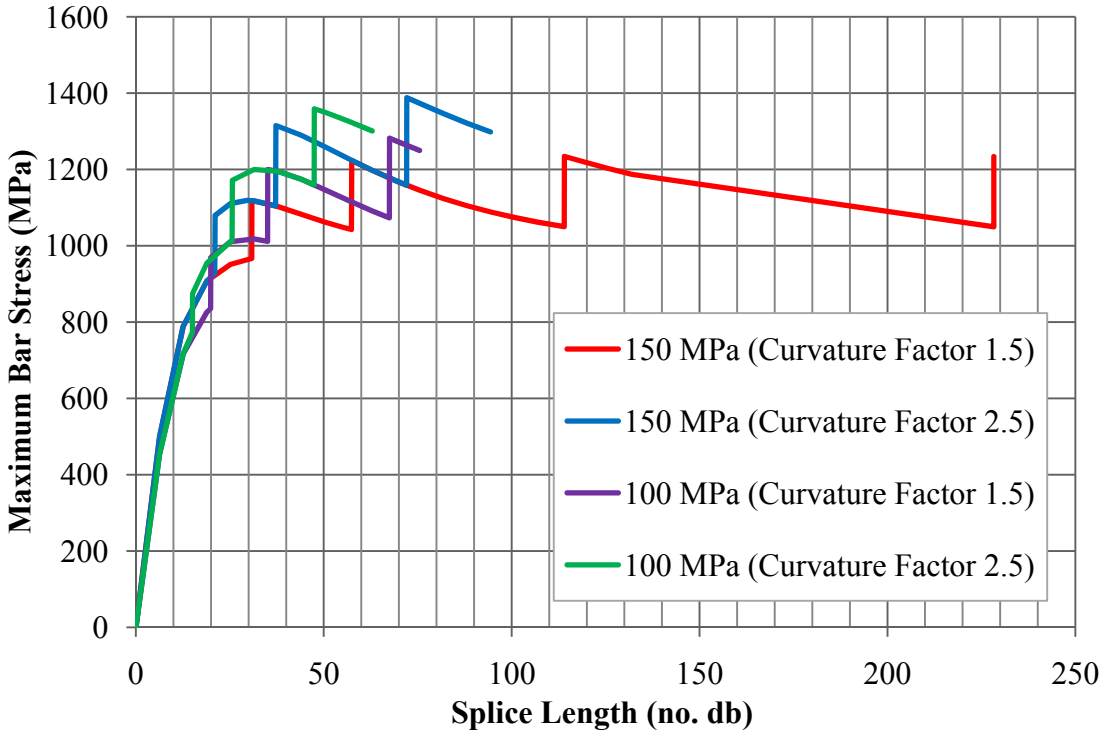

Figure 6.1: Modulus of displacement prediction of minimum splice lengths in UHPC

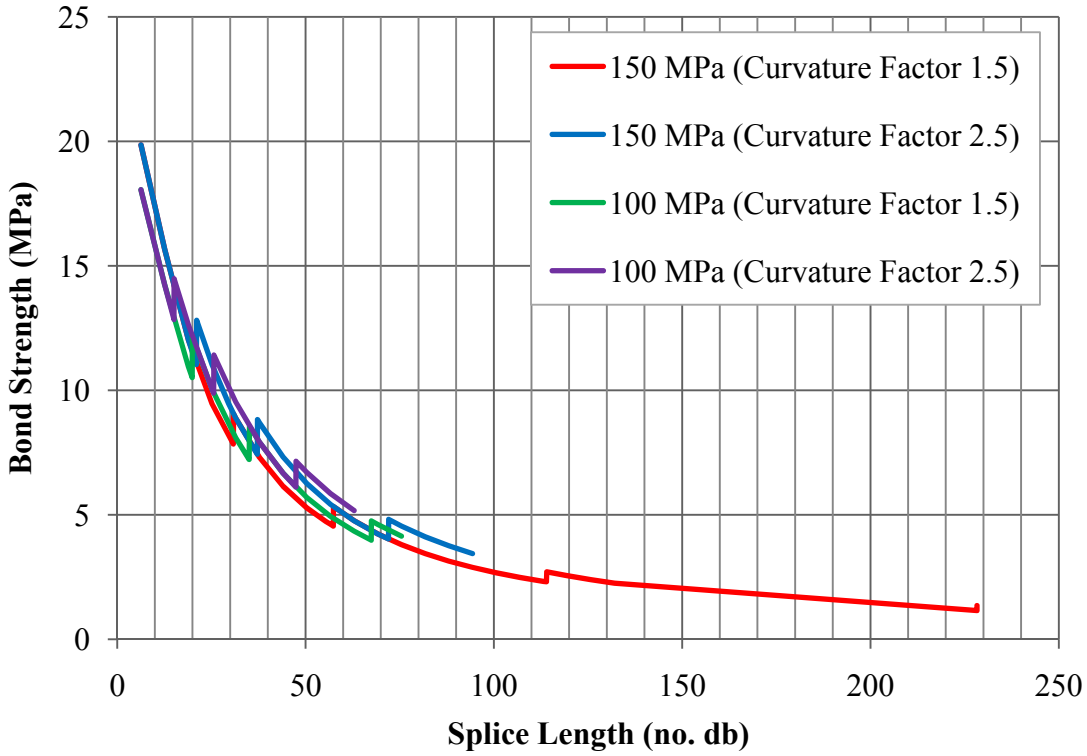

Figure 6.2: Average bond strengths of various splice lengths in UHPC

6.3 Code Prediction of Critical Splice Length

The values used with each code equation for development length are shown in Tables 6.2 to 6.4. The equations are essentially linear functions with some modifications for minimum embedment length and low bar stress values. All three codes recommend a factor of 1.3 on the development length for splices. The design tensile stress in the reinforcing bar is varied to give the distributions shown in Figures 6.3 and 6.4.

CHBDC CAN/CSA-S6-06 (2006)

Equation 6.1 shows the CHBDC (2006) formulation for minimum development length of FRP bars. This equation is an adaptation of the same equation used for steel reinforcement. A similar variation is also found in the CSA A23.3-04 (2006) concrete code.

$$l_d = 0.45 \frac{k_1 k_4}{\left(d_{cs} + k_{tr} \frac{E_{frp}}{E_s} \right)} \left(\frac{f_{frp}}{f_{cr}} \right) A_b \quad where \quad \left(d_{cs} + k_{tr} \frac{E_{frp}}{E_s} \right) \leq 2.5 d_b \quad \text{.....(6.1)}$$

where l_d is the development length, k_1 is the bar location factor equal to 1.3 when more than 300 mm of fresh concrete is cast below the development or splice length and 1.0 for all other cases, k_4 is the bar surface factor representing the ratio of bond strength of FRP to that of a steel rebar having the same cross-sectional area, but not greater than 1.0. (equal to 0.8 in absence of manufacturer data), d_{cs} is the smaller of the distance from the closest concrete surface to the centre of the bar being developed or two-thirds of the centre-to-centre spacing of the bars being developed, E_{frp} is the modulus of elasticity of the FRP bar, E_s is the modulus of elasticity of steel, f_{frp} is the stress in the FRP, f_{cr} is the cracking strength of concrete equal to $0.4\sqrt{f'c}$ for normal density concrete but less than 3.2 MPa, A_b is the area of the reinforcing bar, and k_{tr} is the transverse reinforcement index (not applicable when no transverse reinforcement is present within the splice length).

The CAN/CSA-S6-06 (2006) requires a minimum of 300 mm for the embedment length of reinforcement. It also places a limit on the effective cover, contribution of transverse confining reinforcement and concrete cracking strength to take into account the effect of splitting failure. Unusually, there is a reduction factor, k_4, that reduces the

development length as the bond strength of the FRP bar is reduced relative to a steel bar of equivalent cross-sectional area. This factor should be removed since it provides no logical engineering benefit and can lead to situations of insufficient development length. However, a value of 0.8 is recommended for this factor in lieu of sufficient bond test results. Since no transverse reinforcement was provided within the splice an effective cover of 39.75 mm for d_{cs} was used due to the code limit of $2.5d_b$ (CSA 2006). The values used with equation 6.1 are shown in Table 6.2.

Table 6.2: Values used for CSA-S6-06 (2006) development length equation

Variable	Value
k_1	1.0
k_4	0.8
f_{cr} (MPa)	3.2
A_b (mm^2)	198.6
d_{cs} (mm)	39.75
k_{tr} (mm)	0
E_{frp} (MPa)	64100
f_{frp} (MPa)	1259

CSA S806-02 (2002)

Equation 6.2 is proposed by the CSA S806-02 (2002) FRP design code and is also an adaptation from the CSA A23.3-04 (2006) concrete code for steel reinforcements. This differs from the CHBDC (2006) with modification factors to increase the development length in the case of low concrete density, larger bar diameter, and aramid fibre bar type. An additional factor is also allowed to reduce or increase the development length depending on the surface condition of the rebar and the experimental bond strength. The contribution of transverse confining reinforcement reinforcement to the bond development is not taken into account in this equation although an overall limit to the resistance against splitting failure is imposed with a maximum of $2.5d_b$ for the effective cover (CSA 2002).

$$l_d = 1.15 \frac{k_1 k_2 k_3 k_4 k_5}{d_{cs}} \frac{f_{frp}}{\sqrt{f'c}} A_b \quad \text{.....(6.2)}$$

where l_d is the development length, k_1 is the bar location factor equal to 1.3 when more than 300 mm of fresh concrete is cast below the development or splice length and 1.0 for all other cases, k_2 is the concrete density factor equal to 1.0 for normal density concrete; k_3 is the bar size factor equal to 0.8 for $A_b < 300$ mm^2 or 1.0 for $A_b > 300$ mm^2, k_4 is the bar fibre factor equal to 1.0 for GFRP; k_5 is the bar surface condition factor equal to 1.0 for sand coated bars, d_{cs} is the smaller of the distance from the closest concrete surface to the centre of the bar being developed or two-thirds of the centre-to-centre spacing of the bars being developed not greater than 2.5d_b, A_b is the bar area, f_{frp} is the stress in the FRP bar, and $f'c$ is the concrete compressive strength not greater than 64 MPa. The values used with equation 6.2 are summarized in Table 6.3.

Table 6.3: Values used for CSA S806-02 (2002) development length equation

Variable	Value
k_1	1.0
k_2	1.0
k_3	0.8
k_4	1.0
k_5	1.0
f_{frp} (MPa)	1259
$f'c$ (MPa)	64.0
A_b (mm^2)	198.6
d_{cs} (mm)	39.75

ACI 440.1R-06 (2006)

The ACI code equation for the development length of FRP reinforcing bars shown below is based on empirical relationships developed by Wambeke and Shield (2006) using a compilation of test results from various researchers encompassing both splitting and pullout failures of mainly GFRP beam tests. The ACI code recommends a minimum of 20d_b for embedment lenths however it also says that a linear distribution from zero to the maximum bar stress obtained at 20d_b of embedment can by used for this initial portion. The ACI also provides similar restrictions on the effective cover contribution to the devleopment by imposing a maximum factor of 3.5d_b. However, no restriction is provdied on the concrete strength. Further analysis into the data set also indicated that confining reinforcement and

bar surface condition had little effect on the overall bond performance of FRP bars. Additional research by Darwin et. al (1996) showed that the effect of confining reinforcement is more pronounced as the relative rib area of steel reinforcement is increased. Thus for the current formulation no modifications are provided for the effect of bond surface conditions or transverse reinforcement (ACI Committee 440 2006).

$$l_d = \frac{k_1 \frac{f_{frp}}{\sqrt{f'c}} - 340}{13.6 + \frac{C_1}{d_b}} d_b \quad \text{.....(6.3)}$$

where l_d is the development length, k_1 is the bar location factor equal to 1.5 when more than 300 mm of fresh concrete is cast below the development or splice length and 1.0 for all other cases, d_b is the bar diameter, f_{frp} is the stress in FRP reinforcement, $f'c$ is the concrete compressive strength, C_1 is the effective cover not greater than $3.5d_b$.

Table 6.4: Values used for ACI 440.1R-06 (2006) development length equation

Variable	Value (Type R)	Value (Type D)
k_1	1	1
$f'c$ (MPa)	100	150
f_{frp} (MPa)	1259	1259
d_b (mm)	15.9	15.9
C_1 (mm)	55.65	55.65

6.4 Code Comparison of Splice Lengths

Tables 6.5 and 6.6 show a comparison between the critical splice lengths proposed by the design codes and those calculated using the MDT. A factor of 1.3 was applied to all development length calculations as a requirement for splices. Each table includes a ratio of the code requirement to the MDT using both curvature factors. The ACI code prediction provides the most conservative value with splice lengths ranging from 18.0% to 54.7% more

than the CSA predictions even though no limit was set on the concrete strength. Using the ACI code an increase in concrete strength from 100 MPa to 150 MPa resulted in a 23.7% decrease in splice length. Both the CSA codes provided results similar to one another as expected since they were both adopted from the same equations used for steel reinforcement.

The values reported in the tables using the modulus of displacement method should only be considered as a minimum requirement since a better understanting of the cracking behaviour is needed and splitting failure was not taken into account. Moreover, the splice length provided for 150 MPa concrete and 1.5 curvature factor in Table 6.6 only provides a bar stress of up to 98% of f_{frpu}. The main objective was to determine critical splice length, $l_{critical}$, with respect to the localized bond failure mode. Use of a high tensile strength UHPC concrete may not provide sufficient strain accomodation for a GFRP bar and thus lead to local bond failure prior to reaching the design tensile strength of the rebar. The following is an evaluation of the current code provisions in regards to this behaviour of UHPC splices.

The critical splice lengths for the models that reached f_{frpu} ranged from 592 mm (37.2 d_b) to 1073 mm (67.5 d_b). Aly (2006) estimated the critical splice length of 15.9 mm LM GFRP with f_{frpu} of 590 MPa as approximately $40d_b$ based on spliced beam tests using 40 MPa concrete. The failure mode of those specimens were by splitting and bar rupture. The three modelled beam types corresponding to weaker concrete and higher curvature factor were able to reach maximum bar stress within a definite splice length as shown in Table 6.5 and 6.6, however, the maximum for each occurs at the point of cracking. Thus these predictions are highly dependent on the expected cracking behaviour of the concrete. Additional splice length should be added beyond those provided by this analysis to account for the unpredictable nature of concrete to ensure that sufficient transverse cracking will occur. The beam modelled with 150 MPa concrete and curvature factor of 1.5 was not able to reach a state at which maximum bar stress could be obtained before maximum bond stress. After three stages of cracking the maximum bar stress was about 98% of the design tensile strength at about 114 d_b splice length. The fourth stage of cracking showed no increase in bar force beyond the third cracking stage. When transverse cracking is prevented within the splice it becomes difficult to develop the necessary bond strength throughout the entire embedment and thus localized slip and bond failure is expected to always occur before reaching the bar strength for this particular model.

The higher curvature factor models provide the lowest splice length since it allows a better distribution of bond stress from early transverse cracking. These values are non-conservative compared with the code values which range from 22%-88% higher than the modulus of displacment calculations. The larger values obtained from code results are generally attributed to the account of splitting failure. At this level of curvature an increase in the maximum bond stress from 20 MPa to 22 MPa for 100 MPa to 150 MPa concrete provides a significant improvement on the development length.

A lower curvature factor reduces the tensile stress at the bottom of the concrete section thus impeding the occurrence of transverse cracking. Results obtained from these models show a significant increase in the required splice length over a shallower member. Splice lengths for low concrete strength and low curvature factor fall between the ACI and CSA code predictions. When splitting failure is prevented, the CSA splice lengths are about 12-14% shorter than those from this theory. This could potentially lead to premature slip and bond failure at the loaded end of the splice. On the other hand, the ACI code provides conservative results versus all model types. The exception is with the higher concrete strength and lower curvature factor model that was not able to provide a definite amount of splice length achieving only 98% of f_{frpu}. For deeper members composed of higher tensile strength concrete (>24 MPa) it may not be possible to develop the full strength of a HM GFRP bar without the occurrence of some localized bond loss at the loaded end. This may not pose an immediate structural issue, due to the presence of friction after bond failure, however repeated loadings to f_{frpu} may cause progressive debonding and subsequent serviceablility deficiences such as larger deflections and crack widths. Overall the code predictions are conservative with respect to this failure mode, however, some problems may arise with deeper members and higher concrete tensile strengths.

Table 6.5: Code comparison of critical splice lengths for 100 MPa concrete

Method	$l_{critical}$ (mm)	No. of d_b	Avg. Bond Strength (MPa)	$l_{critical}$ / $MDT_{1.5}$	$l_{critical}$ / $MDT_{2.5}$
CSA S6-06	920	57.8	5.44	0.86	1.22
CSA S806-02	940	59.1	5.32	0.88	1.25
ACI 440.1R-06 (100 MPa)	1423	89.5	3.52	1.33	1.88
MDT (100 MPa, Curvature Factor = 1.5)	>1073	>67.5	<4.66	1.00	1.42
MDT (100 MPa, Curvature Factor = 2.5)	>755	>47.5	<6.63	0.70	1.00

Table 6.6: Code comparison of critical splice lengths for 150 MPa concrete

Method	$l_{critical}$ (mm)	No. of d_b	Avg. Bond Strength (MPa)	$l_{critical}$ / $MDT_{1.5}$	$l_{critical}$ / $MDT_{2.5}$
CSA S6-06	920	57.8	5.44	0.51*	1.55
CSA S806-02	940	59.1	5.32	0.52*	1.59
ACI 440.1R-06 (150 MPa)	1086	68.3	4.61	0.60*	1.83
MDT (150 MPa, Curvature Factor = 1.5)	>1812*	>114*	<2.71*	1.00	3.06*
MDT (150 MPa, Curvature Factor = 2.5)	>592	>37.2	<8.45	0.33*	1.00

*Values calculated at a maximum bar stress of 98% f_{frpu} using MDT analysis with curvature factor of 1.5 since the critical splice length could not be determined.

Figures 6.3 and 6.4 show the distributions for splice length requirements in relation to the design bar stress. Some similarities are noted between the code and theoretical predictions. After about $20d_b$, there is a clear change in the accumulation in bar stress with splice length. The code expectation that the majority of bond stress is concentrated within this initial region proves valid. After this point the diminishing contirbution of bond force is accounted for with an increase in the embedment length versus maximum bar stress relationship.

For shallow members (curvature factor of 2.5) the code provides sufficient splice length throughout the entire distribution. However as the curvature factor is reduced, as with deeper members, transverse cracking is delayed. The point where the 150 MPa concrete begins to exceed the CSA code values for splice length are after the first stage of cracking which occurs at about 88.8% of f_{frpu} and after the second stage of cracking for 100 MPa concrete at about 95.3% of f_{frpu}. These values are fairly high and the current material resistance factors of 0.5-0.55 would normally provide a sufficient envelope to the maximum bar stress to prevent this type of failure.

If transverse cracking is neglected entirely, which may be the case with higher strength concretes and deeper members, the maximum bar stresses that can be developed would resemble those at the first stage of cracking. Beyond this point very little increase in bar force can be expected without the occurrence of significant stiffness degradation of the member. These values generally range from 61.3% to 76.8% of f_{frpu} using the configurations in this analysis. The splice lengths at which this occurs can be observed in Figures 6.3 and 6.4. These values are substantially lower than those obtained with cracking and are very close to the allowable factored design strength of the GFRP bars used in this study. After sufficient tensile strength in the concrete has been provided with the necessary cover to prevent splitting failure, the next governing factor would be this form of localized bond failure. Some code restrictions should be imposed that limits the maximum bar stress that can be developed by GFRP bars spliced in fibre reinforced UHPC to prevent this failure mode from occurring. These provisions should take into account the higher flexural tensile strength of UHPC concrete in the splice as well as larger total depth to cover ratios.

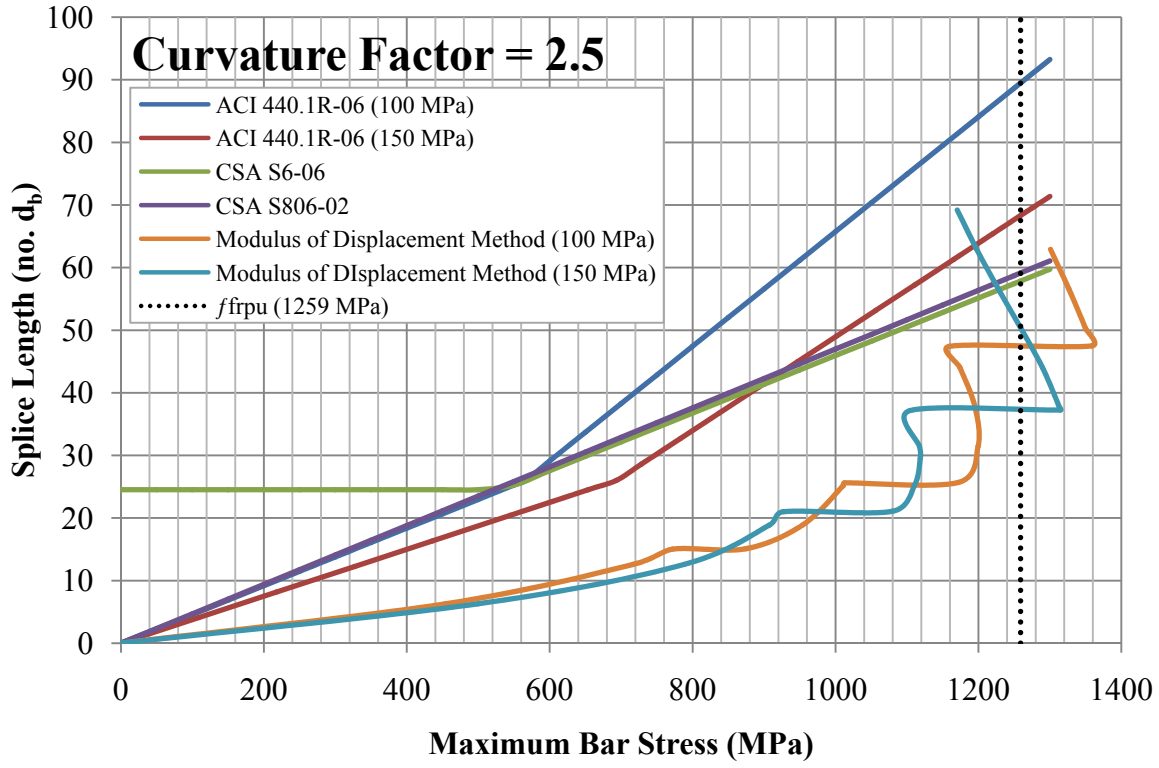

Figure 6.3: Code comparison of minimum splice length for curvature factor of 2.5

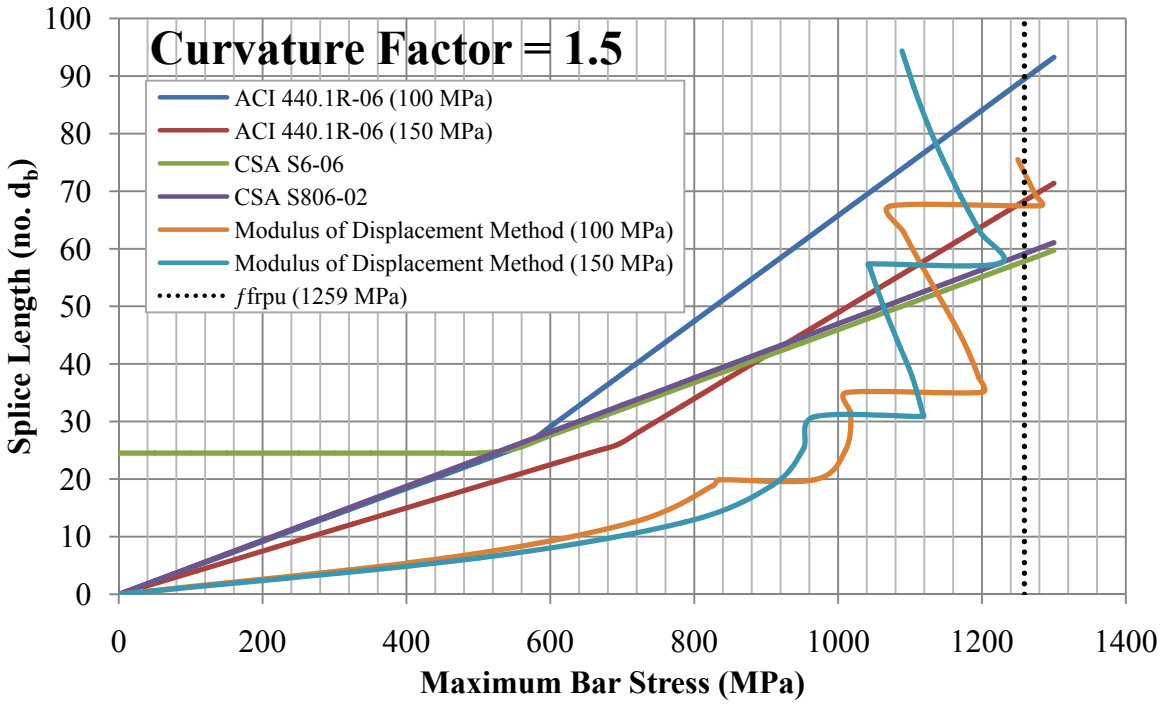

Figure 6.4: Code comparison of minimum splice length for curvature factor of 1.5

Chapter 7 Conclusions and Recommendations

A total of 10 high modulus (HM) spliced slab/beam tests were conducted to investigate the behaviour of sand coated glass fibre reinforced polymer (GFRP) rebar splices cast within ultra high performance concrete (UHPC) with steel fibres. Three splice lengths of 150 mm, 225 mm, and 300 mm were used to investigate the effect of embedment length on the bond strength in full cast beams. Two UHPC with steel fibres designated as type R and D were also included as parameters with target strengths of 100 and 150 MPa in full cast beams. All full cast slab/beams were designed to fit similar dimensions (1800 mm span x 270 mm width x 200 mm depth) and reinforcement configurations as a highway bridge deck. The bond strength of the smallest splice length (150 mm) was also tested using precast beam sections, with a 200 mm width joint and 150 mm lap length, simulating a high performance bridge construction joint application. The precast sections were made of a high strength concrete without fiber (designated as Type K) having a strength greater than 60 MPa while the UHPC (Type D) joint had strength greater than 150 MPa. Each full cast or precast slab/beam was loaded to failure under four-point loading and analyzed in terms of ultimate capacity, bond strength, bar strain behaviour, load deflection response, crack propagation and failure mode. Three of the 150 mm splice slab/beams (D150B, R150B, P150B) were also subjected to fatigue loading prior to being tested to failure with two belonging to each of the UHPC types (D and R) and one from the precast slab/beams. Additional conclusions were obtained from fatigue testing as well.

A limited study was also conducted using pullout tests from the three concrete types (D, R, and K) to examine the effect of harsh environments on the bond strength of low modulus (LM) and HM GFRP bars. Pullout specimens were exposed to 50 cycles of freeze thaw between +60˚C and -30˚C with 50% humidity spending at least 6 hours at each temperature limit. The pullout capacity was then compared to control specimens of the same configuration without being subjected to freeze thaw cycles and analyzed for comparative bond performance. The following conclusions were drawn from this study.

Ultimate Capacity and GFRP Bond Strength

- All splice lengths of Type R slab/beams, with generally weaker concrete strength (100 MPa), performed consistently better in both load capacity and ductility than Type D (150 MPa) slab/beams. Type R slab/beams had 4.3%-18.3% higher load capacity than Type D slab/beams with the same splice length. Similarly, Type R slab/beams had a 6.9%-81.0% higher deflection at failure versus Type D slab/beams of the same splice length. This was due to the weaker modulus of rupture of Type R concrete (6.9-16.5 MPa) versus Type D concrete (21.4-27.1 MPa) that allowed transverse cracking and improved bond stress distribution throughout the splice.
- The overall behaviour of full cast GFRP reinforced UHPC slab/beams was very ductile with central deflections increasing to values between 22.8 mm (span/79) and 58.2 mm (span/ 31) after reaching the maximum load.
- The bond strength of HM GFRP splices ranged from 10.1 MPa to 21.2 MPa and showed an inverse relationship with the splice length. A 100% increase in the splice length showed a 40-50% decrease in the average bond strength across all full cast slab/beam types.
- Type D UHPC showed negligible increases in the bar force (5.3%) when splice lengths doubled versus a moderate increase (19.0%) with Type R UHPC.
- The short embedment lengths of approximately 10-20 d_b yielded bar stress values of approximately 57.3% – 71.7% of the design tensile strength of the HM GFRP bars.
- The use of a linear stress strain distribution for the compression region of UHPC beams provides acceptable results with very little deviation from a more comprehensive analysis with currently accepted models for the compressive behaviour of concrete.
- Analysis using code values for rectangular stress block parameters would have provided erroneous predictions for the concrete compressive stress distribution since the strain at the extreme compression fibre for all full cast slab/beams were well below 0.0035.
- Short neutral axis depth of less than 25% of the total slab/beam depth in full cast slab/ beam specimens were due mainly to the low tensile modulus of GFRP reinforcement.

- Due to the extensive crack widths (10-25 mm) and heights (165-185 mm) caused by the low tensile modulus of GFRP compared to conventional steel reinforcement and by the increased deformability and ductility of GFRP reinforced beams, the contribution of steel fibres to the tensile region at failure was negligible.
- The low flexural tensile strength of Type R concrete contributed to the bond stress distribution of splices through transverse cracking whereas Type D concrete was unable to incur additional cracking within the splice causing premature bond failure at the loaded end of the splice. Although the use of a higher tensile strength UHPC may increase the local bond maximum bond stress such as those obtained with short embedment lengths of 3-5d_b , the average bond stress in longer embedments greater than 10d_b may suffer due to the lack of strain accommodation.
- Strain accommodation is necessary at higher bar loads when GFRP rebar are used as reinforcement, otherwise slip will occur due to the significant strain difference between concrete and GFRP.
- The ductility increased with increasing splice length due to the additional pullout length provided by a longer splice.
- The ductility increased with a decrease in concrete strength (mainly tensile strength) due to the ability of comparatively lower strength concrete to develop a higher bar force through transverse cracking within the splice.
- The strain development at mid-splice of the majority of the full cast slab/beams showed a tri-linear behaviour. The initiation of the second and third stages of loading were marked first by cracking and then by strain separation between the two instrumented and splice bars. Each stage had a significant reduction in the load strain relationship from the one preceding it.
- Strain separation was due to the onset of localized bond failure at the loaded end of the splice and the resulting transfer of load closer towards the free end.

Failure Modes of Full/ Precast Beams

- The prominent failure mode for full cast slab/beams was by pullout failure of the tensile reinforcement at the splice location. R225 and R300 specimens, with 225 and 300 mm splice lengths respectively, showed some signs of crushing of concrete at the

critical section where failure occurred as was expected from the calculated concrete strains.

- The failure mode for precast slab/beams was by shear at the support since no shear reinforcements were used. Shear failure occurred at about 52 to 65% of the maximum bar force obtained from a 150 mm splice in a Type D full cast specimen.
- A 50 mm cover was sufficient in preventing splitting failure for the tested splice lengths using UHPC with steel fibres (Type D and R) in all slab/beam specimens.

Cracking Behaviour of Full/Precast Beams

- For full cast slab/beams cracking initiates at the point of load application and generally progresses inwards towards the splice within the maximum bending moment region. Some cracks also propagated outwards with some being initiated by the presence of shear and transverse reinforcement.
- Type R full cast slab/beams developed cracks within the splice that reached the bottom of the specimen while Type D slab/beams did not.
- For precast slab/beams cracking also initiated at the point of load application but majority of cracks propagated outwards toward the support beginning first as vertical tension cracks and then becoming inclined shear cracks as they moved closer to the support. Some cracks were observed near the joint location mainly due to a separation between the joint fill material and the precast section. Additional longitudinal cracks were also observed at the reinforcement level in the precast concrete section.
- The theoretical neutral axis depths in full cast beams showed good agreement with the crack lengths at the critical section where failure occurred.

Cyclic/Fatigue Behaviour of Full/Precast Beams

- No reduction in load capacity was observed for slab/beams subjected to cyclic loading between 60,000 to 100,000 cycles.
- Full cast slab/beams suffered an increase in residual deflection after cyclic loading in the range of 9.1%-16.0% more than the residual deflection at the initial cracking load.

- The precast slab/beam showed an increase of 162% in residual deflection due to cracking, and separation between the precast sections and joint fill material.
- No observed increase in crack width was noted after the first 20 000 cycles for full cast slab/beams while precast slab/beams showed an increase of 133% after cyclic loading.
- The effect of continuous cyclic loading was found to have a significant effect on the results. R150B slab/beam subjected to continuous loading cycles showed a stiffening of the load deflection curve and accumulated more residual deflection. Whereas for D150B slab/beam, with discontinuous cyclic loading sessions, the residual deflection values were inconsistent while a reduction in stiffness was observed.
- A small increase in load capacity of 5.3% and 6.5% was observed for D150B and R150B (150 mm splice length) fatigue slab/beams respectively, while a large increase of 27.6% was noted for P150B (precast with 150 mm splice length). The shear failure mode of precast (P) slab/beams benefitted more from an increase in concrete strength.

Theoretical Predictions of Bond and Bar Stress Distributions of GFRP Rebar Splices

- The bond stress distributions of spliced sand coated HM GFRP is not constant throughout the splice length.
- The bar stress distribution of spliced sand coated HM GFRP is non-linear.
- The bond stress at the loaded end is higher than at the free end and this difference increases with the splice length.
- The concrete tensile stress within a splice reaches a maximum at the mid-point between two cracks and will typically crack transversely at this location as loads increase.
- For splices with transverse cracking a discontinuity exists in the bond stress distribution at the location of cracking. When the tensile modulus of the reinforcement is relatively low, additional bond stresses can develop closer to the free end after cracking due to the need for the concrete to accommodate high bar strain.

- At the point of transverse cracking the bar stress distribution will have a local maximum since all the tensile force will be taken by the reinforcement. Similarly, the concrete will have a point of zero stress at this location.
- The MDT provides a good estimate of the bar stress and subsequently the bond stress distributions throughout a splice during the elastic stage of loading when a good bond still exists between the concrete and reinforcement.
- A better understanding of the cracking behavior of UHPC in tension lap spliced beams will increase the accuracy of MDT predictions.

Theoretical Predictions of Critical Splice Length of GFRP Rebar

- The modulus of displacement theory (MDT) predictions of maximum bar stress were in good agreement with the values obtained from experimental testing and were used to predict the critical splice length.
- The only major discrepancy between MDT and experimental results was due to the strain separation of the bars at mid-splice during the third (failing) branch of the loading due to progressive localized bond failure of the HM GFRP bar from one side of the slab/beam.
- The lower bound for the range of modulus of displacement should be used when predicting the behaviour of splices just prior to failure and should also be determined using bond slip curves from the loaded end and not from the free end.
- The MDT also proves how the presence of transverse cracking can improve the overall bond performance of splices by transferring additional bond stresses closer to the free end of the GFRP bar splice.
- The critical GFRP splice lengths were calculated with regards to the progressive pullout failure mode demonstrated from experimental slab/beam testing. The values are the minimum required to prevent localized bond failure at the loaded end while still achieving the design tensile stress (f_{frpu}) of 1259 MPa for 15.9 mm HM GFRP bars. Two UHPC concrete strengths were used in addition to two different member depths incorporated by changing the curvature factor of the beam. The results for critical splice length ($l_{critical}$) from each model were as follows:

- For 100 MPa Concrete (Type R with steel fibres):
  - Model 1: $l_{critical}$ = 755 mm (47.5 d_b) for curvature factor of 2.5
  - Model 2: $l_{critical}$ = 1073 mm (67.5 d_b) for curvature factor of 1.5
- For 150 MPa Concrete:
  - Model 3: $l_{critical}$ = 592 mm (37.3 d_b) for curvature factor for 2.5
  - Model 4: $l_{critical}$ = 1812 mm (114 d_b) achieving only 98% of design tensile strength of a HM GFRP bar (f_{frpu}) for curvature factor of 1.5.

- This theory also shows how the high tensile strength of concrete and deep members may produce instances where transverse cracking is delayed and the larger bar strain of GFRP reinforcement can only be accommodated through localized slip at the loaded end preventing the full development of a bar's strength. An example of this was Model 4 where only 98% of the bar stress could be developed.

Code Comparisons of Critical Splice Length with MDT Model Analysis

- For the majority of the bar stress levels, the splice lengths provided by the three design codes (ACI 440.1R-06, CSA S6-06, CSA S806-02) were conservative. Only with the higher concrete strength of 150 MPa at bar stress levels of about 89-95% of f_{frpu} did both CSA S6-06 and CSA S806-02 begin to show an under prediction versus the MDT splice lengths.
- The conservative behaviour of the code is believed to be on account of splitting failure.
- The critical splice length values obtained using a curvature factor of 2.5 (shallow depth) and both concrete types were exceeded by the code by about 22%-88% with the ACI code providing the most conservative result.
- The critical splice length values obtained using a curvature factor of 1.5 (deeper members) were very different depending on the concrete strength. Concrete of 150 MPa (Type D) was only able to attain 98% of f_{frpu} at a splice length which is 66.9%-97.0% more than what the codes recommend. In the case of 100 MPa concrete the CSA codes predicted lower splice lengths which were 86 to 88% of what was determined by the MDT. The ACI code was more conservative with splice lengths being 33% higher than the MDT.

- The effect of high tensile strength concretes and deep members should be considered in future code provisions due to the influences they have on the bond strength of GFRP splices.
- The use of UHPC with sand coated GFRP rebar can provide a reduction in the code required splice lengths at lower stress levels provided that sufficient cover is provided to prevent splitting failure.

Bond Strength of Sand Coated GFRP Rebar Under Aggressive Environment

- Type K concrete of high strength (60-70 MPa) but no steel fibre reinforcement showed considerable degradation after exposure to freeze/thaw cycling and humidity with a 4 to 22% decrease in bond strength.
- Both UHPC showed an overall increase in the bond strength after environmental treatment with Type D having a 40 to 63% increase in bond strength and Type R with a 4 to 27% increase. The increase in concrete strength from the added heat and humidity is believed to have been the contributing factor for this change. However, due to the limited number of specimens more tests are need to verify the consistency of this behaviour.
- The effect of freeze/thaw and high humidity showed no consistent correlation between the two types of bars (LM and HM). However, pullout tests results showed an overall better bond performance of LM bars versus HM bars in all concrete types (R, D and K).

Assessment of HM GFRP Rebars and UHPC in Bridge Deck Construction Joints

- Precast beams with a 200 mm UHPC construction joint and 150 mm GFRP splice showed that the flexural capacity of the joint exceeds the shear capacity of the surrounding precast slab material of HSC.
- Shear failure of precast beams occurred at 52.9% and 67.1% of the maximum bar tensile stress achieved by an average 150 mm splice in Type D full cast beams. This provides an envelope of more than 30% beyond the shear capacity of the rest of the slab/beam.

- The use of a 150 mm splice in UHPC slab/beams (Type R and D) showed bar stresses of 57.3% to 63.6% of f_{frpu} (1259 MPa). This exceeds the maximum allowable bar stress for an FRP bar when using a material resistance factor of 0.5. Furthermore, the maximum developed bar stresses in 150 mm splices using UHPC were about 80%-100% greater than the ultimate tensile stress of a conventional steel rebar (400 MPa).
- No longitudinal splitting cracks were observed in the UHPC joint for precast beams. However, splitting cracks were noted outside of the joint material in the precast sections of Type K concrete demonstrating the superior resistance of UHPC to splitting failure. Transverse cracking was also observed at the interface between the joint and precast sections. Improved joint interface geometry (with shear keys) would help to mitigate these issues by providing additional bond surface area between the two concretes (UHPC and precast concrete).
- Use of GFRP provides an overall reduction in the stiffness of flexural members leading to excessive cracking and deflection. However the presence of fiber reinforcement found in most UHPC will provide some mitigation to these issues within the construction joint and the majority of serviceability degradation will occur in the surrounding material.
- From the results of this research the following conclusions can be made on reduced tension lap splice construction joints using sand coated HM GFRP rebar in UHPC:
    - The governing failure mode will be by shear failure outside the joint in the normal concrete slab section.
    - Reasonable bar stress can be developed in GFRP rebars spliced in UHPC.
    - The use of UHPC provides superior resistance to the effects of freeze/thaw and high humidity.
    - The failure mode of sand coated GFRP bars spliced in UHPC is fairly ductile showing large deflections and crack widths prior to failure. Furthermore, the splice demonstrates progressive bond failure allowing excessive slip prior to total bond loss.
    - The serviceability performance of the UHPC joint exceeds that of the high strength concrete precast sections.

- Based on these findings it is believed that reduced tension lap splice construction joints with sand coated HM GFRP rebar in UHPC are indeed feasible provided that a sufficient reinforcement ratio is provided to increase the stiffness and serviceability performance of the member.

Recommendations for Future Research

Many factors still need to be investigated in order to gain a better understanding of the overall behaviour of GFRP splices in UHPC.

- The effects of bar diameter, bar surface condition, concrete cover, confining reinforcement are all parameters which are necessary for future research into splices in UHPC. Changing these parameters will affect the bond behaviour and possibly the failure mode of each specimen.
- Bar spacing and reinforcement ratio is an important aspect that should be considered in future research since increasing the concentration of reinforcement within a splice may induce other failure modes such as splitting.
- Additional research should be conducted using spliced full width slabs subjected to concentrated wheel loads similar to current highway bridge decks. This will help to evaluate the performance of an UHPC GFRP splice when longitudinal cracking (along the spliced bars) is present due to bending in both directions.
- Fatigue testing should also be conducted using concentrated wheel loads on spliced full width slabs. Cyclic load application should be done using a linear actuator rather than an MTS machine. This would allow continuous cycle application at a higher frequency better representing the loads experienced by a real bridge deck. More cycles could also be applied within a shorter time frame.
- Fatigue testing of UHPC splices should include additional stress ranges.
- The behaviour of UHPC splices under sustained loads requires further investigation.
- Other types of fibre reinforcement such as carbon and aramid fibres have yet to be investigated as a tensile lap splice in UHPC and should also be considered.
- The effect of bar casting position in UHPC is an important aspect that needs further research due to the settlement and bleeding characteristics of this concrete.

- Additional specimens should be tested using various depth to cover ratios and fibre volume fractions. The aim is to better understand the transverse cracking behaviour of concrete within the spliced region so that the MDT can be refined.
- A more accurate range is necessary for the modulus of displacement. Future bond tests using UHPC pullout tests and blocks should include means to measure the loaded end slip as well as the free end slip.
- Future testing of UHPC constructions joints should include various geometries for the joint interface such, as with shear keys, to improve the shear capacity and surface contact of the joint.
- Future testing for concrete compressive modulus should use a compressometer / extensometer instead of strain gauges to allow for readings after cracking of the concrete cylinder.

Appendix - Pullout and Hinged Beam Test Results

Table A.1: Pullout tests with loaded end slip

Researcher	Concrete Strength (MPA)	Bar Type	Diameter (mm)	Embedment Length (mm)	No. Bar Diameters Embedded	Surface Condition	Bar Modulus (GPA)	Bar Tensile Strength (MPA)	Cover (mm)	Maximum Bond Strength (MPA)	Free End Slip at Ultimate (mm)	Loaded End Slip at Ultimate (mm)	Failure Mode	Additional Comments
Aiello et al. (2007)	52.7	LM-GFRP	8.0	52.5	6.6	Fine Sand Coated	42.1	784	96	4.2	0.007	0.341	Pullout	No Confinement
Aiello et al. (2007)	52.7	LM-GFRP	8.0	52.2	6.5	Fine Sand Coated	42.1	784	96	3.4	0.014	0.298	Pullout	No Confinement
Aiello et al. (2007)	52.7	LM-GFRP	8.0	52.5	6.6	Fine Sand Coated	42.1	784	121	5.0	0.009	0.852	Pullout	No Confinement/ Modified Pullout
Aiello et al. (2007)	52.7	LM-GFRP	8.0	52.5	6.6	Fine Sand Coated	42.1	784	121	3.5	0.011	0.296	Pullout	No Confinement/ Modified Pullout
Aiello et al. (2007)	52.7	LM-GFRP	8.0	55.0	6.9	Coarse Sand Coated	42.1	784	96	3.9	0.093	0.389	Pullout	No Confinement
Aiello et al. (2007)	52.7	LM-GFRP	8.0	55.2	6.9	Coarse Sand Coated	43.1	784	96	3.4	0.065	0.396	Pullout	No Confinement
Aiello et al. (2007)	52.7	LM-GFRP	8.0	55.0	6.9	Coarse Sand Coated	44.1	784	121	3.7	0.010	0.702	Pullout	No Confinement/ Modified Pullout
Baena et al. (2009)	53.1	LM-GFRP	10.2	51.1	5.0	Sand Coated	45.0	778	95	17.5	0.079	1.979	Peeling off	No Confinement
Baena et al. (2009)	53.1	LM-GFRP	10.2	51.1	5.0	Sand Coated	45.0	778	95	16.0	0.040	1.931	Peeling off	No Confinement
Baena et al. (2009)	53.1	LM-GFRP	14.1	70.7	5.0	Sand Coated	46.0	782	93	16.8	0.122	1.883	Peeling off	No Confinement
Baena et al. (2009)	53.1	LM-GFRP	14.1	70.7	5.0	Sand Coated	46.0	782	93	15.4	0.059	2.054	Peeling off	No Confinement
Baena et al. (2009)	53.5	LM-GFRP	14.1	70.7	5.0	Sand Coated	46.0	782	93	15.1	0.057	1.791	Peeling off	No Confinement
Baena et al. (2009)	53.1	LM-GFRP	16.4	82.2	5.0	Sand Coated	46.0	803	92	22.2	0.294	3.111	Peeling off	No Confinement
Baena et al. (2009)	53.1	LM-GFRP	16.4	82.2	5.0	Sand Coated	46.0	803	92	21.6	0.242	1.913	Peeling off	No Confinement
Baena et al. (2009)	53.5	LM-GFRP	16.4	82.2	5.0	Sand Coated	46.0	803	92	22.6	N/A	2.401	Peeling off	No Confinement

Table A.2: Pullout tests with free end slip

Researcher	Concrete Strength (MPA)	Bar Type	Diameter (mm)	Embedment Length (mm)	No. Bar Diameters Embedded	Surface Condition	Bar Modulus (GPA)	Bar Tensile Strength (MPA)	Cover (mm)	Ultimate Capacity (MPA)	Free End Slip at Ultimate (mm)	Failure Mode	Additional Comments
Hossain et al. (2011)	100.0	HM	15.9	47.7	3	Sand Coated	64.1	1439	40	14.6	0.025	Pullout / Peeling Off	No Confinement
Hossain et al. (2011)	100.0	HM	15.9	47.7	3	Sand Coated	64.1	1439	60	16.8	0.090	Pullout / Peeling Off	No Confinement
Hossain et al. (2011)	100.0	HM	15.9	79.5	5	Sand Coated	64.1	1439	40	14.4	0.090	Pullout / Peeling Off	No Confinement
Hossain et al. (2011)	100.0	HM	15.9	79.5	5	Sand Coated	64.1	1439	40	12.2	0.027	Pullout / Peeling Off	No Confinement
Hossain et al. (2011)	100.0	HM	15.9	79.5	5	Sand Coated	64.1	1439	60	12.2	0.030	Pullout / Peeling Off	No Confinement
Hossain et al. (2011)	100.0	HM	15.9	79.5	5	Sand Coated	64.1	1439	60	16.4	0.090	Pullout / Peeling Off	No Confinement
Hossain et al. (2011)	145.0	HM	15.9	47.7	3	Sand Coated	64.1	1439	60	19.4	0.082	Pullout / Peeling Off	No Confinement
Hossain et al. (2011)	145.0	HM	15.9	79.5	5	Sand Coated	64.1	1439	40	11.4	0.040	Pullout / Peeling Off	No Confinement
Hossain et al. (2011)	145.0	HM	15.9	79.5	5	Sand Coated	64.1	1439	40	11.0	0.090	Pullout / Peeling Off	No Confinement
Hossain et al. (2011)	145.0	HM	15.9	79.5	5	Sand Coated	64.1	1439	60	11.1	0.082	Pullout / Peeling Off	No Confinement
Hossain et al. (2011)	145.0	HM	15.9	79.5	5	Sand Coated	64.1	1439	60	13.9	0.175	Pullout / Peeling Off	No Confinement
Hossain et al. (2011)	169.0	HM	15.9	47.7	3	Sand Coated	64.1	1439	60	14.9	0.036	Pullout / Peeling Off	No Confinement
Hossain et al. (2011)	169.0	HM	15.9	79.5	5	Sand Coated	64.1	1439	40	9.4	0.038	Pullout / Peeling Off	No Confinement
Hossain et al. (2011)	169.0	HM	15.9	79.5	5	Sand Coated	64.1	1439	40	8.1	0.015	Pullout / Peeling Off	No Confinement
Hossain et al. (2011)	169.0	HM	15.9	79.5	5	Sand Coated	64.1	1439	60	11.7	0.040	Pullout / Peeling Off	No Confinement
Hossain et al. (2011)	169.0	HM	15.9	79.5	5	Sand Coated	64.1	1439	60	10.6	0.082	Pullout / Peeling Off	No Confinement
Ametrano (2011)	45.0	LM	15.9	47.7	3	Sand Coated	48.2	751	60	14.3	0.050	Pullout / Peeling Off	No Confinement
Ametrano (2011)	57.0	LM	15.9	47.7	3	Sand Coated	48.2	751	60	15.3	0.059	Pullout / Peeling Off	No Confinement
Ametrano (2011)	71.0	LM	15.9	47.7	3	Sand Coated	48.2	751	40	19.7	0.109	Pullout / Peeling Off	No Confinement

Researcher	Concrete Strength (MPA)	Bar Type	Diameter (mm)	Embedment Length (mm)	No. Bar Diameters Embedded	Surface Condition	Bar Modulus (GPA)	Bar Tensile Strength (MPA)	Cover (mm)	Ultimate Capacity (MPA)	Free End Slip at Ultimate (mm)	Failure Mode	Additional Comments
Ametrano (2011)	71.0	LM	15.9	47.7	3	Sand Coated	48.2	751	60	20.6	0.147	Pullout / Peeling Off	No Confinement
Ametrano (2011)	100.0	LM	15.9	47.7	3	Sand Coated	48.2	751	60	13.8	0.111	Pullout / Peeling Off	No Confinement
Ametrano (2011)	100.0	LM	15.9	47.7	3	Sand Coated	48.2	751	60	16.6	0.067	Pullout / Peeling Off	No Confinement
Ametrano (2011)	100.0	LM	15.9	47.7	3	Sand Coated	48.2	751	40	13.9	0.040	Pullout / Peeling Off	No Confinement
Ametrano (2011)	100.0	LM	15.9	47.7	3	Sand Coated	48.2	751	60	18.1	0.147	Pullout / Peeling Off	No Confinement
Ametrano (2011)	100.0	LM	15.9	79.5	5	Sand Coated	48.2	751	40	15.4	0.179	Pullout / Peeling Off	No Confinement
Ametrano (2011)	100.0	LM	15.9	79.5	5	Sand Coated	48.2	751	40	13.2	0.116	Pullout / Peeling Off	No Confinement
Ametrano (2011)	100.0	LM	15.9	79.5	5	Sand Coated	48.2	751	60.0	10.6	0.021	Pullout / Peeling Off	No Confinement
Ametrano (2011)	100.0	LM	15.9	79.5	5	Sand Coated	48.2	751	60.0	13.7	0.090	Pullout / Peeling Off	No Confinement
Ametrano (2011)	102.0	LM	15.9	47.7	3	Sand Coated	48.2	751	60.0	13.5	0.080	Pullout / Peeling Off	No Confinement
Ametrano (2011)	102.0	LM	15.9	47.7	3	Sand Coated	48.2	751	60.0	30.5	0.080	Pullout / Peeling Off	No Confinement
Ametrano (2011)	143.0	LM	15.9	47.7	3	Sand Coated	48.2	751	40.0	20.1	0.034	Pullout / Peeling Off	No Confinement
Ametrano (2011)	143.0	LM	15.9	47.7	3	Sand Coated	48.2	751	60.0	23.1	0.103	Pullout / Peeling Off	No Confinement
Ametrano (2011)	143.0	LM	15.9	79.5	5	Sand Coated	48.2	751	40.0	16.9	0.069	Pullout / Peeling Off	No Confinement
Ametrano (2011)	143.0	LM	15.9	79.5	5	Sand Coated	48.2	751	40.0	15.4	0.149	Pullout / Peeling Off	No Confinement
Ametrano (2011)	143.0	LM	15.9	79.5	5	Sand Coated	48.2	751	60.0	17.1	0.114	Pullout / Peeling Off	No Confinement
Ametrano (2011)	143.0	LM	15.9	79.5	5	Sand Coated	48.2	751	60.0	18.9	0.072	Pullout / Peeling Off	No Confinement
Ametrano (2011)	156.0	LM	15.9	47.7	3	Sand Coated	48.2	751	40.0	13.3	0.048	Pullout / Peeling Off	No Confinement
Ametrano (2011)	156.0	LM	15.9	47.7	3	Sand Coated	48.2	751	60.0	15.1	0.069	Pullout / Peeling Off	No Confinement
Ametrano (2011)	156.0	LM	15.9	79.5	5	Sand Coated	48.2	751	40.0	10.4	0.063	Pullout / Peeling Off	No Confinement

Researcher	Concrete Strength (MPA)	Bar Type	Diameter (mm)	Embedment Length (mm)	No. Bar Diameters Embedded	Surface Condition	Bar Modulus (GPA)	Bar Tensile Strength (MPA)	Cover (mm)	Ultimate Capacity (MPA)	Free End Slip at Ultimate (mm)	Failure Mode	Additional Comments
Ametrano (2011)	156.0	LM	15.9	79.5	5	Sand Coated	48.2	751	40.0	10.7	0.063	Pullout / Peeling Off	No Confinement
Ametrano (2011)	156.0	LM	15.9	79.5	5	Sand Coated	48.2	751	60.0	11.5	0.030	Pullout / Peeling Off	No Confinement
Ametrano (2011)	156.0	LM	15.9	79.5	5	Sand Coated	48.2	751	60.0	11.8	0.065	Pullout / Peeling Off	No Confinement
Lee et al. (2008)	40.6	LM	12.7	50.8	4	Sand Coated	42.0	690	68.7	19.3	0.580	Pullout / Peeling Off	No Confinement
Lee et al. (2008)	40.6	LM	12.7	50.8	4	Sand Coated	42.0	690	68.7	23.6	0.250	Pullout / Peeling Off	No Confinement
Lee et al. (2008)	40.6	LM	12.7	50.8	4	Sand Coated	42.0	690	68.7	20.6	0.430	Pullout / Peeling Off	No Confinement
Lee et al. (2008)	56.3	LM	12.7	50.8	4	Sand Coated	42.0	690	68.7	22.2	0.210	Pullout / Peeling Off	No Confinement
Lee et al. (2008)	56.3	LM	12.7	50.8	4	Sand Coated	42.0	690	68.7	19.4	0.390	Pullout / Peeling Off	No Confinement
Lee et al. (2008)	56.3	LM	12.7	50.8	4	Sand Coated	42.0	690	68.7	21.5	0.430	Pullout / Peeling Off	No Confinement
Lee et al. (2008)	75.7	LM	12.7	50.8	4	Sand Coated	42.0	690	68.7	23.4	0.090	Pullout / Peeling Off	No Confinement
Lee et al. (2008)	75.7	LM	12.7	50.8	4	Sand Coated	42.0	690	68.7	24.7	0.080	Pullout / Peeling Off	No Confinement
Lee et al. (2008)	75.7	LM	12.7	50.8	4	Sand Coated	42.0	690	68.7	25.2	0.150	Pullout / Peeling Off	No Confinement
Lee et al. (2008)	92.4	LM	12.7	50.8	4	Sand Coated	42.0	690	68.7	23.4	0.100	Pullout / Peeling Off	No Confinement
Lee et al. (2008)	92.4	LM	12.7	50.8	4	Sand Coated	42.0	690	68.7	25.4	0.100	Pullout / Peeling Off	No Confinement
Lee et al. (2008)	92.4	LM	12.7	50.8	4	Sand Coated	42.0	690	68.7	26.2	0.130	Pullout / Peeling Off	No Confinement

Table A.3: RILEM beam tests with free end slip

Researcher	Concrete Strength (MPA)	Bar Type	Diameter (mm)	Embedment Length (mm)	No. Bar Diameters Embedded	Surface Condition	Bar Modulus (GPA)	Bar Tensile Strength (MPA)	Cover (mm)	Ultimate Capacity (MPA)	Free End Slip at Ultimate (mm)	Failure Mode	Additional Comments
Hossain et. al (2011)	71.2	HM	15.9	47.7	3	Sand Coated	64.1	1439	42	18.5	0.095	Pullout	Confinement
Hossain et. al (2011)	71.2	HM	15.9	79.5	5	Sand Coated	64.1	1439	42	14.5	0.135	Pullout	Confinement
Hossain et. al (2011)	115.5	HM	15.9	47.7	3	Sand Coated	64.1	1439	42	20.1	0.210	Pullout	Confinement
Hossain et. al (2011)	118.3	HM	15.9	79.5	5	Sand Coated	64.1	1439	42	17.4	0.125	Pullout	Confinement
Hossain et. al (2011)	157.4	HM	15.9	47.7	3	Sand Coated	64.1	1439	42	22.9	0.100	Pullout	Confinement
Hossain et. al (2011)	159.4	HM	15.9	79.5	5	Sand Coated	64.1	1439	42	17.9	0.130	Pullout	Confinement
Hossain et. al (2011)	162.6	HM	15.9	47.7	3	Sand Coated	64.1	1439	42	22.1	0.120	Pullout	Confinement
Hossain et. al (2011)	162.6	HM	15.9	79.5	5	Sand Coated	64.1	1439	42	16.4	0.170	Pullout	Confinement
Ametrano (2011)	71.2	LM	15.9	47.7	3	Sand Coated	48.2	751	42	22.7	0.110	Pullout	Confinement
Ametrano (2011)	71.2	LM	15.9	79.5	5	Sand Coated	48.2	751	42	22.3	0.465	Pullout	Confinement
Ametrano (2011)	71.2	LM	15.9	79.5	5	Sand Coated	48.2	751	42	19.1	0.200	Pullout	Confinement
Ametrano (2011)	116.8	LM	15.9	47.7	3	Sand Coated	48.2	751	42	26.0	0.225	Pullout	Confinement
Ametrano (2011)	113.8	LM	15.9	79.5	5	Sand Coated	48.2	751	42	19.9	0.210	Pullout	Confinement
Ametrano (2011)	113.8	LM	15.9	79.5	5	Sand Coated	48.2	751	42	20.0	0.185	Pullout	Confinement
Ametrano (2011)	147.5	LM	15.9	47.7	3	Sand Coated	48.2	751	42	24.0	0.155	Pullout	Confinement
Ametrano (2011)	148.8	LM	15.9	79.5	5	Sand Coated	48.2	751	42	19.3	0.085	Pullout	Confinement
Ametrano (2011)	148.8	LM	15.9	79.5	5	Sand Coated	48.2	751	42	23.3	0.030	Pullout	Confinement
Ametrano (2011)	164.5	LM	15.9	47.7	3	Sand Coated	48.2	751	42	29.8	0.175	Pullout	Confinement
Ametrano (2011)	158.8	LM	15.9	79.5	5	Sand Coated	48.2	751	42	20.0	0.230	Pullout	Confinement
Ametrano (2011)	162.7	LM	15.9	79.5	5	Sand Coated	48.2	751	42	21.6	0.095	Pullout	Confinement

References

Abrishami H.H., and Mitchell, D. (1996). "Analysis of Bond Stress Distributions in Pullout Specimens." *ASCE Journal of Structural Engineering,* 122(3): 255-261.

ACI Committee 440. (2004). *Guide Test Methods for Fiber-Reinforced Polymers (FRPs) for Reinforcing or Strengthening Concrete Structures*. ACI 440.3R-04. American Concrete Institute, Farmington Hills.

ACI Committee 440. (2006). *Guide for the Design and Construction of Structural Concrete Reinforced with FRP Bars*. ACI 440.1R-06. American Concrete Institute, Farmington Hills.

AFGC. (2002). *Ultra High Performance Fibre-Reinforced Concretes – Interim Recommendations*. Association Française de Génie Civil, Paris, France.

Aiello M.A., Leone M., Pecce M. (2007). "Bond Performances of FRP Rebars-Reinforced Concrete." *ASCE Journal of Materials in Civil Engineering*, 19(3): 205-213.

Alsayed S.H. (1998). "Flexural Behaviour of Concrete Beams Reinforced with GFRP Bars." *Cement and Concrete Composite*, 20(1): 1-11.

Aly, Ragi. (2006). "Tensile Lap Splicing of Fibre-Reinforced Polymer Reinforcing Bars in Concrete." *ACI Structural Journal*, 103(6): 857-864.

Aly, Ragi. (2007). "Stress Along Tensile-Lap Spliced Fibre Reinforced Polymer Reinforcing Bars in Concrete." *Canadian Journal of Civil Engineering*, 34(9): 1149-1158.

Ametrano, D. (2011). "Bond Characteristics of Glass Fibre Reinforced Polymer Bars in High Strength and Ultra High Performance Concrete." MASc Thesis, Department of Civil Engineering, Ryerson University, 2011.

Ametrano D., Hossain K.M.A., Lachemi M. (2011). "Bond Characteristics of Glass Fibre Reinforced Polymer Bars Embedded in High Strength and Ultra-High Strength Concrete." *Proceedings of CSCE 2nd International Engineering Mechanics and Materials Specialty Conference*, 14-17 June. Ottawa, Ontario.

ASTM Standard C39 (2009). "Standard Test Method for Compressive Strength of Cylindrical Concrete Specimens," ASTM International, West Conshohocken, PA, 2009, DOI: 10.1520/C0039_C0039M-09a, www.astm.org.

ASTM Standard C78 (2009). "Standard Test Method for Flexural Strength of Concrete (Using Simple Beam with Third-Point Loading)," ASTM International, West Conshohocken, PA, 2009, DOI:10.1520/C0078_C0078M-10, www.astm.org.

ASTM Standard C192 (2007). "Standard Practice for Making and Curing Concrete Test Specimens in the Laboratory," ASTM International, West Conshohocken, PA, 2007, DOI:10.1520/C0192_C0192M-07, www.astm.org.

ASTM Standard C469 (2002). "Standard Test Method for Static Modulus of Elasticity and Poisson's Ratio of Concrete in Compression," ASTM International, West Conshohocken, PA, 2002, DOI: 10.1520/C0469-02E01, www.astm.org.

Baena M., Torres L., Turon A., Barris C. (2009). "Experimental Study of Bond Behaviour Between Concrete and FRP Bars Using a Pull-Out Test." *Composites: Part B*, 40(8): 784-797.

Benmokrane B., Chaallal O., Masmoudi R. (1995). "Glass Fibre Reinforced Plastic (GFRP) Rebars for Concrete Structures." *Construction and Building Materials*, 9(6): 353-364.

Benmokrane B., El-Salakawy E., El-Gamal S., Goulet S. (2007). "Construction of an Innovative Concrete Bridge Deck Totally Reinforced with Glass FRP Bars: Val-Alain Bridge on Highway 20 East." *ASCE Journal of Bridge Engineering*, 12(5): 632-645.

Brzev S., Pao J. (2006). *Reinforced Concrete Design A Practical Approach*. Pearson Prentice Hall, Toronto.

Canadian Standards Association (CSA) (2002). *Design and Construction of Building Components with Fibre-Reinforced Polymers*. CAN/CSA-S806-02. CSA. Mississauga.

Canadian Standards Association (CSA) (2006). *Canadian Highway Bridge Design Code (CHBDC)*. CAN/CSA-S6-06. CSA, Mississauga.

Canadian Standards Association (CSA) (2009). *Concrete Materials and Methods of Concrete Construction*. CSA A23.1-09. CSA, Mississauga.

Cement Association of Canada (CAC) (2006). *Concrete Design Handbook*. CSA A23.3-04. CAC, Ottawa.

Chaallal O., Benmokrane B. (1996). "Fibre-reinforced Plastic Rebars for Concrete Applications." *Composites: Part B,* 27B(3-4): 245-252.

Chen Y., Davalos J.F., Ray I., Kim H. (2007). "Accelerated Aging Tests for Evaluations of Durability Performance of FRP Reinforcing Bars for Concrete Structures." *Composite Structures*, 78(1): 101-111.

Choi D., Ha S., Chun S. (2007) "Bond Stresses in Lap-Spliced RC Beams Using GFRP Bars: Unconfined Splice Test." *12th International Congress on Polymers in Concrete*. 27-28 Sept. Chuncheon, Korea: 525-533.

Choi D., Ha S., Chun S., Park Y., You Y. (2008). "Splice Length of GFRP Bars in Reinforced Concrete Slabs." *Proceedings of the 3rd ACF International Conference-ACF/VCA 2008*, 11-13 Nov. Ho Chi Minh City, Vietnam: 782-789.

Collins M.P., Mitchell D. (1997). *Prestressed Concrete Structures*. Response Publications, Ontario.

Darwin D., Zuo J., Tholen M., Idun E. (1996). "Development Length Criteria for Conventional and High Relative Rib Area Reinforcing Bars." *ACI Structural Journal*, 93(3): 347-359.

Davalos J.F., Chen Y., Ray I. (2008). "Effect of FRP Bar Degradation on Interface Bond with High Strength Concrete." *Cement & Concrete Composites*, 30(8): 722-730.

Ehsani M.R., Saadatmanesh H., Tao S. (1997). "Bond Behaviour of Deformed GFRP Rebars." *Journal of Composite Materials*, 31(14): 1413-1430.

El-Ragaby A., El-Salakawy E., Benmokrane B. (2006). "Experimental Investigation on the Fatigue Behaviour of GFRP Reinforced Concrete Bridge Deck Slabs." *Proceedings of the 1st International Structural Specialty Conference*, 23-26 May. CSCE, Calgary, Alberta.

El-Ragaby A., El-Salakawy E., Benmokrane B. (2007). "Fatigue Analysis of Concrete Bridge Deck Slabs Reinforced with E-glass/Vinyl Ester FRP Reinforcing Bars." *Composites Part B*, 38(5-6): 703-711.

El-Salakawy E., Benmokrane B., El-Ragaby A., Nadeau D. (2005). "Field Investigation of the First Bridge Deck Slab Reinforced with Glass FRP Bars Constructed in Canada." *ASCE Journal of Composites for Construction*, 9(6): 470-479.

Esfahani M.R., Kianoush M.R., Lachemi M. (2005). "Bond Strength of Glass Fibre Reinforced Polymer Reinforcing Bars in Normal and Self-Consolidating Concrete." *Canadian Journal of Civil Engineering*, 32(3): 553-560.

Esfandeh M., Sabet A.R., Rezadoust A.M., Alavi M.B. (2009). “Bond Performance of FRP Rebars with Various Surface Deformations in Reinforced Concrete.” *Polymer Composites*, 30(5): 576-582.

Graybeal B.A. (2006a). "Material Property Characterization of Ultra-High Performance Concrete". *U.S. Department of Transportation. Federal Highway Administration Publication No. FHWA-HRT-06-103*. Office of Infrastructure Research and Development, Mclean, VA.

Graybeal B.A. (2006b). "Structural Behaviour of Ultra-High Performance Concrete Prestressed I-Girders". *U.S. Department of Transportation. Federal Highway Administration Publication No. FHWA-HRT-06-115*. Office of Infrastructure Research and Development, Mclean, VA.

Graybeal B.A. (2007). “Compressive Behaviour of Ultra-High-Performance-Fibre-Reinforced Concrete.” *ACI Materials Journal*, 104(2): 146-152.

Hao Q., Wang Y., He Z., Ou J. (2009). “Bond Strength of Glass Fibre Reinforced Polymer Ribbed Rebars in Normal Strength Concrete.” *Construction and Building Materials*, 23(2): 865-871.

Harajli M., Abouniaj M. (2010). “Bond Performance of GFRP Bars in Tension: Experimental Evaluation and Assessment of ACI 440 Guidelines.” *Journal of Composites for Construction*, 14(6): 659-668.

Harryson P. (2003). “High Performance Joints for Concrete Bridge Applications.” *Structural Engineering International*, 13(1): 69-75.

High Performance Concrete Delivery Team. (2005). "High Performance Concrete Structural Designer’s Guide". *U.S. Department of Transportation. Federal Highway Administration Publication No. FHWA-ERC-02-006*. Office of Infrastructure Research and Development, Mclean, VA.

Holland T.C. (2005). "Silica Fume User’s Manual". *U.S. Department of Transportation. Federal Highway Administration Publication No. FHWA-1F-05-016*. Silica Fume Association, Lovettsville, VA.

Hossain K.M.A., Ametrano D., Mak C., Lachemi M. (2011). "Bond Strength and Development Length of GFRP Bars in Ultra-High Performance Concrete", *MTO Report*, May 2011, p89.

ISIS Canada. (2006). *ISIS Educational Module 2: An Introduction to FRP Composites for Construction*. Canada Research Network, Winnipeg.

ISIS Canada. (2007). *Reinforcing Concrete Structures with Fibre Reinforced Polymers: Design Manual No. 3*. Canada Research Network, Winnipeg.

Issa M.S., Metwally I.M., Elzeiny S.M. (2011). "Influence of Fibres on Flexural Behaviour and Ductility of Concrete Beams with GFRP Rebars." *Engineering Structures*, 33(5): 1754-1763.

JSCE. (1997). *Recommendation for Design and Construction of Concrete Structures Using Continuous Fibre Reinforcing Materials (Design)*. Concrete Library No. 30. JSCE, Japan.

Kanda T., Lin Z., Li V.C. (2000). "Tensile Stress-Strain Modeling of Pseudostrain Hardening Cementitious Composites." *ASCE Journal of Materials in Civil Engineering*, 12(2): 147-156.

KPM Industries. (2011). *HP-S10 Concrete Product Specification*. King Packaged Materials Company, Burlington.

Laoubi K., El-Salakawy E., Benmokrane B. (2006). "Creep and Durability of Sand-coated Glass FRP Bars in Concrete Elements Under Freeze/Thaw Cycling and Sustained Loads." *Cement & Concrete Composites*, 28(10): 869-878.

Larralde J., Silva-Rodriguez R. (1993). "Bond and Slip of FRP Rebars in Concrete." *ASCE Journal of Materials in Civil Engineering*, 5(1): 30-40.

Lee J.Y., Kim T.Y., Kim T.J., Yi C.K., Park J.S., You Y.C., Park Y.H. (2008). "Interfacial Bond Strength of Glass Fibre Reinforced Polymer Bars in High-Strength Concrete." *Composites: Part B*, 39(2): 258-270.

MacGregor J.G., Wight J.K. (2005). *Reinforced Concrete Mechanics and Design Fourth Edition.* Pearson Prentice Hall, New Jersey.

Mak C., Hossain K.M.A., Lachemi M. (2011). "Splice Lengths in Ultra High Performance Concrete." *Proceedings of CSCE 2nd International Engineering Mechanics and Materials Specialty Conference*, 14-17 June. Ottawa, Ontario.

Mendis P. (2003). "Design of High-Strength Concrete Members: State-of-the-Art." *Progress In Structural Materials*, 5(1): 1-15.

Moon D.Y., Sim J., Oh H.S., Benmokrane B. (2008). “An exploratory study of GFRP Rebar with Ribs Containing Milled Glass Fibres.” *Composites Part B*, 39(5): 882-890.

Okelo R. (2007). “Realistic Bond Strength of FRP Rebars in NSC from Beam Specimens.” *ASCE Journal of Aerospace Engineering*, 20(3): 133-140.

Okelo R., Yuan R.L. (2005). “Bond Strength of Fibre Reinforced Polymer Rebars in Normal Strength Concrete." *ASCE Journal of Composites for Construction*, 9(3): 203-213.

Okuma H., Nishikawa K., Iwasaki I., Morita T. (2006). “The First Highway Bridge Applying Ultra High Strength Fibre Reinforced Concrete in Japan.” *Proceedings of the 7th International Conference on Short & Medium Span Bridges*, 23-26 Aug. Montreal, Canada.

Pecce M., Manfredi G., Realfonzo R., Cosenza E. (2001). “Experimental and Analytical Evaluation of Bond Properties of GFRP Bars.” *ASCE Journal of Materials in Civil Engineering*, 13(4): 282-290.

Perry V., Royce M. (2010). “Innovative Field-Cast UHPC Joints for Precast Bridge Decks (Full-Depth Precast Deck Panels), Oneonta, NY – Design, Prototype Testing and Construction.” *Proceedings of the 2010 Concrete Bridge Conference*. 24-26 Feb. Phoenix, Arizona.

Perry V., Scalzo P., Weiss G. (2007) “Innovative Precast Deck Panels and Field Cast UHPC Joints For Bridge Superstructures – CN Overhead Bridge at Rainy Lake, Ontario.” *Proceedings of the CSCE 2007 Annual General Meeting & Conference,* 6-9 June. Yellowknife, Northwest Territories.

Pultrall. (2007). *V-ROD LM Specification*. Pultrall Inc., Thetford Mines, Quebec.

Pultrall. (2008). *V-ROD HM Specification*. Pultrall Inc., Thetford Mines, Quebec.

Pultrall. (2011). *V-ROD Product Guide Specification*. Pultrall Inc., Thetford Mines, Quebec.

Rajlic B. et al. (2010). “The Eagle River Bridge Superstructure Replacement.” *Proceedings of the 8th International Conference on Short and Medium Span Bridges*, 3-6 Aug. Niagara Falls, Canada.

RILEM. (1994). “RC5 Bond Test for Reinforcement Steel. 1. Beam Test, 1982”. *RILEM Recommendations for the Testing and Use of Construction Materials*: 213-217, London E & FN SPON.

Riley W., Sturges L., Morris D. (2007). *Mechanics of Materials: 6th Edition*. John Wiley & Sons, Inc., New Jersey.

Shah B.N., Sennah K., Kianoush M.R., Tu S., Lam C. (2006). "Flange-to-Flange Moment Connections for Precast Deck Bulb-Tee Bridge Girders." *PCI Journal*, Nov-Dec: 2-23.

Shah B.N., Sennah K., Kianoush M.R., Tu S., Lam C. (2007). "Experimental Study on Prefabricated Concrete Bridge Girder-to-Girder Intermittent Bolted Connections System." *ASCE Journal of Bridge Engineering*, 12(5): 570-584.

Tafraoui A., Escadeillas G., Lebaili S., Vidal T. (2009). "Metakaolin in the Formulation of UHPC." *Construction and Building Materials*, 23(2): 669-674.

Tastani S.P. and Pantazopoulou S.J. (2006). "Bond of GFRP Bars in Concrete: Experimental Study and Analytical Interpretation." *ASCE Journal of Composites for Construction*, 10(5): 381-391.

Tepfers, R. (1980). "Bond Stress Along Lapped Reinforcing Bars." *Magazine of Concrete Research*, 32(112): 135-142.

Tepfers, R. (1982). "Lapped Tensile Reinforcement Splices." *ASCE Journal of the Structural Division*, 108(ST1): 283-301.

Tepfers, R. and De Lorenzis, L. (2003). "Bond of FRP Reinforcement in Concrete – A Challenge." *Mechanics of Composite Materials*, 39(4): 315-328.

Thériault M. and Benmokrane B. (1998). "Effects of FRP Reinforcement Ratio and Concrete Strength on Flexural Behaviour of Concrete Beams." *ASCE Journal of Composites for Construction*, 2(1): 7-16.

Tighiouart B., Benmokrane B., Gao D. (1998). "Investigation of Bond in Concrete Members with Fibre Reinforced Polymer (FRP) Bars." *Construction and Building Materials*, 12(8): 453-462.

Tighiouart B., Benmokrane B., Mukhopadhyaya P. (1999). "Bond Strength of Glass FRP Rebar Splices in Beams Under Static Loading." *Construction and Building Materials*, 13(7): 383-392.

Wambeke B., Shield C. (2006). "Development Length of Glass Fibre Reinforced Polymer Bars in Concrete." *ACI Structural Journal*, 103(1):11-17.

Wille K., Kim D.J., Naaman A.E. (2010). “Strain-hardening UHP-FRC With Low Fibre Contents.” *Materials and Structures*, 44(3):583-598.

Won J., Park C., Kim H., Lee S., Jang C. (2008). “Effect of Fibres on the Bonds Between FRP Reinforcing Bars and High-Strength Concrete.” *Composites Part B*, 39(5): 747-755.